CLARKSON UNIVERSITY

Combined Magnetic Vector - Scalar Potential Finite Element Computation of 3D Magnetic Field and Performance of Modified Lundell Alternators in Space Station Applications

A Dissertation

by

Ren H. Wang

Department of Electrical and Computer Engineering

Submitted in partial fulfillment of the requirements

for the degree of

Doctor of Philosophy

(Engineering Science)

Feb. 27, 1991

Accepted by the Graduate School

DATE DEAN

The undersigned have examined the dissertation entitled

"Combined Magnetic Vector - Scalar Potential Finite Element Computation of 3D Magnetic Field and Performance of Modified Lundell Alternators in Space Station Applications,"

presented by **Ren H. Wang**, a candidate for the degree of Doctor of Philosophy, and hereby certify that it is worthy of acceptance.

Feb. 27, 1991
DATE

Nabeel A. O. Demerdash
ADVISER N. A. DEMERDASH

Peter W. Barber
EXAMINING COMMITTEE P. W. BARBER

Henry Domingos
H. DOMINGOS

Robert H. Gallagher
R. H. GALLAGHER

M. Lawrence Glasser
M. L. GLASSER

Abstract

A novel method of combined use of magnetic vector potential (MVP) based finite element (FE) formulations and magnetic scalar potential (MSP) based FE formulations for computation of three-dimensional (3D) magnetostatic fields is developed in this dissertation. This combined MVP-MSP 3D-FE method leads to considerable reduction by nearly a factor of 3 in the number of unknowns in comparison to the number of unknowns which must be computed in global MVP based FE solutions. This method allows one to incorporate portions of iron cores sandwiched in between coils (conductors) in current-carrying regions. Thus, it greatly simplifies the geometries of current carrying regions (in comparison with the exclusive MSP based methods) in electric machinery applications. A unique feature of this approach is that the global MSP solution is single valued in nature, that is, no branch cut is needed. This is again a superiority over the exclusive MSP based methods. A Newton-Raphson procedure with a novel concept of an adaptive relaxation factor was developed and successfully used in solving the 3D-FE problem with magnetic material anisotropy and nonlinearity. Accordingly, this combined MVP-MSP 3D-FE method is most suited for solution of large scale global type magnetic field computations in rotating electric machinery with very complex magnetic circuit geometries, as well as nonlinear and anisotropic material properties.

The combined MVP-MSP 3D-FE solution method, in conjunction with the state-space equations using the natural abc-frame of reference, forms a complete computer aided model to analyze and predict machine parameters and performances. This modeling tool was applied to 3D magnetic field analysis and machine performance computations of an example 14.3 kVA modified Lundell alternator. The energy perturbation approach was used in this investigation to compute machine winding inductances from 3D-FE computed magnetic field results. The effects of magnetic material nonlinearity and the space harmonics due to complex magnetic circuit geometries were fully included in the results of machine winding inductances. Results of computed open-circuit, short-circuit, as well as rated load and over-rated load conditions were found to be in excellent agreement with corresponding test values. In this research, the electromagnetic torque profiles including their ripples (harmonics) were computed in terms of terminal voltage and current profiles as well as stored magnetic energies. In addition, results of use of this modeling and computation method in a design alter-

ation, in which the stator stack length of the example alternator is stretched in order to increase voltage and volt-ampere rating, were studied in this investigation. These results demonstrate the inadequacy of some conventional 2D-based design concepts and the imperative of this type of 3D magnetic field modeling in analysis of such MLA class of machines. This includes almost all machines of the axial flux flow variety. The modeling technique and algorithm developed in this research can serve as an excellent design tool and means of gaining insight into the workings of such machines with truly 3D magnetic field patterns and complex magnetic circuit geometries. The generic nature of this modeling allows one to use it in design optimization and design synthesis studies.

Acknowledgements

The author wishes to express his sincere gratitude to Professor N.A. Demerdash whose encouragement, time, and guidance over the past four years have made this work possible. The support which Professor Demerdash offered, both technical and personal, are very much appreciated and will be always remembered.

The author wishes to acknowledge the help and useful discussions on technical issues related to vector partial differential equations from Professor. M.L. Glasser, Department of Mathematics and Computer Science, Clarkson University. Also, this author likes to express his gratitude to Professor R.H. Gallagher, President of Clarkson University, who raised many concerns, as well as provided useful guidance on basic concepts and principles of finite element methods.

In addition, this author wishes to extend his deep gratitude to all the other members of his Ph.D examining committee for their concerns and support. These committee members are Professor P.W. Barber, and Professor H. Domingos, Department of Electrical and Computer Engineering, Clarkson University.

This research project was sponsored by NASA Lewis research center under Grant No. NG3-818, and monitored by Mr. R. Secunde, Solar Dynamic Module Division, NASA Lewis Research Center, Cleveland, Ohio. The author wishes to express his gratitude to Mr. Secunde for his continuous support, useful discussions, as well as the generous encouragement given throughout this complex investigation.

Most important, the author owes deep appreciation and special thanks to his wife Ping, and his daughter Amanda. Without their patience, support, and encouragement, this author could not succeed in his graduate study.

Contents

List of Tables

List of Figures

Chapter 1

Introduction

1.1 Background of the Problem

It is a well established fact in the body of knowledge on the design of ac electric machinery that the higher the operating speed (frequency) of a given machine the lesser its weight and volume, for a given voltampere rating and a particular set of construction materials. The demand for generators with extra high voltampere to weight and/or volume ratios is most critical in aerospace applications. One of these possible applications is in the anticipated thermal portion of the electric power generation on board NASA's projected Space Station Freedom, namely the solar dynamic (SD) power module [1].

A prime candidate as an extra high speed (> 30,000 r/min) electric generator, for this SD module is the class of modified Lundell alternators (MLA) [2, 3], in which the lack of any rotating windings permits such extra high rated speeds. The main constructional feature of a particular 4-pole MLA is shown in the isometric cut-away cross-section of Figure (1.1.1). The longitudinal cross-section of an example 14.3 kVA, 4-pole, 36,000 r/min high speed MLA [3], as well as its 4-pole rotor's isometric of the magnetic portion are shown in Figures (1.1.2-a) and (1.1.2-b). This is in addition to a rotor photograph of Figure (1.1.3), of this example 14.3 kVA MLA.

In such MLAs, Figures (1.1.1) and (1.1.2), both the armature and field excitation windings are stationary. The armature winding is usually a conventional three-phase, double-layered winding housed in a conventional slotted and laminated armature core, the longitudinal cross-sections of which can be clearly seen in Figure (1.1.2-a). Meanwhile, the stationary field winding consists of two toroidal coils, which are

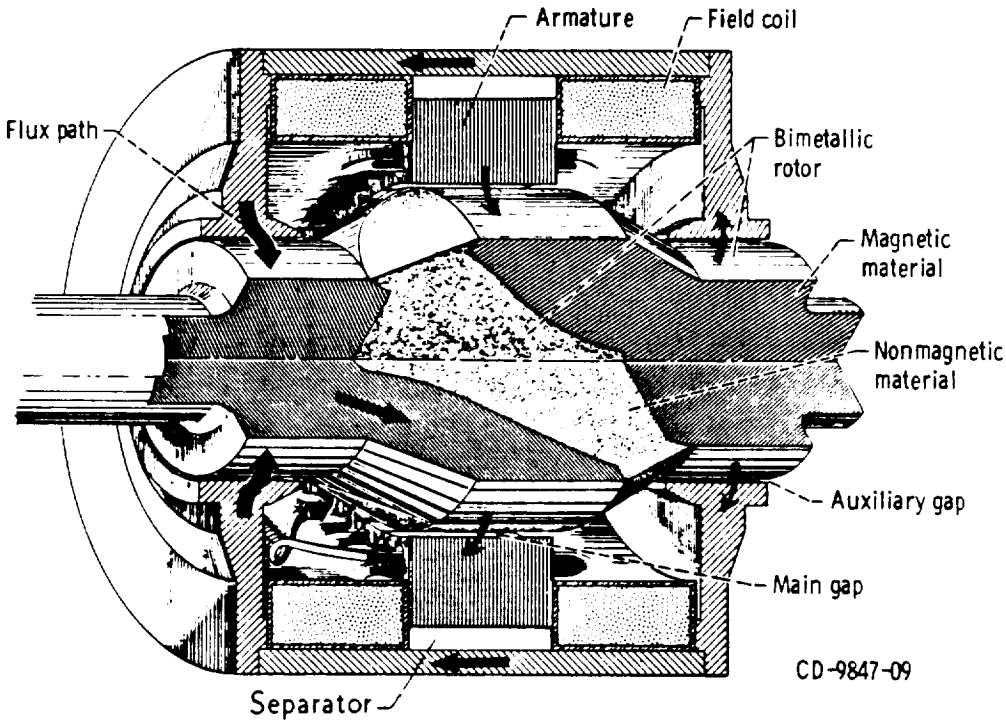

Figure (1.1.1) A Cut-Away View of Modified Lundell Alternator

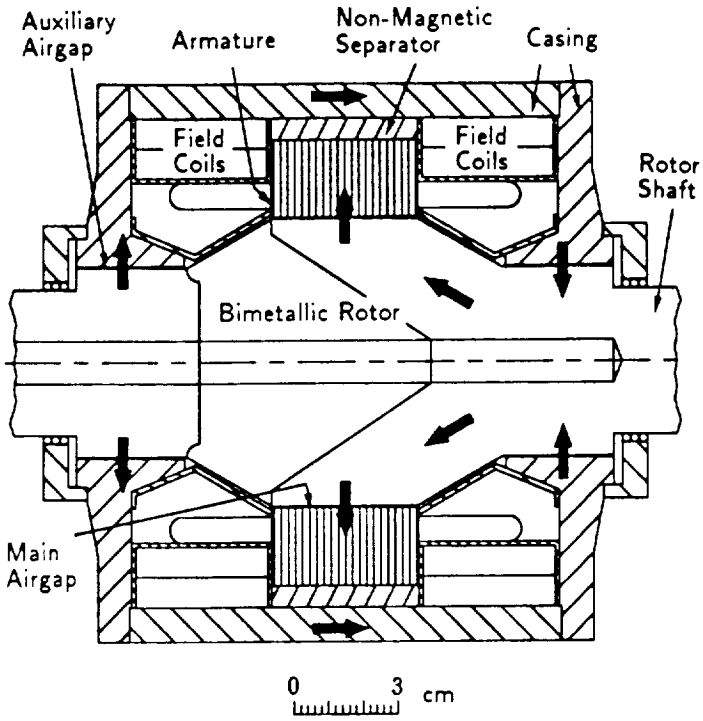

(a) Longitudinal Crosss-Section of the Example 14.3 kVA MLA

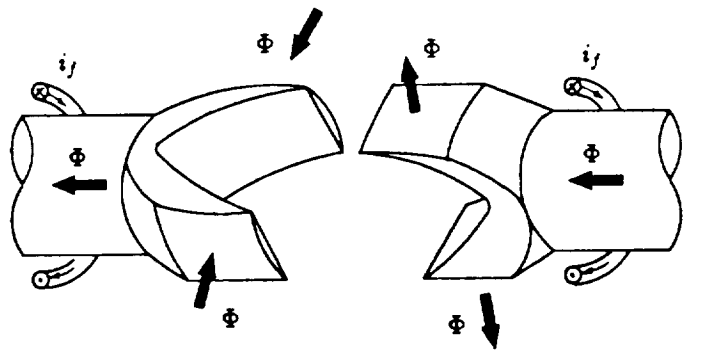

(b) Rotor Magnetic Portions ("Universal Joint" Like Structure)

Figure (1.1.2) The Example 14.3 kVA, 4-pole, 36,000 r/min High Speed MLA

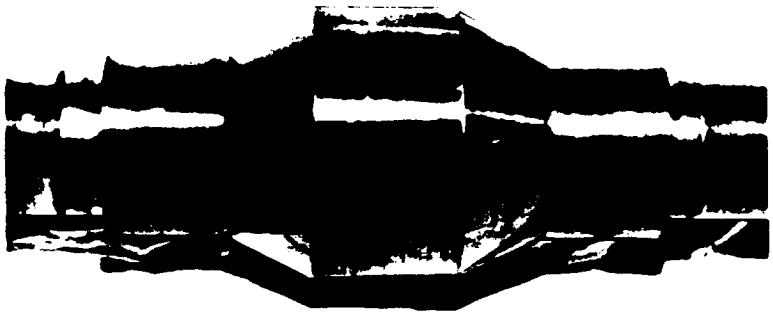

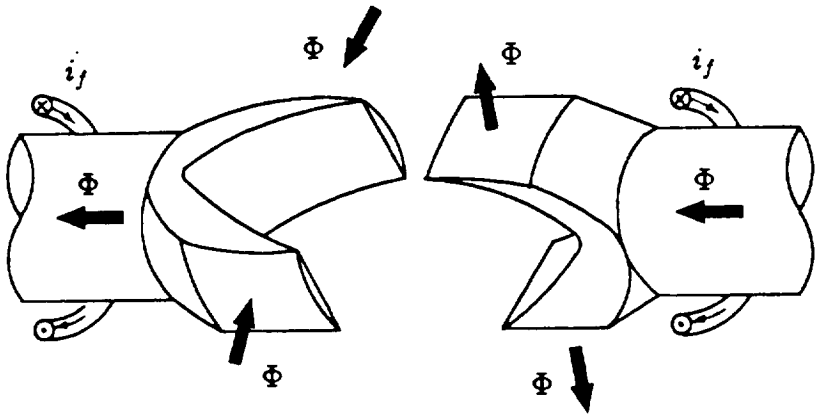

Rotor Magnetic Portions ("Universal Joint" Like Structure)

Figure (1.1.3) Rotor Photogragh of the Example 14.3 kVA MLA

located on both ends of the machine, surrounding the shaft as shown in Figure (1.1.1). The two toroidal field coils are much like two Tesla coils located at both ends of the rotor shaft.

The bimetallic rotor consists of two magnetic metal pieces which are brazed to a nonmagnetic metal piece filling the space in between. The two magnetic pieces form a shape which is very similar to that of a "universal joint" as shown in the isometric diagram of Figure (1.1.2-b). Hence one obtains the 4-pole structure of the example 14.3 kVA MLA. The field coils establish an axial magnetic flux in the rotor shaft which cannot flow axially from one magnetic portion of the rotor to the next due to the nonmagnetic metallic piece brazed to both magnetic pieces of the bimetallic rotor, Figure (1.1.2). Thus the magnetic flux in the shaft is forced to split into two equal portions, each flowing radially outward through the surfaces of the two (north) pole pieces of the rotor across the main airgap, Figure (1.1.2), and into the armature teeth and core, Figure (1.1.2-a). This flux flows circumferentially through the back of the unslotted portion of the laminated iron core to return radially inward through the armature teeth and across the main airgap, and into the two (south) pole pieces of the other magnetic portion of the rotor. See the flux flow arrows in Figure (1.1.2). This flux continues to flow axially through the rotor until it crosses one of the two auxiliary airgaps between the shaft surface and the end-bells. Flux flows axially from one end bell to the other through an outer magnetic casing in the form of a cylindrical shell, which forms, together with the end bells, an integral part of the return flux path from one end of the machine to the other across the two auxiliary airgaps. The rotation of the magnetic fields in this class of machines is caused by the rotation of the "universal joint like" magnetic portion of the bimetallic rotor structure, Figure (1.1.2-b), and not by the rotation of the field windings as in conventional synchronous machines with rotor mounted excitation.

It is obvious that the magnetic flux path and its corresponding spatial flux distribution in this class of MLAs are truly three dimensional (3D) in their nature. That is, the magnetic flux distributions are of simultaneously axial, radial and circumferential orientations, and are at variance with the usual, largely two dimensional (2D), flux patterns encountered in conventional electric machinery. The intrinsically 3D nature of the magnetic field distribution in such MLAs immensely complicates the design, performance computation and prediction processes. The concepts of performance computation which are based on 2D fields and axial symmetry, such as the

computation of voltages in straight armature conductors using the well known formula $l(\overline{v} \times \overline{B}) = lvB$, or the flux linkage concept ($4.44 f \phi N k_w$), or the proportionality of the voltampere rating to volume, $VA \propto D^2 L$, would not apply for such MLAs. Accordingly, one needs powerful computer modeling and computation methods to be able to thoroughly study the nature of the MLA's 3D magnetic field distributions. Meanwhile, new approaches of computation of machine parameters, induced voltages in windings, etc., which are based on the fact that the field is 3D in nature, have to be developed.

Therefore, this dissertation is directed towards the study and development of large scale nonlinear magnetic field three-dimensional finite element (3D-FE) computation methods, as well as machine performance simulation models, for rotating electric machinery with truly 3D magnetic field distributions such as these MLAs at hand. At this stage, a literature review of published work in the area of 3D magnetic field analysis and computation methods is most appropriate. This literature review also includes the review of publications of magnetic field computations on design and performance simulation of ac rotating electric machines.

1.2 Literature Search

Within the last two decades, many numerical modeling approaches for computation of magnetic fields have been developed by investigators and researchers. The fast advances of modern computer technologies made it possible for many numerical computation methods to be used in solving practical engineering problems. Publications on the subject of numerical computation of magnetic fields can be counted in the hundreds throughout the literature. It has been found that magnetic vector potential (MVP) and magnetic scalar potential (MSP) based finite element formulations are most widely used in applications to the magnetic field problems in electrical machines and devices.

In the 1960's, Erdelyi et al were among the earliest to attempt finite difference solutions of magnetostatic problems in electric machinery [4, 5, 6, 7, 8]. These authors used finite difference discretization for solving 2D partial differential equations which govern the MVP or MSP problem in the solution region. Relaxation techniques were applied to the potentials in solving the problems involving magnetic material

saturation in an iterative manner. Demerdash and Hamilton [9, 10] in 1972 developed a model using a finite difference approach for magnetic field computations in large turbo-generators, which related the internal magnetic field distributions directly to the load and terminal voltage conditions through an iterative process. A saturation iteration method based on computations of updated magnetic permeabilities obtained from the most recent flux densities and field intensities was implemented for solving this class of problems involving magnetic material nonlinerities.

In the early 1970's, Silvester and Chari [11, 12] applied the 2D finite element method to the solution of magnetostatic field problems. These authors used first order triangular elements to discretize the 2D solution region. The Newton-Raphson technique [11] was employed for the nonlinear magnetic field computation. Chari [13] has extended the 2D-FE method to the investigation of eddy current problems in 1974. The superiority of the finite element method over the finite difference method was demonstrated in papers by Demerdash and Nehl in 1976 [14] and 1979 [15]. These authors pointed out the strong advantages of the finite element method due to its relative ease in handling complex geometric contours, boundary conditions, as well as requirements of computer resources. Many other investigators have used 2D-FE methods in their research areas. Example publications on the subject of 2D-FE developments and applications can be found in references [16] through [20].

Numerical computation of 3D magnetostatic fields in electrical machines and devices appeared in the literature in the early 1970's. Holziner [21] developed a method based on integral formulations for solving 3D magnetic field problems. Kozakoff and Simons [22] have solved the differential equation associated magnetic scalar potential problems. Muller and Wolff [23], as well as Djurovic and Carpenter [24] have derived 3D finite difference formulations using MSP for magnetostatic computations.

Three dimensional magnetostatic field analysis using 3D-FE methods appeared in the literature in a paper by Guancial and DasGupta [25] in 1977. These authors used curl-curl MVP partial differential equation with the zero divergence constraint on the MVP to formulate their solution method. Also in 1977, Zienkiewicz et al [26] published a paper in which the authors introduced the concept of reduced MSP in solving magnetostatic field problems using the finite element method.

Simkin and Trowbridge [27], in 1980, developed the two scalar potential 3D-FE formulation, which successfully overcame the difficulty of the reduced scalar potential method of reference [26] in computing magnetic fields involving ferromagnetic mate-

rials. Later, the idea introduced by the two scalar potential method [27] was adopted by investigators in developing other scalar potential formulations [28, 29]. In 1982, Campbell et al [30] published a paper in which a 3D-FE MSP modeling method for permanent magnets was presented. A 3D finite difference computation method based on the concept of extended MSP was presented in a paper by Liese et al in 1984 [31].

In 1980, Demerdash et al [32] developed a 3D-FE formulation based on the unconstrained curl-curl MVP partial differential equation for solving 3D magnetostatic problems. The complete 3D-FE formulation and applications to a 1.5 kVA transformer problem as well as experimental verifications were reported in a series of papers by these authors [32, 33, 34, 35]. In this work, magnetic saturation was accounted for using the saturation iteration method developed earlier by Demerdash [9, 10]. Later, the same curl-curl 3D-FE formulation in conjunction with a Newton-Raphson technique for nonlinear magnetic field problems was developed by theses authors [36] in 1986.

Chari et al [37] published a paper in 1981 on 3D-FE magnetostatic field computation problem using a formulation based on the vector Poisson equation which stems from the curl-curl equation with an assumption of zero divergence of the MVP. In the same year, Coulomb [38] presented a formulation for a 3D-FE MVP solution method. In Coulomb's formulation, the author added an extra term to the functional used by Demerdash et al [32] that attempts to impose a zero divergence condition of the MVP.

These three formulations, that is Demerdash's, Chari's and Coulomb's, were discussed by many other investigators. Among these discussions are the papers by Kotiuga and Silvester [39], as well as Csendes et al [40]. The discussions were on the question of the uniqueness of the MVP computed from these three formulations. Many other comments and debates on this uniqueness issue appeared later in the literature. In 1982, Mohammed et al [41, 42] published papers showing the uniqueness of the MVP computed from the unconstrained curl-curl formulation [32] using first-order tetrahedral elements. In 1988, Hoole et al [43] showed test computation results using the above mentioned three different MVP 3D-FE formulations for an air-core coil problem. Hoole et al reported that the unconstrained curl-curl MVP formulation yielded the best results on the magnetic flux densities. Also in this work [43], the authors tried to explain the uniqueness of the numerical results from the unconstrained curl-curl MVP formulation of reference [32].

In recent years, pre-conditioned conjugate gradient methods [44, 45] have been introduced in the area of magnetic field computation for solving the large scale linear systems of equations resulting from 3D-FE analysis. Substantial savings of computer cpu times and memory requirements can be achieved by using this type of solver, which made it possible for one to contemplate solutions of large scale practical magnetic field problem using 3D-FE methods. These savings in computer resources are in comparison to those resource requirements associated with the commonly used solvers, which are based fully on Gauss elimination or Choleski decomposition.

Also, magnetic field 3D-FE computations using edge-elements were introduced by Bossavit [46], and subsequently have been reported on in 3D-FE magnetostatic field analysis by Barton and Csendes [47] in 1987. This method is based on the unconstrained curl-curl MVP equation in conjunction with tetrahedral edge-elements. The total number of unknowns computed in this formulation is equal to the total number of element edges. Meanwhile, among recent works of significance [48] introduced by Nehl and Field, is a method of adaptive refinement of first-order tetrahedral 3D-FE meshes to improve the accuracy of the unconstrained curl-curl MVP method [32].

In the category of application of numerical magnetic field computation methods to the simulation of the performance of ac rotating electric machines, most of the earlier works were centered on the calculation of conventional direct and quadrature axis reactances from 2D field computations. These $d-q$ type reactances (inductances) computed from 2D magnetic field solutions were used in conjunction with network phasor type calculations (frequency domain) to obtain machine performance characteristics. Demerdash et al in 1972 [9, 10], Fuchs and Erdelyi in 1973 [49], Chari et al in 1981 [50], and other investigators published papers of such work on ac machine performance computations. In these methods, the conventional steady state $d-q$ theory forms the basis, and the individual phase winding mmfs (current sheets), and inductances were assumed to vary sinusoidally with respect to the rotor position angle, thus yielding the well known rotor angle independent inductance (or reactance) terms L_d (or x_d), and L_q (or x_q).

In 1981 and 1982, Nehl, Fouad, and Demerdash [17, 18, 51, 52] developed a computer aided model for brushless dc machines, in which a 2D-FE magnetic field computation model and a time domain network model under the natural abc-frame of reference were used for machine performance simulation. In this work, 2D-FE magnetic field computations were performed for a series of rotor positions to obtain

various machine winding inductances as functions of the rotor position. The advantage of the natural abc-frame of reference used by these authors is that the effects of the space harmonics of the magnetic flux distribution can be fully included in studying such machine performance characteristics. Also, upon use of the abc-frame of reference, one directly deals with measurable machine armature phase currents such that the electronically switched power conditioner circuits or loads can be easily and directly incorporated into the simulation network of the whole machine-power electronic system, without the need for any interfacing mathematical transformations. In 1985, Nehl et al [53] applied this model to the study of brushless excitation systems for large turbine-generators. In 1987 Nyamusa and Demerdash [54, 55], and in 1988 Arkadan, Hijazi and Demerdash [56, 57] extended this model to study steady state and transient performance characteristics of various types of permanent magnet motors and generators.

In 1987 and 1989, Kulig et al [58, 59, 60] presented a method to study transient currents in generator windings and damper circuits caused by internal and external faults as well as abnormal operations using a natural abc-frame of reference simulation model. In these authors' work, 2D finite difference methods were employed to the computation of magnetic fields and associated machine inductances at a series of rotor positions.

Other applications of 2D-FE magnetic field computation methods to rotating electric machinery are found to be in electromagnetic torque and force as well as iron loss calculations. References [61] through [63] are examples of work on such research topics.

Publications in the area of application of 3D magnetic field analysis to electric machinery are found to be much less in numbers than those in the 2D magnetic field analysis area. The reasons for this are not only due to the complexity of the problem, but also due to the high cost of such 3D-FE analysis and computation for a practical rotating electric machine. It should be mentioned that between 1963 and 1966 Tegopoulos [64, 65, 66, 67, 68, 69] had used analytical methods to study 3D flux distributions and resulting forces on the end windings of turbine generators. In his work the concept of MVP was used to calculate the 3D distributions of flux densities. The volume current distributions in the winding end-turns were approximated by current sheets. Magnetic forces on the winding end-turns were studied. These methods are the predecessors to the numerical 3D magnetic field analysis in electric machinery.

In 1981, Weiss and Stephen [70] published a paper in which the magnetic fields in the end-turn region of a turbine-generator were studied using a finite elment based method. In this work, the 3D magnetic fields in the end-turn region were computed by superposition of a series 2D-FE solutions, to account for the spatial mmf harmonics, performed in a longitudinal cross-section ($r-z$ plane) of the machine. This method is fully based on the assumptions of magnetic linearity and axisymmetric geometry. In the same year, Davey and King [71] presented a MSP based method of a permeance grid concept to calculate the magnetic field distributions in the end-turn region of a turbine generator. These authors assumed that the MSP distributions in the end-turn region of the generator vary sinusoidally along the circumferential direction. Thus the magnetic field computation was performed by these authors using a 2D permeance grid in a longitudinal cross-section of the machine. Both of the above works represent efforts of using 2D field computations which approximate the actual 3D field problems being solved.

In the area of 3D-FE applications to rotating electric machinery, results of computation of the winding self inductance of a stepping motor using the two scalar potential method were presented by Simkin and Trowbridge [27] in 1980. Synchronous inductances of a superconducting machine were calculated from a MSP method in a paper by Zheng and Wang [28] in 1985. Brauer et al [72, 73] in 1985 and 1988 presented applications of 3D-FE magnetic field computations to an automotive Lundell alternator. The unconstrained curl-curl MVP formulation was used in these authors' 3D-FE model. The end-turn region of the stator winding was not included in this 3D-FE work. Magnetic field analysis using 3D-FE MVP formulations for actuators in automotive applications have been reported in papers by Brauer et al [74] in 1988, as well as Nehl and Field [48, 75] in 1989. However, up to the time of publication of this dissertation, an example of a complete model using 3D magnetic field computation for design, analysis, and prediction of performance of a rotating electric machine could not be found in the literature.

1.3 Definition of the Problem

The objective of this research is the development of computer-aided models for studying effects of various design changes on the machine parameters and performance characteristics of MLAs. The core of this computer-aided modeling is a 3D-FE mag-

netic field computation capability (3D-FE programs), which allows one to compute 3D magnetic field distributions throughout the entire magnetic circuit of this class of MLAs. This 3D-FE computation model can be applied to these MLAs at any desired machine operating conditions (different magnetic saturation levels) with the comprehensive capability for changing various dimensional (geometric) and material ($B - H$ characteristics) parameters for design synthesis and optimization purposes. Such magnetic field computations were to be performed under a series of rotor positions with respect to the stator. These rotor positions cover the entire ac cycle of the associated machine steady state operation. The 3D-FE magnetic field solutions yield the machine winding self and mutual inductances as functions of the rotor position angle. These inductances are used as key parameters in a time-domain, natural *abc*-frame of reference state model (state-space network programs) to simulate various machine performance characteristics. Such an integrated 3D-FE and state-space network computer-aided modeling is anticipated to form a powerful means for the design and analysis, as well as prediction of performance of the MLAs in space station solar dynamic power generation applications. To the best of this author's knowledge, such an effort of global 3D-FE magnetic field computation throughout the complete magnetic circuit of a rotating electric machine coupled to detailed machine performance calculations was carried out in this investigation for the first time.

The basic concept of this computer aided modeling can be used to calculate (predict) instantaneous voltages and currents of electric machinery under any steady state and dynamic conditions. However, the research effort in this dissertation is mainly focused on the simulation of the periodic, yet non-sinusoidal, voltage and current waveforms associated with the MLA's various windings, as well as electromagnetic torque profiles, under MLA steady state operating conditions.

The concepts and package of computer programs developed in this research was tested by their practical applications to a Y-connected, 4-pole, 36 stator slots, 1200 Hz, 36,000 r/min MLA, rated at 14.3 kVA, 0.75 lagging PF, 120 V (L-N). Comparisons between the computed results and laboratory test results [3] are presented in this dissertation whenever possible. The main design data of the example 14.3 kVA MLA is listed in Table (1.3.1) and illustrated in Figures (1.3.1) through (1.3.4). Further details on this example 14.3 kVA MLA can be found in references [2] and [76].

As an initial step towards the development of a successful 3D magnetic field computation model, a thorough investigation of existing 3D-FE magnetic vector potential

Table (1.3.1): Main Design Data of the Example 14.3 kVA MLA

A	Number of Poles	4
	Rated Speed	36,000 r/min
	Frequency	1200 Hertz
	Rated Terminal Voltage	120 Volts (Line to Neutral)
	Rated Output	14.3 kVA (0.75 P.F.)
	Total Weight	51 Pounds
	Electromagnetic Weight	35 Pounds
B	Stator	
	Circuits	4
	Slots	36
	Conductor	5 Strands - No. 24 AWG
	Turns per Coil	9
	Number of Slots Between Coil Sides Plus One	6
	Line to Neutral Resistance	0.0322 Ω (Measured)
	Stack Length	1.65 Inches
C	Rotor	
	Weight	11 Pounds and 15 Ounces
	Outside Diameter	3.26 Inches
	Pole Length	1.65 Inches
D	Fields	
	Conductor	No. 17 AWG
	Total Turns	722
	Resistance	4.85 Ω (Measured)
E	Airgaps	
	Length of Main Airgap	0.02 Inches
	Length of Auxiliary Airgap	0.02 Inches
D	Materials	
	Rotor Poles	SAE 4340
	Rotor Interpole Section	Inconel 718
	Stator Laminations	0.004 Inch AL 4750
	Frame	Annealed 1010 Steel
	Conductors	Copper
	Non-Magnetic Separator	Copper

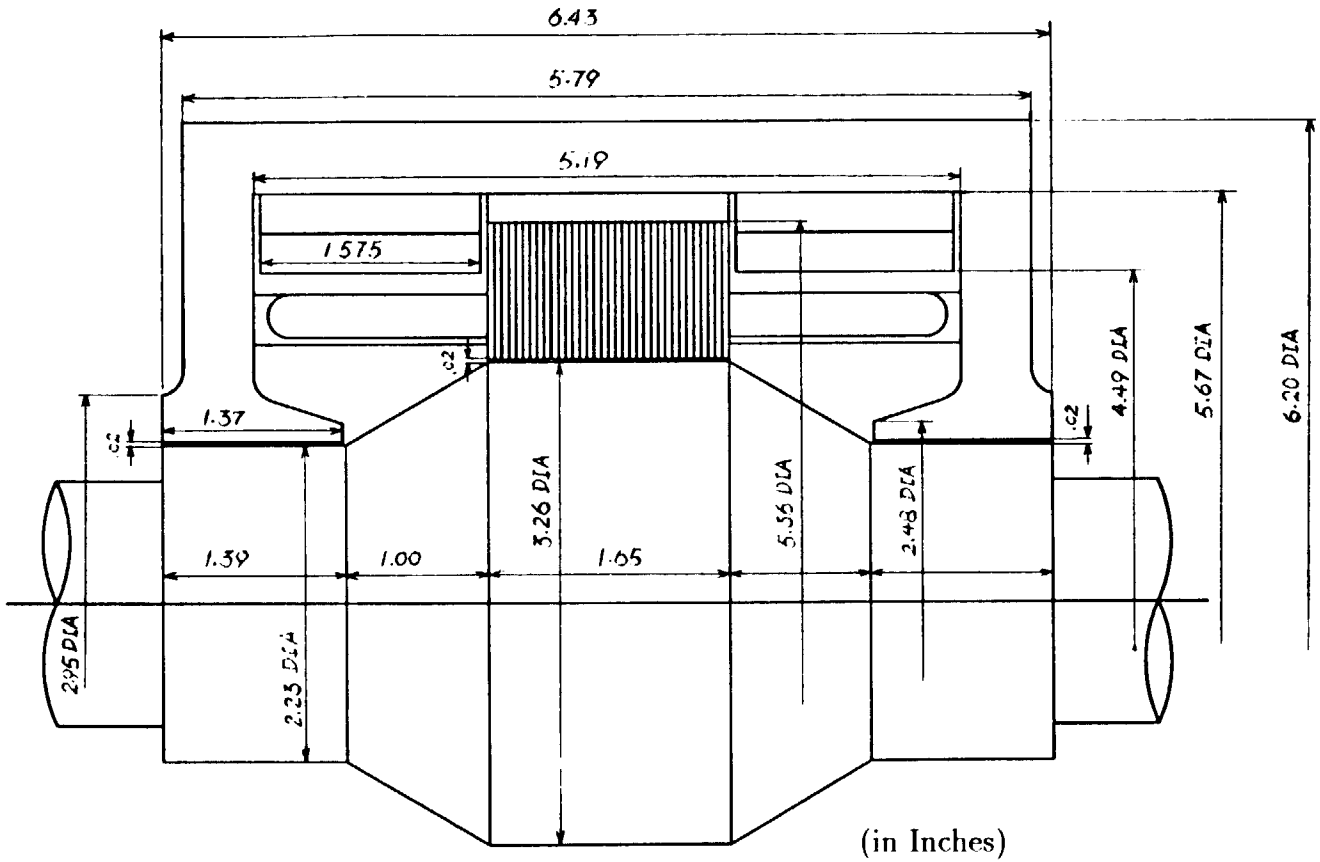

Figure (1.3.1) Main Geometric Dimensions of the Example 14.3 kVA MLA

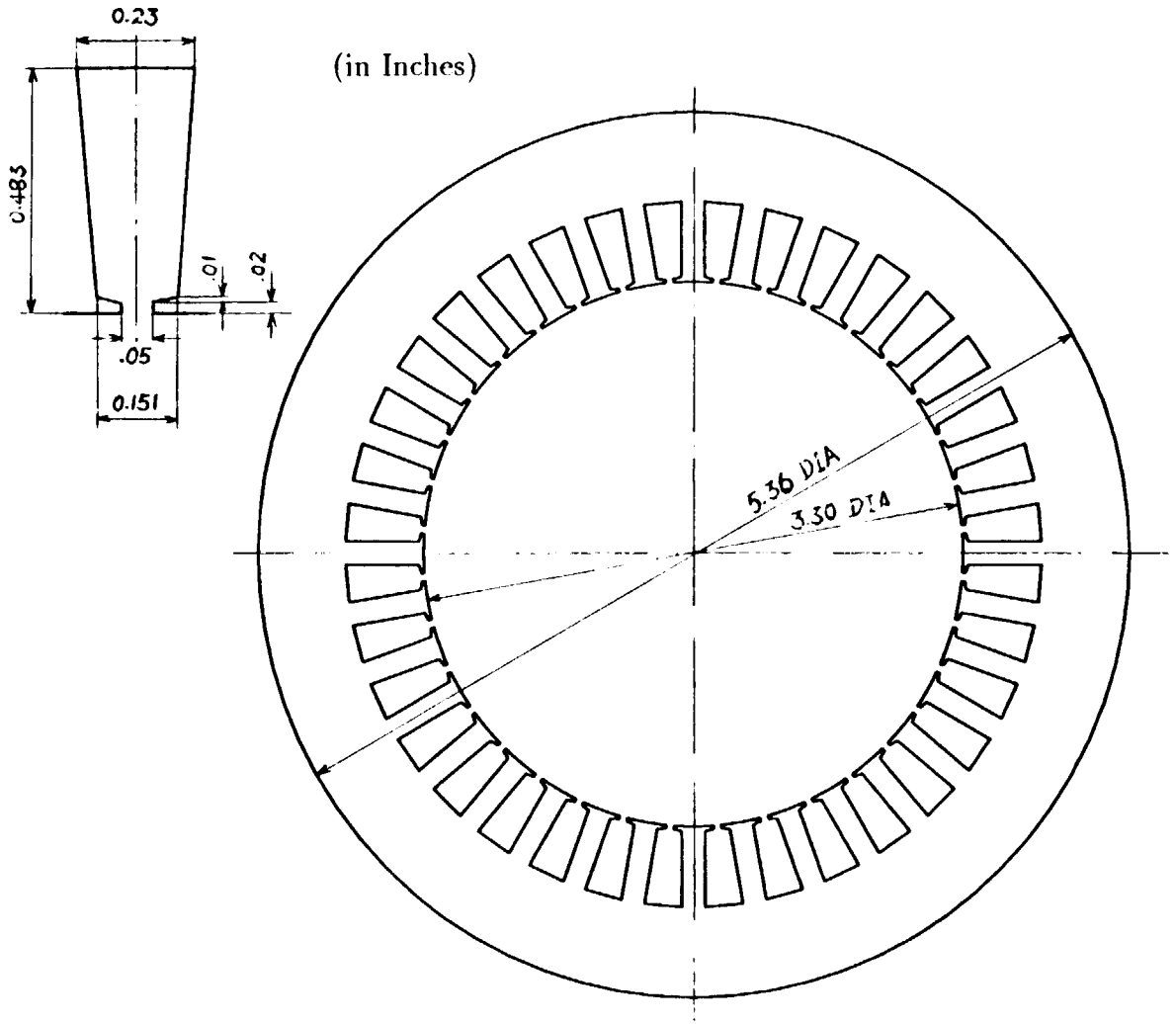

Figure (1.3.2) Dimensions of the Stator Core Lamination

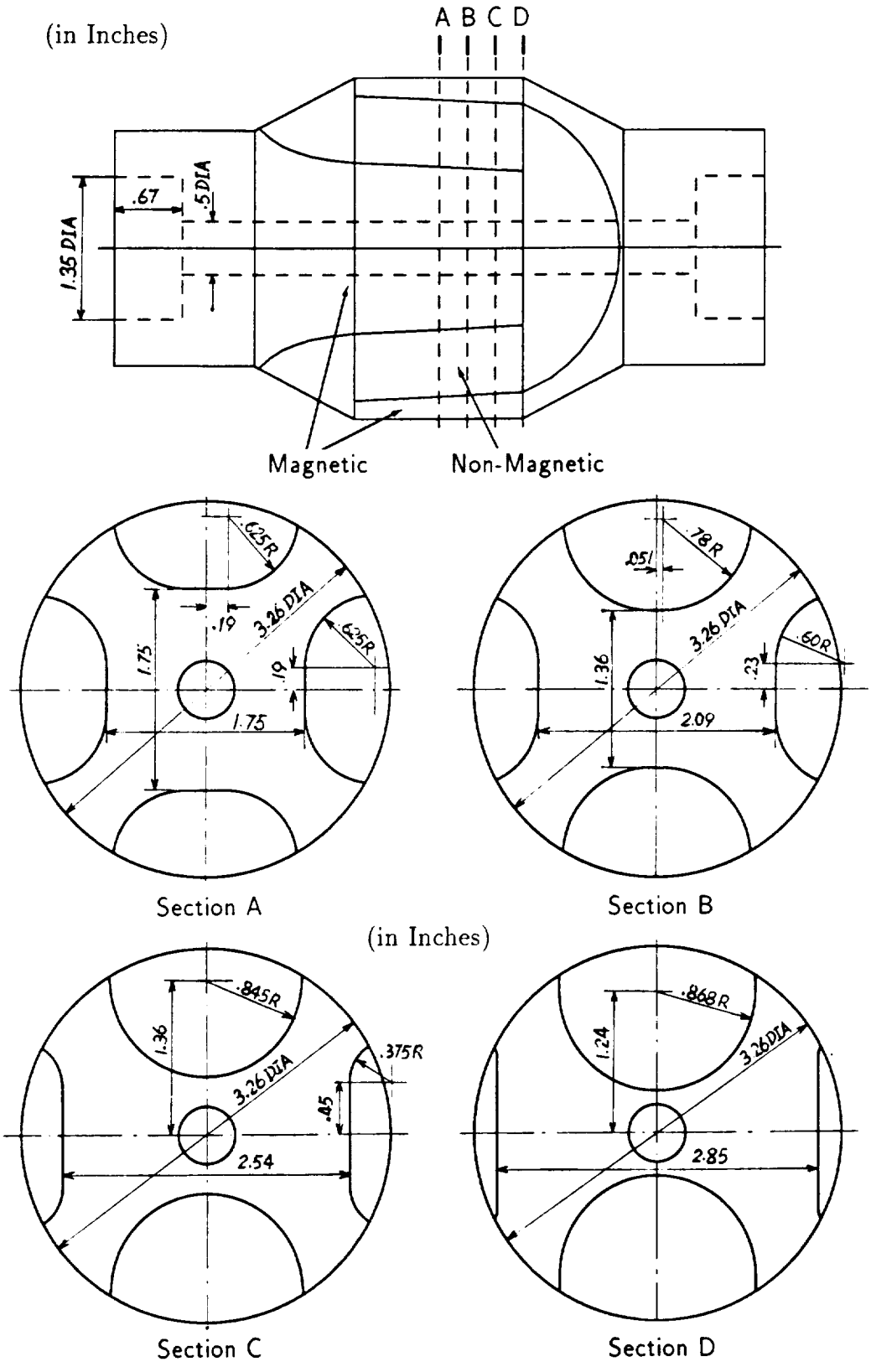

Figure (1.3.3) Dimensions of the Bimetallic Rotor

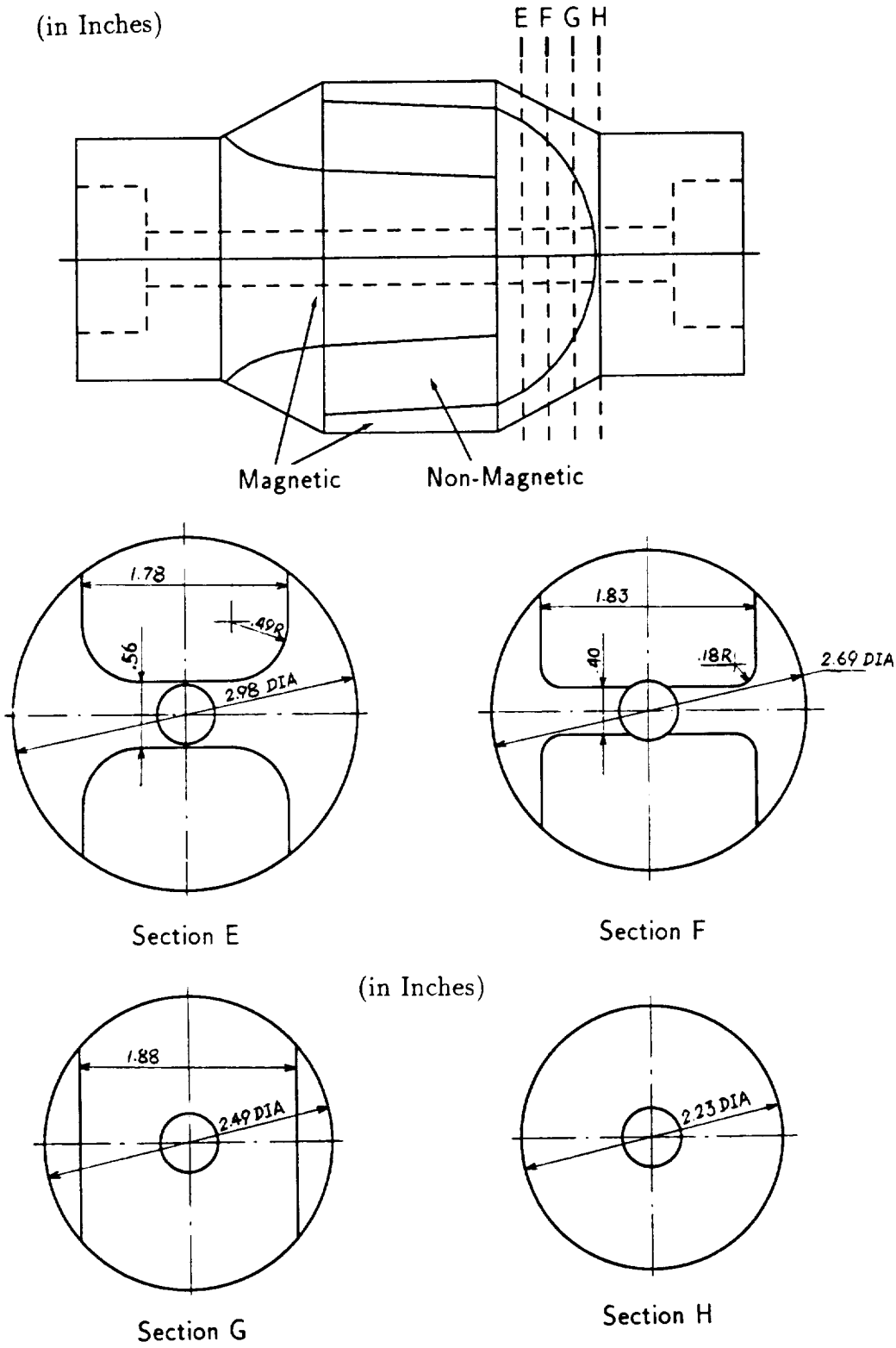

Figure (1.3.4) Dimensions of the Bimetallic Rotor

(MVP) formulations was carried out. Experimental computations were performed using three existing methods [32, 33, 34, 38, 37] to assess their validity and accuracy. It was found by this author that among the three existing 3D-FE MVP formulations only the unconstrained curl-curl formulation [32, 33, 34] yielded stable solutions for problems which involve the side by side presence of air and iron materials. Furthermore, this author found some numerical difficulties associated with the use of the first-order finite elements in the solution of the unconstrained curl-curl MVP method. Thus, these existing 3D-FE MVP formulations cannot be directly employed as the basic computation method for the MLA problem at hand. Details on these aspects can be found in Section 2.1 of Chapter 2 in this dissertation, as well as in references [77] and [78].

An investigation of the existing 3D-FE MSP formulations was also carried out to assess the possibility of using existing MSP based 3D-FE formulations for this MLA problem. The advantage of the MSP based formulations is that there is only one unknown at each node in a resulting finite element grid, which leads to approximately one third of the number of unknowns that must be computed in solutions based on MVP FE formulations. However, due to the difficulties stemming from the inherent incapability of handling volume current distribution in the MSP formulations, the existing MSP methods introduce extreme difficulties in their applications to problems involving very complex geometries and volume current distributions, which is precisely the case in rotating electric machines of the type at hand. A thorough study centered on the two scalar potential method [27] is given in Section 2.2 of Chapter 2 in this dissertation.

Hence, an innovative method of combined use of magnetic vector and scalar potentials, which will be referred to from this point forward in this dissertation as the combined MVP-MSP method, was developed to form the core of this computer-aided modeling effort. In this method, the unconstrained curl-curl MVP formulation with second-order finite elements is used to compute the curl component of the magnetic field intensity in the current-carrying regions of the MLA, while the concept of MSP is used throughout the entire solution region to complete the total magnetic field computation. This innovative method takes advantage of the desirable characteristics of both the exclusive MVP and MSP based formulations. This combined MVP-MSP method was found to be most suited for large scale 3D magnetic field problems in rotating electric machines. The theoretical development of this combined MVP-MSP

method, as well as the implementation of the associated finite element formulation, were carried out in this research, and are detailed in Chapter 3 and Chapter 4.

The developed 3D-FE model is required to have the ability to handle magnetic material nonlinearities and anisotropies. This is because the magnetic circuits of such MLAs are saturable, and the armature cores of such machines are laminated, which results in unequal magnetic permeances in axial versus circumferential and radial orientations. Meanwhile, methods of 3D-FE gridding must be studied and developed to discretize the global solution volume including the extremely difficult geometries of the bimetallic rotor and armature winding end-turn region in this class of MLAs. Also, gridding methods which allows the linking of the stator and rotor 3D-FE grids at any desired rotor to stator relative position needed to be developed in the course of this work, see Chapters 5 and 6. Details on the application of the combined MVP-MSP based 3D-FE model to the computation of magnetic fields in the example 14.3 kVA MLA are given in Chapters 6 and 7.

Again, the main interest of this research is in the simulation of the periodic, yet non-sinusoidal, voltage and current waveforms, as well as the other performance characteristics of such MLAs under various operating conditions. Based on the literature review in the previous section, the concept of time-domain, *abc*-frame of reference state modeling was adopted to form the basis of the machine performance simulation model. Such an *abc*-frame of reference state model allows a full inclusion of the space harmonics associated with machine parameters as obtained from the global 3D-FE magnetic field solutions, as well as the time harmonics in the current and voltage waveforms of the various computed results. Flux linkages were used as the state variables in the simulation model of this investigation. Accordingly, non-sinusoidal winding currents and voltages were calculated from the resultant flux linkages. Details on the development of this state space model are given in Chapters 8 and 9. Also, methods of calculation of electromagnetic torque profiles including torque ripples are detailed in Chapter 9.

This developed state space model was used to compute the open-circuit and short-circuit characteristics, as well as the rated and over-rated load performances of the example 14.3 kVA MLA. Results and experimental verifications are given in Chapters 7 through 9. Finally, conclusions and recommendations for future work are defined in Chapter 10 of this dissertation.

Chapter 2

Survey of 3D Magnetic Field Finite Element Formulations

Basic formulations of 3D-FE magnetostatic field computations have been introduced since the late 1970s. Among these formulations, are two magnetic potential procedures, the magnetic vector potential approach, MVP, and the magnetic scalar potential approach, MSP. In both formulations the continuity of the normal component of the flux density, $\overline{B}$, and the tangential component of the field intensity, $\overline{H}$, are satisfied automatically throughout the solution region (volume). This is accomplished without having to force such continuities at the interfaces between different material regions when the magnetic field is solved for directly.

In Maxwell's equations, which form the basis of both formulations, the magnetostatic fields are expressed in terms of flux density, $\overline{B}$, and field intensity, $\overline{H}$, as follows:

$$\nabla \times \overline{H} = \overline{J} \tag{2.0.1}$$

$$\nabla \cdot \overline{B} = 0 \tag{2.0.2}$$

where $\overline{J}$ is the source current vector. The constitutive relations between the magnetic flux density and the magnetic field intensity can be written as follows:

$$\overline{H} = \overline{\overline{\nu}} \cdot \overline{B} \tag{2.0.3}$$

$$\overline{B} = \overline{\overline{\mu}} \cdot \overline{H} \tag{2.0.4}$$

where $\overline{\overline{\nu}}$, and $\overline{\overline{\mu}}$, are tensors describing the general inhomogeneous, anisotropic reluctivity and permeability of the medium, respectively.

Mathematically, the solenoidal nature of Equation (2.0.2) allows one to express flux density, $\overline{B}$, by a curl operating on another vector field. In this case the vector field is the MVP, $\overline{A}$. Thus, $\overline{B}$, can be expressed in terms of $\overline{A}$ as follows:

$$\overline{B} = \nabla \times \overline{A} \tag{2.0.5}$$

By substituting for $\overline{B}$ from Equation (2.0.5) into Equation (2.0.3), and further substituting the result into Equation (2.0.1), one obtains the following:

$$\nabla \times (\overline{\overline{\nu}} \cdot \nabla \times \overline{A}) = \overline{J} \tag{2.0.6}$$

Equation(2.0.6), in conjunction with appropriate boundary conditions, defines the magnetic field problem in terms of the MVP. Final determination of the magnetic flux density, $\overline{B}$, can be achieved through Equation (2.0.5) by solving for the vector potential $\overline{A}$. Equation (2.0.6) is referred to henceforth as the curl-curl MVP equation, which serves as the basis for various 3D-FE MVP formulations that will be reviewed in Section 2.1. The disadvantage of a MVP based FE solution, as compared with a MSP based approach, is that three degrees of freedom have to be computed at every node of a given FE grid, which requires much longer computer time and larger storage (memory) requirements than the MSP methods.

Meanwhile, the concept of MSP was introduced into magnetic field computations in a similar manner to that by which the electric scalar potential was introduced in electrostatic field problems. In a solution region where the excitation current density, $\overline{J}$, equals zero, Equation (2.0.1) becomes

$$\nabla \times \overline{H} = 0 \tag{2.0.7}$$

Equation (2.0.7) is characteristic of irrotational vector fields. Since any irrotational vector field can be mathematically described as a gradient of a scalar field, one can write the following:

$$\overline{H} = -\nabla \phi \tag{2.0.8}$$

where, ϕ is the MSP. By substituting Equation (2.0.8) into Equation (2.0.4), and

further substituting the result into Equation (2.0.2) one obtains the following:

$$\nabla \cdot (\overline{\overline{\mu}} \nabla \phi) = 0 \tag{2.0.9}$$

Equation (2.0.9), which is in the form of Laplace's equation, together with the accompanying boundary conditions, defines the MSP boundary value problem. This formulation is attractive for FE solutions because it is written in terms of only one variable (one degree of freedom) at each node. Unfortunately, most practical engineering problems involve some electric current distributions in the establishment of a magnetic field. In such cases Equation (2.0.9) cannot be used directly to solve such problems, unless approximations regarding the volume distribution of the source currents or other special treatments are undertaken.

A survey of existing finite element MVP based and MSP based formulations was performed. As a complementary part to this survey, several test problems were computed using the formulations which seemed to have potential as candidate methods for the main 3D magnetic field problem which is the focus of this work. Results, as well as theoretical and/or numerical difficulties explored during this survey activity are reported, and discussed in the following sections of this chapter.

At the end of this chapter, as a culmination of this survey and the exploratory examples, an innovative concept is introduced. It consists of a mix of magnetic vector and scalar potentials. This concept enables the solution of large scale 3D magnetic field problems which involve extremely complex physical geometries, and difficult material topologies, such as the 3D magnetostatic field within the class of MLAs conducted in this research.

2.1 Three Dimensional Finite Element Magnetic Vector Potential Formulations

2.1.1 Three Existing 3D-FE MVP Formulations (Demerdash's, Coulomb's, and Chari's Formulations)

As mentioned earlier (Section 1.2), there are three well known MVP formulations for finite element computation of 3D magnetic field problem, see references [32, 33], [38],

and [37].

The first formulation was developed by Demerdash et al, in 1980 [32, 33]. In Demerdash's 3D-FE formulation, the curl-curl MVP equation, in conjunction with the associated boundary conditions, was used to solve the magnetic field problem. This equation, without any constraint on the divergence of the MVP, can be re-written here as follows:

$$\nabla \times (\overline{\overline{\nu}} \cdot \nabla \times \overline{A}) - \overline{J} = 0 \tag{2.1.1}$$

where, again, $\overline{\overline{\nu}}$ is the tensor of magnetic reluctivity, and $\overline{J}$ is the distributed source current density vector. The functional used in Demerdash's 3D-FE formulation, whose minimum corresponds to the solution of Equation (2.1.1), can be written as

$$F(\overline{A}) = \int_V [\frac{1}{2} (\overline{H} \cdot \overline{B}) - \overline{J} \cdot \overline{A}] \, dv. \tag{2.1.2}$$

This 3D-FE approach is referred to henceforth as the unconstrained curl-curl MVP formulation. In Demerdash's work, first order tetrahedral finite elements were used for discretization of the global solution region, V. Excellent agreement between the computational and experiment results was reported by the authors in their applications to linear magnetic problems (without magnetic material saturation) [34]. Excellent results were subsequently reported in cases involving nonlinear magnetic materials [35, 36]. Anisotropic reluctivity due to laminated iron-cores was easily accommodated in this formulation by setting of the reluctivity tensor along and perpendicular to the planes of the magnetic core laminations.

Applications of this unconstrained curl-curl formulation to magnetic field problems in electrical machines were also reported by other investigators [72]. This first attempt by Demerdash and his colleague to solve linear and nonlinear magnetic field problems using 3D-FE methods was followed by several discussions and rebuttal papers on the question of the uniqness of the vector potential, $\overline{A}$, obtained from this curl-curl formulation and the associated solutions. This uniqueness issue will be discussed in Section 2.1.3.

The second formulation was reported by Coulomb (no relation to the well known Coulomb of the Coulomb's Law and Coulomb's Gauge) in 1981 [38]. Coulomb's formulation makes use of an approach in which one imposes a constraint that seeks to enforce zero divergence of $\overline{A}$ in the curl-curl MVP formulation. Accordingly, Coulomb's

functional is of the form (compare with Equation (2.1.2))

$$F(\overline{A}) = \int_V [\frac{1}{2}(\overline{B} \cdot \overline{H}) - \overline{J} \cdot \overline{A} + \lambda(\nabla \cdot \overline{A})^2] \, dv \tag{2.1.3}$$

where λ is a parameter, commonly referred to as a penalty factor, which sights to set the Coulomb Gauge condition, $\nabla \cdot \overline{A} = 0$, in the solution.

Coulomb and supporters [39, 40] claimed that adding such a divergence term to the functional of the original unconstrained curl-curl MVP formulation is equivalent to forcing a zero divergence of $\overline{A}$ throughout the field solution region, and hence, a unique solution of $\overline{A}$ can be guaranteed. Despite the fact that Coulomb's formulation has been referred to in numerous papers, to the best of this author's knowledge, no numerical results on any practical engineering problem, which contains a mix of air and iron materials, has ever been reported in the literature.

The third MVP finite element formulation was presented by Chari, et al [37], in 1981. In Chari's formulation, the medium material was assumed to have homogeneous and isotropic permeability. This allows one to move the reluctivity term (ν) in Equation (2.1.1) outside the curl-curl operation. Division of both sides of the equation by ν, yields the following:

$$\nabla \times (\nabla \times \overline{A}) = \mu \overline{J} \tag{2.1.4}$$

Equation (2.1.4) can be further split into two parts by the vector identity operation as follows:

$$\nabla \times (\nabla \times \overline{A}) = \nabla(\nabla \cdot \overline{A}) - \nabla^2 \overline{A} = \mu \overline{J} \tag{2.1.5}$$

The term, $\nabla(\nabla \cdot \overline{A})$, in the above equation was removed by Chari et al by a claim that the zero divergence condition, $\nabla \cdot \overline{A} = 0$, must hold for any magnetic potential in engineering problems.

Obviously, the assumption about homogeneous and isotropic permeability restricts Chari's formulation from applicability to many electrical machinery problems which necessarily involve nonlinear material permeabilities due to magnetic saturation, as well as anisotropy due to the presence of laminated iron cores. Besides, contrary to Chari's declaration, zero divergence is not a necessary condition for the solution of the type of bounded magnetic vector potential problems for which his 3D

finite element formulation was intended. This will be shown in Section 2.1.2.

The removal of the divergence term in Equation (2.1.5) reduces the curl-curl equation to a vector Poisson's equation as follows:

$$\nabla^2 \overline{A} = -\mu \overline{J} \tag{2.1.6}$$

The functional utilized by Chari in his formulation can be written as follows:

$$F(\overline{A}) = \int_V [\ \frac{\nu}{2}(\nabla A_x \cdot \nabla A_x + \nabla A_y \cdot \nabla A_y + \nabla A_z \cdot \nabla A_z) - \overline{J} \cdot \overline{A}\ ]\ dv \tag{2.1.7}$$

Element equations of the above three FE formulations, which are used to form the global linear systems in the following finite element examples, are listed for reader's convenience in Appendix (A).

2.1.2 Test Computations and Comparisons on Existing 3D-FE MVP Methods

The above methods are now applied in the solution of some test examples. A similar work of such comparison, but performed only on a simple air-core problem, was reported by Hoole et al [43].

The first example is a coil problem, the detailed design of which is found in reference [80]. This coil is surrounded by air (free space) as shown in Figure (2.1.1). The solution region covered by the 3D-FE grid in Figure (2.1.1) is taken as one octant of the whole coil structure and its surrounding air. Three approaches, namely Demerdash's [32, 33], Coulomb's [38], and Chari's [37], are applied to this problem. Results of the computation of the magnetostatic field of this coil at an excitation current, $I = 5A$, are reported in Table (2.1.1). In addition, Figure (2.1.2) shows the plots, on the grid surfaces, of the equipotential lines, $|\ \overline{A}\ |$, obtained from the three above mentioned methods.

The calculated results in Table (2.1.1) include the following physical quantities and parameters:

(1) The total magnetic energy computed by $\frac{1}{2}\int_V \overline{A} \cdot \overline{J}\ dv$,

(2) The total magnetic energy computed by $\frac{1}{2}\int_V \overline{B} \cdot \overline{H}\ dv$,

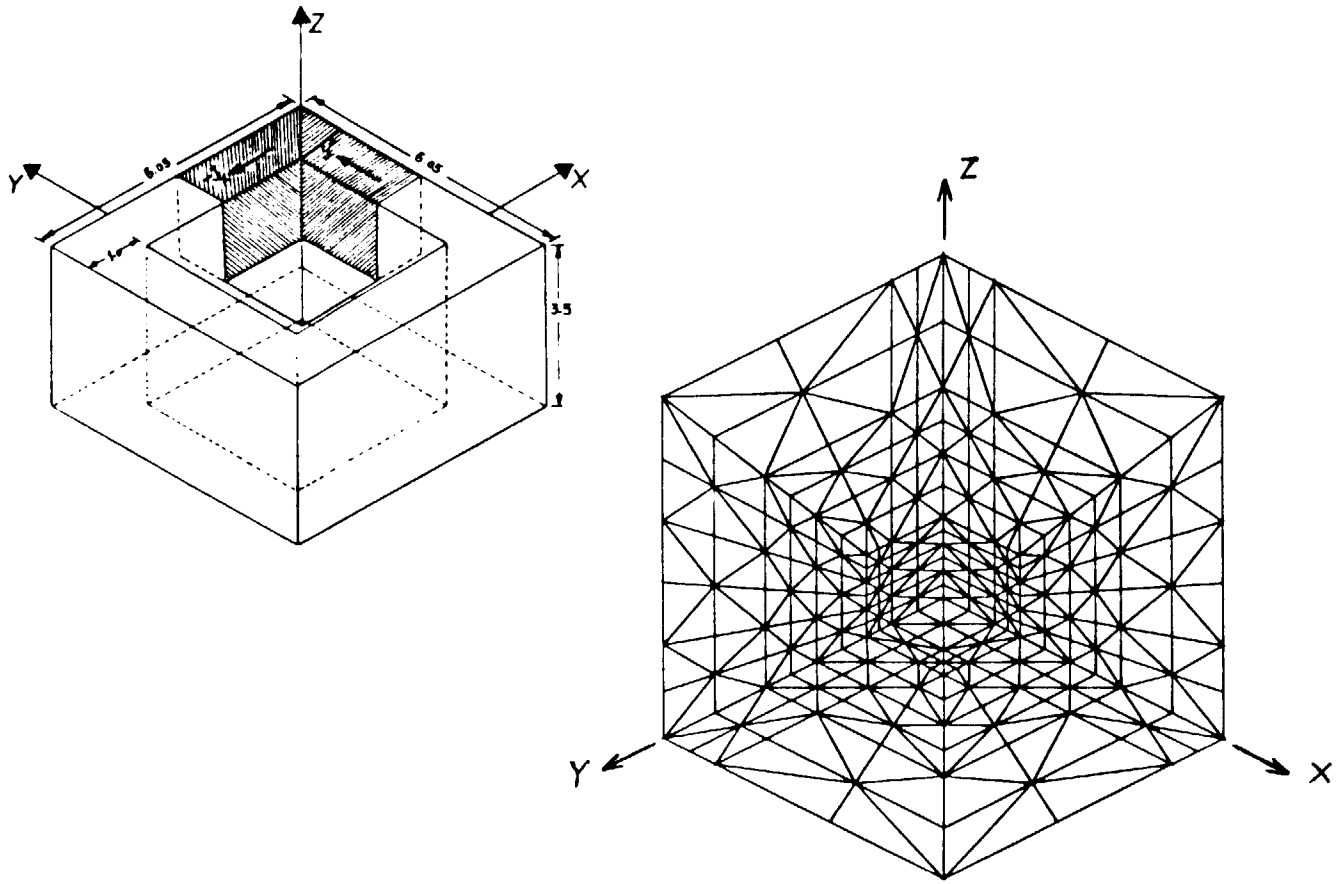

Figure (2.1.1) Coil Example and Its First-Order FE Grid

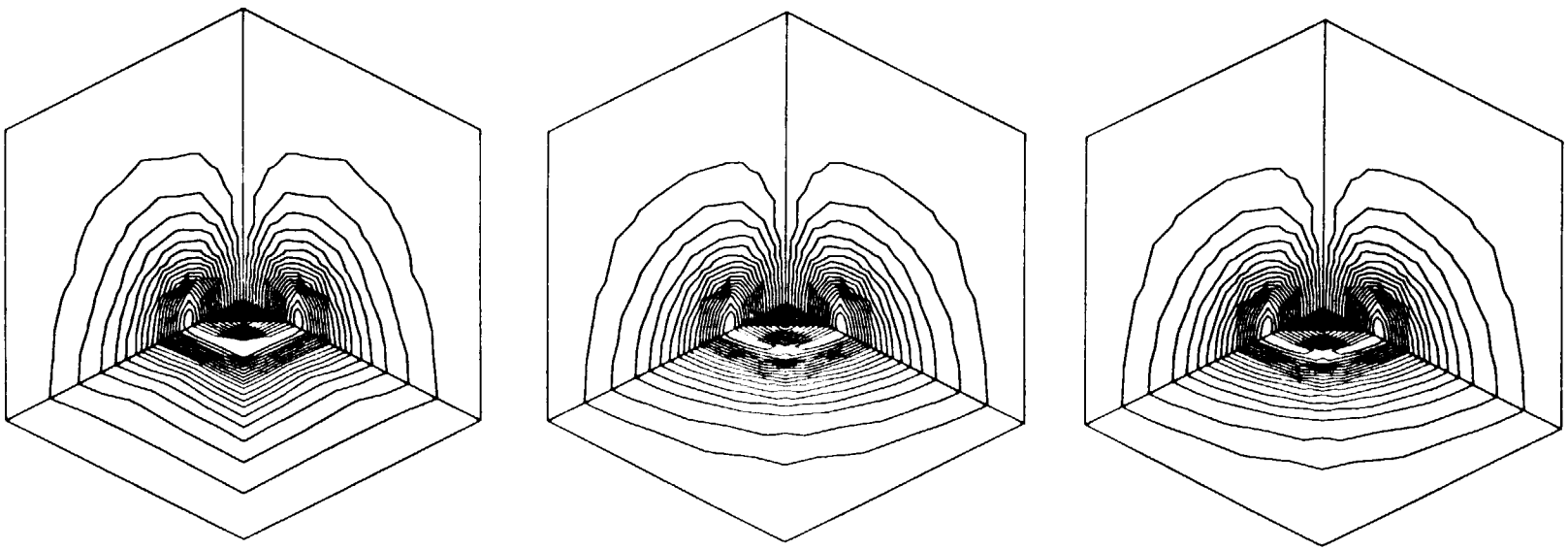

Result of Demerdash's Formulation

Result of Coulomb's Formulation

Result of Chari's Formulation

Figure (2.1.2) Plots of Equipotential Lines of Magnitude of MVP on Grid Surfaces

Table (2.1.1): Coil Results (I = 5.0 A)

Formulation	Demerdash's	Coulomb's	Chari's
Energy from $\frac{1}{2}\int \overline{A}\cdot\overline{J}dv$ (J)	0.1167	0.1142	0.1142
Energy from $\frac{1}{2}\int \overline{B}\cdot\overline{H}dv$ (J)	0.1167	0.1142	0.1142
Maximum $\mid \nabla\times\overline{A}\mid (T)$	0.03977	0.04014	0.04014
Maximum $\mid \nabla\cdot\overline{A}\mid (T)$	0.01303	0.00499	0.00499
Max. $\mid \frac{\nabla\cdot\overline{A}}{\nabla\times\overline{A}}\mid$	5.88	2.23	2.23
Ave. $\mid \frac{\nabla\cdot\overline{A}}{\nabla\times\overline{A}}\mid$	0.533	0.239	0.239
Calculated Inductance (H)	0.0746	0.0726	0.0726
Measured Value of Inductance:		0.0734 (H)	

(3) The highest value of calculated elemental flux density, Max. $| \nabla \times \overline{A} |$,

(4) The highest value of calculated divergence of the vector potential, Max. $| \nabla \cdot \overline{A} |$,

(5) The highest value of the ratio of the divergence to the curl of the vector potential, Max. $| (\nabla \cdot \overline{A})/(\nabla \times \overline{A}) |$, calculated at the centroids of the elements,

(6) The weighted average value of the ratio of the divergence to the curl of the vector potential, Ave. $| (\nabla \cdot \overline{A})/(\nabla \times \overline{A}) |$, calculated at the centroids of the elements (the weighting factors are the elemental volumes), and

(7) The terminal inductances.

The values of the divergence of $\overline{A}$ shown in Table (2.1.1) are calculated from the resultant vector potential at the centroid of each element. The following is the equation used for the divergence calculation:

$$\begin{aligned} \nabla \cdot \overline{A} &= \sum_{i=1}^{4} \nabla \cdot (N_i A_{ix} \hat{a}_x + N_i A_{iy} \hat{a}_y + N_i A_{iz} \hat{a}_z) \\ &= \sum_{i=1}^{4} (\frac{\partial N_i}{\partial x} A_{ix} + \frac{\partial N_i}{\partial y} A_{iy} + \frac{\partial N_i}{\partial z} A_{iz}) \end{aligned} \tag{2.1.8}$$

where A_{ix}, A_{iy}, and A_{iz} are the components of the calculated nodal vector potentials, and the N_i's are the finite element shape functions calculated at the centroids of the elements.

It can be seen that the three methods yield similar results on total stored magnetic energy and on maximum flux density magnitude, Max. $\nabla \times A$. The coil inductances deduced from stored energy are in agreement with the laboratory test value obtained [80] within a reasonable error margin. However, the maximum divergence $(\nabla \cdot \overline{A})$ has a non-negligible value (nearly 38.5% of that obtained in solutions based on Demerdash's method) in both the Chari and Coulomb solutions. A zero divergence is a basic condition on both of these formulations.

The second example is a 1.5 kVA, 120/277 V, shell-type transformer, the detailed design of which can be found in references [34, 80]. The structure of the transformer, and the tetrahedral grid which occupies one octant of the whole transformer magnetic circuit region, are shown in Figure (2.1.3). Since Chari's method [37] does not include magnetic material saturation, a lower excitation current of about 20% of its rated magnetizing current was chosen to represent an unsaturated iron core condition.

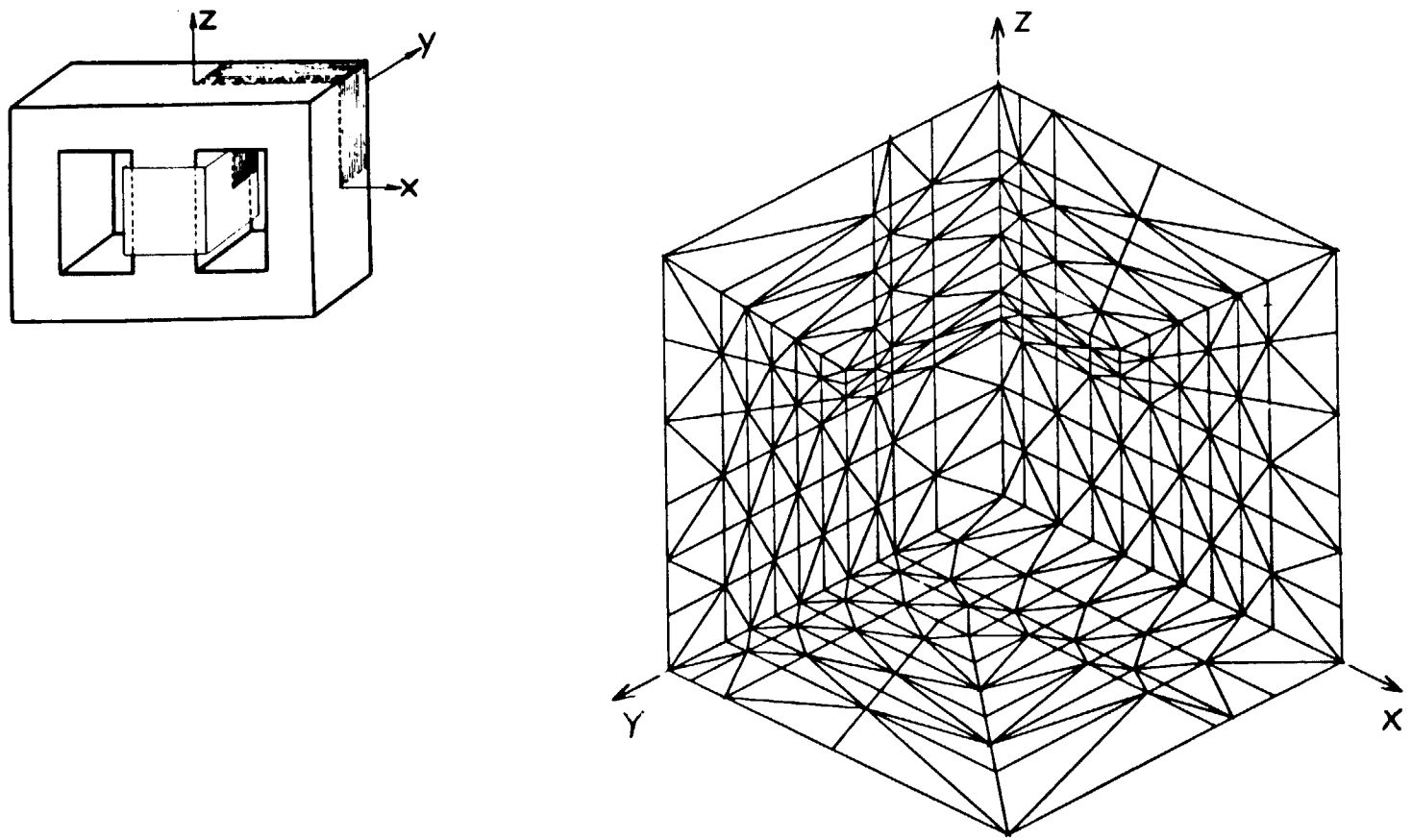

Figure (2.1.3) 1.5 kVA Shell-Type Transformer and Its First-Order FE Grid

A further limitation of Chari's formulation is the fact that the inherent anisotropy introduced by the presence of iron lamination on material permeability cannot be included. That meant the iron reluctivities in the x, y, and z directions have to be taken equal, that is $\nu_x = \nu_y = \nu_z = \nu_{iron}$.

The same set of physical quantities and parameters previously calculated in the case of the coil example, namely the flux densities, stored energy and device inductances, were calculated in this example. The results are summarized in Table (2.1.2). The MVP equipotential lines, $| \overline{A} |$, computed from Demerdash's formulation, are shown in Figure (2.1.4).

As can be seen in Table (2.1.2), Demerdash's formulation gives a result for the unsaturated magnetizing inductance of the transformer which is in reasonable agreement with the measured inductance value from the laboratory test. However, the other two methods [38, 37] yield totally unreasonable values of the stored energy, the flux density, ($\overline{B} = \nabla \times A$), and the unsaturated magnetizing inductance. It is obvious that both Coulomb's [38] and Chari's [37] methods totally break down in iron cores of the type given in this transformer problem.

The third example is a simplified magnetic circuit of the 14.3 kVA Modified Lundell Alternator discussed earlier in Chapter 1. A cut-away picture for one half axial length of the magnetic circuit geometry is shown in Figure (2.1.5). This magnetic circuit consists of an iron rotor, an iron outer casing, and two ring-shaped field coils mounted at the stator side (casing) towards the two end-bells. In between the rotor and the inner holes of the end bell (casing) there are two identical airgaps at the two ends of the machine to allow the rotor to rotate. Because of symmetry, only a quarter of the total magnetic circuit volume needs to be taken as the solution region. The 3D tetrahedral grid covering the solution region is also shown in Figure (2.1.5).

Since the permeability of the iron material has a much higher value than the air permeability, almost all the magneto-motive force due to the excitation of the two field coils is expected to be consumed across the airgaps. In this case an estimation of the radial flux density component, $\overline{B}_r$, in the airgap can be obtained by simple computation, using the following equation:

$$B_r = \mu_0(2I_fN_f)/(2l) = \mu_0 I_f N_f / l \tag{2.1.9}$$

where I_fN_f is the ampere-turns of one field coil, and l is the radial length of one

Table (2.1.2): 1.5kVA Transformer Results (I = 0.25 A)

Formulation	Demerdash's	Coulomb's	Chari's
Energy from $\frac{1}{2}\int \overline{A}\cdot\overline{J}dv$ (J)	2.774×10^{-3}	0.0083×10^{-3}	0.0010×10^{-3}
Energy from $\frac{1}{2}\int \overline{B}\cdot\overline{H}dv$ (J)	2.774×10^{-3}	0.014×10^{-3}	0.0035×10^{-3}
Maximum $\mid \nabla\times\overline{A}\mid (T)$	2.0992	0.0072	0.0015
Maximum $\mid \nabla\cdot\overline{A}\mid (T)$	5.571	0.00412	0.00091
Max. $\mid \frac{\nabla\cdot\overline{A}}{\nabla\times\overline{A}}\mid$	66.0×10^{3}	23.01	65.68
Ave. $\mid \frac{\nabla\cdot\overline{A}}{\nabla\times\overline{A}}\mid$	0.114×10^{3}	0.814	0.780
Calculated Inductance (H)	0.7102	0.0037	0.0009
Measured Inductance : 0.737 (H), from Open Circuit Test at I = 0.25 (A)			

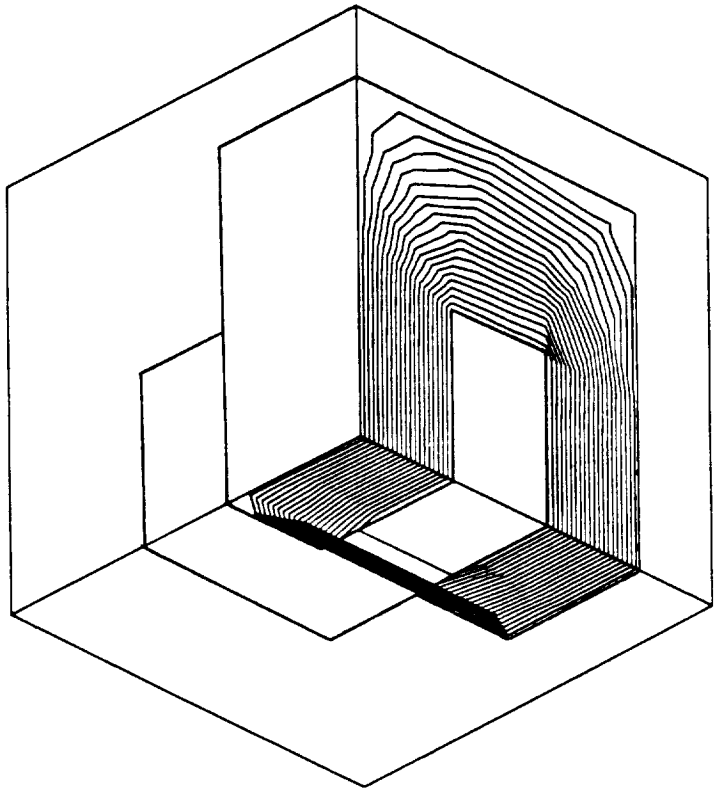

Figure (2.1.4) Plot of Equipotential Lines of Magnitude of MVP on Grid Surface of 1.5 kVA Transformer

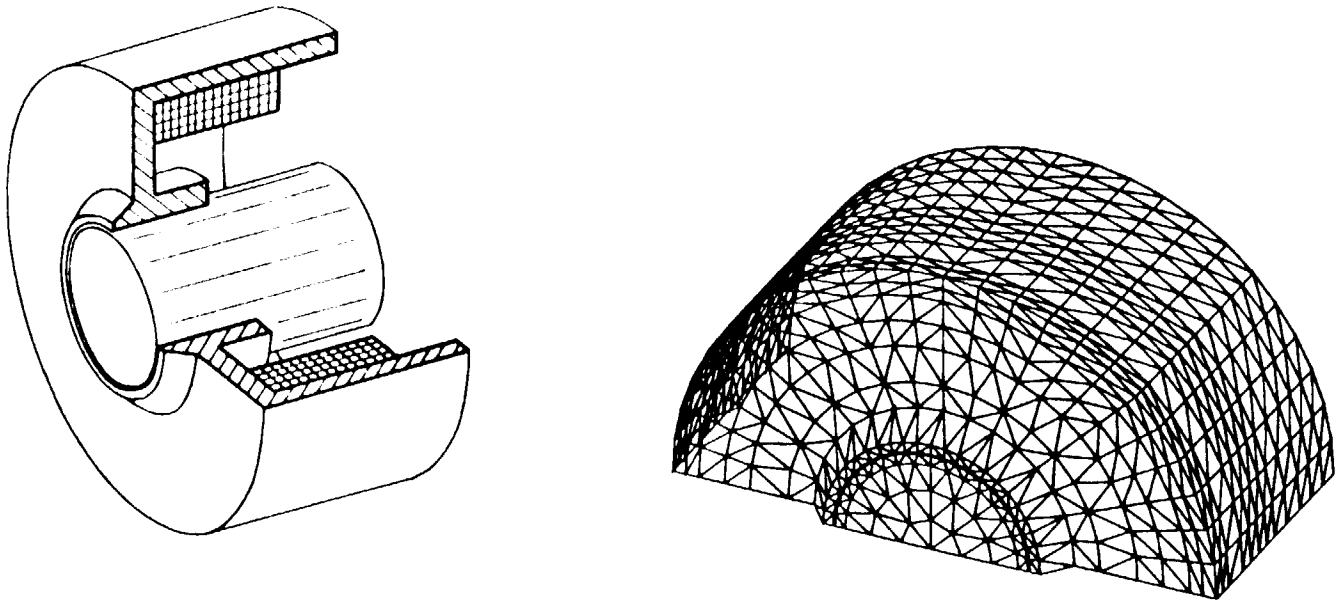

Figure (2.1.5) Simplified Magnetic Circuit of the 14.3 kVA Modified Lundell Alternator and Its First-Order FE Grid

airgap.

The estimated value of the radial flux density component, B_r, for this test example is shown in Table (2.1.3), together with the results computed by means of the three methods. Naturally, one would expect the value of B_r obtained from 3D-FE computation to be close to this estimate. Again, as can be seen from the table, only Demerdash's formulation yields a reasonable answer. The other two methods yield totally unreasonable (meaningless) results.

From the above test computations, one can conclude that the curl-curl formulation without explicit constraint on $(\nabla \cdot \overline{A})$ is the only reliable method among the existing MVP formulations, particularly when a mix of air and iron cores is encountered. Moreover, one can also see that divergence of $\overline{A}$ in a vector potential boundary value problem does not naturally assume a zero value. The non-zero values of $(\nabla \cdot \overline{A})$ in the results of Demerdash's method did not affect the accuracy of the numerical result of the flux densities and other dependent quantities such as energy and inductances.

The non-zero $(\nabla \cdot \overline{A})$ values in the results of the other two methods [38, 37] shown in Table (2.1.1-2.1.3) indicate that these formulations failed to enforce the zero divergence condition, which is a basic condition of both formulations. The fact that $(\nabla \cdot \overline{A})$ is not equal to zero in the results obtained from Coulomb's and Chari's methods is a direct violation of the necessary $\nabla \times (\nu \nabla \times \overline{A}) = \overline{J}$ condition in their approaches. This explains why Coulomb's and Chari's formulations do not succeed in certain types of magnetic field problems, particularly in those applications involving more than one type of material within the global solution volume.

2.1.3 Theoretical and Numerical Difficulties in the Curl-Curl MVP Formulation

As stated in Section 2.1.1, Demerdash's unconstrained curl-curl MVP formulation is based on the curl-curl MVP equation without any explicit constraint on the divergence of the MVP. However, according to Helmhotz theorem [86] a vector field is defined only if both its curl and divergence components have been defined. Thus, a uniqueness question arises with regard to the results of the magnetic vector potential obtained from Demedash's formulation. Many investigators [41, 43, 75] have acknowledged the fact that the non-uniqueness of $\overline{A}$ does not affect the validity of the resulting

Table (2.1.3): Simplified Magnetic Circuit - Modified Lundell Alternator Results

Formulation	Demerdash's	Coulomb's	Chari's
Energy from $\frac{1}{2}\int \overline{A}\cdot\overline{J}dv$ (J)	0.05862	0.01043	0.00411
Energy from $\frac{1}{2}\int \overline{B}\cdot\overline{H}dv$ (J)	0.05862	0.01489	0.00269
Maximum $\mid \nabla\times\overline{A}\mid (T)$	1.3636	0.3288	0.0376
Maximum $\mid \nabla\cdot\overline{A}\mid (T)$	2.3985	0.1316	0.0355
Max. $\mid \frac{\nabla\cdot\overline{A}}{\nabla\times\overline{A}}\mid$	5.78×10^{3}	30.20	1.83
Ave. $\mid \frac{\nabla\cdot\overline{A}}{\nabla\times\overline{A}}\mid$	0.14×10^{3}	0.692	0.0355
B_r in Airgap (T)	0.2901	0.0700	0.0045
Airgap B_r Calculated from $\oint \overline{H}\cdot d\bar{l} = I_{enclosed}$: $0.28 < B_r < 0.30$ Tesla			

flux density vector, $\overline{B}$. All along, correct values of $\overline{B}$ are our main objective in field computation in applications of the type at hand. However, if the uniqueness of $\overline{A}$ is not guaranteed, the resultant linear global system of FE equations based on the unconstrained curl-curl formulation may lead to an infinite number of solutions. That is, the global system of equations may be nearly singular (highly ill-conditioned), thus resulting in a numerically unstable system. The description of the uniqness problem can be explained below.

Consider the curl-curl boundary value problem stated as

$$\nabla \times (\nu \nabla \times \overline{A}) = \overline{J} \qquad in\ V \tag{2.1.10}$$

$$\overline{A}\,|_S = Constant\ Vector \qquad on\ S \tag{2.1.11}$$

where V is the 3D solution region, and S is the boundary of the region, V. In addition, the reluctivity, ν, is a constant throughout the solution region. Assume that both $\overline{A}_1$ and $\overline{A}_2$, $\overline{A}_1 \neq \overline{A}_2$, satisfy the curl-curl equation, Equation (2.1.10), as well as the boundary condition, Equation (2.1.11). The difference between these two solutions can be expressed as

$$\overline{\delta A} = \overline{A}_1 - \overline{A}_2 \neq 0 \tag{2.1.12}$$

It can be seen that this non-zero $\overline{\delta A}$ is subject to the following conditions:

$$\nabla \times \overline{\delta A} = \nabla \times (\overline{A}_1 - \overline{A}_2) = \overline{B} - \overline{B} = 0 \qquad in\ V \tag{2.1.13}$$

and

$$\overline{\delta A}\,|_S = \overline{A}_1\,|_S - \overline{A}_2\,|_S = 0 \qquad on\ S \tag{2.1.14}$$

The irrotational nature of the field $\overline{\delta A}$ as expressed by Equation (2.1.13) is a necessary and sufficient condition for the existence of a scalar function, ϕ, whose gradient equals $\overline{\delta A}$. That is, one can express $\overline{\delta A}$ as follows:

$$\overline{\delta A} = \nabla \phi \tag{2.1.15}$$

At the boundary, such a scalar function, ϕ satisfies the following:

$$\overline{\delta A} = \nabla\phi = 0 \qquad on\ S \tag{2.1.16}$$

According to the definition of $\overline{B} = \nabla \times \overline{A}$, $\overline{A}_1$ and $\overline{A}_2$ must be differentiable, so $\overline{\delta A}$, or $\nabla\phi$ must also be differentiable. Thus, by taking the divergence of $\nabla\phi$, this scalar function can be further expressed as follows:

$$\nabla \cdot \nabla\phi = \rho(x, y, z) \neq 0 \qquad in\ V \tag{2.1.17}$$

Meanwhile, on the boundary one has

$$\nabla\phi \mid_S = 0 \qquad on\ S \tag{2.1.18}$$

Equation (2.1.17), in conjunction with Equation (2.1.18), is a boundary value problem defined by Poisson's equation in the same solution region as the MVP problem of Equation (2.1.10) and Equation (2.1.11). Here, the constraint of non-zero value for ρ is used to exclude the trivial case of a constant ϕ distribution from various possible solutions to this Poisson's type of problem. (The constant ϕ distribution leads to a zero $\nabla\phi$, or a zero $\overline{\delta A}$, which violates the original assumption of Equation (2.1.12), that is $\overline{\delta A} \neq 0$)

For any other nontrivial ϕ which satisfies the boundary value problem defined by Equations (2.1.17) and (2.1.18), a non-zero $\nabla\phi = \overline{\delta A}$, subject to Equations (2.1.13) and (2.1.14), must exist. In such case, $\overline{A}$, defined by the curl-curl boundary value problem of the Equations (2.1.10)-(2.1.11), would not be unique.

Now, we show that such a nontrivial solution of ϕ can be described in a unit sphere. Consider an MVP boundary value problem defined by Equations (2.1.10) and (2.1.11), where the solution region is a sphere of unit radius. Also, consider the following scalar function in this spherical region:

$$\phi = (r^2 - 1)^n \qquad n = 2, 3, 4, ... \tag{2.1.19}$$

where ϕ is defined in the spherical coordinate system. The (∇), and $(\nabla \cdot \nabla)$ vector operations on ϕ (Equations (2.1.17) and (2.1.18)), yields the following:

$$\nabla\phi \mid_{r=1} = 2nr(r^2 - 1)^{n-1} \mid_{r=1} = 0 \tag{2.1.20}$$

(b) Grid #2

(a) Grid #1

Figure (2.1.8) Alterations of the First-Order FE Grid for the Simplified MLA

39-45

Table (2.1.6): Results of the Simplified Magnetic Circuit of 14.3 kVA MLA

Grid	Number of Nodes	Type of Element	Number of Unknowns	Calculated Energy (J)	Calculated Br (T)
#1	3458	first order	8208	0.05862	0.2901
#2	3458	first order	8208	0.05030	0.2469
#1	4425	second order	11088	0.05882	0.2899
#2	4425	second order	11088	0.05867	0.2889
	Estimated B_r from $\oint \overline{H} \cdot d\bar{l} = I_{enclosed}$: $0.28 < B_r < 0.30$ Tesla				

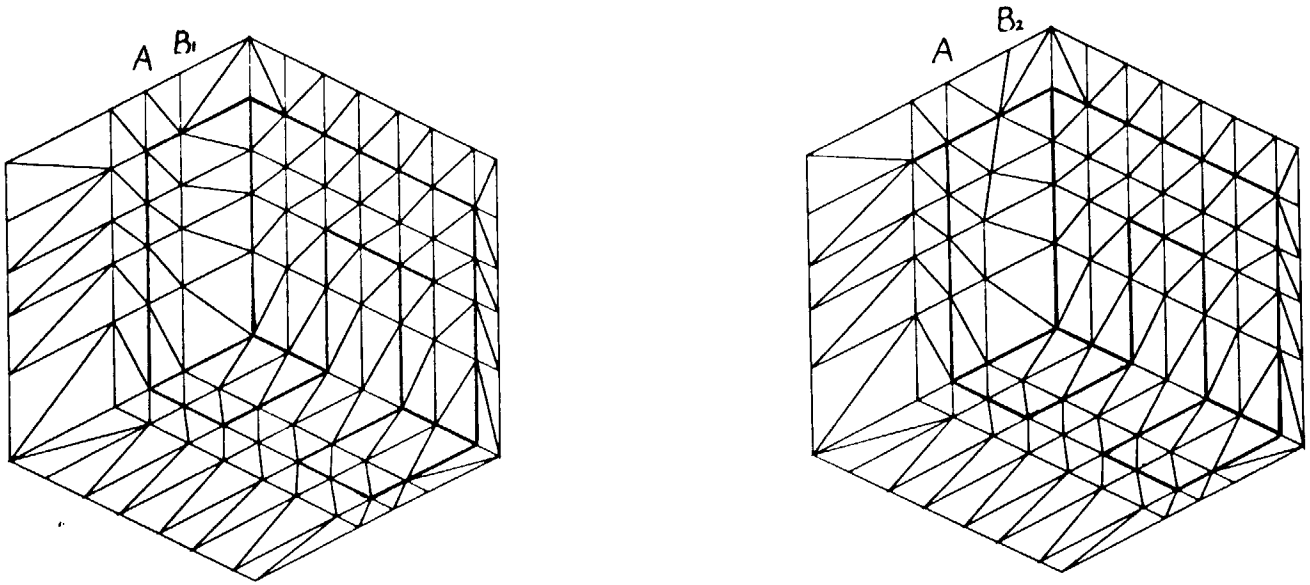

(a) Grid #1

(b) Grid #2

Figure (2.1.9) Second-Order FE Grids for 1.5 kVA Transformer Problem

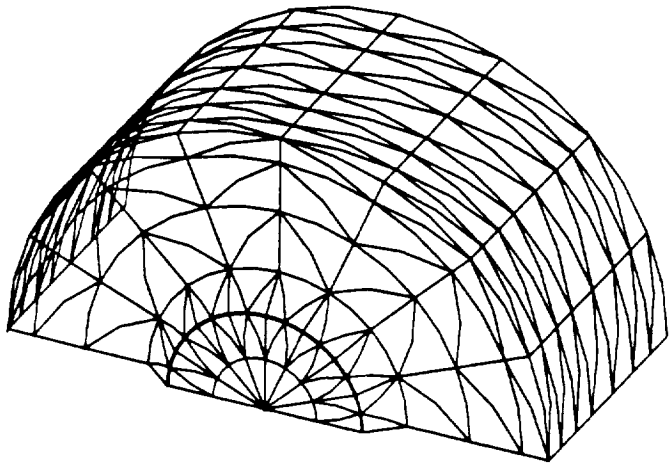

(a) Grid #1

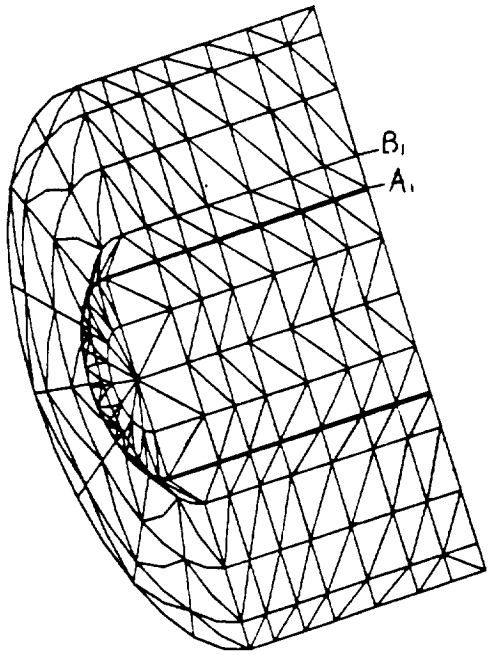

(b) Grid #2

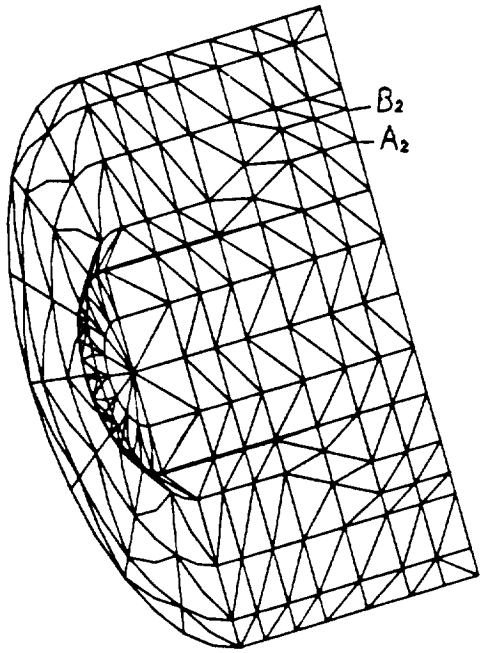

Figure (2.1.10) Second-Order FE grids for the Simplified MLA Problem

2.2 Three Dimensional Magnetic Scalar Potential Formulations

In the category of 3D-FE MSP methods, one of the earliest successful applications, without replacing current density volume distribution by approximations, was presented by Zienkiewicz, et al [26]. It is called the reduced scalar potential formulation. In this approach the magnetic field intensity, $\overline{H}$, is computed by superposition of two fields, $\overline{H}_s$, and $\nabla\phi$, as follows:

$$\overline{H} = \overline{H}_s - \nabla\phi \tag{2.2.1}$$

In Equation (2.2.1) the field $\overline{H}_s$ is the rotational, or curl, part of the total magnetic field intensity, and is calculated by Biot-Savart's law as:

$$\overline{H}_s = \frac{1}{4\pi}\int_V \overline{J} \times \nabla(\frac{1}{r})dv \tag{2.2.2}$$

where r is the distance from the integration point to the observation point, Figure (2.2.1), and the volume integration extends over all the solution space. The rotational property of $\overline{H}_s$, $\nabla \times \overline{H}_s = \overline{J}$, is insured by Biot-Savart's law in Equation (2.2.2). The remaining part of the field intensity, which is irrotational, is computed by magnetic scalar potential using 3D finite elements. It should be pointed out that, on the basis of Equation (2.2.1), $\nabla \times \overline{H} = \nabla \times \overline{H}_s - \nabla \times (\nabla\phi) = \nabla \times \overline{H}_s$.

The name, "reduced scalar potential", is introduced for ϕ because the gradient of this potential only represents part of the total field intensity. The zero divergence condition of flux density, $\nabla \cdot \overline{B} = 0$, is then used to obtain the governing equation for the reduced scalar potential, which yields the following:

$$\nabla \cdot \mu(\nabla\phi) = 0 \tag{2.2.3}$$

This reduced scalar potential approach is seldom used because a severe numerical discrepancy in the value of $\overline{H}$ occurs in magnetic material regions due to the superposition of the two components given in Equation (2.2.1). It is found that results of $\overline{H}_s$ and $(-\nabla\phi)$ in magnetic material regions have very large magnitudes which are close to each other in value, but are in opposite directions. The net field has to be calculated by superposition according to Equation (2.2.1). Thus, the cancellation of

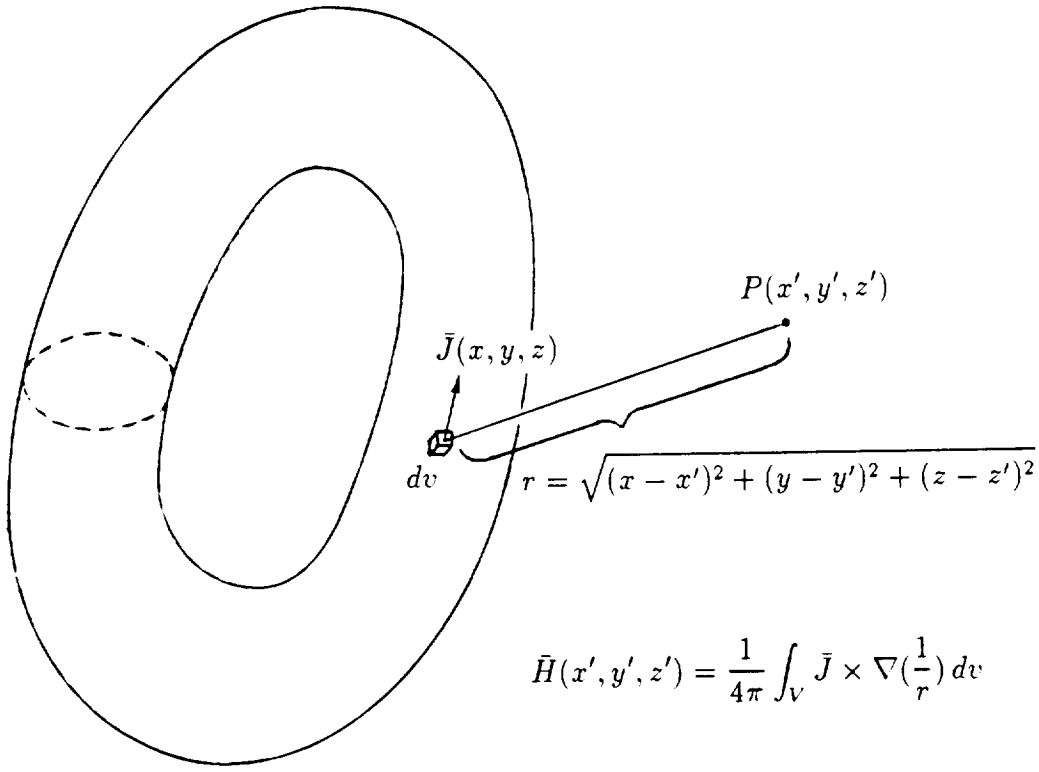

Figure (2.2.1) Biot-Savart's Law

two quantities close in value which are not computed to precisely the same degree of accuracy reduces the overall precision of the results [82].

A solution to this numerical problem was introduced by Simkin and Trowbridge [27], and is referred to as the "two scalar potential" solution method. In the two scalar potential approach, the solution region, Ω, is divided into two subregions, Ω_1, and Ω_2. The subregion, Ω_1 contains all the electric current sources, but it should not include any magnetic material with $\mu \gg \mu_0$. The magnetic field and its associated MSP problem in Ω_1 are described in the same way as the reduced scalar potential method, Equation (2.2.1). Therefore, in subregion Ω_1, one can write the following:

$$\overline{H} = \overline{H}_s - \nabla\phi_1 \qquad in\ \Omega_1 \tag{2.2.4}$$

$$\nabla \cdot (\mu \nabla \phi_1) = 0 \qquad in\ \Omega_1 \tag{2.2.5}$$

where, again, $\overline{H}_s$ is obtainable via numerical integration by Biot-Savart's law.

The subregion Ω_2 covers all the remainder of the 3D solution space. It does not contain any electric current source, but includes all magnetic materials. In this region $\overline{H}$ is irrotational. That is, a scalar potential, ϕ_2, can be directly introduced to calculate the field intensity, where

$$\overline{H} = -\nabla\phi_2 \qquad in\ \Omega_2 \tag{2.2.6}$$

Here, ϕ_2 is called the total scalar potential because its gradient defines the entire field intensity. That is, no superposition is required. Since $\overline{H}$ is formulated differently in subregions Ω_1, and Ω_2, respectively, the continuity of normal component of the flux density, $\overline{B}_n$, and the tangential component of the field intensity, $\overline{H}_t$, have to be explicitly forced at the interface between the two subregions. These continuity conditions can be written as follows for the continuity of $\overline{B}_n$:

$$\mu_1(\overline{H}_s - \nabla\phi_1) \cdot \hat{n}_1 = -\mu_2(\nabla\phi_2) \cdot \hat{n}_1 \tag{2.2.7}$$

and for the continuity of $\overline{H}_t$:

$$(\overline{H}_s - \nabla\phi_1) \cdot \hat{t} = -(\nabla\phi_2) \cdot \hat{t} \tag{2.2.8}$$

where $\hat{n}_1$ is the normal unit vector on the $\Omega_1 - \Omega_2$ interface pointing from Ω_1 to Ω_2, and $\hat{t}$ is any unit tangential vector on the interface. Equation, (2.2.7) can be further rearranged as follows:

$$\mu_1 \frac{\partial \phi_1}{\partial n_1} - \mu_2 \frac{\partial \phi_2}{\partial n_1} = \mu_1 \overline{H}_s \cdot \hat{n}_1 \tag{2.2.9}$$

This equation shows that the discontinuity of the $(\mu \partial \phi / \partial n)$ term has to be forced at the interface of Ω_1 and Ω_2 to insure the continuity of the normal component of the flux density. Meanwhile, from Equation (2.2.8), one obtains the following:

$$\nabla \phi_2 \cdot \hat{t} - \nabla \phi_1 \cdot \hat{t} + \overline{H}_s \cdot \hat{t} = 0 \tag{2.2.10}$$

Consider a line integration of the left side of this equation on the $\Omega_1 - \Omega_2$ interface from an arbitrary point A to an arbitrary point B. It yields the following:

$$\int_A^B \nabla \phi_2 \cdot d\bar{l} - \int_A^B \nabla \phi_1 \cdot d\bar{l} = - \int_A^B \overline{H}_s \cdot d\bar{l} \tag{2.2.11}$$

or

$$(\phi_{2B} - \phi_{2A}) - (\phi_{1B} - \phi_{1A}) = - \int_A^B \overline{H}_s \cdot d\bar{l} \tag{2.2.12}$$

One can set the point A in Equation (2.2.12) as a reference point at which ϕ_2 is equal to ϕ_1. It then follows from Equation (2.2.12) that

$$\phi_{2B} - \phi_{1B} = - \int_A^B \overline{H}_s \cdot d\bar{l} \tag{2.2.13}$$

Note that Equation (2.2.13) holds for any point B on the interface between Ω_1 and Ω_2. Therefore, in order to guarantee the continuity of the tangential component of the field intensity, the discontinuity between ϕ_1 and ϕ_2 (the potential jump), which is explicitly expressed by Equation (2.2.13), has to be forced (imposed) on the interface.

In this two scalar potential method, the superposition of field intensity, shown by Equation (2.2.4), is carried out only in Ω_1, the region without any magnetic material. This effectively avoids the numerical problem associated with subtracting of two large numbers one from the other (the cancellation problem) as found in the reduced scalar potential approach alluded to earlier in this section. It should be pointed out that $\overline{H}_s$ in Equation (2.2.4) can be obtained by methods other than the Biot Savart's

integration. In fact, any vector field with its curl component equal to the electric current distribution can be considered as a suitable $\overline{H}_s$. Under certain circumstances, $\overline{H}_s$ can be obtained by very simple hand calculations, as demonstrated in earlier work done by this author, see reference [28].

The disadvantage of the two scalar potential formulation, as compared with the vector potential formulation, is its inconvenience in applications. The subregion, Ω_1, has to be chosen with extreme care and judgement so that it includes all currents, but it cannot contain any portions of iron material such as laminated cores or cast and forged ferromagnetics, etc. This requirement will force Ω_1 to extremely difficult contours and geometry in most practical engineering problems. For example, a problem of any electric machine armature winding with its coil sides embedded in iron-core slots would immediately lead to difficult contours for subregion, Ω_1.

In many instances the current-carrying subregion, Ω_1, has to be a multiply-connected region in order to satisfy the partition requirement, such as the shell-type transformer problem shown in Figure (2.2.2). In this case, ϕ_2 in subregion Ω_2 may become a multi-valued scalar distribution. This can be further explained through the following integration which describes the nature of the magnetic scalar potential in Ω_2, that is

$$\phi_2 = \int_a^b \nabla\phi_2 \cdot d\bar{l} = -\int_a^b \overline{H} \cdot d\bar{l} \tag{2.2.14}$$

where point a is the reference point and point b is the location at which ϕ_2 is considered. Multi-values can happen if the integral path laps around the currents in Ω_1 by one or more times, see Figure (2.2.2). To avoid this situation, one has to set up a barrier, or branch cut (to use more precise mathematical terminology), in Ω_2, so that any closed path in Ω_2 cannot enclose currents in Ω_1. However, after the barrier is set, another potential discontinuity has to be forced on the barrier with respect to ϕ_2 at its two sides; for further details Straton [86] should be consulted. This adds additional difficulties to the process of determination of potential discontinuity conditions at various interface boundaries.

Therefore, although the two scalar potential solution method allows one to avoid the cancellation problem, it poses extreme geometric contour difficulties in dealing with magnetic field problems having practical current-carrying region such as machine windings, as well as current-iron mutually chain-linked geometries (see Figure (2.2.2)).

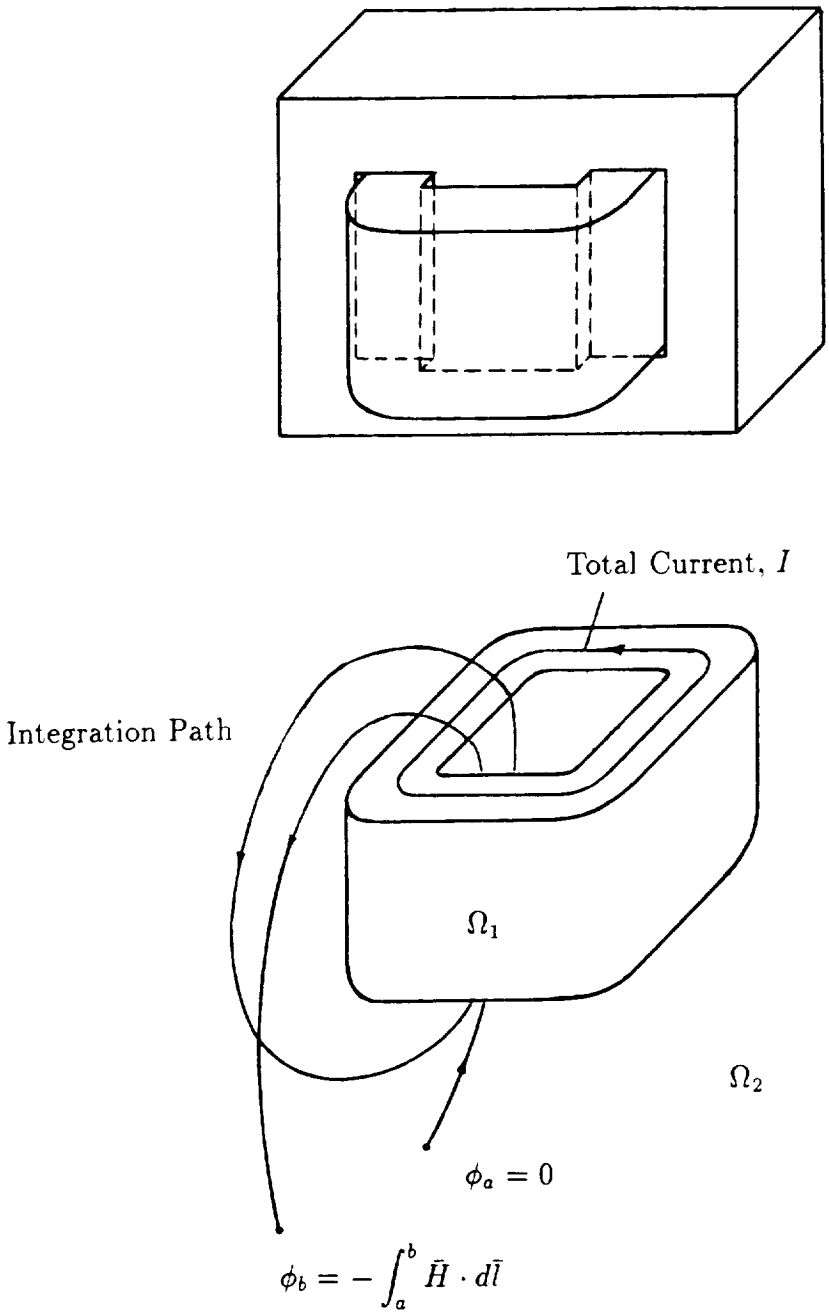

Figure (2.2.2) Multi-Valued Scalar Potential in Shell-Type Transformer Problem

Chapter 3

A Combined Magnetic Vector and Scalar Potential 3D Finite Element Analysis Procedure

The foregoing survey of existing 3D FE formulations discloses that 3D FE magnetic field computations for electric machines and devices, such as the modified Lundell alternator (MLA) problem, cannot be a straightforward effort of simply adopting an available solution method. The second-order curl-curl MVP formulation is a suitable candidate because of its accuracy in results and its convenience in application. This method, however, yields a huge number of unknowns in the global FE system of equations; in the hundreds of thousands for the MLA problem being investigated in this research. On the other hand, the two scalar potential method [27], poses extreme difficulties in dealing with machine armature geometry and current distribution in the presence of armature slotting and end-turn configurations as well as overlaps. This is despite the fact that the resulting size of the computational work in a real engineering problem using the two scalar potential approach does not seem to be beyond the capability of the newly developed super-computers such as the Cray-II and Cray-YMP.

Under these circumstances, a new technique based on a combination of the second-order MVP formulation and the MSP approach, has been developed. This new approach will be demonstrated to be especially useful for the computation of 3D magnetic fields in electrical devices with complex magnetic circuit and winding geometries, such as the MLA.

3.1 Description of the Combined MVP-MSP Approach

In this combined MVP-MSP approach, the entire solution region (volume), Ω, is discretized by first-order finite elements. The second-order finite element MVP solution is first applied locally on current-carrying regions to obtain the curl component of the magnetic field intensity. This is done just once. Then, nonlinear MSP finite element analyses are performed throughout the entire solution region to carry out the magnetic field computations under all possible practical combinations of current excitations and rotor positions in the MLA.

To apply the MVP and MSP solutions separately, the entire grid region Ω is partitioned into two sets of subregions. One is the current-carrying subregion, Ω_1. The other is the remaining part, Ω_2, of the original global region, such that $\Omega_1 \cup \Omega_2 = \Omega$. Here, Ω_1 is a general notation for the current-carrying subregion, since more than one current-carrying sub-subregions are allowed within Ω_1 to effectively accommodate various excitation windings (coils). Furthermore, it should be pointed out that the subregion Ω_1 not only contains conductors with current distributions, but also can include iron material, which cannot be present in the two scalar potential method (see Section 2.2).

At this stage of the partition of Ω there are certain absolute constraints that govern the geometries of the subregions, Ω_1 and Ω_2. They can be summarized as follows:

(1) There should be no possibility of a closed magnetic path entirely enclosed in Ω_2, within which there exists any net current (non-zero current) from subregion Ω_1.

(2) No electric current should exit or enter the outer surface of the subregion Ω_1.

The ability to include iron material in Ω_1, which is a characteristic of this new approach, is very important. It allows one to easily satisfy the above absolute constraints in practical engineering problems. Figure (3.1.1) shows a possible partition pattern for an example shell-type transformer problem. In this example, the current-carrying subregion Ω_1 contains the whole transformer coil, as well as the portion of the laminated iron core within the coil structure. One can see from the example of Figure

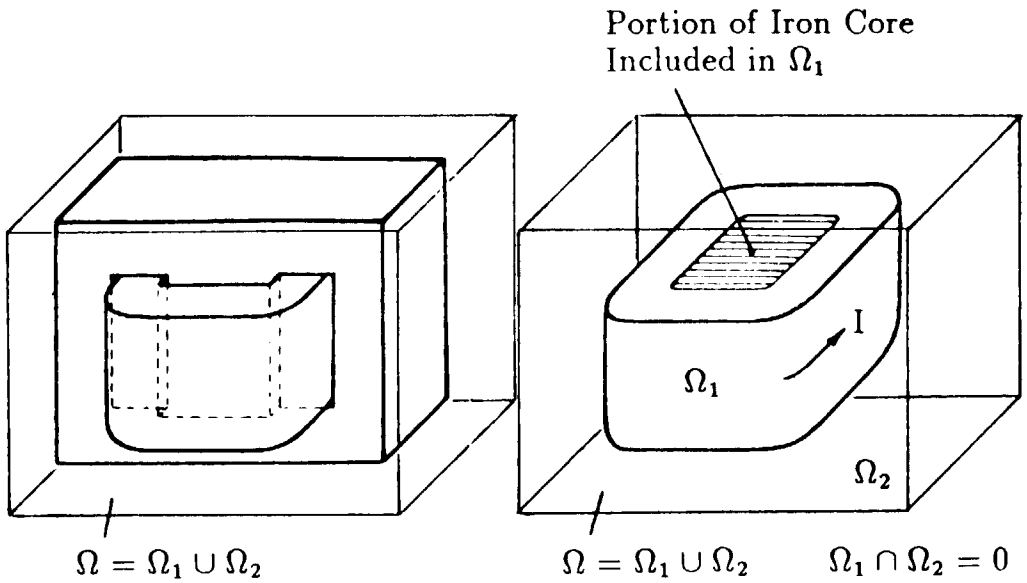

Figure (3.1.1): Partition Pattern for the Solution Region of a Shell-Type Transformer

(3.1.1) that any closed path in Ω_2 cannot enclose the current in the transformer coil.

It will be shown later in detail that the first constraint guarantees a single valued MSP in Ω_2, and the second constraint guarantees a single valued MSP jump distribution (function) on the surface of Ω_1. The advantage of a single valued potential in Ω_2, and a single valued potential jump distribution on the surface of Ω_1, renders the new approach a much more effective and preferable method than the two scalar potential method.

In this MVP-MSP approach, the magnetic field intensity, $\overline{H}$, within the current-carrying region, Ω_1, can be expressed as follows:

$$\overline{H} = \overline{H}_{mvp} - \nabla\phi \qquad in\ \Omega_1 \tag{3.1.1}$$

where $\overline{H}_{mvp}$ is the curl component of the total magnetic field intensity. As mentioned earlier in this section, the curl component of the field intensity, $\overline{H}_{mvp}$, is computed within Ω_1 through use of the curl-curl MVP second-order finite element formulation.

It should be pointed out again that the first-order finite element grid is first established throughout the solution region, Ω, which includes Ω_1 and Ω_2. The second-order finite element grid in subregion Ω_1 for the MVP computation can be obtained by adding extra nodes on the edges of the original first-order elements. The governing equation for this stage of MVP computation (Equation (2.0.6)) is rewritten here for the reader's convenience

$$\nabla \times (\nu \nabla \times \overline{A}) = \overline{J} \tag{3.1.2}$$

Experience suggests that the boundary condition of $\overline{A}$ for this stage of the MVP computation is $\overline{A} = 0$, which physically means that all calculated magnetic fields are bounded within Ω_1 [32]. As will be seen later, such a bounded magnetic field (flux) pattern simplifies the MSP jump distribution on the outer surface of Ω_1. This MSP jump distribution, as will also be seen later, is the main forcing function for the MSP part of the whole MVP-MSP solution.

When subregion Ω_1 includes iron materials, the preferred choice is to use extremely high values of permeability for the iron material portions in the MVP part of the solution. These permeabilities should not be confused with the final saturated values which will emerge as a result of the MSP part of the solution.

In discussing this matter, the part of Ω_1 occupied by materials with air permeability is denoted as Ω_1^{air}; and the part of Ω_1, occupied by iron materials is denoted as Ω_1^{iron}.

In an example analysis of a problem with iron material in Ω_1, a relative iron permeability, $\mu_r = 10^6$, was used by this author at this stage for the elements which belong to the sub-subregion Ω_1^{iron}. From knowledge of magnetic fields, the calculated field intensity in the region with the extremely high permeability will be extremely small, and for all practical purposes near zero value. This allows one to further express $\overline{H}_{mvp}$ in Ω_1^{iron} and in Ω_1^{air} as follows:

$$\overline{H}_{mvp} = \nu_0 \overline{B}_{mvp} = \nu_0(\nabla \times \overline{A}) \qquad in\ \Omega_1^{air} \tag{3.1.3}$$

$$\overline{H}_{mvp} = 0 \qquad in\ \Omega_1^{iron} \tag{3.1.4}$$

In view of Equations (3.1.3) and (3.1.4), Equation (3.1.1) can be rewritten in sub-subregions Ω_1^{air} and Ω_1^{iron}, as follows:

$$\overline{H} = \overline{H}_{mvp} - \nabla\phi \qquad in\ \Omega_1^{air} \tag{3.1.5}$$

$$\overline{H} = 0 - \nabla\phi = -\nabla\phi \qquad in\ \Omega_1^{iron} \tag{3.1.6}$$

Therefore, the field variables, $\overline{H}_{mvp}$, and $(-\nabla\phi)$, which form the complete field intensity, $\overline{H}$, in subregion Ω_1, will simultaneously have non-zero values only within the non-magnetic sub-subregion Ω_1^{air}. Hence, the numerical cancellation problem in the iron material region associated with the reduced scalar potential method [26], which results from the superposition of two extremely large numbers with opposite signs, does not occur here.

The field intensity $\overline{H}$ in Ω_1^{air}, described by Equation (3.1.5) satisfies the curl constraint on the magnetic field intensity in Ampere's part of Maxwell's equations. This can be shown as follows:

$$\nabla \times \overline{H} = \nabla \times \overline{H}_{mvp} - \nabla \times (\nabla\phi)$$

and, with $\nabla \times (\nabla\phi) = 0$ and with $\overline{H}_{mvp} = \nu_0 \overline{B}_{mvp}$ and $\overline{B}_{mvp} = \nabla \times \overline{A}$

$$\nabla \times \overline{H} = \nabla \times (\nu_0 \nabla \times \overline{A}) \qquad in\ \Omega_1^{air}$$

The computed $\overline{A}$ satisfies Equation (3.1.2), thus one obtains

$$\nabla \times \overline{H} = \overline{J} \qquad in\ \Omega_1^{air} \tag{3.1.7}$$

Similarly, by taking the curl of the $\overline{H}$ in sub-subregion Ω_1^{iron}, which is defined by Equation (3.1.6), one can write the following:

$$\nabla \times \overline{H} = \nabla \times (-\nabla\phi) = 0 \qquad in\ \Omega_1^{iron} \tag{3.1.8}$$

In sub-subregion Ω_1^{iron} the excitation current density has a zero value, hence, Equation (3.1.8) shows that the field intensity, $\overline{H}$, in Ω_1^{iron} defined by Equation (3.1.6) also satisfies Maxwell's equations.

In addition to the above curl requirement on the field intensity, $\overline{H}$, the flux density, $\overline{B}$, must satisfy the zero divergence constraint, $\nabla \cdot \overline{B} = 0$. By applying this constraint to the flux density, with $\overline{B} = \mu_0\overline{H}$, and Equation (3.1.5), one obtains the following:

$$\begin{aligned}
\nabla \cdot \overline{B} &= \nabla \cdot [\mu_0(\overline{H}_{mvp} - \nabla\phi)] \\
&= \nabla \cdot (\mu_0\overline{H}_{mvp}) - \nabla \cdot (\mu_0\nabla\phi) \\
&= \nabla \cdot (\overline{B}_{mvp}) - \nabla \cdot (\mu_0\nabla\phi) \\
&= \nabla \cdot (\nabla \times \overline{A}) - \nabla \cdot (\mu_0\nabla\phi) = 0 \qquad in\ \Omega_1^{air}
\end{aligned} \tag{3.1.9}$$

Upon substituting the vector identity, $\nabla \cdot (\nabla \times \overline{A}) = 0$, into Equation (3.1.9) one deduces the following constraint on the MSP, ϕ, in Ω_1^{air}:

$$\nabla \cdot (\mu_0\nabla\phi) = 0 \qquad in\ \Omega_1^{air} \tag{3.1.10}$$

Equation (3.1.10) is the governing equation for the MSP in Ω_1^{air}.

Similarly, by applying the zero divergence constraint to the flux density, $\overline{B}$, in Ω_1^{iron}, where $\overline{B} = \overline{\overline{\mu}}\overline{H}$, and upon substituting for $\overline{H}$ from Equation (3.1.6), one can write the following:

$$\nabla \cdot \overline{B} = \nabla \cdot [\overline{\overline{\mu}}(-\nabla\phi)] = -\nabla \cdot (\overline{\overline{\mu}}\nabla\phi) = 0 \qquad in\ \Omega_1^{iron}$$

Here, $\overline{\overline{\mu}}$ is the permeability tensor which enables one to include anisotropic properties of the magnetic media, such as laminated iron cores in electrical machinery. By multiplying both sides of the above equation by (-1), one obtains

$$\nabla \cdot (\overline{\overline{\mu}} \nabla \phi) = 0 \qquad in\ \Omega_1^{iron} \tag{3.1.11}$$

Equation (3.1.11) is the governing equation for the magnetic scalar potential in sub-subregion Ω_1^{iron}.

Meanwhile, in subregion, Ω_2, which is free from current-carrying conductors, the field intensity, $\overline{H}$, is defined directly in terms of the magnetic scalar potential, ϕ, as follows:

$$\overline{H} = -\nabla \phi \qquad in\ \Omega_2 \tag{3.1.12}$$

Upon applying $\nabla \cdot \overline{B} = 0$ in Ω_2, one can write the following:

$$\nabla \cdot (\overline{\overline{\mu}} \nabla \phi) = 0 \qquad in\ \Omega_2 \tag{3.1.13}$$

From the above equations, Equation (3.1.10), (3.1.11), and (3.1.13), one can see that the MSP, ϕ, in Ω_1^{air} and Ω_1^{iron}, as well as in Ω_2, is governed by Laplace type equations. Therefore, one can join these separate MSP problems within Ω_1^{air}, Ω_1^{iron}, as well as Ω_2, together into one global MSP problem encompassing the entire solution region, Ω. This is accomplished by imposing the necessary field boundary conditions on the interfaces between these subregions. The mechanics of this step in the MVP-MSP approach are explained next.

As discussed earlier in Section 2.2 with regard to the two scalar potential method, two types of discontinuity conditions, the discontinuity of the MSP, and the discontinuity of the derivative of the MSP, have to be forced on certain interfaces within the global solution region, Ω. In the case of this MVP-MSP method, the magnetic field intensity in Ω_1^{air} is obtained by the superposition of $\overline{H}_{mvp}$ and $(-\nabla\phi)$ as given in Equation (3.1.5), and the magnetic field intensity in Ω_2 and Ω_1^{iron} is only from $(-\nabla\phi)$ as given in Equation (3.1.6) and Equation (3.1.12). Accordingly, discontinuity conditions have to be imposed at the interface between Ω_1 and Ω_2, denoted here as the surface, Γ_{12}, as well as the interface between Ω_1^{air} and Ω_1^{iron}, denoted as the surface, Γ_1^{ai}.

In order to help the reader visualize these types of interfaces (surfaces), consider the example transformer problem of Figure (3.1.1), which is illustrated here again in Figure (3.1.2) through a cut-away picture for its current-carrying subregion, Ω_1.

The derivation procedure discussed in detail in section 2.2 for the two scalar potential method is used here to determine the MSP discontinuity conditions on Γ_{12}, and Γ_1^{ai}. The derived equation which is in the same pattern as Equations (2.2.9) and (2.2.13) shown earlier in Section 2.2, are given here in a general form as follows

$$\phi_{2B} - \phi_{1B} = -\int_A^B \overline{H}_{mvp} \cdot d\bar{l} \qquad \text{on } \Gamma_{12} \text{ and } \Gamma_1^{ai} \tag{3.1.14}$$

$$\mu_1 \frac{d\phi_1}{dn_1} - \mu_2 \frac{d\phi_2}{dn_1} = \mu_1 \overline{H}_{mvp} \cdot \hat{n}_1 \qquad \text{on } \Gamma_{12} \text{ and } \Gamma_1^{ai} \tag{3.1.15}$$

where the point A is a reference point on the associated interface, at which the potential discontinuity has a zero value; $(\phi_{2B} - \phi_{1B})$ is the MSP jump to be imposed at the point B on that interface. Meanwhile, $\mu_1 \overline{H}_{mvp} \cdot \hat{n}_1$ is the MSP derivative discontinuity to be imposed on the associated interface.

As was stated earlier in this section, the MVP part of this MVP-MSP method is performed in Ω_1 under an outer boundary condition of zero MVP. The computed normal component of the field intensity, $\overline{H}_{mvp}$, at the outer surface of Ω_1 must therefore be zero. In the case of the transformer problem, such a calculated flux pattern can be drawn on a structurally symmetric cross-section of the transformer, shown in Figure (3.1.3). On the interface between Ω_1 and Ω_2 (Γ_{12}), one only needs to impose the discontinuity of the MSP given in Equation (3.1.14). This discontinuity condition can be rewritten on the interface, Γ_{12}, as follows:

$$\phi_{2B} - \phi_{1B} = -\int_A^B \overline{H}_{mvp} \cdot d\bar{l} \qquad \text{on } \Gamma_{12} \tag{3.1.16}$$

Again, in the above equation, point A is a reference point on the surface, Γ_{12}, and the line integral from point A to point B can be carried out through any possible path on the surface, Γ_{12}.

As noted previously, the MVP in the subregion, Ω_1, is computed by assigning the permeability of the iron material in sub-subregion Ω_1^{iron} an extremely high value. As a result of this high permeability, the computed field intensity $\overline{H}_{mvp}$, in Ω_1^{air} must be perpendicular to the air-iron interfaces. Such a property of the field intensity, $\overline{H}$,

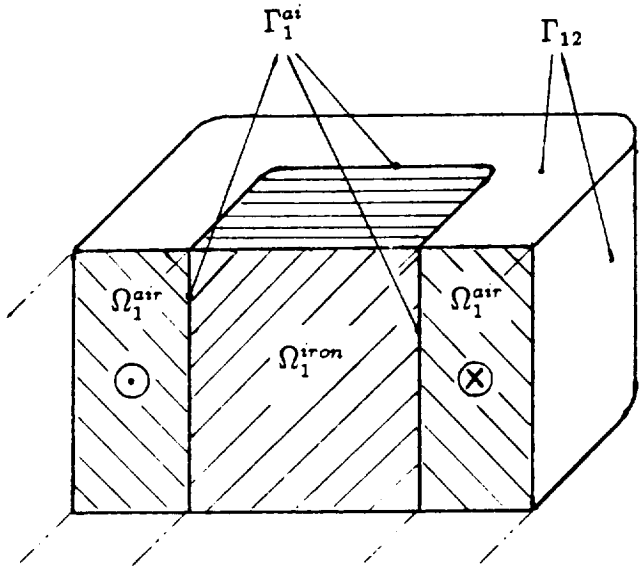

Figure (3.1.2): A Cut-Away View of the Current-Carrying Region, Ω_1

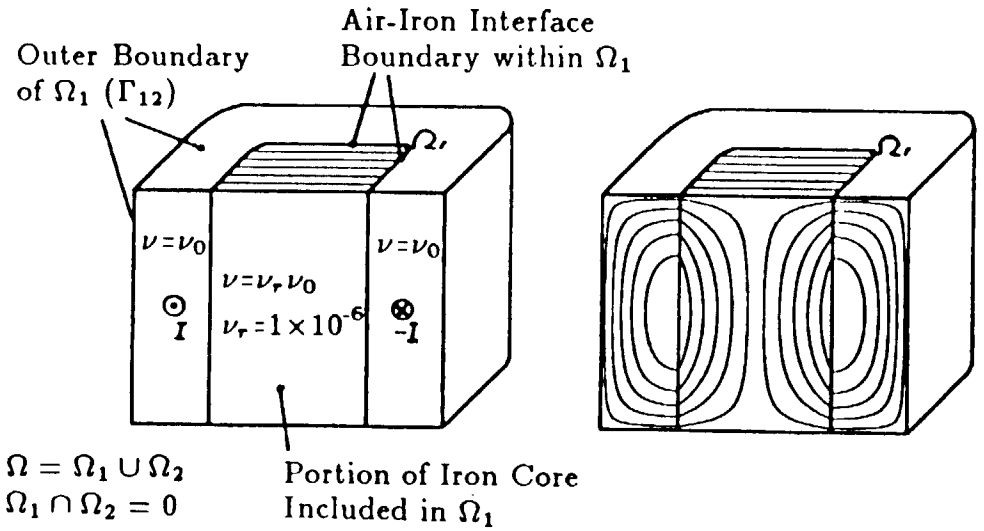

Figure (3.1.3): Flux Line Pattern in Ω_1 from the MVP Part of Solution

near to the interface between Ω_1^{air} and Ω_1^{iron}, that is Γ_1^{ai}, can be seen in Figure (3.1.3) of the transformer example. In this case, the tangential component of $\overline{H}_{mvp}$ is zero all over the interface and no MSP jump has to be forced on this interface. However, the discontinuity of the MSP derivative which was previously given in Equation (3.1.15), must be imposed on the surface, Γ_1^{ai}.

This MSP derivative discontinuity is restated here on Γ_1^{ai}, for the reader's convenience, as follows:

$$\mu_0 \frac{d\phi_1}{dn} - \mu_2 \frac{d\phi_2}{dn} = \mu_0 \overline{H}_{mvp} \cdot \hat{n} = B_{mvpn} \qquad on\ \Gamma_1^{ai} \tag{3.1.17}$$

In Equation (3.1.17), μ_0 is the air permeability of the nonmagnetic material in Ω_1^{air}; μ_2 is the iron permeability of the iron material in Ω_1^{iron}. Meanwhile, ϕ_1 is the MSP in Ω_1^{air}; ϕ_2 is the MSP in Ω_1^{iron}; and $\hat{n}$ is the normal unit vector on interface Γ_{12} pointing from Ω_1^{air} to Ω_1^{iron}. Here, B_{mvpn} is the value of the MSP derivative discontinuity on Γ_1^{ai}.

Values for the discontinuity conditions expressed in Equations (3.1.16) and (3.1.17) have to be calculated before the global MSP solution can proceed. The values of discontinuity of the MSP derivative, $\mu_0 \overline{H}_{mvp} \cdot \hat{n}_1$, in Equation (3.1.17) can be directly obtained from the second order MVP solution at the associated elemental surfaces.

The method of calculation of the values of the MSP discontinuity along Γ_{12} requires further discussion. The current-carrying subregion, Ω_1, is chosen in such a way (see the partition absolute constraints discussed earlier in this section) that any closed path on Γ_{12} cannot enclose net electric current within Ω_1. Therefore, by magnetic Ampere's law, $I_{enclosed} = \oint \overline{H} \cdot d\bar{l}$, the following closed loop integral must hold:

$$\oint_c \overline{H}_{mvp} \cdot d\bar{l} = 0 \qquad on\ \Gamma_{12} \tag{3.1.18}$$

where, "c" can be any closed path on Γ_{12}. Equation (3.1.18) indicates that the tangential component of $\overline{H}_{mvp}$ on Γ_{12}, which is denoted here as $\overline{H}_{mvpt}$, has a conservative nature [86]. Thus, $\overline{H}_{mvpt}$ can be expressed as the gradient of a single valued scalar function distributed on Γ_{12}. Using the notation $\Delta\phi$ for this single valued scalar po-

tential on Γ_{12}, one can write the following

$$-\nabla(\Delta\phi) = \overline{H}_{mvpt} \qquad on\ \Gamma_{12} \tag{3.1.19}$$

Again, $\overline{H}_{mvpt}$ in Equation (3.1.19) is computed from the previous MVP part of this MVP-MSP approach.

It should be pointed out that Equation (3.1.19) is the differential form of the integral expression in Equation (3.1.16). Therefore, the single valued scalar function, $\Delta\phi$, in Equation (3.1.19) is the MSP jump distribution denoted by $(\phi_{2B} - \phi_{1B})$ in Equation (3.1.16). In order to effectively calculate this single valued MSP jump distribution, $\Delta\phi$, a surface finite element analysis is introduced and carried out at this stage throughout the surface, Γ_{12}, to numerically solve Equation (3.1.19).

The functional to be minimized in this surface FE analysis, which is based on applying the least square residual rule to Equation (3.1.19), can be written as follows:

$$F(\Delta\phi) = \int_a \mid \nabla(\Delta\phi) + \overline{H}_{mvpt} \mid^2 da \tag{3.1.20}$$

where the integration is carried out all over surface, Γ_{12}. In this functional, $\overline{H}_{mvpt}$ is obtained from the previous MVP solution, while $\Delta\phi$ is the unknown variable to be solved for at every grid node on Γ_{12}. At this stage, the surface grid of the original first-order 3D FE grid on Γ_{12} can be directly used for this FE computation. Details of this surface FE computation will be given in Chapter 4.

These concepts and ideas regarding the combined MVP-MSP 3D-FE formulation can be summarized into three major FE computation steps. These three steps are as follows:

(1) The 3D second-order finite element computations based on the curl-curl MVP formulation in the current-carrying region, Ω_1, to calculate the curl component of the field intensity.

(2) The surface finite element computation on the outer surface of Ω_1, that is Γ_{12}, which takes the resultant $\overline{H}_{mvpt}$ from the MVP solution in step (1) as the input data, and calculates the MSP jump distributions, $\Delta\phi$, on Γ_{12}, which are the forcing function input data for the next step of computation.

(3) The first-order 3D-FE Laplace's MSP computations in the entire solution region

to complete the task of the nonlinear magnetic field solution.

These FE computation steps, as well as the data transfer in between these steps, are demonstrated by a flow chart shown in Figure (3.1.4). It should be emphasized again that in the MVP stage of this MVP-MSP approach, the permeability for the iron material in Ω_1 should be set to an extremely high constant value. Moreover, in a practical machine problem containing more than one excitation winding, it is often required to compute 3D magnetic fields under various combinations of field excitation currents in these windings. In such a case, one can perform the MVP-FE computation in Ω_1 and the surface FE computation on Γ_{12} with only unit excitation current in each one of these windings singly (not simultaneously), one at a time. That is, one repeats the same FE computations with every winding singly energized, one after another.

The results from these computations, namely $\Delta\phi$, B_{mvpn}, and the elemental $\overline{H}_{mvp}$, which are to be used as the input data for the later stage of MSP computations, are stored in a series of data files. Thus, for any given set of winding current excitations, one is able to calculate the values of $\Delta\phi$, B_{mvpn}, and the elemental $\overline{H}_{mvp}$ due to this given set of excitations, by a simple linear combination of the data values previously stored in the data files. Accordingly, the MVP-FE and the surface FE computations mentioned above are only required to be carried out once for a given machine design geometry. The global nonlinear 3D-MSP computations will have to be repeatedly performed under all possible and practical combinations of current excitations, as well as rotor positions. Also, the magnetic material nonlinearity, and anisotropic permeability due to laminated iron cores in machinery, are fully included in the MSP part of this combined MVP-MSP approach. The implementation of various types of finite element analysis mentioned above will be further discussed in Chapter 4 of this dissertation.

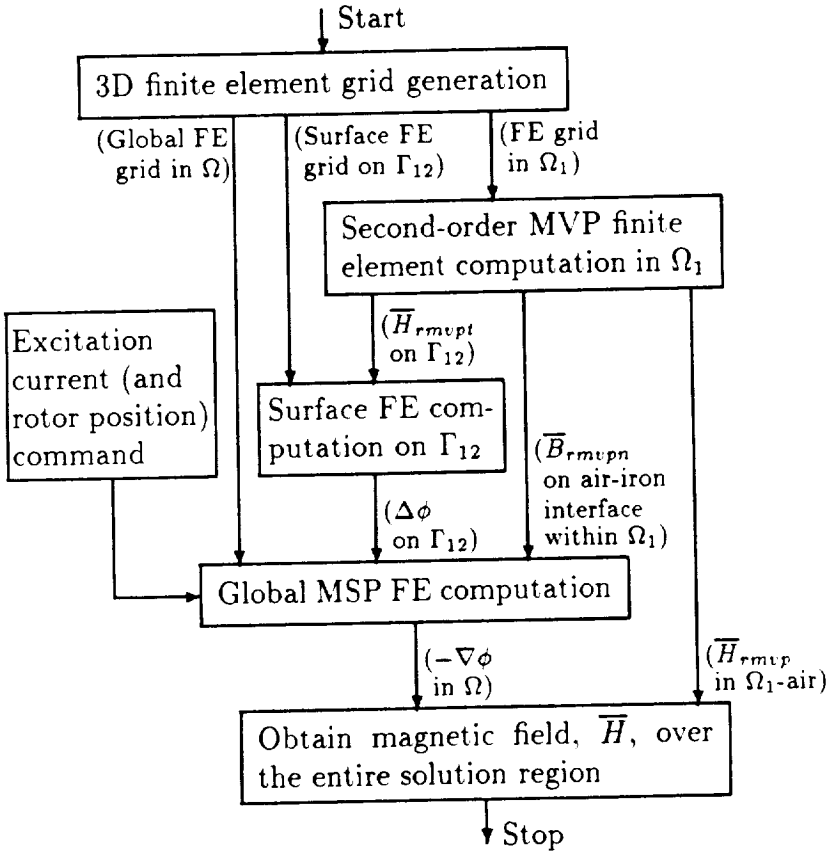

Figure (3.1.4): Flow Chart of the Combined MVP-MSP 3D-FE Solution Method

3.2 Application of the Combined MVP-MSP Approach to a Demonstration Example - 1.5 kVA Shell-Type Transformer

In this section, an application of the combined MVP-MSP method to a demonstration example, namely the 1.5 kVA shell-type transformer of Chapter 2, is given. The computed results from the MVP-MSP method will be compared with the results from the second-order finite element MVP method whose validity was demonstrated earlier in Chapter 2. This comparison will provide necessary evidence for the validity of the new combined MVP-MSP approach .

The structure of the 1.5 kVA, 120/277 V, shell-type transformer which was given earlier in Figure (2.1.3) is shown here again in Figure (3.2.1). Magnetic field computation was carried out in one octant of the transformer structure and its surrounding space. The global solution region shown in Figure (3.2.1) is denoted as Ω. In order to apply the combined MVP-MSP method, the transformer winding coil, including the portion of the iron core laminations within the coil structure, was chosen as the MVP subregion, Ω_1 (see Figure (3.2.1)). A first-order FE grid was generated by computer which covers one octant of the entire solution space, Ω, as shown in Figure (3.2.2-a). This global first-order FE grid contains 1440 tetrahedral elements and 378 nodes. The portion of the grid which covers the MVP subregion is shown separately in Figure (3.2.2-b).

Two Fortran program routines were generated and used to solve this transformer problem using the new combined MVP-MSP method. The first computer program includes a series of subroutines which generate a second-order FE grid by adding extra nodes at the middle of each edge of the first-order tetrahedral elements in Ω_1. The same program is used to solve for the MVP within Ω_1, and perform surface FE computation to obtain the MSP jump distributions on the associated interfaces. The second computer program is used to solve the global MSP problem on the entire solution region, Ω. Again, the forcing functions, or the excitations used in the second Fortran program are the MSP jump and MSP derivative discontinuities, which result from the running of the first computer program.

The total excitation current in the transformer winding was kept as its earlier value of 0.25 A as given previously in Chapter 2. The computed energy, and cor-

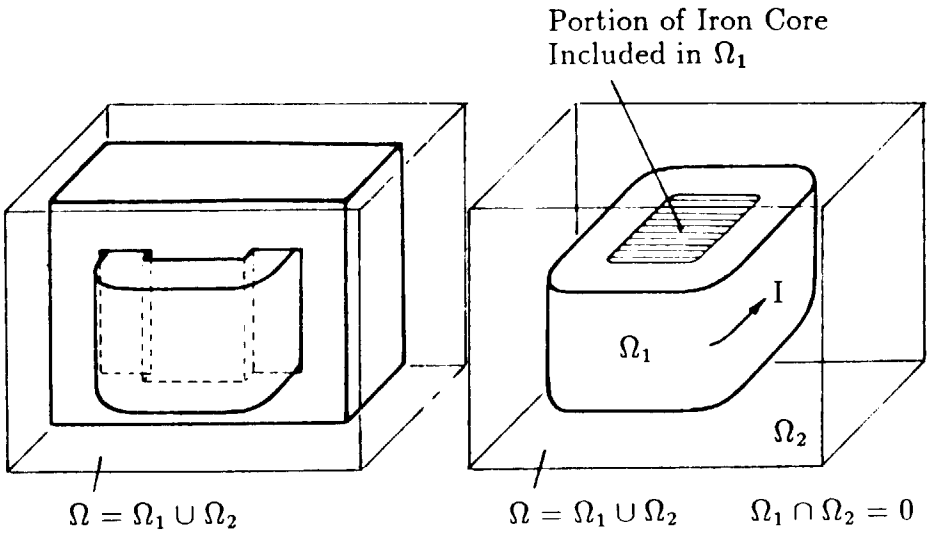

Figure (3.2.1): The 1.5 kVA Shell-Type Transformer Problem

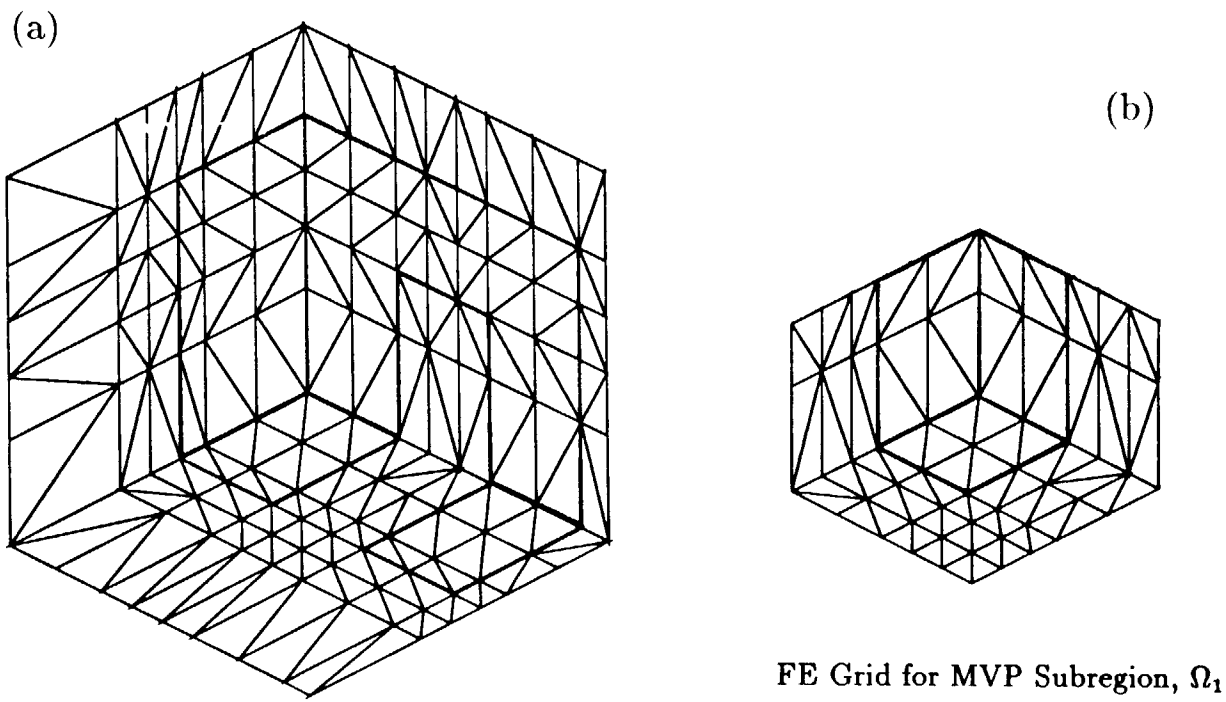

Global FE Grid

FE Grid for MVP Subregion, Ω_1

Figure (3.2.2): FE Grid for 1.5 kVA Shell-Type Transformer

responding magnetizing inductance are given in Table (3.2.1). The computed flux densities at the grid surface, (x-y) plane, are plotted by arrows in Figure (3.2.3-a). In this figure, the lengths of the arrows are proportional to the magnitudes of the flux densities, and the directions of the arrows show the directions of the flux density vectors. Table (3.2.2) shows some typical values of the flux density calculated in the iron core and conductor; the locations associated with the tabulated values are indicated in a companion figure, Figure (3.2.4).

Meanwhile, another global second-order MVP FE computation for the same transformer was carried out. The second-order grid for this computation is generated by adding extra nodes at the middle of every edge of the first-order FE grid which was used originally for the combined MVP-MSP computation. The computed energy, inductance, typical flux densities, as well as the flux density plots, are shown in Tables (3.2.1) and (3.2.2), as well as Figures (3.2.3-b) and (3.2.4-b), side by side with the results from the MVP-MSP method. Comparison between the two sets of results shows excellent agreement between these two methods. Also, the calculated inductances of 0.742 H resulting from the combined MVP-MSP FE method, and 0.731 H resulting from the second-order MVP FE method, are in excellent agreement with the measured inductance value of 0.737 H. These comparisons give strong evidence of the validity of the combined MVP-MSP FE formulation.

To study the numerical sensitivity of the MVP-MSP computed results to grid geometry alterations, a revised first-order FE grid was generated with a grid line shift pattern similar to those shown earlier in Figure (2.1.7) of Chapter 2. This revised grid is given in Figure (3.2.5). The calculated result of inductance from this revised grid, using the combined MVP-MSP approach, is 0.742 H. The computed inductance value in this case is almost unchanged from the value computed by the original grid in Figure (3.2.2). This shows the insensitivity of the computed global results to the grid geometry, which further verifies the efficacy and reliability of the combined MVP-MSP FE formulation. This formulation and method are therefore less vulnerable to grid ill-conditioning which was demonstrated earlier in Chapter 2 for the first-order MVP formulation.

In this demonstration example, the effect of iron lamination on the material reluctivity of the iron core is fully included. Because of the lamination, ν_y has a much lower value than ν_x and ν_z. However, since the excitation current is low, the magnetic saturation of the iron material is almost nonexistent, and therefore has not been taken

Table (3.2.1): Computed Energies and Inductances Versus Test Values for the 1.5 kVA Transformer (I=0.25A)

Method of	Stored Energy	Inductance
MVP (Second-Order Elements)	2.857×10^{-3} (J)	0.731 (H)
Combined MVP-MSP	2.897×10^{-3} (J)	0.742 (H)
From Laboratory Measurement	2.879×10^{-3} (J)	0.737 (H)

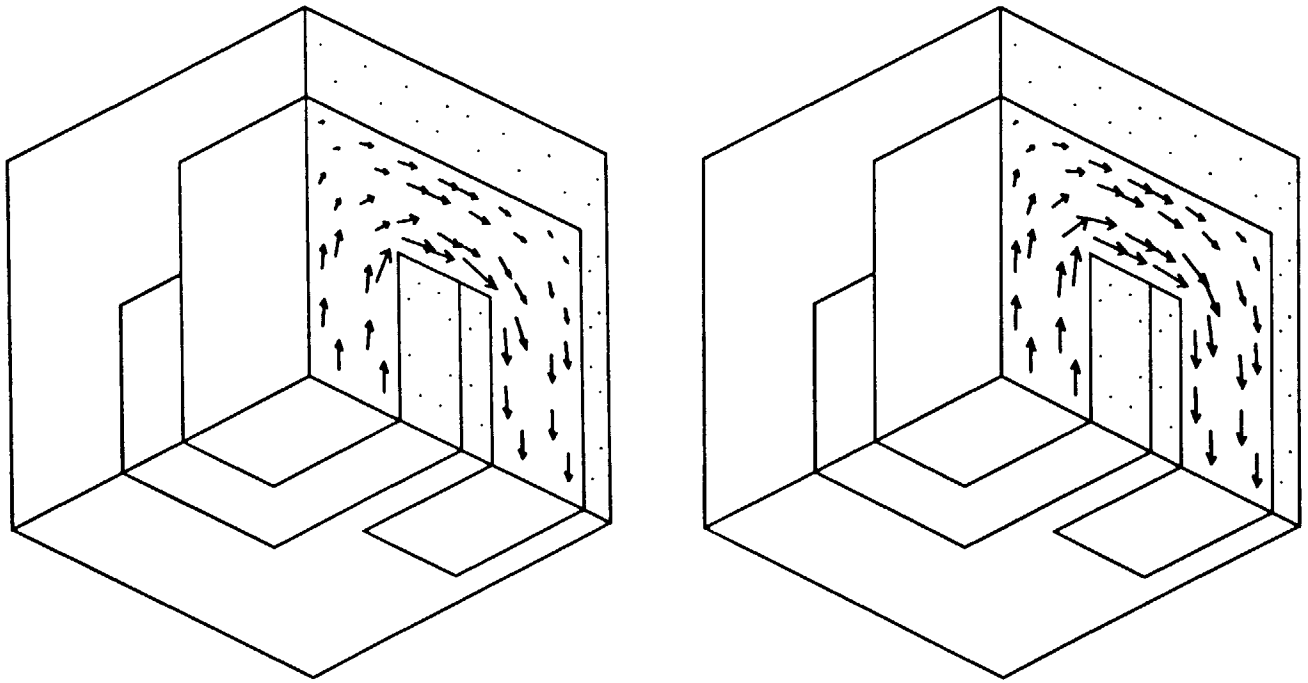

(a): Computed from MVP-MSP FE

(b): Computed from Global Second-Order MVP FE

Figure (3.2.3): Flux Density Vector Distribution at Grid Surfaces

Table (3.2.2): Typical Values of the Calculated Flux Densities in the Iron Core and in the Conductor of the 1.5 kVA Transformer

Method of	Location Number			
	1	2	3	4
MVP (Second-Order Elements)	0.534 (T)	0.467 (T)	0.511 (T)	70×10^{-6} (T)
Combined MVP-MSP	0.540 (T)	0.472 (T)	0.532 (T)	67×10^{-6} (T)

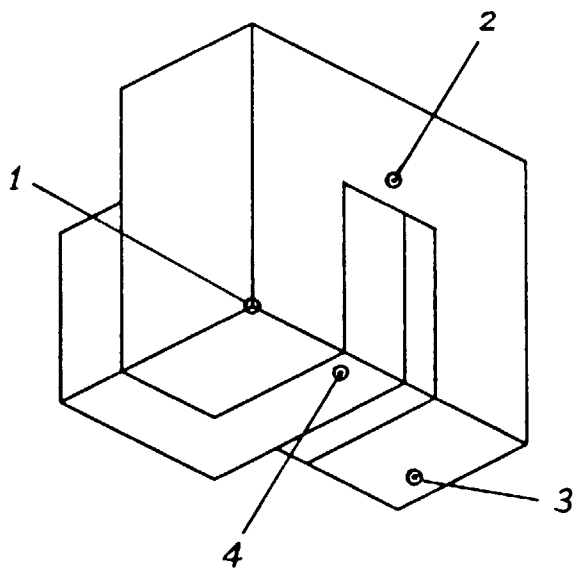

Figure (3.2.4): Locations Associated with Tabulated Flux Density Values in Table (3.2.2)

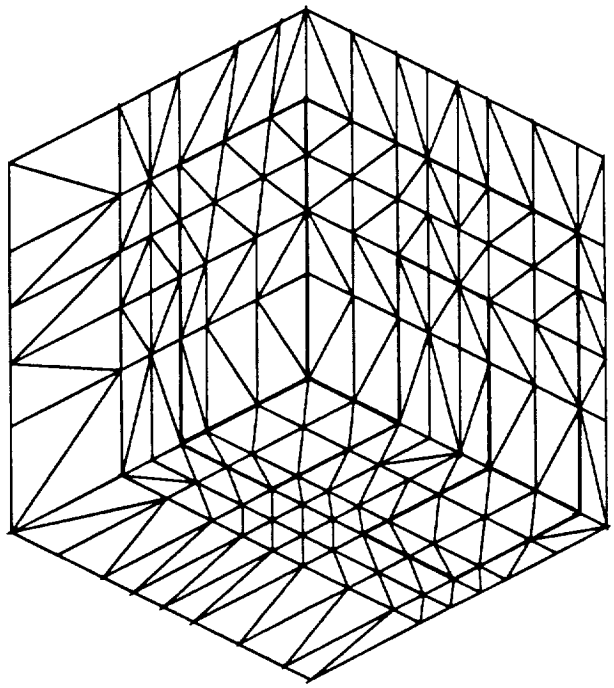

Figure (3.2.5): First-Order FE Grid for the 1.5 kVA Transformer with Shifted Grid Lines

into account. Meanwhile, at higher excitations and corresponding pronounced degrees of saturation, the nonlinearity in the magnetic field can be computed during the MSP stage of the combined MVP-MSP method by use of the Newton-Raphson iterative technique. Such applications involving magnetic material saturation will be given later. Applications of this combined MVP-MSP approach to a large scale nonlinear magnetic field problem, that is the magnetic field computation of the 14.3 kVA MLA, will be reported in detail in later chapters.

Chapter 4

Three-Dimensional Finite Element Formulations for the Combined MVP-MSP Solution Method

This chapter details the finite element formulations used in the new combined MVP-MSP solution method. As stated in Chapter 3, this combined MVP-MSP method consists of three consecutive FE computation steps. The first step is the MVP computation using second-order finite elements in the current-carrying subregions to obtain the curl component of the magnetic field intensity, $\overline{H}_{mvp}$. The second step is the surface FE computation performed on the outer boundary surface of the current-carrying subregion to obtain the MSP jump distribution. Finally, the MSP computation is performed using first-order finite elements in the entire solution region, including the current-carrying subregions. The first and the second steps of the FE computations are required to be carried out only once for a given machine design geometry; the third step of the MSP-FE computation is to be performed repeatedly for each new combination of current excitations and rotor positions. The variational problems which underlie these three different FE computations, and the finite element equations resulting from minimization of the corresponding functionals, are given in the following.

4.1 The Curl-Curl MVP Second-Order Finite Element Formulation

4.1.1 The Variational Problem Associated with the Curl-Curl MVP Formulation

The variational problem associated with the curl-curl MVP boundary value problem was detailed in the previous work by Demerdash et al [32, 33, 34]. This problem is described here again in a compact math form (using vector operators in equations) as a complementary effort. The pertinent energy functional, $F(\overline{A})$, which is to be minimized within the solution volume, V, can be written as: (see Equation (2.1.2))

$$F(\overline{A}) = \int_V [\frac{1}{2}(\overline{H} \cdot \overline{B}) - \overline{J} \cdot \overline{A}]\, dv$$

and, with $\overline{H} = \overline{\overline{\nu}}\overline{B}$ (Equation (2.0.3)) and $\overline{B} = \nabla \times \overline{A}$ (Equation (2.0.5))

$$F(\overline{A}) = \int_V [\frac{1}{2}(\overline{\overline{\nu}}\nabla \times \overline{A}) \cdot (\nabla \times \overline{A}) - \overline{J} \cdot \overline{A}]\, dv \tag{4.1.1}$$

In general, when magnetic saturation of iron material is encountered, the material reluctivities, ν_x, ν_y, and ν_z of the term, $\overline{\overline{\nu}}$, in $F(\overline{A})$ are functions of the flux density, $\overline{B} = \nabla \times \overline{A}$, hence they must be functions of $\overline{A}$. However, nonlinear magnetic field problems caused by nonlinearity of the material property are usually solved by iterative technique such as the saturation iteration method [35] or the Newton-Raphson method [36] in conjunction with the FE computations. Fixed reluctivities are used in each iteration step of the associated FE computation. Therefore, at the stage of derivation of the variational problem of the curl-curl MVP FE formulation, the reluctivities, ν_x, ν_y, and ν_z can be treated as quantities independent of the vector potential, $\overline{A}$.

The variational problem described by the functional of Equation (4.1.1) must be solved under given magnetic field boundary conditions. In practical engineering problems, the commonly used outer boundary conditions are either: (a) the normal component of the flux density is equal to zero ($\overline{B}_n = 0$), which means that all calculated magnetic fields are bounded within the solution region, or (b) the tangential component of the field intensity is equal to zero ($\overline{H}_t = 0$), which means the calculated

fields are perpendicular to the boundary surface. These two types of field boundary conditions at the outer boundary, S, of the solution volume, V, can be described through the MVP, $\overline{A}$, as follows:

$$\overline{B}_n = 0 \qquad or \qquad \overline{A} = 0 \qquad at\ S_B \tag{4.1.2}$$

$$\overline{H}_t = 0 \qquad or \qquad (\overline{\overline{\nu}}\nabla \times \overline{A}) \times \hat{n} = 0 \qquad at\ S_H \tag{4.1.3}$$

where $S_B \cup S_H = S$, $S_B \cap S_H = 0$, and $\hat{n}$ is the normal unit vector at the outer boundary, S_H.

According to variational principles, minimization of the above mentioned functional, Equation (4.1.1) can be achieved by setting the first variation of the functional to zero. This can be stated as follows:

$$\begin{aligned}
\delta F(\overline{A}) &= \int_V [\frac{1}{2}(\overline{\overline{\nu}}\nabla \times \delta\overline{A}) \cdot (\nabla \times \overline{A}) + \frac{1}{2}(\overline{\overline{\nu}}\nabla \times \overline{A}) \cdot (\nabla \times \delta\overline{A}) - \overline{J} \cdot \delta\overline{A}] dv \\
&= \int_V [\frac{1}{2}(\overline{\overline{\nu}}\nabla \times \overline{A}) \cdot (\nabla \times \delta\overline{A}) + \frac{1}{2}(\overline{\overline{\nu}}\nabla \times \overline{A}) \cdot (\nabla \times \delta\overline{A}) - \overline{J} \cdot \delta\overline{A}] dv \\
&= \int_V [(\overline{\overline{\nu}}\nabla \times \overline{A}) \cdot (\nabla \times \delta\overline{A}) - \overline{J} \cdot \delta\overline{A}]\, dv = 0
\end{aligned} \tag{4.1.4}$$

By using the following vector identity,

$$\nabla \cdot (\overline{a} \times \overline{b}) = (\nabla \times \overline{a}) \cdot \overline{b} - \overline{a} \cdot (\nabla \times \overline{b}) \tag{4.1.5}$$

with a correspondence of $\overline{a}$ to $\delta\overline{A}$, and $\overline{b}$ to $(\overline{\overline{\nu}}\nabla \times \overline{A})$, one can expand Equation (4.1.4) as follows:

$$\begin{aligned}
\delta F(\overline{A}) &= \int_V \{\nabla \cdot [\delta\overline{A} \times (\overline{\overline{\nu}}\nabla \times \overline{A})] + [\nabla \times (\overline{\overline{\nu}}\nabla \times \overline{A})] \cdot \delta\overline{A} - \overline{J} \cdot \delta\overline{A}\}\, dv \\
&= 0
\end{aligned} \tag{4.1.6}$$

According to Gauss's theorem, for a volume V whose outer surface is a, one can write $\int_V (\nabla \cdot \overline{D}) dv = \oint_s \overline{D} \cdot d\overline{s}$. The first term of the volume integration in Equation (4.1.6) can therefore be replaced by a closed surface integration. Thus one obtains

the following:

$$\delta F(\overline{A}) = \oint_S \delta\overline{A} \times (\overline{\overline{\nu}}\nabla \times \overline{A}) \cdot \hat{n}\, ds + \int_V [\nabla \times (\overline{\overline{\nu}}\nabla \times \overline{A}) - \overline{J}] \cdot \delta\overline{A}\, dv$$

$$= 0 \tag{4.1.7}$$

Furthermore, by substituting ($\overline{H} = \overline{\overline{\nu}}\overline{B} = \overline{\overline{\nu}}\nabla \times \overline{A}$) into the closed surface integration of Equation (4.1.7), and by changing the position order for the terms $\delta\overline{A}$, $\overline{H}$, and $\hat{n}$ in the integrand of the surface integral part of Equation (4.1.7), one can re-arrange this closed surface integral, using vector algebra, as follows:

$$\oint_S \delta\overline{A} \times (\overline{\overline{\nu}}\nabla \times \overline{A}) \cdot \hat{n}\, ds = \oint_S (\delta\overline{A} \times \overline{H}) \cdot \hat{n}\, ds = -\oint_S (\hat{n} \times \overline{H}) \cdot \delta\overline{A}\, ds$$

$$= \oint_S (\overline{H} \times \hat{n}) \cdot \delta\overline{A}\, ds = \oint_S (\overline{H}_t \times \hat{n}) \cdot \delta\overline{A}\, ds \tag{4.1.8}$$

From Equation (4.1.2) $\delta\overline{A}\,|_{S_B} = 0$ since the magnetic vector potential on S_B is fixed; and from Equation (4.1.3) $\overline{H}_t\,|_{S_H} = 0$. Thus, the closed surface integral in Equation (4.1.8), which is on the outer boundary, $S = S_B \cup S_H$, must vanish when the boundary conditions are imposed. Hence the variational, $\delta F(\overline{A})$, in Equation (4.1.7) can be further reduced to the following:

$$\delta F(\overline{A}) = \int_V [\nabla \times (\overline{\overline{\nu}}\nabla \times \overline{A}) - \overline{J}] \cdot \delta\overline{A}\, dv = 0 \tag{4.1.9}$$

According to variational principles, $\delta F(\overline{A})$ stipulated by Equation (4.1.9) must vanish for any possible variation of the MVP, that is, for any $\delta\overline{A}$ in Equation (4.1.9). The necessary condition for the vanishing of $\delta F(\overline{A})$ is therefore that the term, $[\nabla \times (\overline{\overline{\nu}}\nabla \times \overline{A}) - \overline{J}]$, in Equation (4.1.9) must be equal to zero. Accordingly, the $\overline{A}$ subject to the boundary conditions in Equations (4.1.2) and (4.1.3), which minimizes the functional of Equation (4.1.1) must satisfy the curl-curl MVP equation,

$$\nabla \times (\overline{\overline{\nu}}\nabla \times \overline{A}) = \overline{J}$$

In the finite element method, one solves the curl-curl MVP boundary value problem through numerical minimization of the energy functional, $F(\overline{A})$, given in Equation (4.1.1). In the case of the MVP part of the new combined MVP-MSP method, the minimization of the functional is to be achieved by the use of second-

order finite elements.

4.1.2 Element Equations for Second-Order Tetrahedral Finite Elements

Second-order tetrahedral elements, see Figure (4.1.1), are used as the building blocks for the geometric discretization in applications of the MVP-MSP method described herein. The second order polynomial in three dimensions consists of 10 terms. Thus ten nodes are located at the vertices and on the edges, of the tetrahedron. Also, the edges of the element can be of quadratic shape, which better fits the solution regions that have curved boundaries.

In this finite element formulation, the MVP, $\overline{A}$, within one element is approximated by an interpolation in between the elemental nodal MVP values, $\overline{A}_i$'s. Here, the MVP at the i-th node of an element, $\overline{A}_i$, can be generally stated as

$$\overline{A}_i = (A_{ix}\hat{a}_x + A_{iy}\hat{a}_y + A_{iz}\hat{a}_z) \tag{4.1.10}$$

where, $\hat{a}_x$, $\hat{a}_y$, and $\hat{a}_z$ are the unit directional vectors; A_{ix}, A_{iy}, and A_{iz} are the directional components of the nodal MVP, $\overline{A}_i$. The interpolation polynomial of $\overline{A}$ in the element can be written as follows:

$$\overline{A} = \sum_{k=1}^{10} N_k \overline{A}_k = \sum_{k=1}^{10} N_k (A_{kx}\hat{a}_x + A_{ky}\hat{a}_y + A_{kz}\hat{a}_z) \tag{4.1.11}$$

where N_k is the coefficient of the interpolation, or "shape function". In second order finite elements, these interpolation coefficients can be expressed explicitly as second-order polynomials in local coordinate systems, which will be further explained later in Section 4.1.3.

By substituting $\overline{A}$ of Equation (4.1.11) into Equation (4.1.1), one can describe the volume integration of the functional, $F(\overline{A})$, by a summation of volume integrations in every element. This yields the following:

$$F = \sum_{e=1}^{NE} F_e = \sum_{e=1}^{NE} \int_{V_e} [\frac{1}{2}(\overline{\overline{\nu}}\nabla \times \overline{A}) \cdot (\nabla \times \overline{A}) - \overline{J} \cdot \overline{A}] \, dv$$

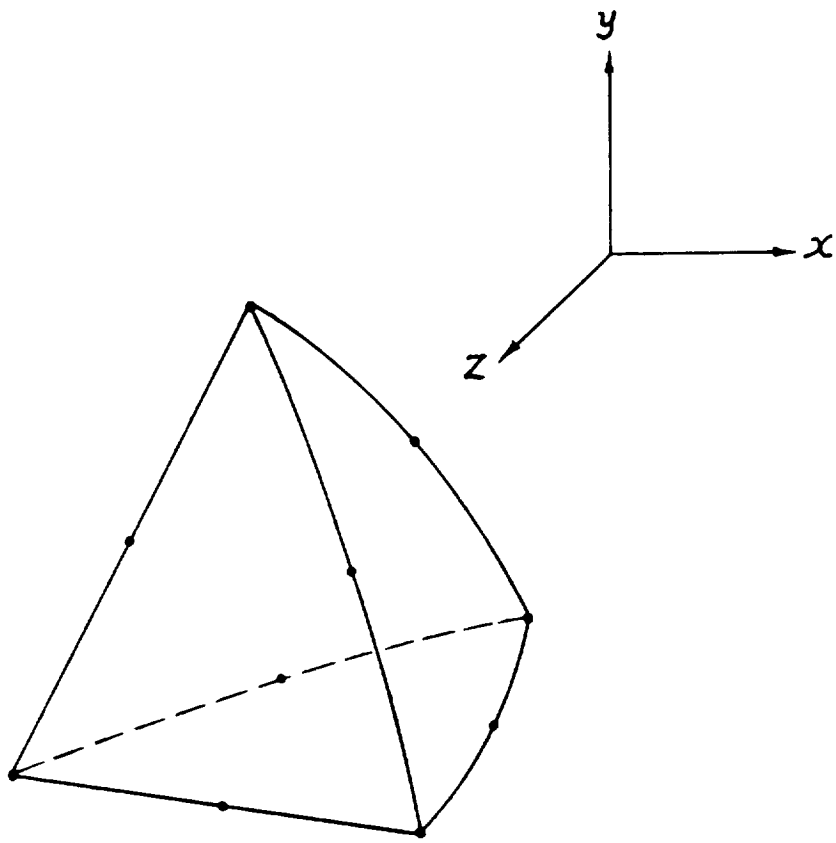

Figure (4.1.1) A Second-Order Tetrahedral Type Element

$$= \sum_{e=1}^{NE} \int_{V_e} [\frac{1}{2}(\overline{\overline{\nu}}\nabla \times \sum_{k=1}^{10} N_k \overline{A}_k) \cdot (\nabla \times \sum_{k=1}^{10} N_k \overline{A}_k) - \overline{J} \cdot \sum_{k=1}^{10} \overline{A}_k] \, dv \qquad (4.1.12)$$

where, NE is the total number of elements in a given FE grid. Therefore, the functional $F(\overline{A})$ is approximated by a function of the nodal values of three directional components of the MVP. The total number of the nodal value components is 3×NN for a given FE grid with total nodes of NN.

From knowledge of the differential calculus, the minimization of the function in Equation (4.1.12) can be achieved by setting its first derivatives with respect to these 3×NN nodal variables to zero. Namely, one equates the following derivatives to zero:

$$\frac{\partial F}{\partial A_{ix}} = 0, \qquad \frac{\partial F}{\partial A_{iy}} = 0, \qquad \frac{\partial F}{\partial A_{iz}} = 0, \qquad for\ i = 1, 2, ...NN \qquad (4.1.13)$$

The differential operations stated in Equation (4.1.13) are taken for every element one after another. For each element it yields a set of elemental equations (element equations). Then the total NE sets of element equations can be assembled into a global system of equations. Solving the global system of equations, one obtains the nodal MVPs as well as the other related magnetic field quantities. Therefore, the key to the implementation of the curl-curl MVP FE analysis using second-order elements is the element equations. This is discussed next.

In one second-order tetrahedral element, the partial derivative term, $\partial F/\partial A_{ix} = 0$, in Equation (4.1.13) can be expanded and rearranged as follows (the number of nodes in an element, nn, is equal to 10 in the case of second-order tetrahedral element):

$$\frac{\partial F_e}{\partial A_{ix}} = \frac{\partial}{\partial A_{ix}} \int_{V_e} \{\frac{1}{2}[\overline{\overline{\nu}}\nabla \times \sum_{k=1}^{nn}(N_k \overline{A}_k)] \cdot [\nabla \times \sum_{k=1}^{nn}(N_k \overline{A}_k)] - \overline{J} \cdot \sum_{k=1}^{nn}(N_k \overline{A}_k)\} dv$$

$$= \int_{V_e} \{\overline{\overline{\nu}}[\nabla \times \sum_{k=1}^{nn}(N_k \overline{A}_k)] \cdot \frac{\partial}{\partial A_{ix}}[\nabla \times \sum_{k=1}^{nn}(N_k \overline{A}_k)] - \overline{J} \cdot \frac{\partial}{\partial A_{ix}} \sum_{k=1}^{nn}(N_k \overline{A}_k)\} dv$$

$$= \int_{V_e} \{[\sum_{k=1}^{nn} \overline{\overline{\nu}}\nabla \times (N_k \overline{A}_k)] \cdot [\nabla \times (N_i \hat{a}_x)] - N_i \overline{J} \cdot \hat{a}_x\} dv$$

$$= \int_{V_e} \{[\sum_{k=1}^{nn} \overline{\overline{\nu}}\nabla \times (N_k \overline{A}_k)] \cdot (\frac{\partial N_i}{\partial z}\hat{a}_y - \frac{\partial N_i}{\partial y}\hat{a}_z) - N_i J_x\} dv$$

C-2

$$= \sum_{k=1}^{nn} \int_{V_e} \{\frac{\partial N_i}{\partial z}[\overline{\overline{\nu}}\nabla \times (N_k \overline{A}_k)] \cdot \hat{a}_y - \frac{\partial N_i}{\partial y}[\overline{\overline{\nu}}\nabla \times (N_k \overline{A}_k)] \cdot \hat{a}_z\} \, dv - \int_{V_e} N_i J_x \, dv$$

$$= \sum_{k=1}^{nn} \int_{V_e} [\frac{\partial N_i}{\partial z}(\nu_y \frac{\partial N_k}{\partial z} A_{kx} - \nu_y \frac{\partial N_k}{\partial x} A_{kz}) - \frac{\partial N_i}{\partial y}(\nu_z \frac{\partial N_k}{\partial x} A_{ky} - \nu_z \frac{\partial N_k}{\partial y} A_{kx})] \, dv$$

$$- \int_{V_e} N_i J_x \, dv$$

$$= \sum_{k=1}^{nn} \{[\int_{V_e} (\nu_z \frac{\partial N_i}{\partial y} \frac{\partial N_k}{\partial y} + \nu_y \frac{\partial N_i}{\partial z} \frac{\partial N_k}{\partial z}) dv] A_{kx} - [\int_{V_e} (\nu_z \frac{\partial N_i}{\partial y} \frac{\partial N_k}{\partial x}) dv] A_{ky}$$

$$- [\int_{V_e} (\nu_y \frac{\partial N_i}{\partial z} \frac{\partial N_k}{\partial x}) dv] A_{kz}\} - \int_{V_e} N_i J_x \, dv = 0$$

$$for \;\; i = 1, 2, ..., nn \qquad (4.1.14)$$

Again, nn is the general notation for the number of total nodes in an element, in the case of second-order tetrahedral element nn is equal to 10. Similarly, the other two partial derivative terms in Equation (4.1.13), $\partial F/\partial A_{iy} = 0$, and $\partial F/\partial A_{iz} = 0$ can be expanded and rearranged, within one elemental volume, as follows:

$$\frac{\partial F_e}{\partial A_{iy}} = \frac{\partial}{\partial A_{iy}} \int_{V_e} \{\frac{1}{2}[\overline{\overline{\nu}}\nabla \times \sum_{k=1}^{nn} (N_k \overline{A}_k)] \cdot [\nabla \times \sum_{k=1}^{nn} (N_k \overline{A}_k)] - \overline{J} \cdot \sum_{k=1}^{nn} (N_k \overline{A}_k)\} dv$$

$$= \int_{V_e} \{\overline{\overline{\nu}}[\nabla \times \sum_{k=1}^{nn} (N_k \overline{A}_k)] \cdot \frac{\partial}{\partial A_{iy}} [\nabla \times \sum_{k=1}^{nn} (N_k \overline{A}_k)] - \overline{J} \cdot \frac{\partial}{\partial A_{iy}} \sum_{k=1}^{nn} (N_k \overline{A}_k)\} dv$$

$$= \int_{V_e} \{[\sum_{k=1}^{nn} \overline{\overline{\nu}}\nabla \times (N_k \overline{A}_k)] \cdot [\nabla \times (N_i \hat{a}_y)] - N_i \overline{J} \cdot \hat{a}_y\} dv$$

$$= \int_{V_e} \{[\sum_{k=1}^{nn} \overline{\overline{\nu}}\nabla \times (N_k \overline{A}_k)] \cdot (\frac{\partial N_i}{\partial x} \hat{a}_z - \frac{\partial N_i}{\partial z} \hat{a}_x) - N_i J_y\} dv$$

$$= \sum_{k=1}^{nn} \int_{V_e} \{\frac{\partial N_i}{\partial x}[\overline{\overline{\nu}}\nabla \times (N_k \overline{A}_k)] \cdot \hat{a}_z - \frac{\partial N_i}{\partial z}[\overline{\overline{\nu}}\nabla \times (N_k \overline{A}_k)] \cdot \hat{a}_x\} \, dv - \int_{V_e} N_i J_y \, dv$$

$$= \sum_{k=1}^{nn} \int_{V_e} [\frac{\partial N_i}{\partial x}(\nu_z \frac{\partial N_k}{\partial x} A_{ky} - \nu_z \frac{\partial N_k}{\partial y} A_{kx}) - \frac{\partial N_i}{\partial z}(\nu_x \frac{\partial N_k}{\partial y} A_{kz} - \nu_x \frac{\partial N_k}{\partial z} A_{ky})] \, dv$$

$$- \int_{V_e} N_i J_y \, dv$$

$$= \sum_{k=1}^{nn} \{ -[\int_{V_e} (\nu_z \frac{\partial N_i}{\partial x} \frac{\partial N_k}{\partial y}) dv] A_{kx} + [\int_{V_e} (\nu_x \frac{\partial N_i}{\partial z} \frac{\partial N_k}{\partial z} + \nu_z \frac{\partial N_i}{\partial x} \frac{\partial N_k}{\partial x}) dv] A_{ky}$$

$$- [\int_{V_e} (\nu_x \frac{\partial N_i}{\partial z} \frac{\partial N_k}{\partial y}) dv] A_{kz} \} - \int_{V_e} N_i J_y \, dv = 0$$

$$for \quad i = 1, 2, ..., nn \tag{4.1.15}$$

and

$$\frac{\partial F_e}{\partial A_{iz}} = \frac{\partial}{\partial A_{iz}} \int_{V_e} \{ \frac{1}{2} [\overline{\overline{\nu}} \nabla \times \sum_{k=1}^{nn} (N_k \overline{A}_k)] \cdot [\nabla \times \sum_{k=1}^{nn} (N_k \overline{A}_k)] - \overline{J} \cdot \sum_{k=1}^{nn} (N_k \overline{A}_k) \} dv$$

$$= \int_{V_e} \{ \overline{\overline{\nu}} [\nabla \times \sum_{k=1}^{nn} (N_k \overline{A}_k)] \cdot \frac{\partial}{\partial A_{iz}} [\nabla \times \sum_{k=1}^{nn} (N_k \overline{A}_k)] - \overline{J} \cdot \frac{\partial}{\partial A_{iz}} \sum_{k=1}^{nn} (N_k \overline{A}_k) \} dv$$

$$= \int_{V_e} \{ [\sum_{k=1}^{nn} \overline{\overline{\nu}} \nabla \times (N_k \overline{A}_k)] \cdot [\nabla \times (N_i \hat{a}_z)] - N_i \overline{J} \cdot \hat{a}_z \} dv$$

$$= \int_{V_e} \{ [\sum_{k=1}^{nn} \overline{\overline{\nu}} \nabla \times (N_k \overline{A}_k)] \cdot (\frac{\partial N_i}{\partial y} \hat{a}_x - \frac{\partial N_i}{\partial x} \hat{a}_y) - N_i J_z \} dv$$

$$= \sum_{k=1}^{nn} \int_{V_e} \{ \frac{\partial N_i}{\partial y} [\overline{\overline{\nu}} \nabla \times (N_k \overline{A}_k)] \cdot \hat{a}_x - \frac{\partial N_i}{\partial x} [\overline{\overline{\nu}} \nabla \times (N_k \overline{A}_k)] \cdot \hat{a}_y \} \, dv - \int_{V_e} N_i J_z \, dv$$

$$= \sum_{k=1}^{nn} \int_{V_e} [\frac{\partial N_i}{\partial y} (\nu_x \frac{\partial N_k}{\partial y} A_{kz} - \nu_x \frac{\partial N_k}{\partial z} A_{ky}) - \frac{\partial N_i}{\partial x} (\nu_y \frac{\partial N_k}{\partial z} A_{kx} - \nu_y \frac{\partial N_k}{\partial x} A_{kz})] \, dv$$

$$- \int_{V_e} N_i J_z \, dv$$

$$= \sum_{k=1}^{nn} \{ -[\int_{V_e} (\nu_y \frac{\partial N_i}{\partial x} \frac{\partial N_k}{\partial z}) dv] A_{kx} - [\int_{V_e} (\nu_x \frac{\partial N_i}{\partial y} \frac{\partial N_k}{\partial z}) dv] A_{ky}$$

$$+ [\int_{V_e} (\nu_y \frac{\partial N_i}{\partial x} \frac{\partial N_k}{\partial x} + \nu_x \frac{\partial N_i}{\partial y} \frac{\partial N_k}{\partial y}) dv] A_{kz} \} - \int_{V_e} N_i J_z \, dv = 0$$

$$for \;\; i = 1, 2, ..., nn \qquad (4.1.16)$$

In the case of second-order tetrahedral type finite element Equations (4.1.14) through (4.1.16) yield 30 simultaneous algebraic equations associated with 30 unknown variables, A_{ix}, A_{iy}, A_{iz}, for i=1,2,...,10. These 30 simultaneous equations are called the element equations. Generally, the set of element equations can be written in a compact matrix form as follows

$$\underline{S_e}\,\underline{A_e} = \underline{I_e} \qquad (4.1.17)$$

where, the $\underline{S_e}$ is a (30×30) square matrix, commonly referred to as the element coefficient matrix; and the $\underline{I_e}$ vector is commonly referred to as the element forcing function vector. The various terms in the element coefficient matrix, $\underline{S_e}$, and the column vectors, $\underline{A_e}$, as well as the column vector, I_e, in Equation (4.1.17) can be further expressed by means of sub-matrices and sub-column-vectors. That is, Equation (4.1.17) can be written as follows:

$$\begin{bmatrix} \underline{S}_{1,1} & \underline{S}_{1,2} & \underline{S}_{1,3} & \cdots & \cdots & \underline{S}_{1,nn} \\ \underline{S}_{2,1} & \underline{S}_{2,2} & \cdots & \cdots & \cdots & \underline{S}_{2,nn} \\ \vdots & & & & & \vdots \\ \vdots & & & & & \vdots \\ \cdots & \cdots & & \underline{S}_{i,k} & \cdots & \cdots \\ \vdots & & & & & \vdots \\ \underline{S}_{nn,1} & \underline{S}_{nn,2} & \cdots & \cdots & \cdots & \underline{S}_{nn,nn} \end{bmatrix} \begin{Bmatrix} \underline{A}_1 \\ \underline{A}_2 \\ \vdots \\ \vdots \\ \underline{A}_i \\ \vdots \\ \underline{A}_{nn} \end{Bmatrix} = \begin{Bmatrix} \underline{I}_1 \\ \underline{I}_2 \\ \vdots \\ \vdots \\ \underline{I}_i \\ \vdots \\ \underline{I}_{nn} \end{Bmatrix} \qquad (4.1.18)$$

where, the general term, $\underline{S}_{i,k}$, in the element coefficient matrix is a (3×3) sub-matrix

which is given by,

$$\underline{S}_{i,k} = \left[\begin{array}{c|c|c} \int_{V_e} \nu_y \frac{\partial N_i}{\partial z}\frac{\partial N_k}{\partial z} dv + \int_{V_e} \nu_z \frac{\partial N_i}{\partial y}\frac{\partial N_k}{\partial y} dv & -\int_{V_e} \nu_z \frac{\partial N_i}{\partial y}\frac{\partial N_k}{\partial x} dv & -\int_{V_e} \nu_y \frac{\partial N_i}{\partial z}\frac{\partial N_k}{\partial x} dv \\ \hline -\int_{V_e} \nu_z \frac{\partial N_i}{\partial x}\frac{\partial N_k}{\partial y} dv & \int_{V_e} \nu_x \frac{\partial N_i}{\partial z}\frac{\partial N_k}{\partial z} dv + \int_{V_e} \nu_z \frac{\partial N_i}{\partial x}\frac{\partial N_k}{\partial x} dv & -\int_{V_e} \nu_x \frac{\partial N_i}{\partial z}\frac{\partial N_k}{\partial y} dv \\ \hline -\int_{V_e} \nu_y \frac{\partial N_i}{\partial x}\frac{\partial N_k}{\partial z} dv & -\int_{V_e} \nu_x \frac{\partial N_i}{\partial y}\frac{\partial N_k}{\partial z} dv & \int_{V_e} \nu_y \frac{\partial N_i}{\partial x}\frac{\partial N_k}{\partial x} dv + \int_{V_e} \nu_x \frac{\partial N_i}{\partial y}\frac{\partial N_k}{\partial y} dv \end{array}\right] \tag{4.1.19}$$

Here, the general term, $\underline{A}_i$, in the column vector, $\underline{A}_e$, is a (3×1) sub-column-vector given by

$$\underline{A}_i = \left\{\begin{array}{c} A_{ix} \\ A_{iy} \\ A_{iz} \end{array}\right\} \tag{4.1.20}$$

and the general term, $\underline{I}_i$ in the element forcing function is a (3×1) sub-column-vector which can be written as follows:

$$\underline{I}_i = \left\{\begin{array}{c} \int_{V_e} N_i J_x dv \\ \int_{V_e} N_i J_y dv \\ \int_{V_e} N_i J_z dv \end{array}\right\} \tag{4.1.21}$$

Notice that the sub-matrix $\underline{S}_{k,i}$ is exactly equal to the transpose of the sub-matrix $\underline{S}_{i,k}$, thus the element coefficient matrix is symmetric.

It should be pointed out here that the element equations in Equation (4.1.18-4.1.21) are written in a general form, applicable to any type of element. This general form also takes into account anisotropic reluctivity of the medium. As the MVP computation in the new combined MVP-MSP method is carried out only in regions with media of constant isotropic reluctivity, the three diagonal terms of the reluctivity tensor have identical material reluctivity values.

4.1.3 Coordinate Transformation and Numerical Integration

In order to calculate the element coefficient matrix and the element forcing function vector given in Equation (4.1.18), (4.1.19), and (4.1.21), one needs to compute various elemental volume integration terms. These integrations can be summarized as

$$\int_{V_e} \nu \frac{\partial N_i}{\partial u} \frac{\partial N_k}{\partial w} dv$$

and

$$\int_{V_e} N_i J_u dv$$

Here, u and w can be either x, y, or z and V_e is the volume of a given tetrahedral element. Considering ν and J_u to be known within the element, one can further express these two types of integrations in a general form as follows:

$$Int = \int_{V_e} G(N_i, \frac{\partial N_j}{\partial x}, \frac{\partial N_k}{\partial y}, \frac{\partial N_l}{\partial z})\, dv \tag{4.1.22}$$

Generally, a second-order tetrahedral type element can have irregular shape with curved edges and curved surfaces as shown earlier in Figure (4.1.1). In this case, it is extremely difficult to obtain an uniform pattern of an analytical algorithm to compute the integration in Equation (4.1.22) for every element. Accordingly, a technique which involves coordinate transformation and numerical integration is used here to calculate these volume integrations, and consequently, to obtain the element coefficient matrices and forcing function vectors. This technique of coordinate transformation and numerical integration can be found in numerous text books on the finite element method [83] [84] [85]. However, a brief summary of this technique,

especially on the application to second-order tetrahedral type elements, is given next.

The basic idea of this technique is that one maps every tetrahedral type element, which may have irregular shape under the global coordinate system, into a fixed volume of a right tetrahedron, such that the integration defined by Equation (4.1.22) can be calculated using a uniform numerical integration algorithm. The right tetrahedron used in coordinate transformation in this research is shown in Figure (4.1.2). The locations of the ten nodes of this right tetrahedron are described by (α, β, γ), which will be referred to as local coordinates.

A ten node interpolation is used to approximate a given function, u, over the right tetrahedron by means of the local coordinate system. This interpolation can be expressed as follows:

$$u = \sum_{k=1}^{10} N_k(\alpha, \beta, \gamma) u_k \tag{4.1.23}$$

where u_k is the value of the function at k-th node, and $N_k(\alpha, \beta, \gamma)$ is the coefficient for the interpolation. By using the following notations

$$f_1 = 1 - \alpha - \beta - \gamma$$

$$f_2 = \alpha$$

$$f_3 = \beta$$

$$f_4 = \gamma$$

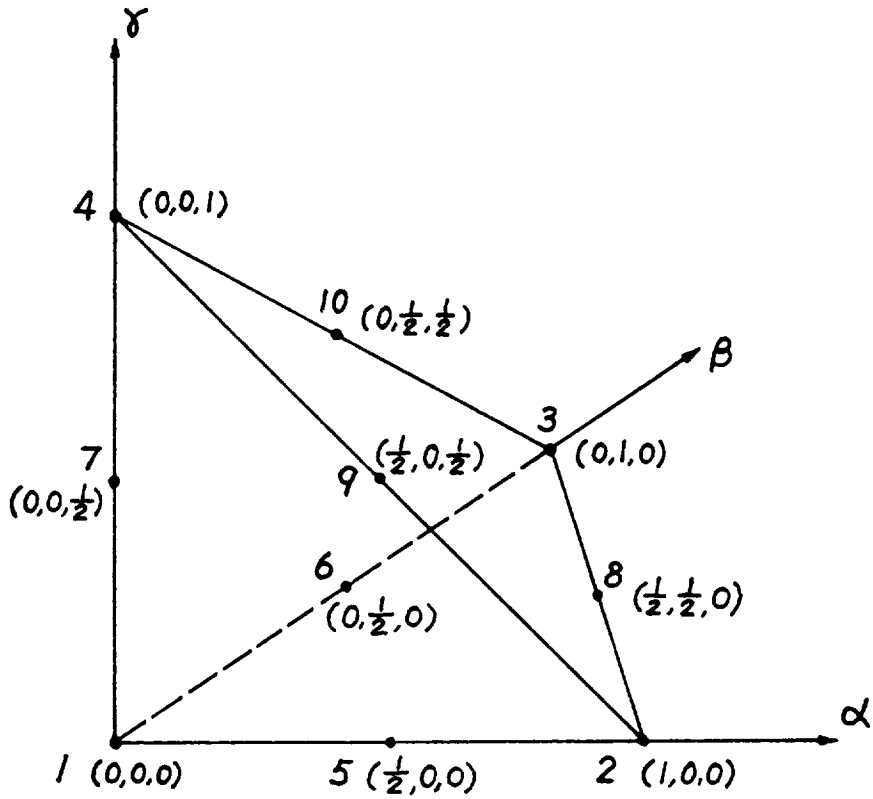

Figure (4.1.2) Right Tetrahedral Element in Local Coordinate System

the interpolation function, N_k, can be written as follows:

$$N_k = \begin{cases} f_1(2f_1 - 1) = (1 - \alpha - \beta - \gamma)(1 - 2\alpha - 2\beta - 2\gamma) & k = 1 \\ f_2(2f_2 - 1) = \alpha(2\alpha - 1) & k = 2 \\ f_3(2f_3 - 1) = \beta(2\beta - 1) & k = 3 \\ f_4(2f_4 - 1) = \gamma(2\gamma - 1) & k = 4 \\ 4f_1f_2 = 4\alpha(1 - \alpha - \beta - \gamma) & k = 5 \\ 4f_1f_3 = 4\beta(1 - \alpha - \beta - \gamma) & k = 6 \\ 4f_1f_4 = 4\gamma(1 - \alpha - \beta - \gamma) & k = 7 \\ 4f_2f_3 = 4\alpha\beta & k = 8 \\ 4f_2f_4 = 4\alpha\gamma & k = 9 \\ 4f_3f_4 = 4\beta\gamma & k = 10 \end{cases} \tag{4.1.24}$$

The partial derivatives of N_k with respect to α, β, and γ, which will be used later when the discussion is carried on further, can be written here as follows:

$$\frac{\partial N_k}{\partial \alpha} = \begin{cases} 1 - 4f_1 = 4\alpha + 4\beta + 4\gamma - 3 & k = 1 \\ 4f_2 - 1 = 4\alpha - 1 & k = 2 \\ 0 & k = 3 \\ 0 & k = 4 \\ 4(f_1) - 4f_2 = 4(1 - 2\alpha - \beta - \gamma) & k = 5 \\ -4f_3 = -4\beta & k = 6 \\ -4f_4 = -4\gamma & k = 7 \\ 4f_3 = 4\beta & k = 8 \\ 4f_4 = 4\gamma & k = 9 \\ 0 & k = 10 \end{cases} \tag{4.1.25}$$

$$\frac{\partial N_k}{\partial \beta} = \begin{cases} 1 - 4f_1 = 4\alpha + 4\beta + 4\gamma - 3 & k = 1 \\ 0 & k = 2 \\ 4f_3 - 1 = 4\beta - 1 & k = 3 \\ 0 & k = 4 \\ -4f_2 = -4\alpha & k = 5 \\ 4(f_1) - 4f_3 = 4(1 - \alpha - 2\beta - \gamma) & k = 6 \\ -4f_4 = -4\gamma & k = 7 \\ 4f_2 = 4\alpha & k = 8 \\ 0 & k = 9 \\ 4f_4 = 4\gamma & k = 10 \end{cases} \tag{4.1.26}$$

$$\frac{\partial N_k}{\partial \gamma} = \begin{cases} 1 - 4f_1 = 4\alpha + 4\beta + 4\gamma - 3 & k = 1 \\ 0 & k = 2 \\ 0 & k = 3 \\ 4f_4 - 1 = 4\gamma - 1 & k = 4 \\ -4f_2 = -4\alpha & k = 5 \\ -4f_3 = -4\beta & k = 6 \\ 4(f_1) - 4f_4 = 4(1 - \alpha - \beta - 4\gamma) & k = 7 \\ 0 & k = 8 \\ 4f_2 = 4\alpha & k = 9 \\ 4f_4 = 4\beta & k = 10 \end{cases} \tag{4.1.27}$$

In order to establish the mapping between the element in the global coordinate system and the right tetrahedron in the local coordinate system, one substitutes x, y, and z for u in Equation (4.1.23), respectively. Namely, one can write the following:

$$\left.\begin{aligned} x &= \sum_{k=1}^{10} N_k(\alpha, \beta, \gamma) x_k \\ y &= \sum_{k=1}^{10} N_k(\alpha, \beta, \gamma) y_k \\ z &= \sum_{k=1}^{10} N_k(\alpha, \beta, \gamma) z_k \end{aligned}\right\} \tag{4.1.28}$$

Equation (4.1.28) enables one to locate any given point in (x, y, z) in the global coordinate system, whose corresponding image point in the local coordinate system has coordinates (α, β, γ). Meanwhile, approximation of the MVP within the right tetrahedral can be obtained by substituting the nodal MVP components for u in

Equation (4.1.23). This yields the following:

$$\left.\begin{aligned} A_x &= \sum_{k=1}^{10} N_k(\alpha,\beta,\gamma)A_{kx} \\ A_y &= \sum_{k=1}^{10} N_k(\alpha,\beta,\gamma)A_{ky} \\ A_z &= \sum_{k=1}^{10} N_k(\alpha,\beta,\gamma)A_{kz} \end{aligned}\right\} \tag{4.1.29}$$

Notice, in Equation (4.1.28) and (4.1.29) both geometry transformation and MVP interpolation are described by the same set of parameters of $N_k(\alpha,\beta,\gamma)$. Such a representation is called "isoparametric". Hence the elements are called isoparametric elements, and the transformation is called isoparametric transformation. Details of this topic can be found in references [84] and [85].

Since Equation (4.1.28) describes a point to point mapping between (x, y, z) and (α, β, γ), it implies that α, β, and γ can be considered as functions in x, y, and z. Thus, by chain rule differentiation, one can write the following:

$$\left.\begin{aligned} \frac{\partial N_i}{\partial \alpha} &= \frac{\partial N_i}{\partial x}\frac{\partial x}{\partial \alpha} + \frac{\partial N_i}{\partial y}\frac{\partial y}{\partial \alpha} + \frac{\partial N_i}{\partial z}\frac{\partial z}{\partial \alpha} \\ \frac{\partial N_i}{\partial \beta} &= \frac{\partial N_i}{\partial x}\frac{\partial x}{\partial \beta} + \frac{\partial N_i}{\partial y}\frac{\partial y}{\partial \beta} + \frac{\partial N_i}{\partial z}\frac{\partial z}{\partial \beta} \\ \frac{\partial N_i}{\partial \gamma} &= \frac{\partial N_i}{\partial x}\frac{\partial x}{\partial \gamma} + \frac{\partial N_i}{\partial y}\frac{\partial y}{\partial \gamma} + \frac{\partial N_i}{\partial z}\frac{\partial z}{\partial \gamma} \end{aligned}\right\} \quad i = 1,2,...10 \tag{4.1.30}$$

Equation (4.1.30) can be further written into a compact form as

$$\begin{Bmatrix} \frac{\partial N_i}{\partial \alpha} \\ \frac{\partial N_i}{\partial \beta} \\ \frac{\partial N_i}{\partial \gamma} \end{Bmatrix} = \begin{bmatrix} \frac{\partial x}{\partial \alpha} & \frac{\partial y}{\partial \alpha} & \frac{\partial z}{\partial \alpha} \\ \frac{\partial x}{\partial \beta} & \frac{\partial y}{\partial \beta} & \frac{\partial z}{\partial \beta} \\ \frac{\partial x}{\partial \gamma} & \frac{\partial y}{\partial \gamma} & \frac{\partial z}{\partial \gamma} \end{bmatrix} \begin{Bmatrix} \frac{\partial N_i}{\partial x} \\ \frac{\partial N_i}{\partial y} \\ \frac{\partial N_i}{\partial z} \end{Bmatrix} \tag{4.1.31}$$

where the 3 × 3 matrix is a Jacobian matrix, referred to as $\underline{J}$. By taking differential operations on x, y, and z in Equation (3.1.28), with respect to α, β, and γ, and inserting the results into this matrix, one can write the Jacobian matrix as follows:

$$\underline{J} = \begin{bmatrix} \sum_{k=1}^{10} \frac{\partial N_k}{\partial \alpha} x_k & \sum_{k=1}^{10} \frac{\partial N_k}{\partial \alpha} y_k & \sum_{k=1}^{10} \frac{\partial N_k}{\partial \alpha} z_k \\ \sum_{k=1}^{10} \frac{\partial N_k}{\partial \beta} x_k & \sum_{k=1}^{10} \frac{\partial N_k}{\partial \beta} y_k & \sum_{k=1}^{10} \frac{\partial N_k}{\partial \beta} z_k \\ \sum_{k=1}^{10} \frac{\partial N_k}{\partial \gamma} x_k & \sum_{k=1}^{10} \frac{\partial N_k}{\partial \gamma} y_k & \sum_{k=1}^{10} \frac{\partial N_k}{\partial \gamma} z_k \end{bmatrix} \tag{4.1.32}$$

Furthermore, by multiplying both side of Equation (4.1.31) by $\underline{J}^{-1}$, one obtains the following:

$$\begin{Bmatrix} \frac{\partial N_i}{\partial x} \\ \frac{\partial N_i}{\partial y} \\ \frac{\partial N_i}{\partial z} \end{Bmatrix} = \begin{bmatrix} \sum_{k=1}^{10} \frac{\partial N_k}{\partial \alpha} x_k & \sum_{k=1}^{10} \frac{\partial N_k}{\partial \alpha} y_k & \sum_{k=1}^{10} \frac{\partial N_k}{\partial \alpha} z_k \\ \sum_{k=1}^{10} \frac{\partial N_k}{\partial \beta} x_k & \sum_{k=1}^{10} \frac{\partial N_k}{\partial \beta} y_k & \sum_{k=1}^{10} \frac{\partial N_k}{\partial \beta} z_k \\ \sum_{k=1}^{10} \frac{\partial N_k}{\partial \gamma} x_k & \sum_{k=1}^{10} \frac{\partial N_k}{\partial \gamma} y_k & \sum_{k=1}^{10} \frac{\partial N_k}{\partial \gamma} z_k \end{bmatrix}^{-1} \begin{Bmatrix} \frac{\partial N_i}{\partial \alpha} \\ \frac{\partial N_i}{\partial \beta} \\ \frac{\partial N_i}{\partial \gamma} \end{Bmatrix} \tag{4.1.33}$$

It should be pointed out that each term at the right hand side of Equation (4.1.33) is a combination of $\partial N_i/\partial \alpha$, $\partial N_i/\partial \beta$, and $\partial N_i/\partial \gamma$, which are the functions explicitly given in Equation (4.1.25) through (4.1.27). Accordingly, values of $\partial N_i/\partial \alpha$, $\partial N_i/\partial \beta$, and $\partial N_i/\partial z$, are calculable for any given set of (α, β, γ). Hence, the values of the integrand in equation (4.1.22) can be determined for any given (α,β, γ).

Meanwhile, from differential geometry formulation and nomenclature (see [85]), the unit volume, dv, in Equation (4.1.22) can be written in the global coordinates, as well as in the local coordinates as follows:

$$dv = dx\, dy\, dz = \mid \underline{J} \mid d\alpha\, d\beta\, d\gamma \tag{4.1.34}$$

where $\mid \underline{J} \mid$ is the determinant of the Jacobian matrix for a given element, which was expressed in Equation (4.1.32). Thus, using the local coordinates, the integration

given in Equation (4.1.22) can be rewritten as follows:

$$Int = \int_{V_e} G(N_i, \frac{\partial N_j}{\partial x}, \frac{\partial N_k}{\partial y}, \frac{\partial N_l}{\partial z})\, dv$$

$$= \int_0^1 \int_0^{1-\alpha} \int_0^{1-\alpha-\beta} G(N_i, \frac{\partial N_j}{\partial x}, \frac{\partial N_k}{\partial y}, \frac{\partial N_l}{\partial z}) \mid \underline{J} \mid d\alpha\, d\beta\, d\gamma$$

$$= \int_0^1 d\alpha \int_0^{1-\alpha} d\beta \int_0^{1-\alpha-\beta} G^*(\alpha, \beta, \gamma) d\gamma \tag{4.1.35}$$

where, $G^*(\alpha, \beta, \gamma) = G(N_i, \frac{\partial N_j}{\partial x}, \frac{\partial N_k}{\partial y}, \frac{\partial N_l}{\partial z}) \mid \underline{J} \mid$.

Gaussian quadrature is used here to numerically integrate Equation (4.1.35). In order to apply the standard Gaussian quadrature algorithm, which is valid only in case that the integration volume is a cubic region centered at the origin with its edge length equal to 2 units, Equation (4.1.35) has to be rearranged through a series of integration variable substitutions. This substitution procedure is as follows:

(1) Let $\gamma = \frac{(1-\alpha-\beta)(1+t_k)}{2}$, $d\gamma = \frac{(1-\alpha-\beta)}{2} dt_k$

$$Int = \int_0^1 d\alpha \int_0^{1-\alpha} d\beta \int_0^{1-\alpha-\beta} G^*(\alpha, \beta, \gamma) d\gamma$$

$$= \int_0^1 d\alpha \int_0^{1-\alpha} d\beta \int_{-1}^{1} \frac{(1-\alpha-\beta)}{2} G^*(\alpha, \beta, \frac{(1-\alpha-\beta)(1+t_k)}{2})\, dt_k$$

(2) Let $\beta = \frac{(1-\alpha)(1+t_j)}{2}$, $d\beta = \frac{(1-\alpha)}{2} dt_j$

$$Int = \int_0^1 d\alpha \int_0^{1-\alpha} d\beta \int_{-1}^{1} \frac{(1-\alpha-\beta)}{2} G^*(\alpha, \beta, \frac{(1-\alpha-\beta)(1+t_k)}{2})\, dt_k$$

$$= \int_0^1 d\alpha \int_{-1}^{1} \int_{-1}^{1} \frac{(1-\alpha)^2(1-t_j)}{8} G^*(\alpha, \frac{(1-\alpha)(1+t_j)}{2}, \frac{(1-\alpha)(1-t_j)(1+t_k)}{4})\, dt_j\, dt_k$$

(3) Let $\alpha = \frac{(1+t_i)}{2}$, $d\alpha = \frac{1}{2} dt_i$

$$Int = \int_0^1 d\alpha \int_{-1}^{1} \int_{-1}^{1} \frac{(1-\alpha)^2(1-t_j)}{8} G^*(\alpha, \frac{(1-\alpha)(1+t_j)}{2}, \frac{(1-\alpha)(1-t_j)(1+t_k)}{4})\, dt_j\, dt_k$$

$$= \int_{-1}^{1} \int_{-1}^{1} \int_{-1}^{1} \frac{(1-t_i)^2(1-t_j)}{64} G^*(\frac{1+t_i}{2}, \frac{(1-t_i)(1+t_j)}{4}, \frac{(1-t_i)(1-t_j)(1+t_k)}{8})\, dt_i\, dt_j\, dt_k$$

(4.1.36)

At this stage, a standard Gaussian quadrature, with an order of three in each coordinate direction, is applied to Equation (4.1.36). This yields the following:

$$Int = \sum_{i=1}^{3}\sum_{j=1}^{3}\sum_{k=1}^{3}\{W_iW_jW_k\frac{(1-t_i)^2(1-t_j)}{64}G^*(\tfrac{1+t_i}{2}, \tfrac{(1-t_i)(1+t_j)}{4}, \tfrac{(1-t_i)(1-t_j)(1+t_k)}{8})\}$$

(4.1.37)

where W_i, W_j, and W_k, are the weighting factors, and t_i, t_j, as well as t_k are the stations, of the Gaussian quadrature. The values of these weighting factors and stations are given in Table (4.1.1). A simpler form for Equation (4.1.37), which is the actual formula used in the computer program, can be written as follows:

$$Int = \sum_{i=1}^{3}\sum_{j=1}^{3}\sum_{k=1}^{3}\{W_iW_jW_k\frac{(1-t_i)^2(1-t_j)}{64}G^*(\tfrac{1+t_i}{2}, \tfrac{(1-t_i)(1+t_j)}{4}, \tfrac{(1-t_i)(1-t_j)(1+t_k)}{8})\}$$

$$= \sum_{m=1}^{27} W_m^* G^*(\alpha_m, \beta_m, \gamma_m) \qquad (4.1.38)$$

where, W_m^* is the modified weighting factor, and α_m, β_m, as well as γ_m are the modified stations. Values of the modified weighting factors and stations calculated from the following equations:

$$W_m^* = W_iW_jW_k\frac{(1-t_i)^2(1-t_j)}{64}$$

$$\alpha_m = \frac{1+t_i}{2}$$

$$\beta_m = \frac{(1-t_i)(1+t_j)}{4}$$

$$\gamma_m = \frac{(1-t_i)(1-t_j)(1+t_k)}{8}$$

for m=1, 2,..., 27, with respect to the corresponding subscripts of i, j, and k in Equation (4.1.38), are listed in Table (4.1.2).

Table (4.1.1): Weighting Factors and Stations of Gaussian Quadrature ($n = 3$)

k	W_k	x_k
1	5/9	$-\sqrt{15}/5$
2	8/9	0
3	5/9	$\sqrt{15}/5$

Table (4.1.2): Weighting Factors and Stations Used in the Modified Form of Gaussian Quadrature

m	(i,j,k)	W_m^*	α_m	β_m	γ_m
1	(1, 1, 1)	0.0149728	0.1127017	0.1000000	0.0887298
2	(2, 1, 1)	0.0076072	0.5000000	0.0563508	0.0500000
3	(3, 1, 1)	0.0002416	0.8872983	0.0127017	0.0112702
4	(1, 2, 1)	0.0134996	0.1127017	0.4436492	0.0500000
5	(2, 2, 1)	0.0068587	0.5000000	0.2500000	0.0281754
6	(3, 2, 1)	0.0002178	0.8872983	0.0563508	0.0063508
7	(1, 3, 1)	0.0019018	0.1127017	0.7872984	0.0112702
8	(2, 3, 1)	0.0009662	0.5000000	0.4436492	0.0063508
9	(3, 3, 1)	0.0000307	0.8872983	0.1000000	0.0014315
10	(1, 1, 2)	0.0239564	0.1127017	0.1000000	0.3936492
11	(2, 1, 2)	0.0121714	0.5000000	0.0563508	0.2218246
12	(3, 1, 2)	0.0003865	0.8872983	0.0127017	0.0500000
13	(1, 2, 2)	0.0215994	0.1127017	0.4436492	0.2218246
14	(2, 2, 2)	0.0109739	0.5000000	0.2500000	0.1250000
15	(3, 2, 2)	0.0003485	0.8872983	0.0563508	0.0281754
16	(1, 3, 2)	0.0030429	0.1127017	0.7872984	0.0500000
17	(2, 3, 2)	0.0015460	0.5000000	0.4436492	0.0281754
18	(3, 3, 2)	0.0000491	0.8872983	0.1000000	0.0063508
19	(1, 1, 3)	0.0149728	0.1127017	0.1000000	0.6985685
20	(2, 1, 3)	0.0076072	0.5000000	0.0563508	0.3936492
21	(3, 1, 3)	0.0002416	0.8872983	0.0127017	0.0887298
22	(1, 2, 3)	0.0134996	0.1127017	0.4436492	0.3936492
23	(2, 2, 3)	0.0068587	0.5000000	0.2500000	0.2218246
24	(3, 2, 3)	0.0002178	0.8872983	0.0563508	0.0500000
25	(1, 3, 3)	0.0019018	0.1127017	0.7872984	0.0887298
26	(2, 3, 3)	0.0009662	0.5000000	0.4436492	0.0500000
27	(3, 3, 3)	0.0000307	0.8872983	0.1000000	0.0112702

Again, as stated earlier in this section, G^* is calculable for any given set of (α, β, γ), hence the summation in Equation (4.1.38) is calculable. Therefore, computations of various terms in the element coefficient matrix and forcing function vector, which was given by Equations (4.1.18), (4.1.19), and (4.1.21), can be implemented using the numerical integration algorithm in Equation (4.1.38) with its weighting factors and stations given in Table (4.1.2).

4.2 The Surface Finite Element Analysis

In this section, the formulation of the surface finite element analysis involved in the MVP-MSP approach is discussed in detail. This surface FE analysis is for computation of the MSP jump distribution on the outer surfaces of the current carrying MVP subregions. As described in Section 3.1, this is the intermediate step which links the prior MVP portion and the later MSP portion of the combined MVP-MSP magnetic field solution approach.

4.2.1 Derivation of the Element Equation

To avoid possible confusion associated with the mathematical notations used here, the MSP jump distribution, which was previously denoted by $\Delta\phi$ in Section 3.1, is denoted by T throughout this section. The governing partial differential equation, Equation (3.1.19) of Section 3.1, for this surface FE problem can be written in terms of T as follows:

$$-\nabla T = \overline{H}_{mvpt} \qquad on\ \Gamma_{12} \tag{4.2.1}$$

where, Γ_{12} is the outer surface of any current carrying MVP subregion under consideration, $\overline{H}_{mvpt}$ is the tangential component of the field intensity on Γ_{12} computed from the previous MVP solution.

The functional associated with this surface FE analysis is chosen as

$$F(T) = \int_{\Gamma_{12}} | \nabla T + \overline{H}_{mvpt} |^2 \ ds \tag{4.2.2}$$

where ds is a differential surface area on Γ_{12}. This functional is non-negative, with its minimum equal to zero. Accordingly, the minimum (zero) of $F(T)$ in Equation (4.2.2) can be reached only if the integrand function, $\mid \nabla T + \overline{H}_{mvpt} \mid^2$, is equal to zero everywhere on Γ_{12}. Apparently, this condition is equivalent to that $\nabla T + \overline{H}_{mvpt} = 0$. Thus, the function, T, which minimizes the functional, Equation (4.2.2), must satisfy the partial differential equation, Equation (4.2.1). Accordingly, the MSP jump distribution can be obtained by minimizing the functional, $F(T)$, in Equation (4.2.2).

The surface finite element grid is the outer surface grid of the 3D-FE tetrahedral grid of the MVP subregion. The magnetic scalar potential jump distribution is computed at every grid node in the surface finite element analysis. As will be seen later, this type of nodal MSP jump value can be directly applied as a forcing function to the later stage of the global MSP computation.

Figure (4.2.1) shows a surface triangular element with its three nodes numbered as l, m, and n. Within this triangular element, first order interpolation is used to approximate the variable MSP jump function, T. This interpolation can be written as follows:

$$T = N_l T_l + N_m T_m + N_n T_n \tag{4.2.3}$$

where, N_l, N_m, and N_n are interpolation coefficients, and T_l, T_m, as well as T_n are the nodal values of T, at the three nodes l, m, and n, respectively. In the surface finite element problem, a triangular element can have an arbitrary orientation with respect to the global coordinate planes. Thus, using a local coordinate system for element analysis is more effective and convenient than directly formulating the problem in terms of the global 3D coordinate system. Figure (4.2.1) shows the local coordinate system, u, v, and w, for the surface FE analysis. In this system, the u-axis is chosen along the edge lm of the triangle, the v-axis is chosen in the plane of the triangle and in quadrature with the u-axis, and the w-axis is normal to the plane of the triangle such that u, v, and w follow the right hand rule of the coordinate notation. Details on the formation of the local coordinate axes, as well as the coordinate transformation are given later in this section. Under this chosen local coordinate system, T is a function of u and v, and the interpolation coefficients, N_l, N_m, and N_n are functions (first order polynomials) in u and v. Meanwhile, the forcing function vector $\overline{H}_{mvpt}$ in

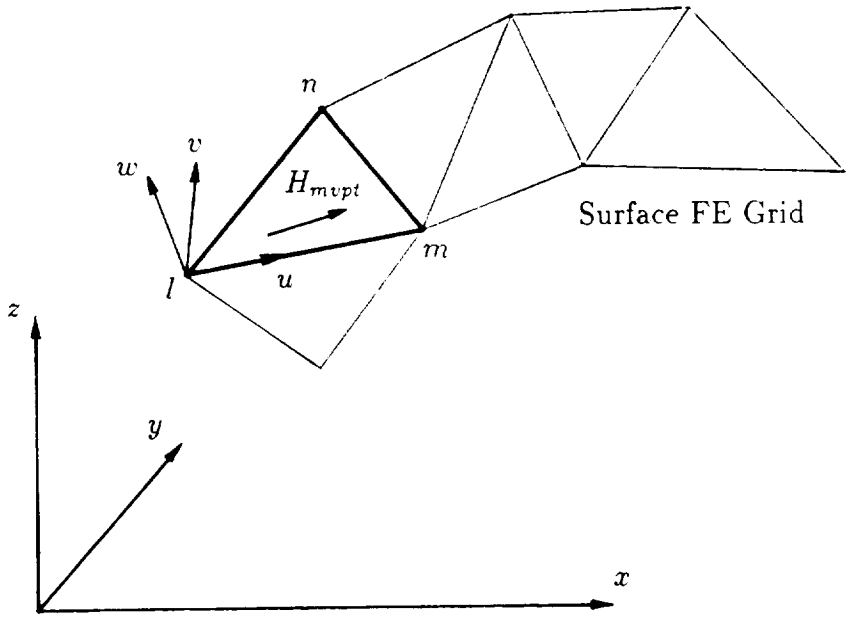

Figure (4.2.1) Surface Finite Element Grid

the plane of the element can be expressed as follows:

$$\overline{H}_{mvpt} = H_u \hat{a}_u + H_v \hat{a}_v \tag{4.2.4}$$

where $\hat{a}_u$ and $\hat{a}_v$ are unit vectors in the u and v directions, respectively. Here, H_u and H_v are directional components of $\overline{H}_{mvpt}$ expressed in terms of the chosen local coordinate system.

The global integral of the functional in Equation (4.2.2) can be expanded as a summation of a series of integrations on each element. Namely, one can write the following:

$$F(T) = \int_{\Gamma_{12}} \mid \nabla T + \overline{H}_{mvpt} \mid^2 \; ds = \sum_{e=1}^{NE} \int_{S_e} \mid \nabla T + \overline{H}_{mvpt} \mid^2 \; ds \tag{4.2.5}$$

where S_e is an elemental surface area and NE is the total number of the surface elements. Furthermore, using the local coordinate system for each element, and Equation (4.2.4), one can rewrite the functional as follows:

$$F(T) = \sum_{e=1}^{NE} \int_{S_e} \mid \nabla T(u,v) + \overline{H}_{mvpt}(u,v) \mid^2 \; dudv$$

$$= \sum_{e=1}^{NE} \int_{S_e} [(\frac{\partial T}{\partial u} + H_u)^2 + (\frac{\partial T}{\partial v} + H_v)^2] \; dudv \tag{4.2.6}$$

At this stage, Equation (4.2.3) is substituted for T in Equation (4.2.6). The derivatives of this functional with respect to each nodal variable must be equated to zero to meet the requirement of functional minimization. This procedure leads to a general form for the element equations of this surface FE analysis. The derivation is detailed as follows:

$$\frac{\partial}{\partial T_i} \int_{S_e} \{(\frac{\partial T}{\partial u} + H_u)^2 + (\frac{\partial T}{\partial v} + H_v)^2\} dudv$$

$$= \frac{\partial}{\partial T_i} \int_{S_e} \{[\frac{\partial}{\partial u}(N_l T_l + N_m T_m + N_n T_n) + H_u]^2$$

$$+ [\frac{\partial}{\partial v}(N_l T_l + N_m T_m + N_n T_n) + H_v]^2\} dudv$$

$$= \int_{S_e} \{\frac{\partial}{\partial T_i}[\frac{\partial N_l}{\partial u}T_l + \frac{\partial N_m}{\partial u}T_m + \frac{\partial N_n}{\partial u}T_n + H_u]^2$$

$$+ \frac{\partial}{\partial T_i}[\frac{\partial N_l}{\partial v}T_l + \frac{\partial N_m}{\partial v}T_m + \frac{\partial N_n}{\partial v}T_n + H_v]^2\}dudv$$

$$= \int_{S_e} \{2\frac{\partial N_i}{\partial u}[\frac{\partial N_l}{\partial u}T_l + \frac{\partial N_m}{\partial u}T_m + \frac{\partial N_n}{\partial u}T_n + H_u]$$

$$+ 2\frac{\partial N_i}{\partial v}[\frac{\partial N_l}{\partial v}T_l + \frac{\partial N_m}{\partial v}T_m + \frac{\partial N_n}{\partial v}T_n + H_v]\}dudv$$

$$= 2\int_{S_e} \{(\frac{\partial N_i}{\partial u}\frac{\partial N_l}{\partial u} + \frac{\partial N_i}{\partial v}\frac{\partial N_l}{\partial v})T_l + (\frac{\partial N_i}{\partial u}\frac{\partial N_m}{\partial u} + \frac{\partial N_i}{\partial v}\frac{\partial N_m}{\partial v})T_m$$

$$+ (\frac{\partial N_i}{\partial u}\frac{\partial N_n}{\partial u} + \frac{\partial N_i}{\partial v}\frac{\partial N_n}{\partial v})T_n + \frac{\partial N_i}{\partial u}H_u + \frac{\partial N_i}{\partial v}H_v\}dudv$$

$$= 0 \qquad for\ i = l,\ m,\ n \tag{4.2.7}$$

Because of the first order nature of the interpolation function in these triangular elements, the derivative terms in Equation (4.2.7), $\partial N_i/\partial u$, $\partial N_i/\partial v$, for $i = l, m, n$, are constants in each element. Thus, from Equation (4.2.7), one obtains the following:

$$2\Delta(\frac{\partial N_i}{\partial u}\frac{\partial N_l}{\partial u} + \frac{\partial N_i}{\partial v}\frac{\partial N_l}{\partial v})T_l + 2\Delta(\frac{\partial N_i}{\partial u}\frac{\partial N_m}{\partial u} + \frac{\partial N_i}{\partial v}\frac{\partial N_m}{\partial v})T_m$$

$$+ 2\Delta(\frac{\partial N_i}{\partial u}\frac{\partial N_n}{\partial u} + \frac{\partial N_i}{\partial v}\frac{\partial N_n}{\partial v})T_n$$

$$= -2\Delta(\frac{\partial N_i}{\partial u}H_u + \frac{\partial N_i}{\partial v}H_v) \qquad for\ i = l, m, n \tag{4.2.8}$$

where, Δ is the area of the triangular element. This element equation can be further expressed in matrix form as follows:

$$\begin{bmatrix} S_{ll} & S_{lm} & S_{ln} \\ S_{ml} & S_{mm} & S_{mn} \\ S_{nl} & S_{nm} & S_{nn} \end{bmatrix} \begin{Bmatrix} T_l \\ T_m \\ T_n \end{Bmatrix} = \begin{Bmatrix} C_l \\ C_m \\ C_n \end{Bmatrix} \tag{4.2.9}$$

where

$$S_{ll} = 2\Delta(\frac{\partial N_l}{\partial u}\frac{\partial N_l}{\partial u} + \frac{\partial N_l}{\partial v}\frac{\partial N_l}{\partial v})$$

$$S_{mm} = 2\Delta(\frac{\partial N_m}{\partial u}\frac{\partial N_m}{\partial u} + \frac{\partial N_m}{\partial v}\frac{\partial N_m}{\partial v})$$

$$S_{nn} = 2\Delta(\frac{\partial N_n}{\partial u}\frac{\partial N_n}{\partial u} + \frac{\partial N_n}{\partial v}\frac{\partial N_n}{\partial v})$$

$$S_{lm} = S_{ml} = 2\Delta(\frac{\partial N_l}{\partial u}\frac{\partial N_m}{\partial u} + \frac{\partial N_l}{\partial v}\frac{\partial N_m}{\partial v})$$

$$S_{ln} = S_{nl} = 2\Delta(\frac{\partial N_l}{\partial u}\frac{\partial N_n}{\partial u} + \frac{\partial N_l}{\partial v}\frac{\partial N_n}{\partial v})$$

$$S_{mn} = S_{nm} = 2\Delta(\frac{\partial N_m}{\partial u}\frac{\partial N_n}{\partial u} + \frac{\partial N_m}{\partial v}\frac{\partial N_n}{\partial v})$$

and

$$C_l = -2\Delta(\frac{\partial N_l}{\partial u}H_u + \frac{\partial N_l}{\partial v}H_v)$$

$$C_m = -2\Delta(\frac{\partial N_m}{\partial u}H_u + \frac{\partial N_m}{\partial v}H_v)$$

$$C_n = -2\Delta(\frac{\partial N_n}{\partial u}H_u + \frac{\partial N_n}{\partial v}H_v)$$

By repeating Equation (4.2.9) for every surface element, and assembling these element equations, one obtains the global system of equations for the surface 2D-FE analysis. Solving the global equations, one accomplishes the computation of the MSP jump distribution T, or $\Delta\phi$ as denoted in Section 3.1.

As discussed in Section 3.1, a reference point is needed for the relative MSP jump distribution. In this case, one needs to enforce a zero value of $\Delta\phi$ on one grid node. This node can be arbitrarily chosen from the surface finite element grid.

4.2.2 The Element Equation Under a Local Coordinate System

The element coefficient matrix and forcing function vector in Equation (4.2.9) are given in terms of the local coordinate system shown in Figure (4.2.1). These terms are combinations of partial derivatives of element interpolation coefficients with respect to the local coordinates, u, and v. To obtain the element interpolation coefficients (shape functions) and consequently their derivatives, one needs to know the local coordinates of each triangular vertex. This is done by a special coordinate transformation described next.

For a given triangular element, see Figure (4.2.1), the local coordinate axis, u, is directed along the elemental side, lm. The unit directional vector, $\hat{a}_u$, can be therefore defined as follows:

$$\hat{a}_u = \frac{x_{ml}}{\sqrt{x_{ml}^2 + y_{ml}^2 + z_{ml}^2}}\hat{a}_x + \frac{y_{ml}}{\sqrt{x_{ml}^2 + y_{ml}^2 + z_{ml}^2}}\hat{a}_y + \frac{z_{ml}}{\sqrt{x_{ml}^2 + y_{ml}^2 + z_{ml}^2}}\hat{a}_z \tag{4.2.10}$$

where, $x_{ml} = x_m - x_l$, $y_{ml} = y_m - y_l$, $z_{ml} = z_m - z_l$, etc.

The w-direction, which is normal to the plane of the triangle, can be obtained by a cross-product of any two vectors in that plane. One of these vectors is chosen as the vector from node l to node m, the other vector is chosen as the vector from node l to node n. From vector algebra, the cross-product of the two vectors has a magnitude (length) equal to twice of the triangular area, Δ. Thus the unit directional vector $\hat{a}_w$ can be written as follows:

$$\hat{a}_w = \frac{1}{2\Delta}\begin{vmatrix} \hat{a}_x & \hat{a}_y & \hat{a}_z \\ x_m - x_l & y_m - y_l & z_m - z_l \\ x_n - x_l & y_n - y_l & z_n - z_l \end{vmatrix}$$

$$= \frac{y_{ml}z_{nl} - z_{ml}y_{nl}}{2\Delta}\hat{a}_x + \frac{z_{ml}x_{nl} - x_{ml}z_{nl}}{2\Delta}\hat{a}_y + \frac{x_{ml}y_{nl} - y_{ml}x_{nl}}{2\Delta}\hat{a}_z \tag{4.2.11}$$

where Δ is the area of the triangular element, and 2Δ can be calculated using the following equation:

$$2\Delta = \sqrt{(y_{ml}z_{nl} - z_{ml}y_{nl})^2 + (z_{ml}x_{nl} - x_{ml}z_{nl})^2 + (x_{ml}y_{nl} - y_{ml}x_{nl})^2}$$

Finally, the v-axis can be obtained as the cross-product of $\hat{a}_w$ and $\hat{a}_u$. That is , one can write the following:

$$\hat{a}_v = \hat{a}_w \times \hat{a}_u$$

$$= \frac{1}{2\Delta\sqrt{x_{ml}^2 + y_{ml}^2 + z_{ml}^2}} \begin{vmatrix} \hat{a}_x & \hat{a}_y & \hat{a}_z \\ (y_{ml}z_{nl} & (z_{ml}x_{nl} & (x_{ml}y_{nl} \\ -z_{ml}y_{nl}) & -x_{ml}z_{nl}) & -y_{ml}x_{nl}) \\ x_{ml} & y_{ml} & z_{ml} \end{vmatrix}$$

$$= \frac{z_{ml}(z_{ml}x_{nl} - x_{ml}z_{nl}) - y_{ml}(x_{ml}y_{nl} - y_{ml}x_{nl})}{2\Delta\sqrt{x_{ml}^2 + y_{ml}^2 + z_{ml}^2}}\hat{a}_x$$

$$+\frac{x_{ml}(x_{ml}y_{nl} - y_{ml}x_{nl}) - z_{ml}(y_{ml}z_{nl} - z_{ml}y_{nl})}{2\Delta\sqrt{x_{ml}^2 + y_{ml}^2 + z_{ml}^2}}\hat{a}_y$$

$$+\frac{y_{ml}(y_{ml}z_{nl} - z_{ml}y_{nl}) - x_{ml}(z_{ml}x_{nl} - x_{ml}z_{nl})}{2\Delta\sqrt{x_{ml}^2 + y_{ml}^2 + z_{ml}^2}}\hat{a}_x \qquad (4.2.12)$$

The three unit vectors described above can be written in a general form as follows:

$$\left.\begin{aligned} \hat{a}_u &= u_x\hat{a}_x + u_y\hat{a}_y + u_z\hat{a}_z \\ \hat{a}_v &= v_x\hat{a}_x + v_y\hat{a}_y + v_z\hat{a}_z \\ \hat{a}_w &= w_x\hat{a}_x + w_y\hat{a}_y + w_z\hat{a}_z \end{aligned}\right\} \qquad (4.2.13)$$

where, u_x, u_y, ..., were detailed in Equations (4.2.10) through (4.2.12). Physically, each of these terms is the cosine of the angle between a local coordinate axis and a global coordinate axis.

Having Equations (4.2.10) through (4.2.13), the local coordinates of the triangular vertices, u_i and v_i, can be calculated by the following coordinate transformation:

$$\begin{Bmatrix} u_i \\ v_i \end{Bmatrix} = \begin{bmatrix} u_x & u_y & u_z \\ v_x & v_y & v_z \end{bmatrix} \begin{Bmatrix} x_i - x_l \\ y_i - y_l \\ z_i - z_l \end{Bmatrix} \qquad for\, i = l,\ m,\ n \tag{4.2.14}$$

The local coordinate w_i, for $i = l,\ m,\ n$ has not been included in the above equation. This is because the computation of the element matrix and forcing function is a two-dimensional process under the chosen local coordinate system, hence the w-coordinates are not needed.

Meanwhile, consider that H_u and H_v are the projections of $\overline{H}_{mvpt}$ on the u and v axes respectively, one can calculate the values of H_u and H_v using the following:

$$\left.\begin{aligned} H_u &= \overline{H}_{mvpt} \cdot \hat{a}_u \\ H_v &= \overline{H}_{mvpt} \cdot \hat{a}_v \end{aligned}\right\} \tag{4.2.15}$$

The remaining work on the element matrix and forcing function vector is straightforward. The element shape functions, as well as their derivatives, of the first order triangular elements can be adopted from well established two-dimensional finite element work. The following is the formulation:

$$\left.\begin{aligned} N_l &= \frac{1}{2\Delta}(p_l + q_l u + r_l v) \\ N_m &= \frac{1}{2\Delta}(p_m + q_m u + r_m v) \\ N_n &= \frac{1}{2\Delta}(p_n + q_n u + r_n v) \end{aligned}\right\} \tag{4.2.16}$$

$$\left.\begin{array}{ll} \dfrac{\partial N_l}{\partial u} = \dfrac{q_l}{2\Delta}, & \dfrac{\partial N_l}{\partial v} = \dfrac{r_l}{2\Delta}, \\ \dfrac{\partial N_m}{\partial u} = \dfrac{q_m}{2\Delta}, & \dfrac{\partial N_m}{\partial v} = \dfrac{r_m}{2\Delta}, \\ \dfrac{\partial N_n}{\partial u} = \dfrac{q_n}{2\Delta}, & \dfrac{\partial N_n}{\partial v} = \dfrac{r_n}{2\Delta}, \end{array}\right\} \tag{4.2.17}$$

where

$$\left.\begin{array}{lll} p_l = u_m v_n - u_n v_m, & q_l = v_m - v_n, & r_l = u_n - u_m \\ p_m = u_n v_l - u_l v_n, & q_m = v_n - v_l, & r_m = u_l - u_n \\ p_l = u_l v_m - u_m v_l, & q_n = v_l - v_m, & r_n = u_m - u_l \end{array}\right\} \tag{4.2.18}$$

Finally, by substituting Equations (4.2.16) and (4.2.17) into Equation (4.2.9), the element equation can be written as follows:

$$\frac{1}{2\Delta}\begin{bmatrix} q_l q_l + r_l r_l & q_l q_m + r_l r_m & q_l q_n + r_l r_n \\ q_m q_l + r_m r_l & q_m q_m + r_m r_m & q_m q_n + r_m r_n \\ q_n q_l + r_n r_l & q_n q_m + r_n r_m & q_n q_n + r_n r_n \end{bmatrix} \begin{Bmatrix} T_l \\ T_m \\ T_n \end{Bmatrix}$$

$$= \begin{Bmatrix} -q_l H_u - r_l H_v \\ -q_m H_u - r_m H_v \\ -q_n H_u - r_n H_v \end{Bmatrix} \tag{4.2.19}$$

Equations (4.2.18) and (4.2.19), in conjunction with the coordinate transformation described in Equations (4.2.10) through (4.2.14), complete the formulation of the element equation of the surface finite element analysis. The MSP jump distribution is computed by this surface finite element procedure. Again, as stated earlier in Section 3.1, this computed MSP jump distribution will be the main forcing function in the MSP portion of the combined MVP-MSP approach. Implementation of the MSP-FE formulation will be discussed next.

4.3 Magnetic Scalar Potential 3D-FE Formulation Using First Order Elements

The 3D magnetic scalar potential finite element formulation of the MVP-MSP approach is discussed in this section. The solution region of the MSP part of this approach is the entire magnetic field solution volume. This region includes the current-free subregion as well as the current carrying MVP subregion. On the interfaces between these two subregions, the MSP jump distribution has to be enforced to guarantee the continuity of the tangential component of the field intensity along these interface boundaries. Meanwhile, on the interfaces between the air and iron within the MVP subregion, the discontinuity of the normal derivative of the MSP has to be enforced to guarantee the continuity of the normal component of the flux density. The physical aspects of these two discontinuity conditions were discussed in Chapter 2 and Chapter 3 of this dissertation. The enforcement of these discontinuities is carried out within the confines of the MSP FE formulations.

In general, magnetic field problems in electric machinery can be nonlinear due to magnetic saturation in the iron material, and these problems can contain anisotropies due to machine iron core laminations. Such features can be fully included within the MSP-FE computation stage in the combined MVP-MSP approach subject of this research. The procedure of the MSP-FE problem with material magnetic anisotropy is given in Section 4.3.1. The enforcement of the MSP discontinuity conditions, which is established through the element equation of the MSP-FE analysis, is expressed in Section 4.3.2. The MSP field problem involving material magnetic nonlinearity will be discussed later-on in Chapter 5.

4.3.1 The MSP FE Problem with Material Anisotropy

In the MSP problem, the governing partial differential equation, which was discussed in Section 3.1, can be rewritten here for the reader's convenience as follows:

$$\nabla \cdot (\overline{\overline{\mu}} \nabla \phi) = 0 \tag{4.3.1}$$

Generally, the outer boundary conditions of the magnetic fields in the MSP problem associated with electric machines can be expressed as

$$H_t = 0, \quad or \quad \phi = Constant, \qquad at\ S_H \tag{4.3.2}$$

and

$$B_n = 0, \quad or \quad \frac{\partial \phi}{\partial n} = 0, \qquad at\ S_B \tag{4.3.3}$$

where $S_B \cup S_H$ constitutes the entire outer boundary surface of the solution volume. Equations (4.3.1) through (4.3.3) specify the MSP problem over the solution region with a single type of medium, in which $\overline{B}$, $\overline{H}$, and $\overline{\overline{\mu}}$ are continuous everywhere. The condition of Equation (4.3.2) can be enforced by assigning a constant potential value to the nodes on the boundary S_H. That is, the nodes on the outer surface S_H are treated as known nodes in the FE formulation. While the boundary condition of Equation (4.3.3), as will be seen, is the natural boundary condition of the FE formulation.

The element equation of the MSP-FE analysis can be obtained through either a variational method, or the method of weighted residual with Galerkin criterion [84]. Both methods yield the same finite element formulation. The derivation of the element equation using the method of weighted residual is used here to develop the MSP-FE formulation.

In each first order tetrahedral element, the scalar potential ϕ can be approximated by an interpolation between its nodal potential values. This interpolation can be written as

$$\phi = \sum_{k=1}^{4} N_k \phi_k \tag{4.3.4}$$

where N_k is a first order polynomial in terms of the coordinate variables, commonly referred to as a shape function. The subscripts in Equation (4.3.4) are numbered locally in each element. Notice, an important property of the shape function N_k is that it equals one at node k, zero at all other nodes.

Applying Equation (4.3.4) to every element, with the nodes numbered globally, one can write the expression for ϕ over the whole solution region as follows:

$$\phi = \sum_{k=1}^{NN} N_k \phi_k \tag{4.3.5}$$

where NN is the number of total grid nodes.

Since ϕ in Equation (4.3.5) is an approximation of piecewise continuous polynomials to the true solution, its substitution into the governing partial differential equation, Equation (4.3.1), will result in a residual. One then seeks the "best" solution, by minimizing the residual throughout the whole solution volume. This minimization is done by attempting to force a series of weighted integrals of residuals to zero. In the Galerkin method (the method of weighted residual with Galerkin criterion), the element shape functions, N_i, are chosen as the weighting functions to these residual integrals. Thus for each N_i, one can write the following:

$$\int_V N_i \nabla \cdot \overline{\overline{\mu}} (\nabla \sum_{k=1}^{NN} N_k \phi_k) \, dv = 0 \tag{4.3.6}$$

This constitutes a set of algebraic equations from which the nodal MSP values, ϕ_1, ϕ_2, ... can be obtained. Because the nodal MSP on S_H is known, Equation (4.3.2), the number of the nodal MSP variables to be solved for using Equation (4.3.6) is less than the total number of grid nodes, NN. In this case, in order to have a nonsingular system of algebraic equations, one only sets Equation (4.3.6) by use of the weighting functions N_i associated with the unknown nodes. Therefore, the total number of the algebraic equations resulting from Equation (4.3.6) is equal to the number of the total unknown nodes in the MSP-FE grid.

By applying the vector identity $\nabla \cdot (f\overline{F}) = f(\nabla \cdot \overline{F}) + \overline{F} \cdot (\nabla f)$, with a correspondence of f to N_i, and $\overline{F}$ to $\overline{\overline{\mu}} \nabla \phi$, one can expand Equation (4.3.6) as follows:

$$\int_V N_i \nabla \cdot \overline{\overline{\mu}} (\nabla \sum_{k=1}^{NN} N_k \phi_k) \, dv$$

$$= -\int_V \nabla N_i \cdot [(\overline{\overline{\mu}} \nabla \sum_{k=1}^{NN} N_k \phi_k)] \, dv + \int_V \nabla \cdot [N_i \overline{\overline{\mu}} (\nabla \sum_{k=1}^{NN} N_k \phi_k)] \, dv = 0 \tag{4.3.7}$$

Notice that, by Gauss's theorem; $\int_V (\nabla \cdot \overline{D}) dv = \oint_S \overline{D} \cdot d\overline{s}$, the second volume integration term in Equation (4.3.7) can be replaced by a closed surface integral. Thus, one obtains the following:

$$-\int_V \nabla N_i \cdot [\overline{\overline{\mu}}(\nabla \sum_{k=1}^{NN} N_k \phi_k)]\, dv + \oint_S N_i (\overline{\overline{\mu}} \nabla \sum_{k=1}^{NN} N_k \phi_k) \cdot \hat{n} ds = 0$$

where S is the outer boundary of the solution volume. Multiplying the above equation by (-1), and making use of the definition that $\nabla \phi \cdot \hat{n} = \partial \phi / \partial n$, yields the following:

$$\int_V \nabla N_i \cdot [\overline{\overline{\mu}}(\nabla \sum_{k=1}^{NN} N_k \phi_k)]\, dv - \oint_S N_i \mu_n \frac{\partial \phi}{\partial n} ds = 0 \tag{4.3.8}$$

where μ_n is the permeability along the normal $\hat{n}$ direction to the surface.

Notice, Equation (4.3.8) is written for every unknown node, thus the values of N_i at the nodes on the surface S_H, which is the portion of the outer boundary with the known nodes, are always equal to zero. Hence, the surface integral term in Equation (4.3.8) appears only on the surface S_B, which is the portion of the outer boundary with unknown nodes. It is obvious that substituting the boundary condition on S_B of Equation (4.3.3) into Equation (4.3.8) eliminates the surface integral from the equation. Therefore, the MSP-FE discretization equation can finally be written as

$$\int_V \nabla N_i \cdot [\overline{\overline{\mu}}(\nabla \sum_{k=1}^{NN} N_k \phi)]\, dv = 0 \tag{4.3.9}$$

Again, this equation has already included the outer boundary condition of Equation (4.3.3). In other words, the outer boundary condition in Equation (4.3.3) is inherently satisfied, thus it is a natural boundary condition.

Here, it should be pointed out that Equation (4.3.9) is also valid for problems involving more than one type of material. In this case, $\overline{B}$, $\overline{H}$, and $\overline{\overline{\mu}}$ are no longer continuous throughout the whole solution region, thus Equation (4.3.8) has to be simultaneously applied to each single-medium subregion of the problem. On the interface boundaries between these subregions, and in the absence of surface currents, ϕ must be continuous. This guarantees the continuity of the tangential components of the field intensity across the interface boundaries. Meanwhile, a surface integral similar to that in Equation (4.3.8) has to be taken into account on the outer boundaries of each single-medium subregion. Hence, on the interface boundaries in between

different material regions, the surface integral term emerges on both sides. Notice that $B_n = -\mu\partial\phi/\partial n$ on both sides of the interface boundary must be equal for the reason that B_n must be continuous across such a boundary. Also, notice that the surface integrals from each side are carrying opposite signs when one uses the same normal direction, $\hat{n}$, in their integral expressions. The contributions of the surface integrals from the two sides to the global system therefore cancelled each other. Hence, the surface integral of Equation (4.3.8) on the interface boundary of the multi-media problem is not needed. However, the total contribution of this surface integral term may not be zero when a discontinuity in $\mu\partial\phi/\partial n$ on the interface boundary needs to be enforced. This condition may happen in the MSP portion of the combined MVP-MSP approach, and will be further discussed later in this section.

The volume integral in Equation (4.3.9) can be expressed by a summation of a series integrals in every tetrahedral element. This allows one to rewrite Equation (4.3.9) into the following form:

$$\sum_{e=1}^{NE}\{\int_{V_e}\nabla N_i\cdot[\overline{\overline{\mu}}(\nabla\sum_{k=1}^{NN}N_k\phi)]\,dv\}=0 \tag{4.3.10}$$

where V_e is the volume of a given tetrahedral element, NE is the total number of tetrahedral elements. Notice, within a given tetrahedral element, only four shape functions, which are those shape functions related to the four nodes of that element, have non-zero values. Thus, the contribution to the global system from one of the elemental volume integrals in Equation (4.3.10) can be written as follows:

$$\int_{V_e}\nabla N_i\cdot[\overline{\overline{\mu}}(\nabla\sum_{k=1}^{4}N_k\phi_k)]\,dv=0 \qquad for\ i=1,\ 2,\ 3,\ 4 \tag{4.3.11}$$

Equation (4.3.11) is the element equation of the MSP-FE analysis.

The above element equation can be further expanded and rearranged as follows

$$\int_{V_e}\nabla N_i\cdot[\overline{\overline{\mu}}(\nabla\sum_{k=1}^{4}N_k\phi_k)]\,dv=\int_{V_e}\nabla N_i\cdot[\sum_{k=1}^{4}(\overline{\overline{\mu}}\nabla N_k)\phi_k]\,dv$$

$$=\sum_{k=1}^{4}\int_{V_e}\nabla N_i\cdot(\overline{\overline{\mu}}\nabla N_k)\phi_k\,dv$$

$$= \sum_{k=1}^{4} \int_{V_e} (\mu_x \frac{\partial N_i}{\partial x}\frac{\partial N_k}{\partial x} + \mu_y \frac{\partial N_i}{\partial y}\frac{\partial N_k}{\partial y} + \mu_z \frac{\partial N_i}{\partial z}\frac{\partial N_k}{\partial z})\phi_k \, dv$$

$$= 0 \qquad \text{for } i = 1, 2, 3, 4 \tag{4.3.12}$$

For first order tetrahedral elements, the derivatives of the shape functions are constants, hence they can be taken outside the integral. Accordingly, the element equations can be written into a compact matrix form as follows:

$$\begin{bmatrix} s_{11} & s_{12} & s_{13} & s_{14} \\ s_{21} & s_{22} & s_{23} & s_{24} \\ s_{31} & s_{32} & s_{33} & s_{34} \\ s_{41} & s_{42} & s_{43} & s_{44} \end{bmatrix} \begin{Bmatrix} \phi_1 \\ \phi_2 \\ \phi_3 \\ \phi_4 \end{Bmatrix} = \begin{Bmatrix} 0 \\ 0 \\ 0 \\ 0 \end{Bmatrix} \tag{4.3.13}$$

where

$$s_{ik} = (\mu_x \frac{\partial N_i}{\partial x}\frac{\partial N_k}{\partial x} + \mu_y \frac{\partial N_i}{\partial y}\frac{\partial N_k}{\partial y} + \mu_z \frac{\partial N_i}{\partial z}\frac{\partial N_k}{\partial z}) \, Vol$$

and

$$Vol = \textit{Volume of a given Tetrahedral Element}$$

The calculation of the derivatives of the shape functions in Equation (4.3.13) is adopted from previous work on the 3D magnetic vector potential formulation by Demerdash et al [33]. For completeness these derivative terms are listed in Appendix (B) of this dissertation. Next, the forcing function part of the element equation stemming from the enforcement of the interface boundary conditions is discussed.

4.3.2 The FE Formulation Including the MSP Discontinuities at the Interface Boundary

The two types of MSP discontinuity conditions, the MSP jump, $\Delta\phi$, on the outer boundary of the current-carrying subregion, and the discontinuity of $\mu\partial\phi/\partial n$, on the

air-iron interface within this MVP subregion, can be included in the element equations of the MSP-FE analysis. Again, as stated in the previous sections, $\Delta\phi$ is obtained from the MVP computed results using the surface FE procedure. Also, the $\mu\partial\phi/\partial n$ distribution is obtained from the same MVP computed results.

Consider the two adjacent tetrahedral elements located on both sides of the outer boundary of the MVP subregion, Figure (4.3.1). Because of the MSP jump distribution, the MSPs on each side of the interface between the two elements may have different values. The difference is $\Delta\phi$. In order to avoid increasing the total number of unknown variables in the FE computation, the scalar potential value computed at the 3D FE grid node is considered to be the MSP value on the side of the current-free region. Consequently, on the side of the MVP subregion, the MSP at node i, ϕ_i, can be expressed as follows:

$$\phi_i = \phi_i^{node} - \Delta\phi_i \tag{4.3.14}$$

where, ϕ_i^{node} is the nodal MSP at the opposite side of the MSP subregion computed directly from the 3D-FE computation, and $\Delta\phi_i$ is the MSP jump value at the node, i. Accordingly, the element equation (Equation (4.3.13)) for the element on the side of the MVP subregion becomes

$$\begin{bmatrix} s_{11} & s_{12} & s_{13} & s_{14} \\ s_{21} & s_{22} & s_{23} & s_{24} \\ s_{31} & s_{32} & s_{33} & s_{34} \\ s_{41} & s_{42} & s_{43} & s_{44} \end{bmatrix} \begin{Bmatrix} \phi_1^{node} - \Delta\phi_1 \\ \phi_2^{node} - \Delta\phi_2 \\ \phi_3^{node} - \Delta\phi_3 \\ \phi_4^{node} - \Delta\phi_4 \end{Bmatrix} = 0 \tag{4.3.15}$$

For the grid node which is not on the outer boundary of the MVP subregion, the associated term, $\Delta\phi$, in Equation (4.3.15), should assume a zero value. For instance, $\Delta\phi_4$ for the element in Figure (4.3.1) is zero.

By moving $\Delta\phi$'s to the right hand side of Equation (4.3.15), one obtains the

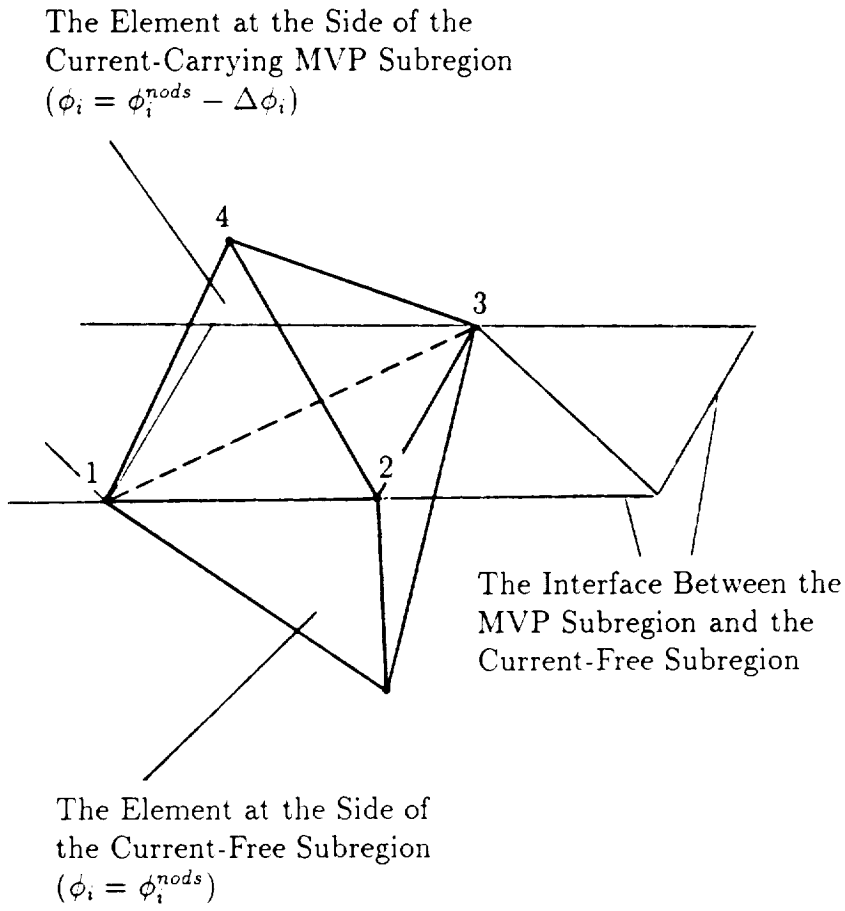

Figure (4.3.1) Two Adjacent Tetrahedral Elements on Each Side of the Outer Surface of the MVP Subregion

following

$$\begin{bmatrix} s_{11} & s_{12} & s_{13} & s_{14} \\ s_{21} & s_{22} & s_{23} & s_{24} \\ s_{31} & s_{32} & s_{33} & s_{34} \\ s_{41} & s_{42} & s_{43} & s_{44} \end{bmatrix} \begin{Bmatrix} \phi_1^{node} \\ \phi_2^{node} \\ \phi_3^{node} \\ \phi_4^{node} \end{Bmatrix} = \begin{bmatrix} s_{11} & s_{12} & s_{13} & s_{14} \\ s_{21} & s_{22} & s_{23} & s_{24} \\ s_{31} & s_{32} & s_{33} & s_{34} \\ s_{41} & s_{42} & s_{43} & s_{44} \end{bmatrix} \begin{Bmatrix} \Delta\phi_1 \\ \Delta\phi_2 \\ \Delta\phi_3 \\ \Delta\phi_4 \end{Bmatrix} \tag{4.3.16}$$

Equation (4.3.16) is the element equation for the elements on the side of the MVP subregion. It can be seen that the enforcement of the MSP jump distribution results in the forcing function term at the right hand side of the element equation. Equation (4.3.16) can be easily extended to use for all elements in the MSP solution region. This application is done by assigning zero values for $\Delta\phi$'s at all interior FE nodes of the MVP subregion, and at all nodes in the current-free subregion. This extension has greatly simplified the computer program structure of the MSP-FE computation.

Another interface boundary condition, which has to be enforced through the FE formulation, is the discontinuity of $\mu\partial\phi/\partial n$ on the air-iron interface within the MVP subregion. Figure (4.3.2) shows a case with two adjacent elements located on each side of the air-iron interface. From the discussion in Chapter 2 and Chapter 3, this discontinuity can be written as

$$\mu_0 \frac{\partial\phi_1}{\partial n} - \mu_n \frac{\partial\phi_2}{\partial n} = B_{mvpn} \tag{4.3.17}$$

where, ϕ_1 is the MSP on the air side of the interface boundary; ϕ_2 is the MSP on the iron side of that boundary; n is the normal direction unit vector on that interface boundary pointing from the air side to the iron side; μ_n is the permeability of the iron region along the n-direction; and B_{mvpn} is the normal component of the flux density computed from the MVP part of this combined MVP-MSP approach.

As discussed earlier in this section, in the case of multi-media problems, Equation (4.3.8) should be applied separately to the air and iron subregions, and the magnetic field boundary condition needs to be examined on the interface between the

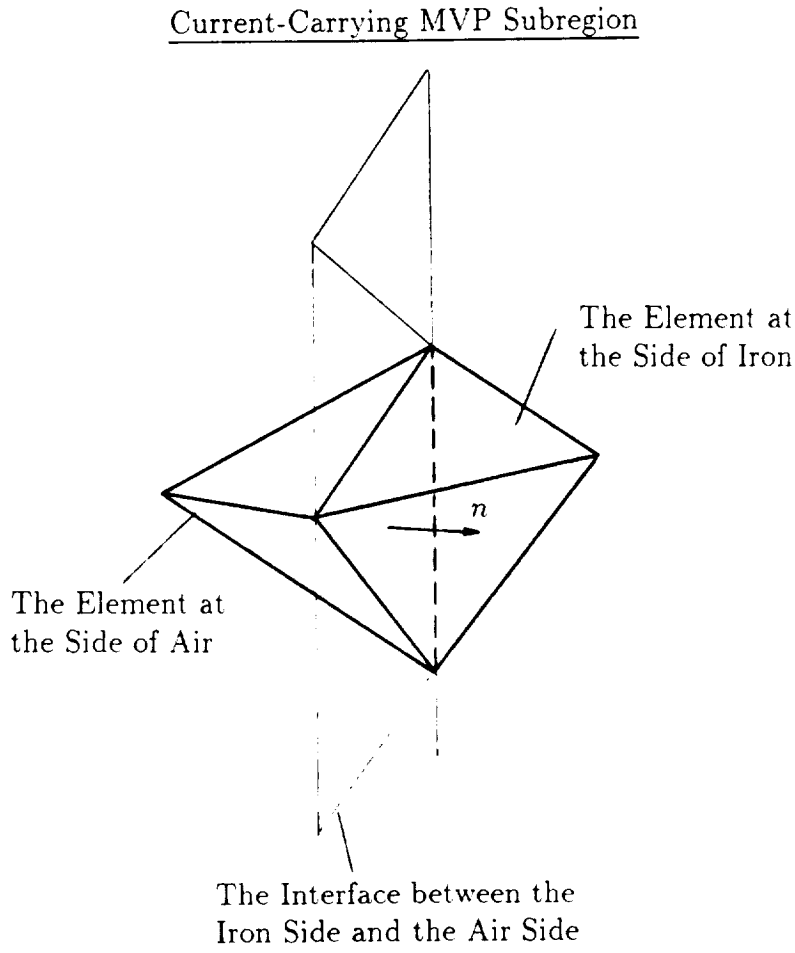

Figure (4.3.2) Two Adjacent Tetrahedral Elements on Each Side of the Air-Iron Interface Within the MVP Subregion

air and iron. Thus, by applying Equation (4.3.8) in both subregions, the resultant contribution to the global system can be written as follows:

$$\int_V \nabla N_i \cdot [\overline{\overline{\mu}}(\nabla \sum_{k=1}^{NN} \phi_k)]\, dv - (\int_S N_i \mu_0 \frac{\partial \phi_1}{\partial n}\, ds - \int_S N_i \mu_n \frac{\partial \phi_2}{\partial n})\, ds = 0 \qquad (4.3.18)$$

where S is the interface between the air and iron, and its normal direction $\hat{n}$ points from the side of air to the side of iron. By substituting the interface boundary condition of Equation (4.3.17) into the surface integral terms in Equation (4.3.18), the total contribution of the surface integrals to the global system can be written as

$$\begin{aligned} &\int_S N_i \mu_0 \frac{\partial \phi_1}{\partial n}\, ds - \int_S N_i \mu_n \frac{\partial \phi_2}{\partial n}\, ds \\ &= \int_S N_i (\mu_0 \frac{\partial \phi_1}{\partial n} - \mu_n \frac{\partial \phi_2}{\partial n})\, ds \\ &= \int_S N_i B_{mvpn}\, ds \end{aligned} \qquad (4.3.19)$$

This leads one to rewrite Equation (4.3.18) into the following form:

$$\int_V \nabla N_i \cdot [\overline{\overline{\mu}}(\nabla \sum_{k=1}^{NN} \phi_k)]\, dv = \int_S N_i B_{mvpn}\, ds \qquad (4.3.20)$$

Again, the surface integral term in Equation (4.3.20) is carried out at the outward surface of the air side with its normal direction pointing from the air to the iron. It is obvious that this surface intergal becomes part of the forcing function in the MSP finite element analysis.

In a given tetrahedral element, the surface integral term in Equation (4.3.19) may occur on any one of its four surface triangles. Since one surface triangle contains three nodes, the forcing function term due to the surface integral on that triangle should be contributed to the three element equations corresponding to the three related nodes. In order to include this into a general form of element equation, a fixed connection pattern of elemental nodes and elemental surface triangles is used for every element. This connection pattern is shown in Figure (4.3.3). Using this connection pattern, with the notations s_i for the i-th surface triangle in Figure (4.3.3), and B^i_{mvpn} for the normal component of the flux density computed from the MVP at the i-th surface triangle, the associated forcing function of the element equation can

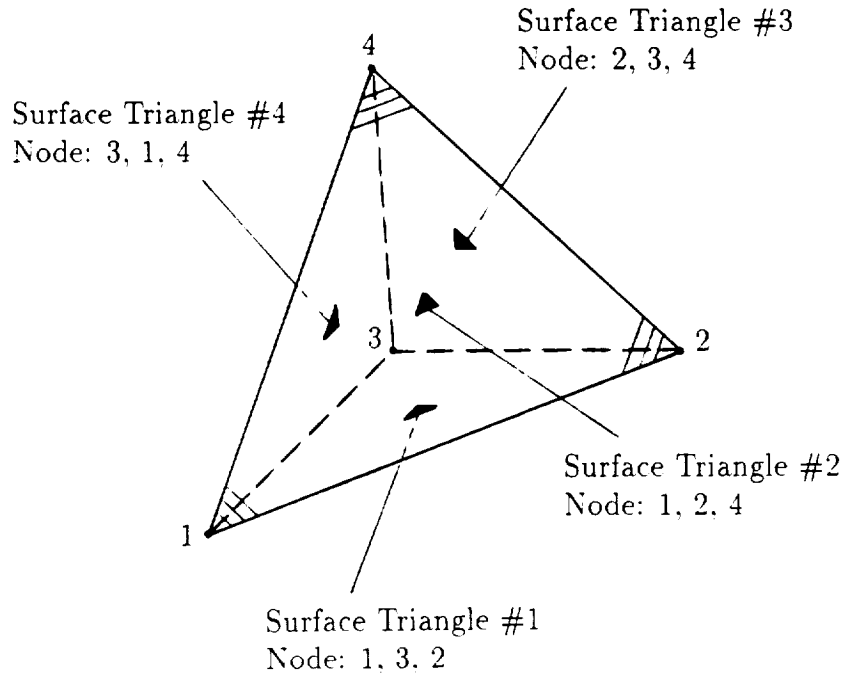

Figure (4.3.3) Connection Pattern of Elemental Nodes and Surface Triangles

be written in a vector form, $\underline{P_e}$, as follows:

$$\underline{P_e} = \left\{ \begin{array}{c} p_1 \\ p_2 \\ p_3 \\ p_4 \end{array} \right\} = \left\{ \begin{array}{l} \int_{s_1} N_1 B^1_{mvpn} ds + \int_{s_2} N_1 B^2_{mvpn} ds + \int_{s_4} N_1 B^4_{mvpn} ds \\ \int_{s_1} N_2 B^1_{mvpn} ds + \int_{s_2} N_2 B^2_{mvpn} ds + \int_{s_3} N_2 B^3_{mvpn} ds \\ \int_{s_1} N_3 B^1_{mvpn} ds + \int_{s_3} N_3 B^3_{mvpn} ds + \int_{s_4} N_3 B^4_{mvpn} ds \\ \int_{s_2} N_4 B^2_{mvpn} ds + \int_{s_3} N_4 B^3_{mvpn} ds + \int_{s_4} N_4 B^4_{mvpn} ds \end{array} \right\}$$

The integral terms in the above column vector can be further simplified using the formulation of the area integration [84]. Here, the B^i_{mvpn} terms are constants, so they can be taken outside of the surface integrals. The area integrations used here are in the following form:

$$\int_{s_i} N_k ds = \frac{\Delta_i}{3}$$

where Δ_i is the area of the i-th surface triangle of the tetrahedral element. Hence, the above vector form of the forcing function can be rewritten as follows:

$$\underline{P_e} = \left\{ \begin{array}{c} p_1 \\ p_2 \\ p_3 \\ p_4 \end{array} \right\} = \frac{1}{3} \left\{ \begin{array}{l} B^1_{mvpn}\Delta_1 + B^2_{mvpn}\Delta_2 + B^4_{mvpn}\Delta_4 \\ B^1_{mvpn}\Delta_1 + B^2_{mvpn}\Delta_2 + B^3_{mvpn}\Delta_3 \\ B^1_{mvpn}\Delta_1 + B^3_{mvpn}\Delta_3 + B^4_{mvpn}\Delta_4 \\ B^2_{mvpn}\Delta_2 + B^3_{mvpn}\Delta_3 + B^4_{mvpn}\Delta_4 \end{array} \right\} \tag{4.3.21}$$

Finally, adding the above vector to the right hand side of Equation (4.3.16) leads to the complete element equation enforcing the MSP discontinuities across the

elemental surfaces, which can now be written as follows:

$$\begin{bmatrix} s_{11} & s_{12} & s_{13} & s_{14} \\ s_{21} & s_{22} & s_{23} & s_{24} \\ s_{31} & s_{32} & s_{33} & s_{34} \\ s_{41} & s_{42} & s_{43} & s_{44} \end{bmatrix} \begin{Bmatrix} \phi_1^{node} \\ \phi_2^{node} \\ \phi_3^{node} \\ \phi_4^{node} \end{Bmatrix} = \begin{bmatrix} s_{11} & s_{12} & s_{13} & s_{14} \\ s_{21} & s_{22} & s_{23} & s_{24} \\ s_{31} & s_{32} & s_{33} & s_{34} \\ s_{41} & s_{42} & s_{43} & s_{44} \end{bmatrix} \begin{Bmatrix} \Delta\phi_1 \\ \Delta\phi_2 \\ \Delta\phi_3 \\ \Delta\phi_4 \end{Bmatrix} +$$

$$\frac{1}{3} \begin{Bmatrix} B^1_{mvpn}\Delta_1 + B^2_{mvpn}\Delta_2 + B^4_{mvpn}\Delta_4 \\ B^1_{mvpn}\Delta_1 + B^2_{mvpn}\Delta_2 + B^3_{mvpn}\Delta_3 \\ B^1_{mvpn}\Delta_1 + B^3_{mvpn}\Delta_3 + B^4_{mvpn}\Delta_4 \\ B^2_{mvpn}\Delta_2 + B^3_{mvpn}\Delta_3 + B^4_{mvpn}\Delta_4 \end{Bmatrix} \tag{4.3.22}$$

This is also the general form for the tetrahedral element formulation of the MSP portion of the MVP-MSP FE approach at hand. In this form the MSP discontinuity conditions become the forcing function of the element equation. The computation of the terms in the coefficient matrix was detailed in Equation (4.3.13). When this form is used for the elements within the iron portion of the MVP subregion, the B_{mvpn} terms in the equation must assume zero values. When this form is used for the elements in the current free subregion, the whole forcing function part at the right hand side of the element equation must equal zero.

Chapter 5

Newton-Raphson Method in Nonlinear MSP Problems

In general, magnetic field problems in electrical devices and machines are of nonlinear nature due to magnetic saturation in ferromagnetic materials used in the construction of the cores of these machines. The main magnetic flux path of the MLA at hand consists of the stator armature iron core laminations, rotor shaft and poles, as well as the end-bells and casing. The magnetic saturation in these iron portions has substantial effects on the global and local magnetic field distributions in such MLAs. Also, the magnetic saturation affects various MLA machine parameters such as the winding inductances, the required field excitations, and the induced armature emfs under different machine operating conditions. Therefore, the nonlinearity problem related to the magnetic material saturation has to be taken rigorously into full account in computation of magnetic fields in such MLAs. This is in addition to the fact that the magnetic properties of these iron portions can be anisotropic due to the laminated nature of portions of the iron core laminations.

In the combined MVP-MSP 3D finite element method, the magnetic anisotropy and nonlinearity related to the ferromagnetic materials can be included within the MSP part of the solution method. As was discussed in Section 4.3, the resultant global system of equations of the 3D-FE MSP analysis can be written as follows:

$$\underline{\underline{S}} \cdot \underline{\phi} = \underline{\underline{S}} \cdot (\underline{\Delta\phi}) + \underline{P} \tag{5.0.1}$$

where, $\underline{\underline{S}}$ is a coefficient matrix, $\underline{\phi}$ is a column vector containing the unknown MSPs, $(\underline{\Delta\phi})$ is a column vector containing the MSP jumps at the FE grid nodes, and $\underline{P}$ is a column vector containing the terms resulting from the enforcement of the MSP

derivative discontinuity. The associated element equations were detailed in Equations (4.3.13) and (4.3.22) of Section 4.3. Notice that the coefficient matrix, $\underline{\underline{S}}$, contains the material permeability terms, μ_x, μ_y, and μ_z, see Equation (4.3.13). These permeability values within the iron cores depend on the magnitude of the field intensity (or flux density), consequently they are functions of the unknown MSP variable, $\underline{\phi}$. In such a case, the coefficient matrix, $\underline{\underline{S}}$ in Equation (5.0.1) becomes a function of the unknown MSP variable, $\underline{\phi}$, hence, (5.0.1) is a set of nonlinear equations.

In solving this nonlinear problem, a Newton-Raphson iterative method is used. The associated 3D MSP finite element formulation in conjunction with the Newton-Raphson procedure is detailed in this chapter. Also, relaxation factors applied in the process of updating the permeability derivative terms, $\partial\mu_I/\partial H_I$, and $\partial\mu_I/\partial\phi_k$, were used in the Newton-Raphson iterative procedure, which successfully improved the quality of convergence of the method for the nonlinear MSP problem. Application of these relaxation factors to the MSP-FE formulation is discussed in Section 5.2. In this chapter, the notation $\underline{\phi}$ refers to the nodal MSP values in the 3D-FE global system of equations. This $\underline{\phi}$ represents the actual MSPs at the nodes within the current free subregion. Meanwhile, the actual MSPs at the nodes within the current-carrying MVP subregion are expressed by $(\underline{\phi} - \underline{\Delta\phi})$, where $\underline{\Delta\phi}$ is the MSP jump at the nodes on the outer surface of the MVP subregion.

5.1 The Newton-Raphson Iterative Procedure for the 3D-FE MSP Problem

In order to derive the Newton-Raphson iterative algorithm, consider the following column vector, $\underline{F}(\underline{\phi})$:

$$\begin{aligned}\underline{F}(\underline{\phi}) &= \underline{\underline{S}} \cdot \underline{\phi} - \underline{\underline{S}} \cdot (\underline{\Delta\phi}) - \underline{P} \\ &= \underline{\underline{S}} \cdot (\underline{\phi} - \underline{\Delta\phi}) - \underline{P}\end{aligned} \tag{5.1.1}$$

where $\underline{\underline{S}}$, $\underline{\phi}$, $\underline{\Delta\phi}$, and $\underline{P}$ are the same as those used in Equation (5.0.1). If one substitutes a column vector, $\underline{\phi}$, equal to the exact solution of Equation (5.0.1) into Equation (5.1.1), $\underline{F}(\underline{\phi})$ in Equation (5.1.1) becomes a null (zero) vector.

Using a curtailed (truncated) Taylor expansion for $\underline{F}(\underline{\phi})$ with respect to $\underline{\phi}$, at $\underline{\phi}_0$, one can write the following:

$$\underline{F}(\underline{\phi}) = \underline{F}(\underline{\phi}_0) + \underline{J}(\underline{\phi}_0) \cdot (\underline{\phi} - \underline{\phi}_0) \tag{5.1.2}$$

where $\underline{J}$ is a global Jacobian matrix. The associated element matrix form of this Jacobian matrix can be written as follows:

$$\underline{J_e} = \begin{bmatrix} \frac{\partial f_1}{\partial \phi_1} & \frac{\partial f_1}{\partial \phi_2} & \frac{\partial f_1}{\partial \phi_3} & \frac{\partial f_1}{\partial \phi_4} \\ \frac{\partial f_2}{\partial \phi_1} & \frac{\partial f_2}{\partial \phi_2} & \frac{\partial f_2}{\partial \phi_3} & \frac{\partial f_2}{\partial \phi_4} \\ \frac{\partial f_3}{\partial \phi_1} & \frac{\partial f_3}{\partial \phi_2} & \frac{\partial f_3}{\partial \phi_3} & \frac{\partial f_3}{\partial \phi_4} \\ \frac{\partial f_4}{\partial \phi_1} & \frac{\partial f_4}{\partial \phi_2} & \frac{\partial f_4}{\partial \phi_3} & \frac{\partial f_4}{\partial \phi_4} \end{bmatrix} \tag{5.1.3}$$

Assume a case in which $\underline{\phi}_0$ is a column vector that is very close to the exact solution of Equation (5.0.1), $\underline{\phi}$. The resulting $\underline{F}$ from the above Taylor expansion is expected to be nearly the exact $\underline{F}$ at $\underline{\phi}$. That is, based on Equation (5.1.1) the left hand side of Equation (5.1.2) becomes a null column vector. Thus, one can rewrite Equation (5.1.2) as follows:

$$\underline{J}(\underline{\phi}_0) \cdot (\underline{\phi} - \underline{\phi}_0) = -\underline{F}(\underline{\phi}_0) \tag{5.1.4}$$

or

$$\underline{J}(\underline{\phi}_0) \cdot \underline{\delta\phi} = -\underline{F}(\underline{\phi}_0) \tag{5.1.5}$$

where

$$\underline{\delta\phi} = \underline{\phi} - \underline{\phi}_0 \qquad \text{and} \qquad \underline{\phi} = \underline{\phi}_0 + \underline{\delta\phi}$$

In this case, one can solve Equation (5.1.5) for $\underline{\delta\phi}$, and use $(\underline{\phi} = \underline{\phi}_0 + \underline{\delta\phi})$ to obtain the exact solution of the nonlinear Equation (5.0.1).

However, if $\underline{\phi}_0$ in Equation (5.1.5) is not close enough to the exact solution of Equation (5.0.1), solving Equation (5.1.5) may not result in a solution which exactly satisfies Equation (5.0.1). In this case, one can use the computed $\underline{\phi}$ as an updated

$\underline{\phi}_0$ to set up a new linear system of equations as given in Equation (5.1.5). One then solves this new linear system of equations to obtain a new set of nodal MSPs which is a better estimate than the previous one (closer to the exact solution of Equation (5.0.1)). This process can be repeatedly used until a satisfactory solution is obtained.

The iterative method described above is called the Newton-Raphson iterative procedure. The theory of the Newton-Raphson method can be found in numerous text books [87]. The convergence of this iteration can be tested by checking whether the norm of $\underline{F}$ in Equation (5.1.2) approaches zero or an insignificant number.

The Newton-Raphson procedure used in this research for solving the nonlinear MSP problem can be mathematically expressed as follows:

$$\begin{cases} \underline{J}(\underline{\phi}^i) \cdot \underline{\delta\phi^i} = -\underline{F}(\underline{\phi}^i) \\ \underline{\phi}^{i+1} = \underline{\phi}^i + \underline{\delta\phi^i} \end{cases} \qquad \text{for } i = 0, 1, 2, \ldots \tag{5.1.6}$$

where $\underline{\phi}^i$ is the MSP nodal value computed from the previous step of iteration, $\underline{\delta\phi^i}$ is the variable to be solved in the i-th step of the Newton-Raphson iteration, and $\underline{\phi}^{i+1}$ is the updated MSP nodal value after the i-th iteration. Here, $\underline{\delta\phi^i}$ should not be confused with $\underline{\Delta\phi}$ which is the MSP jump computed from the surface FE part of this combined MVP-MSP method. The initial guess, $\underline{\phi}_0$, can be chosen as a zero column vector. In each step of this iteration, the Jacobian matrix, $\underline{J}(\underline{\phi}^i)$, and the right hand side, $-\underline{F}(\underline{\phi}^i)$, can be obtained based on the most recently updated MSP. Thus, in each step of the Newton-Raphson iteration, one solves a set of linear algebraic equations. The various terms in the Jacobian matrix and the right hand side of Equation (5.1.6) is discussed next.

The global Jacobian matrix and forcing function column vector are assembled using element equations contributed from every first-order tetrahedral element. According to Equations (5.1.6) and (5.1.1), the right hand side of the element equation,

$-\underline{F_e}(\underline{\phi})$, can be written as follows:

$$-\underline{F_e}(\underline{\phi}) = \begin{Bmatrix} -f_1 \\ -f_2 \\ -f_3 \\ -f_4 \end{Bmatrix} = - \begin{bmatrix} s_{11} & s_{12} & s_{13} & s_{14} \\ s_{21} & s_{22} & s_{23} & s_{24} \\ s_{31} & s_{32} & s_{33} & s_{34} \\ s_{41} & s_{42} & s_{43} & s_{44} \end{bmatrix} \begin{Bmatrix} \phi_1 - \Delta\phi_1 \\ \phi_2 - \Delta\phi_2 \\ \phi_3 - \Delta\phi_3 \\ \phi_4 - \Delta\phi_4 \end{Bmatrix} + \begin{Bmatrix} p_1 \\ p_2 \\ p_3 \\ p_4 \end{Bmatrix} \quad (5.1.7)$$

Here, f_i can be further expressed as:

$$f_i = \sum_{m=1}^{4} s_{im}(\phi_m - \Delta\phi_m) - p_i \quad (5.1.8)$$

where, the s_{im} terms were given earlier in Equation (4.3.13), and are rewritten here for the reader's convenience as follows:

$$s_{im} = Vol[(\mu_x \frac{\partial N_i}{\partial x}\frac{\partial N_m}{\partial x}) + (\mu_y \frac{\partial N_i}{\partial y}\frac{\partial N_m}{\partial y}) + (\mu_z \frac{\partial N_i}{\partial z}\frac{\partial N_m}{\partial z})],$$

$$i, m = 1, 2, 3, 4 \quad (5.1.9)$$

The vector $\underline{P}$ containing the p_i terms in Equation (5.1.8) was given earlier in Equation (4.3.21). The permeabilities, μ_x, μ_y, and μ_z used in Equation (5.1.9), which arise due to the laminated nature of some of the iron cores, will be further discussed in this section.

Meanwhile, the general term in the element Jacobian matrix, Equation (5.1.3), can be expanded as follows:

$$\frac{\partial f_i}{\partial \phi_k} = \frac{\partial}{\partial \phi_k} \sum_{m=1}^{4} s_{im}(\phi_m - \Delta\phi_m) - \frac{\partial p_i}{\partial \phi_k}$$

Since p_i is a constant, the term $\partial p_i / \partial \phi_k = 0$. Hence, one can rewrite the above general term in the Jacobian matrix as follows:

$$\frac{\partial f_i}{\partial \phi_k} = s_{ik} + \sum_{m=1}^{4} \frac{\partial s_{im}}{\partial \phi_k}(\phi_m - \Delta\phi_m) \quad (5.1.10)$$

It should be pointed out that the term, $(\phi_m - \Delta\phi_m)$, in Equation (5.1.10) represents the actual MSP value which includes the MSP jump at the nodes of that element. Accordingly, the Newton-Raphson procedure for this nonlinear MSP-FE analysis can be further stated as follows:

(1) Use the most recently computed $\underline{\phi}$ to calculate the actual MSP value, $(\underline{\phi}^i - \underline{\Delta\phi})$, for each element, compute the corresponding elemental field intensities and consequently update the material permeabilities for each element.

(2) Set up the element Jacobian matrices and forcing functions using the updated material permeabilities and the updated actual MSP, $(\underline{\phi}^i - \underline{\Delta\phi})$, calculated from step (1).

(3) Assemble the element equations to form a global system, and solve this system for $\delta\underline{\phi}^i$.

(4) Update $\underline{\phi}$ using $(\underline{\phi}^{i+1} = \underline{\phi}^i + \delta\underline{\phi}^i)$. This updated $\underline{\phi}$ will be used in the next Newton-Raphson iteration step. Repeat the steps (1) through (4) until convergence is achieved.

The details regarding the computation of the general term, $\partial s_{im}/\partial\phi_k$, in the element Jacobian matrix are discussed next. First, using Equation (5.1.9), one can expand $\partial s_{im}/\partial\phi_k$ as follows:

$$\frac{\partial s_{im}}{\partial \phi_k} = Vol[(\frac{\partial N_i}{\partial x}\frac{\partial N_m}{\partial x})(\frac{\partial \mu_x}{\partial \phi_k}) + (\frac{\partial N_i}{\partial y}\frac{\partial N_m}{\partial y})(\frac{\partial \mu_y}{\partial \phi_k}) + (\frac{\partial N_i}{\partial z}\frac{\partial N_m}{\partial z})(\frac{\partial \mu_z}{\partial \phi_k})] \quad (5.1.11)$$

Notice, the elemental permeability values in Equation (5.1.9) and their derivatives with respect to ϕ_k in Equation (5.1.11), that is, the terms,

$$\mu_x, \quad \mu_y, \quad \mu_z, \quad \frac{\partial \mu_x}{\partial \phi_k}, \quad \frac{\partial \mu_y}{\partial \phi_k}, \quad \frac{\partial \mu_z}{\partial \phi_k}$$

are dependent upon on the orientation of the iron laminations. In the case of this MLA class of machines, the stator iron laminations are stacked along the z-direction, as illustrated in Figure (5.1.1), with a stacking factor equal to k_s. The formulation of the elemental permeabilities and their derivatives in this particular case are explained next.

An equivalent permeance model, which was developed in reference [35] is used here to determine the elemental permeability values, μ_x, μ_y, and μ_z. In this model,

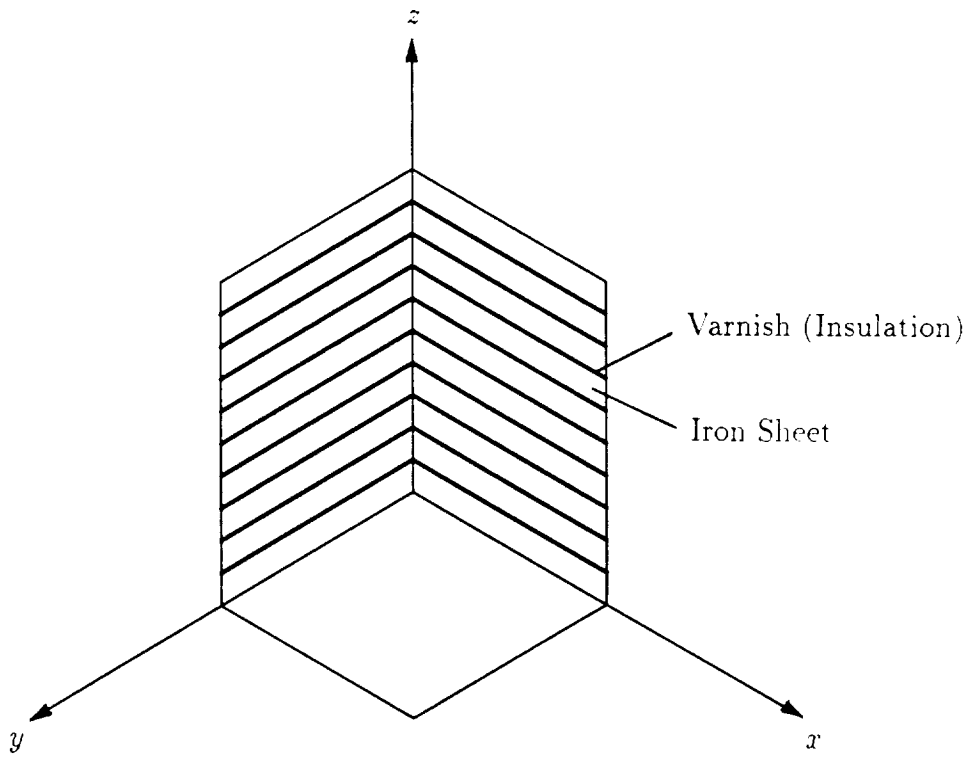

Figure (5.1.1) Iron-Varnish Composite with Iron Laminations Piled up along the z-Direction

the iron-varnish composite material within an element is substituted by a simple material with anisotropic magnetic property.

Along the planes of the laminations (parallel to xoy reference plane), the permeance of the substituted material is equal to that of the composite material consisting of iron and varnish forming parallel flux paths as shown in Figure (5.1.2). According to the derivation in reference [35], this leads to equivalent permeability values, μ_x, and μ_y for the substituted material as follows:

$$\mu_x = \mu_y = k_s \mu_I + \mu_0(1 - k_s) \tag{5.1.12}$$

where μ_I is the permeability of the iron material. Notice, the mmf required to drive a given amount of magnetic flux through a unit length of the composite material is equal to the mmf required for the substituted material. This allows one to write the following:

$$H_{Ix} = H_{ex}, \quad \text{and} \quad H_{Iy} = H_{ey} \tag{5.1.13}$$

where H_{Ix} and H_{Iy} are the x and y components of the field intensity in the iron portion of the composite material. Meanwhile, H_{ex} and H_{ey} are the x and y components of the field intensity in the substituted material.

Along the z-direction, which is the direction normal to the lamination planes, the permeance of the substituted material in this direction is equal to the permeance of the composite material consisting of iron and varnish in series as shown in Figure (5.1.3). According to the derivation in reference [35], the equivalent permeability value μ_z can be written as follows:

$$\mu_z = \frac{\mu_0 \mu_I}{\mu_0 k_s + (1 - k_s)\mu_I} \tag{5.1.14}$$

Notice, in this direction, the magnetic flux flowing through the iron of the composite material is equal to that through the substituted material. Thus, one can write the following:

$$B_{Iz} = B_{ez} \tag{5.1.15}$$

where B_{Iz} is the z-component of the flux density in the iron portion of the composite material, and B_{ez} is the z-component of the flux density in the substituted material.

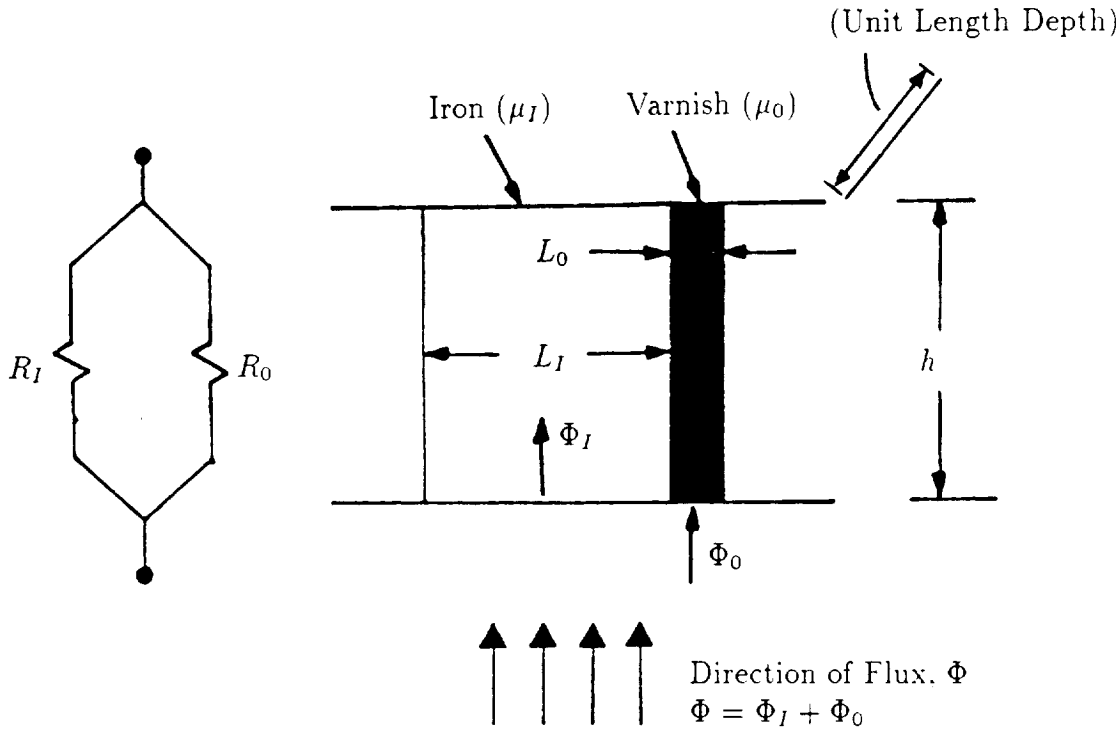

$$R_I = \frac{h}{\mu_I L_I}, \quad R_0 = \frac{h}{\mu_0 L_0}, \quad k_s = \frac{L_I}{L_I + L_0}$$

$$\mu_x = \mu_y = \frac{h}{(\frac{R_I R_0}{R_I + R_0})(L_I + L_0)} = k_s \mu_I + (1 - k_s)\mu_0$$

Figure (5.1.2) Permeabilities μ_x and μ_y Along the Planes of the Iron Laminations

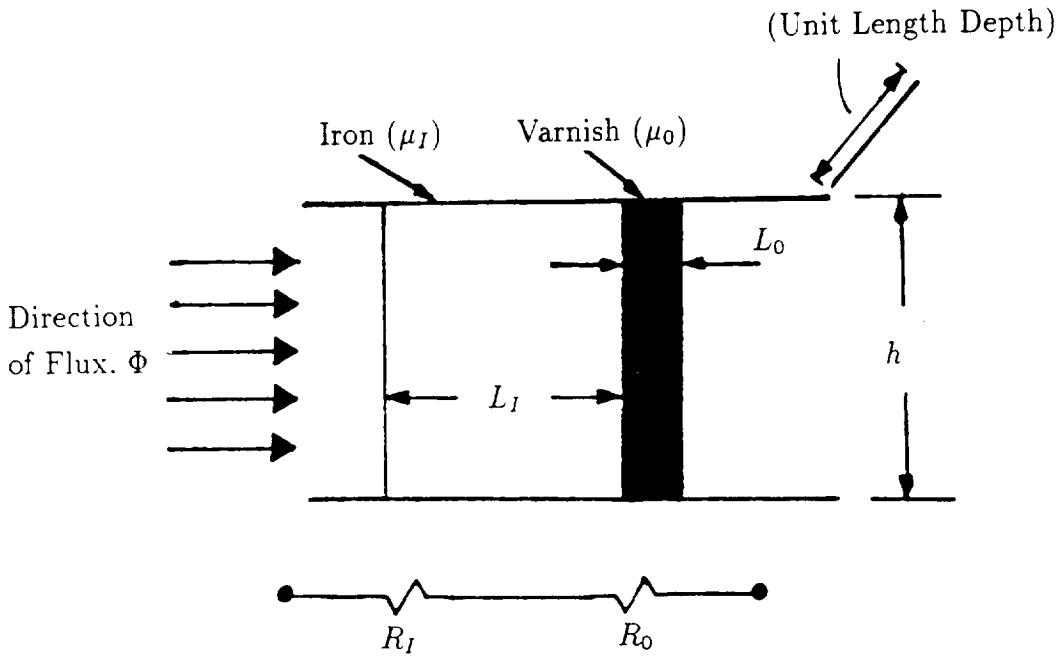

$$R_I = \frac{L_I}{\mu_I h}, \quad R_0 = \frac{L_0}{\mu_0 h}, \quad k_s = \frac{L_I}{L_I + L_0}$$

$$\mu_z = \frac{L_I + L_0}{(R_I + R_0)h} = \frac{\mu_0 \mu_I}{k_s \mu_0 + (1 - k_s)\mu_I}$$

Figure (5.1.3) Permeability μ_z in the Direction Perpendicular to the Planes of the Iron Laminations

Thus, one can rewrite the relationship expressed in Equation (5.1.15) using the field intensities as follows:

$$\mu_I H_{Iz} = \mu_z H_{ez}$$

where H_{Iz} is the z-component of the field intensity in the iron portion of the composite material, and H_{ez} is the z-component of the field intensity in the substituted material. This consequently leads to the following relationship:

$$H_{Iz} = \frac{\mu_z}{\mu_I} H_{ez} \tag{5.1.16}$$

Equations (5.1.13) and (5.1.16) enables one to find the field intensity in the iron portion of the composite material using the field intensity in the substituted material.

In each step of the Newton-Raphson procedure, one obtains the elemental field intensities (the field intensities in the substituted material), H_{ex}, H_{ey}, and H_{ez}, by taking the gradient of the computed MSPs. Using Equations (5.1.13) and (5.1.16), one can find the resultant field intensity value in the iron portion of the composite material as follows:

$$\begin{aligned} H_I &= \sqrt{H_{Ix}^2 + H_{Iy}^2 + H_{Iz}^2} \\ &= \sqrt{H_{ex}^2 + H_{ey}^2 + (\frac{\mu_z}{\mu_I})^2 H_{ez}^2} \end{aligned} \tag{5.1.17}$$

Consequently, using H_I, the iron permeability μ_I can be obtained through an interpolation on the B-H curve associated with the iron portion of the composite material. In this research, the cubic spline interpolation [87] is used for the numerical $B - H$ curve fit. Finally, one uses Equations (5.1.12) and (5.1.14) to calculate the elemental permeabilities, μ_x, μ_y, and μ_z.

Meanwhile, using the relationship between the iron permeability and the elemental permeabilities (Equations (5.1.12) and (5.1.14)), the derivatives of the elemental permeabilities with respect to the nodal MSP in Equation (5.1.11) can be written as follows:

$$\frac{\partial \mu_x}{\partial \phi_k} = k_s \frac{\partial \mu_I}{\partial \phi_k} \tag{5.1.18}$$

$$\frac{\partial \mu_y}{\partial \phi_k} = k_s \frac{\partial \mu_I}{\partial \phi_k} \tag{5.1.19}$$

and

$$\frac{\partial \mu_z}{\partial \phi_k} = k_s (\frac{\mu_z}{\mu_I})^2 \frac{\partial \mu_I}{\partial \phi_k} \tag{5.1.20}$$

The term, $\partial \mu_I / \partial \phi_k$, used in the above three equations can be calculated as follows:

$$\frac{\partial \mu_I}{\partial \phi_k} = \frac{\partial \mu_I}{\partial H_I} \frac{\partial H_I}{\partial \phi_k} = \frac{\partial H_I}{\partial \phi_k} \frac{d\mu_I}{dH_I} \tag{5.1.21}$$

where, $d\mu_I / dH_I$ can be found from the cubic spline interpolation associated with the B-H curve fitting process. Furthermore, in order to obtain the value of $\partial H_I / \partial \phi_k$, one can write the following:

$$\frac{\partial H_I}{\partial \phi_k} = \frac{\partial}{\partial \phi_k} \sqrt{H_{Ix}^2 + H_{Iy}^2 + H_{Iz}^2}$$

Substituting for H_{Ix}, H_{Iy}, and H_{Iz} from Equations (5.1.13) and (5.1.16) yields

$$\begin{aligned} \frac{\partial H_I}{\partial \phi_k} &= \frac{\partial}{\partial \phi_k} \sqrt{H_{ex}^2 + H_{ey}^2 + (\frac{\mu_z}{\mu_I})^2 H_{ez}^2} \\ &= \frac{H_{ex} \frac{\partial H_{ex}}{\partial \phi_k} + H_{ey} \frac{\partial H_{ey}}{\partial \phi_k} + (\frac{\mu_z}{\mu_I} H_{ez}) \frac{\partial}{\partial \phi_k} (\frac{\mu_z}{\mu_I} H_{ez})}{H_I} \end{aligned} \tag{5.1.22}$$

where

$$\frac{\partial H_{ex}}{\partial \phi_k} = \frac{\partial}{\partial \phi_k} (-\frac{\partial \phi}{\partial x}) = -\frac{\partial}{\partial x} (\frac{\partial}{\partial \phi_k} \sum_{h=1}^{4} N_h \phi_h) = -\frac{\partial N_k}{\partial x} \tag{5.1.23}$$

$$\frac{\partial H_{ey}}{\partial \phi_k} = \frac{\partial}{\partial \phi_k} (-\frac{\partial \phi}{\partial y}) = -\frac{\partial}{\partial y} (\frac{\partial}{\partial \phi_k} \sum_{h=1}^{4} N_h \phi_h) = -\frac{\partial N_k}{\partial y} \tag{5.1.24}$$

and

$$\frac{\partial}{\partial \phi_k} (\frac{\mu_z}{\mu_I} H_{ez}) = H_{ez} \frac{\partial}{\partial \phi_k} (\frac{\mu_z}{\mu_I}) + \frac{\mu_z}{\mu_I} \frac{\partial H_{ez}}{\partial \phi_k}$$

$$= H_{ez}\frac{\partial}{\partial\phi_k}[\frac{\mu_0}{\mu_0 k_s + (1-k_s)\mu_I}] - \frac{\mu_z}{\mu_I}\frac{\partial N_k}{\partial z}$$

$$= \frac{-\mu_0(1-k_s)H_{ez}}{[\mu_0 k_s + (1-k_s)\mu_I]^2}\frac{\partial\mu_I}{\partial\phi_k} - \frac{\mu_z}{\mu_I}\frac{\partial N_k}{\partial z} \tag{5.1.25}$$

Substituting Equations (5.1.23), (5.1.24), and (5.1.25) into Equation (5.1.22), and further substituting the resultant $\partial H_I/\partial\phi_k$ of Equation (5.1.22) into Equation (5.1.21), one obtains the following:

$$\frac{\partial\mu_I}{\partial\phi_k} = -(\frac{d\mu_I}{dH_I})\frac{H_{ex}\frac{\partial N_k}{\partial x} + H_{ey}\frac{\partial N_k}{\partial y} + (\frac{\mu_z}{\mu_I})^2 H_{ez}\frac{\partial N_k}{\partial z}}{H_I}$$

$$-(\frac{d\mu_I}{dH_I})\frac{\mu_z\mu_0(1-k_s)H_{ez}^2}{\mu_I[\mu_0 k_s + (1-k_s)\mu_I]^2 H_I}(\frac{\partial\mu_I}{\partial\phi_k}) \tag{5.1.26}$$

Notice that both sides of Equation (5.1.26) contains the term $\partial\mu_I/\partial\phi_k$. Rearranging Equation (5.1.26), one obtains the explicit algorithm form for $\partial\mu_I/\partial\phi_k$ as follows:

$$\frac{\partial\mu_I}{\partial\phi_k} = -(\frac{d\mu_I}{dH_I})\frac{H_{ex}\frac{\partial N_k}{\partial x} + H_{ey}\frac{\partial N_k}{\partial y} + H_{ez}\frac{\partial N_k}{\partial z}(\frac{\mu_z}{\mu_I})^2}{H_I + \frac{(1-k_s)\mu_z^3 H_{ez}^2}{\mu_0\mu_I^3}(\frac{d\mu_I}{dH_I})} \tag{5.1.27}$$

Finally, the element equation for the Newton-Raphson iteration can be summarized using the following equations:

$$\begin{bmatrix} \frac{\partial f_1}{\partial\phi_1} & \frac{\partial f_1}{\partial\phi_2} & \frac{\partial f_1}{\partial\phi_3} & \frac{\partial f_1}{\partial\phi_4} \\ \frac{\partial f_2}{\partial\phi_1} & \frac{\partial f_2}{\partial\phi_2} & \frac{\partial f_2}{\partial\phi_3} & \frac{\partial f_2}{\partial\phi_4} \\ \frac{\partial f_3}{\partial\phi_1} & \frac{\partial f_3}{\partial\phi_2} & \frac{\partial f_3}{\partial\phi_3} & \frac{\partial f_3}{\partial\phi_4} \\ \frac{\partial f_4}{\partial\phi_1} & \frac{\partial f_4}{\partial\phi_2} & \frac{\partial f_4}{\partial\phi_3} & \frac{\partial f_4}{\partial\phi_4} \end{bmatrix} \begin{Bmatrix} \delta\phi_1 \\ \delta\phi_2 \\ \delta\phi_3 \\ \delta\phi_4 \end{Bmatrix} = \begin{Bmatrix} -\sum_{m=1}^{4} s_{1,m}(\phi_m - \Delta\phi_m) + p_1 \\ -\sum_{m=1}^{4} s_{2,m}(\phi_m - \Delta\phi_m) + p_2 \\ -\sum_{m=1}^{4} s_{3,m}(\phi_m - \Delta\phi_m) + p_3 \\ -\sum_{m=1}^{4} s_{4,m}(\phi_m - \Delta\phi_m) + p_4 \end{Bmatrix}$$

(5.1.28)

where,

$$s_{i,m} = Vol[(\mu_x \frac{\partial N_i}{\partial x}\frac{\partial N_m}{\partial x}) + (\mu_y \frac{\partial N_i}{\partial y}\frac{\partial N_m}{\partial y}) + (\mu_z \frac{\partial N_i}{\partial z}\frac{\partial N_m}{\partial z})] \tag{5.1.29}$$

$$\frac{\partial f_i}{\partial \phi_k} = Vol[(\mu_x \frac{\partial N_i}{\partial x}\frac{\partial N_k}{\partial x}) + (\mu_y \frac{\partial N_i}{\partial y}\frac{\partial N_k}{\partial y}) + (\mu_z \frac{\partial N_i}{\partial z}\frac{\partial N_k}{\partial z})]$$

$$+ Vol\frac{\partial \mu_I}{\partial \phi_k}\sum_{m=1}^{4}[k_s \frac{\partial N_i}{\partial x}\frac{\partial N_m}{\partial x} + k_s \frac{\partial N_i}{\partial y}\frac{\partial N_m}{\partial y} + (\frac{\mu_z}{\mu_I})^2 \frac{\partial N_i}{\partial z}\frac{\partial N_m}{\partial z}](\phi_m - \Delta\phi_m) \tag{5.1.30}$$

Here, $\partial\mu_I/\partial\phi_k$ is given in Equation (5.1.27), and p_i is given in Equation (4.3.21). Again, μ_I is the permeability of the iron portion of the core laminations which can be obtained from the $B-H$ curve associated with that particular iron material using H_I given in Equation (5.1.17).

The 3D-FE MSP formulation discussed above was successfully applied to the large scale nonlinear magnetic field problem in the example 14.3 kVA MLA at hand. Relaxation factors were used to avoid numerical divergence, and to improve the quality of convergence, of this Newton-Raphson method under some circumstances involving heavy magnetic saturation. This is explained in the following section.

5.2 Adaptive Relaxation Factors for the Newton-Raphson Procedure

It was found that the use of the standard MSP Newton-Raphson procedure expressed in Section 5.1 could not lead to proper convergence when heavy degrees of magnetic saturation were involved in the computation. In fact the method tended to diverge in some cases of such heavy saturation. For this reason this author found it useful to slow the corrective component of the iterative process by means of relaxation factors. These relaxation factors were applied through modifying the process of updating the permeability derivatives, $d\mu_I/dH_I$, and $\partial\mu_I/\partial\phi_k$, in each step of the MSP Newton-Raphson iteration.

In the standard MSP Newton-Raphson method, the term $d\mu_I/dH_I$ in equation

(5.1.27) is updated using the value obtained from the associated material characteristic ($B-H$ curve) of the iron at the most recently computed field intensity, H_I. This process can be written as follows:

$$(\frac{d\mu_I}{dH_I})^i = \left.\frac{d\mu_I}{dH_I}\right|_{\text{most recent}} \tag{5.2.1}$$

where $d\mu_I/dH_I|_{\text{most recent}}$ is calculated using cubic spline interpolation from the associated $B-H$ curve of the iron at H_I, and $(d\mu_I/dH_I)^i$ is the term used in Equation (5.1.27) for the i-th step of Newton-Raphson iteration. This updating process was slowed down by a relaxation factor of 0.9 applied to Equation (5.2.1), which can be expressed as follows:

$$(\frac{d\mu_I}{dH_I})^i = (1-0.9)(\frac{d\mu_I}{dH_I})^{i-1} + 0.9\left.\frac{d\mu_I}{dH_I}\right|_{\text{most recent}} \tag{5.2.2}$$

where, $(d\mu_I/dH_I)^{i-1}$ is the permeability derivative used in the (i-1)th step in the Newton-Raphson iteration. This relaxation factor was found to be useful in improving the quality of convergence of the Newton-Raphson iteration under heavy saturation conditions. That is, this relaxation factor helps a well-conditioned convergence of the results in the sense of both converged global result (stored magnetic energy) and local results (elemental magnetic field quantities).

Another type of relaxation factor was used to slow down the updating process of $\partial\mu_I/\partial\phi_k$ in the element equations. Using this relaxation factor, the term in an element of the Jacobian matrix, $\partial f_i/\partial\phi_k$, which was given by Equation (5.1.30), can be rewritten as follows:

$$\frac{\partial f_i}{\partial\phi_k} = Vol[(\mu_x\frac{\partial N_i}{\partial x}\frac{\partial N_k}{\partial x}) + (\mu_y\frac{\partial N_i}{\partial y}\frac{\partial N_k}{\partial y}) + (\mu_z\frac{\partial N_i}{\partial z}\frac{\partial N_k}{\partial z})]+$$

$$(\beta)Vol\frac{\partial\mu_I}{\partial\phi_k}\sum_{m=1}^{4}[k_s\frac{\partial N_i}{\partial x}\frac{\partial N_m}{\partial x} + k_s\frac{\partial N_i}{\partial y}\frac{\partial N_m}{\partial y} + (\frac{\mu_z}{\mu_I})^2\frac{\partial N_i}{\partial z}\frac{\partial N_m}{\partial z}](\phi_m - \Delta\phi_m) \tag{5.2.3}$$

where β is the relaxation factor. The value of β used in the above equation is calculated on an element by element basis, and depends on the normalized change of elemental permeability in the latest Newton-Raphson iteration steps. That is, a

higher value of β is chosen for the element where only a small change in elemental permeability occurred in the last iteration step, while a lower value of β is chosen for the element where a bigger change in elemental permeability occurred in the last iteration step. Hence these factors are referred to in this dissertation as adaptive relaxation factors. The adaptive relaxation factors were calculated using the following equations, which are functions of the change in the permeability, $\Delta\mu_e$, in relation to an adaptive iterative factor, α ($0 \leq \alpha \leq 1$), which is explained later on in this section:

$$\left.\begin{array}{lll} \beta = 1 & for & \Delta\mu_e < \alpha \\ \beta = (\dfrac{1-\Delta\mu_e}{1-\alpha})^2 & for & \alpha \leq \Delta\mu_e \leq 1 \\ \beta = 0 & for & \Delta\mu_e > 1 \end{array}\right\} \quad for \quad 0 \leq \alpha < 1 \tag{5.2.4}$$

and

$$\beta = 1 \qquad for \quad \alpha = 1 \tag{5.2.5}$$

In Equation (5.2.4) $\Delta\mu_e$ is the normalized change of elemental permeability in the latest iterations. $\Delta\mu_e$ can be calculated as follows:

$$\Delta\mu_e = \frac{|\mu_e^i - \mu_e^{i-1}|}{0.5(\mu_e^i + \mu_e^{i-1})} \tag{5.2.6}$$

where μ_e^i and μ_e^{i-1} are the material permeabilities for the element e obtained from the latest two (i-th and (i-1)th) iterations. In Equations (5.2.4) and (5.2.5), α is an adaptive iterative factor which allows one to adjust the calculation of the adaptive relaxation factor, β, under different saturation conditions. The relationship between β and $\Delta\mu_e$, with respect to the adaptive iterative factor, α, which was expressed by Equation (5.2.4), is shown by curves in Figure (5.2.1). The adaptive iterative factor, α, can be chosen between one and zero.

When α is chosen to be one, the adaptive relaxation factor, β, from Equation (5.2.5) is always equal to unity for any $\Delta\mu_e$. In this case, the iteration process is a standard Newton-Raphson procedure as derived in Section 5.1. When α is chosen to be less than one, the adaptive relaxation factor, β, from Equation (5.2.4) becomes equal to unity, or a value in between one and zero, depending on the most recent

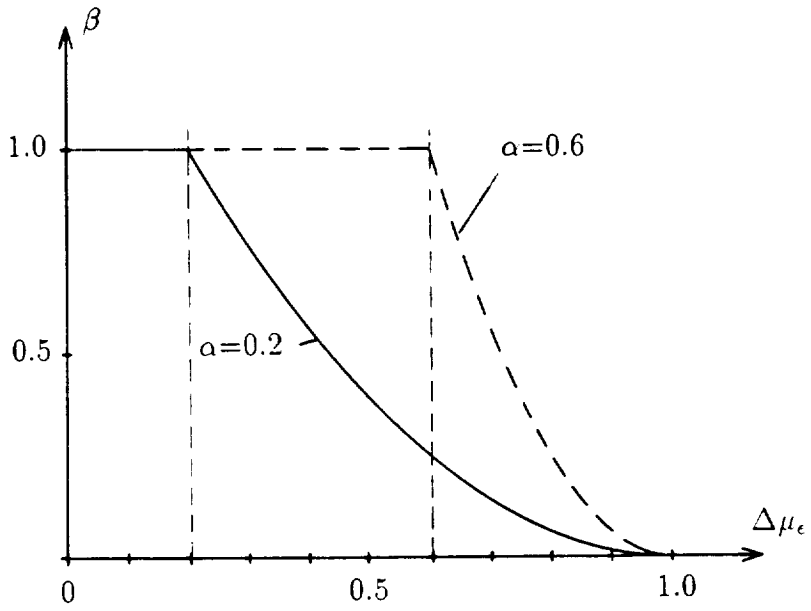

Figure (5.2.1) Adaptive Relaxation Factor, β, and Adaptive Iterative Factor, α.

change of elemental permeability. Thus a deliberate slowing down in the rate of change of $\partial\mu_I/\partial\phi_k$ is achieved in this case, which successfully avoids possible divergence that could take place in the Newton-Raphson iterative process. From this author's experience, the adaptive relaxation factors improved the stability of the convergence of the Newton-Raphson procedure without adversely affecting the convergence speed in any significant manner. The most appropriate value for the adaptive iterative factor, α, for a lightly saturated problem was found to be between 1.0 and 0.9. While for a heavily saturated problem, a value of α between 0.2 and 0.1 is suggested.

Table (5.2.1) shows some example cases of nonlinear magnetic field computations for the 14.3 kVA modified Lundell alternator. The total number of elements in these examples is 113,660, and the total number of unknowns is 20,112. The first case shown in Table (5.2.1) is a no-load, rated terminal voltage case with a total field excitation of 980 AT. In this case only a moderate saturation condition is expected in the main magnetic circuit path of the MLA. One can observe that the adaptive iterative factor, α, can be chosen to be equal to unity, which means that one is using the standard Newton-Raphson iteration, and one obtains a very fast convergence. The second case is a no-load condition with a total field excitation of 3000 AT, which is nearly three times as high an excitation as the rated field mmf in the first case. Under this field excitation, the main magnetic circuit of the MLA is driven into very heavy saturation. One can see that the standard Newton-Raphson procedure did not converge under this condition. However, using the adaptive relaxation factors with an adaptive iterative factor of 0.5, one obtains a fast and stable convergence. The third example shown in Table (5.2.1) is the rated load case with a field excitation equal to 2300 AT. In this load case, both the field winding and the three phase armature windings were carrying currents, and the airgap flux density distribution is distorted by the armature reaction. In such a case extremely heavy saturation occurs in the portions of the stator teeth area near the trailing side of the airgap flux density distribution. As one can see from Table (5.2.1), under this condition the adaptive iterative factor, α, should be chosen to be between 0.2 and 0.1.

In the above examples, two convergence test criteria were used to check whether the iterative process approaches the correct answer or not. The first criterion is based on the change of the computed total magnetic energy from two consecutive Newton-Raphson iteration steps. This change of total magnetic energy was computed as a

Table (5.2.1): Number of Iterations of the Newton-Raphson Method in the Magnetic Field Problems of the 14.3 kVA MLA

Case	Adaptive Iterative Factor			
	$\alpha = 1.0$	$\alpha = 0.5$	$\alpha = 0.2$	$\alpha = 0.1$
No-Load (I_f=980 AT)	7	8	9	12
No-Load (I_f=3000AT)	Diverged	14	18	21
Rated-Load (I_f=2300AT)	Diverged	Diverged	17	19
Energy Tolerance: $\Delta W = 10^{-5}$ Per Unit Permeability Tolerance: $\Delta\mu = 10^{-2}$				

normalized quantity, ΔW^i, as follows:

$$\Delta W^i = \frac{|W^i - W^{i-1}|}{0.5(W^i + W^{i-1})} \qquad \text{per unit} \tag{5.2.7}$$

where W^i is the total magnetic energy computed from the i-th step of the iteration, and W^{i-1} is the total magnetic energy computed from the (i-1)th step of the iteration. The second convergence criterion is based on the computed maximum change of the elemental permeabilities between two consecutive Newton-Raphson iterations. This maximum permeability change is computed as a normalized quantity, $\Delta\mu^i$, expressed as follows:

$$\Delta\mu^i = \max_{e=1,2,\ldots} \left\{ \frac{|\mu_e^i - \mu_e^{i-1}|}{0.5(\mu_e^i + \mu_e^{i-1})} \right\} \tag{5.2.8}$$

where μ_e^i and μ_e^{i-1} are the material permeabilities for the element e obtained during the i-th and (i-1)th iterations. When both of these changes, ΔW^i and $\Delta\mu^i$, become sufficiently low, that is well within the given tolerance values, the iteration is brought to an end. The second convergence criterion is important, because it has been found that in some heavy saturation cases the computed total energy seemed to cease changing while the computed flux densities and the associated permeabilities in some local elements were diverging. Simultaneous use of these two convergence criteria guarantees that one obtains the results from a well converged solution. In the example computations shown in Table (5.2.1) both energy type convergence and permeability type convergence tolerances were set to very small numbers of 1×10^{-5} and 1×10^{-2} per unit respectively. This indicates that excellent convergences have been reached in all these computation examples. Results of the application of the Newton-Raphson method to the modified Lundell alternator under different operating conditions are given in later chapters.

Chapter 6

The 3D Finite Element Grid for the 14.3 kVA Modified Lundell Alternator

In order to compute the magnetostatic field distribution throughout the magnetic circuit of an MLA, using the combined MVP-MSP method explained in previous chapters, one must develop a discretization of the global solution volume, into a suitable 3D-FE global grid. Such a 3D-FE grid was developed in this research for the example 4-pole, 14.3 kVA MLA. Details on the geometry dimensions and design data of this machine were given earlier in Chapter 1.

Because of the repetitive pattern of the geometry and excitation current distribution in every pair of poles of this class of machines, the 3D space which covers a span of a pair of poles in the MLA was chosen as the global magnetic field solution region. Two 3D-FE grids were generated separately to cover the stator portion of the global grid geometry, as well as the rotor portion of the global grid geometry. The stator 3D-FE grid and the rotor 3D-FE grid can be connected at any desired rotor position to form a global 3D-FE grid. In this chapter, some basic techniques used in the 3D-FE grid generation are explained. The resultant 3D-FE grids for the example 14.3 kVA MLA are presented.

6.1 Basic Techniques for the 3D-FE Grid Generation

The basic building block used in the 3D-FE grid for the combined MVP-MSP method is the tetrahedral element. The choice of the tetrahedral element is based on the flex-

ibility of this type of element in handling very complicated geometry and material topology associated with the MLAs under consideration. However, it is not convenient to directly handle tetrahedral elements to generate 3D-FE grids because of the difficulty in visualization and computer implementation for these elements in forming FE grids to cover a specified 3D volume. The complex nature of the machine geometry of the MLA, such as the armature winding end turn region, as well as the difficult geometries of the interfaces between the magnetic poles and the non-magnetic separator of the bimetallic rotor, adds substantial difficulties to this discretization work.

Two types of techniques have been used to assist in the generation of the 3D-FE grids. In one of these techniques, one uses triangular prisms as super-elements to build up 3D-FE grids for some portions of the machine. The second technique, which will be called the tetrahedral element filling technique, was developed to handle very difficult grid geometries. In this filling technique one divides a space into a number of straps (bars or toroids) with triangular cross-sections, each strap is then filled by tetrahedral elements one by one, for one strap after another, see Figure (6.1.1) for a schematic demonstration. These two techniques are further detailed in the following subsections.

6.1.1 Triangular Prism Super-Elements

As an aid in constructing the 3D-FE gridding for covering some portions of the machine geometry, triangular prisms are used as super-elements to help discretize the 3D volume for the first step in the generation of the 3D-FE tetrahedral gird. Each of these triangular prisms is then subdivided into three tetrahedrons to complete the grid topology. There are two basic ways to divide a triangular prism into three tetrahedrons, as shown in Figure (6.1.2). Alternately using these two types of super-elements makes it possible to avoid crossing of edges of tetrahedrons from two super-elements, which might happen at the interfaces, and which must not take place in a 3D FE grid. A triangular prism can be itself a finite element. However, because of the restrictions on geometric shapes which are amenable to discretization by prism geometry, the triangular prisms are only used for assisting in the generation of the tetrahedral type FE grids for some portions of the MLA geometry. Nevertheless, the final grid model used in this work of 3D-FE magnetic field computation is totally based on tetrahedrons.

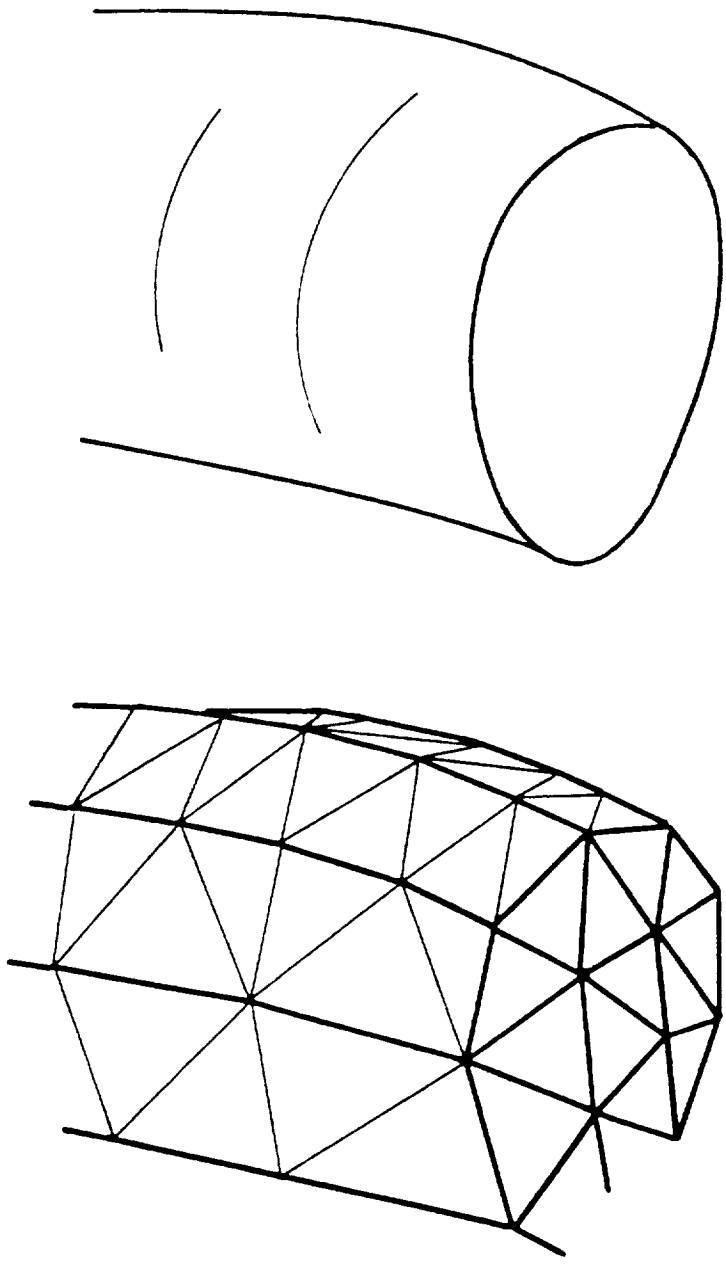

Figure (6.1.1) Tetrahedral Element Filling Technique

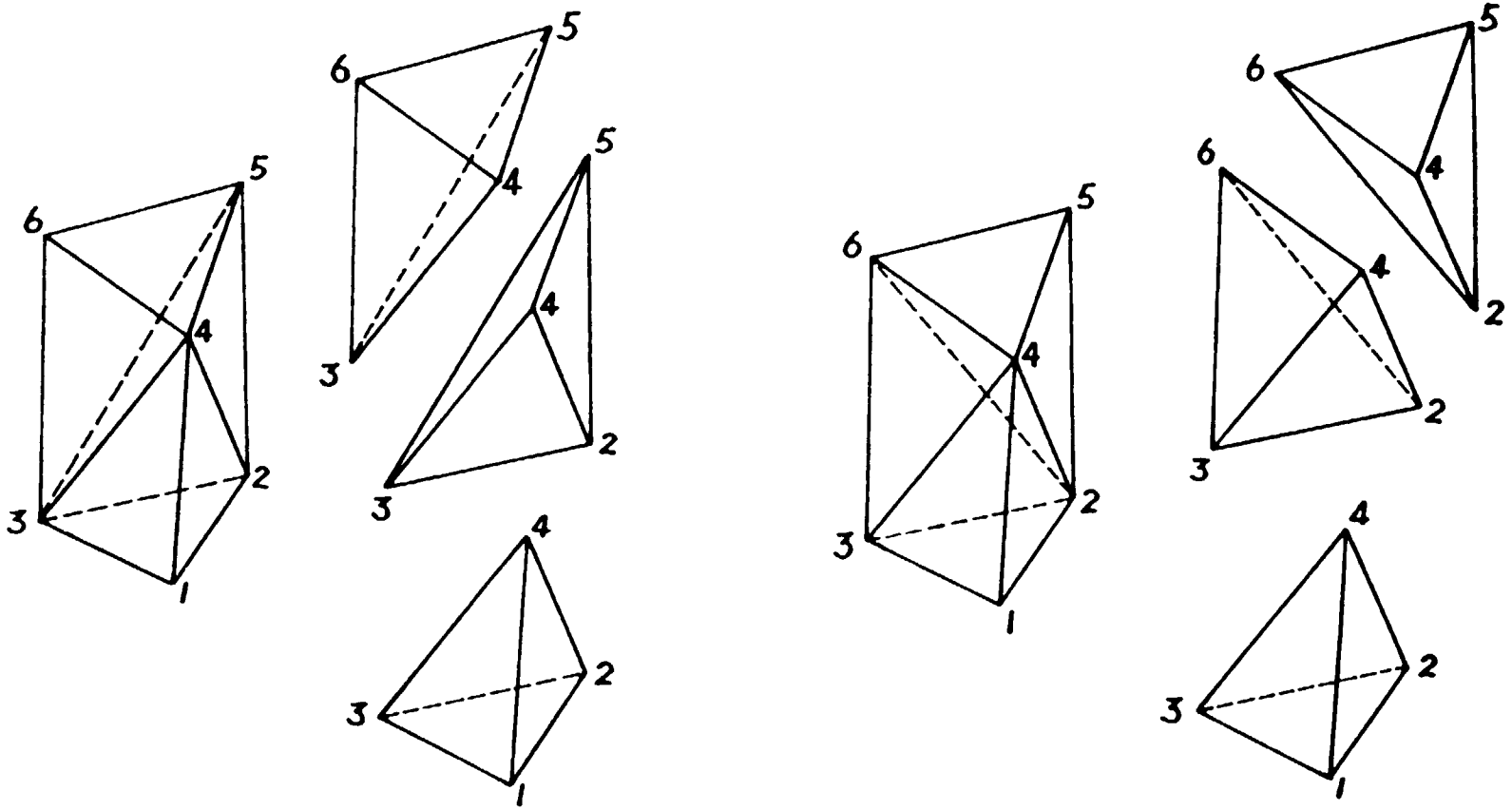

Figure (6.1.2) A Triangular Prism Super-Element Break Down to Tetrahedrons

Using a triangular prism or even considering two triangular prisms forming one hexahedral block as a super-element, is a very efficient and convenient way to construct the necessary 3D-FE grids. Many machine parts such as the field coils, the housing, and the rotor shaft, can be easily discretized using triangular prisms. However, there are some circumstances in which the triangular prism super-elements are not suitable. For example, when elements must be filled into a gap between two machine parts, where the two surfaces of the gap have different surface triangular patterns, the method of triangular prism super-elements will not work. Thus a filling technique must be developed to tackle such difficulties.

6.1.2 The Tetrahedral Element Filling Technique

The main idea of this tetrahedral element filling technique is that one can fill tetrahedrons one after another into a triangular strap (a bar or toroid with triangular cross-section) when two side walls (or surfaces) of this strap have been already discretized into triangular grids. After this strap is fully filled with tetrahedrons, the third side wall of this strap is automatically in a pattern of a triangular surface grid, which will be in turn used to determine the tetrahedral element filling manner of the adjacent strap. The following is an example of the application of this tetrahedral element filling technique.

Consider Figure (6.1.3), a gap between two surfaces, with fixed surface triangular grids on each, is to be filled with tetrahedral elements. In order to apply the filling process, the space of the gap is separated into five straps as shown in the lower part of Figure (6.1.3). Notice that each of the straps has one of its three side walls (surfaces) with a given set of surface triangles. Meanwhile, the side wall, S_1, of the first strap has to be discretized into a suitable set of triangles before the element filling process starts, see (a) of Figure (6.1.4).

The strap, 1, in Figure (6.1.3), is first put through the tetrahedral element filling process. At the end of the this filling process a surface triangular grid will have been established on the third wall (surface), S_3, of the first strap (bar), see (a) of Figure (6.1.4). This side wall, S_3, is the interface between the first strap (bar), 1, and the second strap (bar), 2, see Figure (6.1.3). Thus, after the filling process for the first strap is finished, the second strap will have been ready with surface triangular grids on two of its three side walls. The second strap can be then put through the same

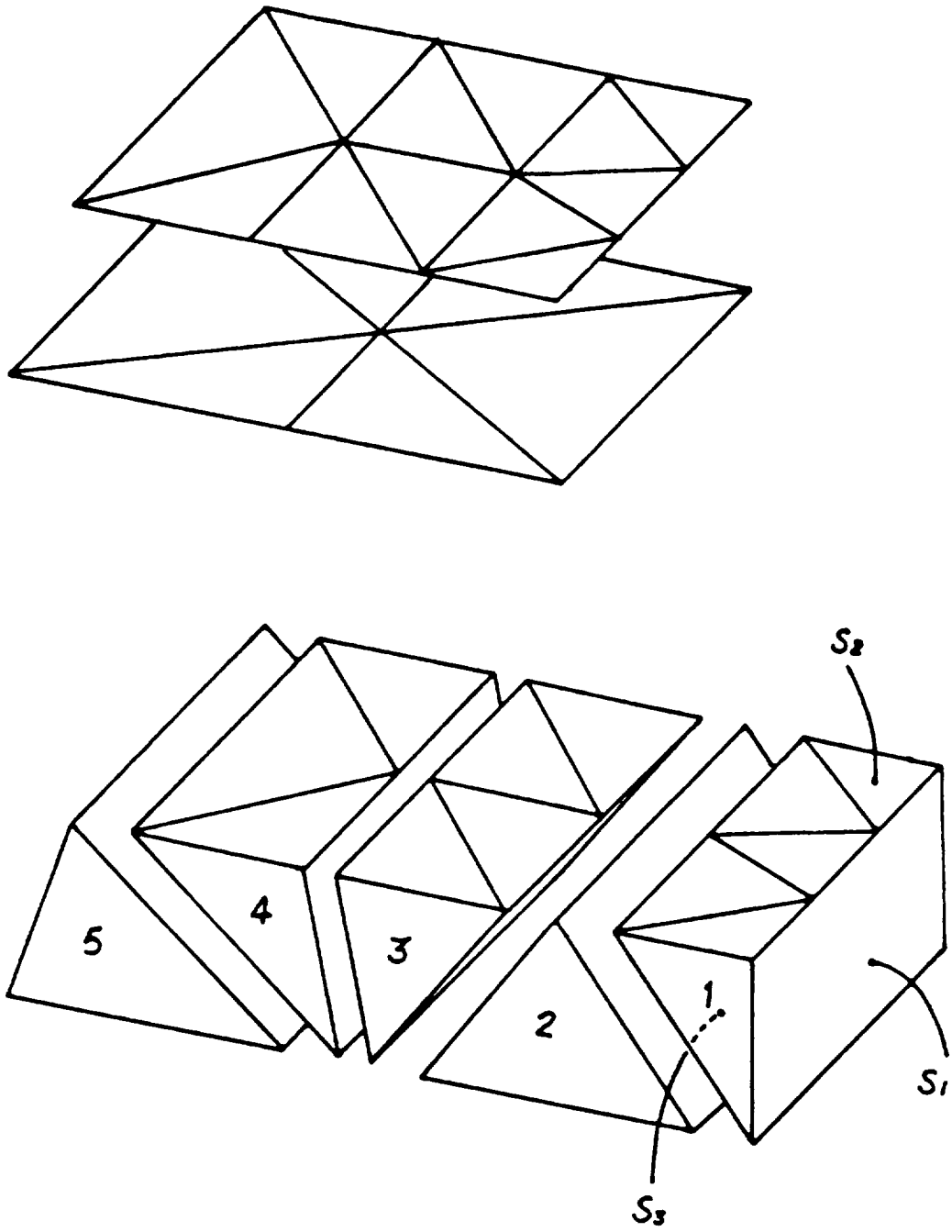

Figure (6.1.3) An Example Application of the Element Filling Technique to a Gap Between Surfaces

filling process as used for the first strap. Similarly, the third, the fourth, and the fifth straps (bars), Figure (6.1.3), can be filled with tetrahedral elements by sequential application of the above procedure in a chain manner. The resulting grid which fills the gap of Figure (6.1.3) with tetrahedral elements is shown in Figure (6.1.4).

Next, consider the first strap (bar) in Figure (6.1.3) as an example to demonstrate how a tetrahedral grid is computer generated to fill the bar volume under consideration. Let one imagine that this strap is now put in an upright position as shown in Figure (6.1.5), graphs (1) through (3), for the convenience of visualization. The front side wall (surface) with nodes 1, 7, 8, 9, and 2, see graph (2) of Figure (6.1.5), is the wall without a given triangular grid. Each tetrahedron will be generated by a sequential procedure which can be best summarized as follows:

(1) Chose a triangular base for the tetrahedron,

(2) Find a new node as the fourth vertex of the tetrahedron,

(3) Link the new node to each vertex on the base to complete a tetrahedron.

Applying the three steps given above, the triangle with nodes 1, 7, and 3, designated by (1,7,3,1), see graph (3) in Figure (6.1.5), is chosen as the base for the first tetrahedron. A searching process is then carried out, which shows that triangle (1,3,4,1) and triangle (3,7,4,3), graph (3) in Figure (6.1.5), share edges 1-3, and 3-7, with the triangular base (1,7,3,1), respectively. From this information, only node 4 is eligible to be the new vertex of the tetrahedron being formed. Accordingly, nodes 1, 7, 3, and 4, make the first tetrahedral element {1,7,3,4}, as shown in graph (4), Figure (6.1.5). After this tetrahedral element is made, node 4 takes place of node 3 to make a new triangular base (1,7,4,1) for the second tetrahedron under formation.

Repeating the same searching process as explained above for the first tetrahedron, triangle (1,4,2,1) and triangle (4,7,8,4) are found to share edges, 1-4, and 4-7, with the base triangle (1,7,4,1) being currently considered, respectively. Under this condition, either node 2 or node 8 can be taken as the new vertex of the second tetrahedral element. A criterion has to be developed to decide which node should be chosen to yield a resulting tetrahedral element with the least possible 3D geometry ill-conditioning. The criterion established here can best be adhered to using the following concept: choose one node among these two candidate nodes such that the edge appearing on the front wall, 1-7-8-9-2-1, will be the shortest. Thus node 8 is chosen as the new vertex, because the distance from node 1 to node 8 is shorter than

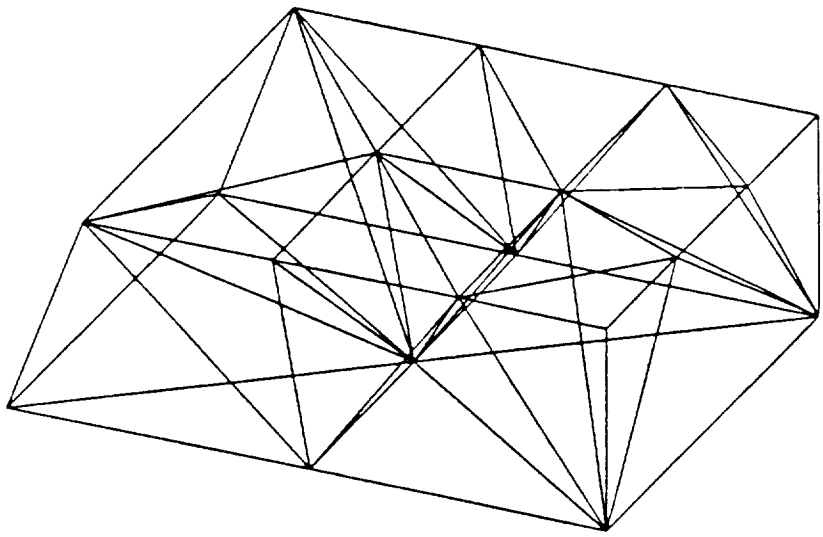

Figure (6.1.4) The FE Grid for the Gap Example in Figure (6.1.3)

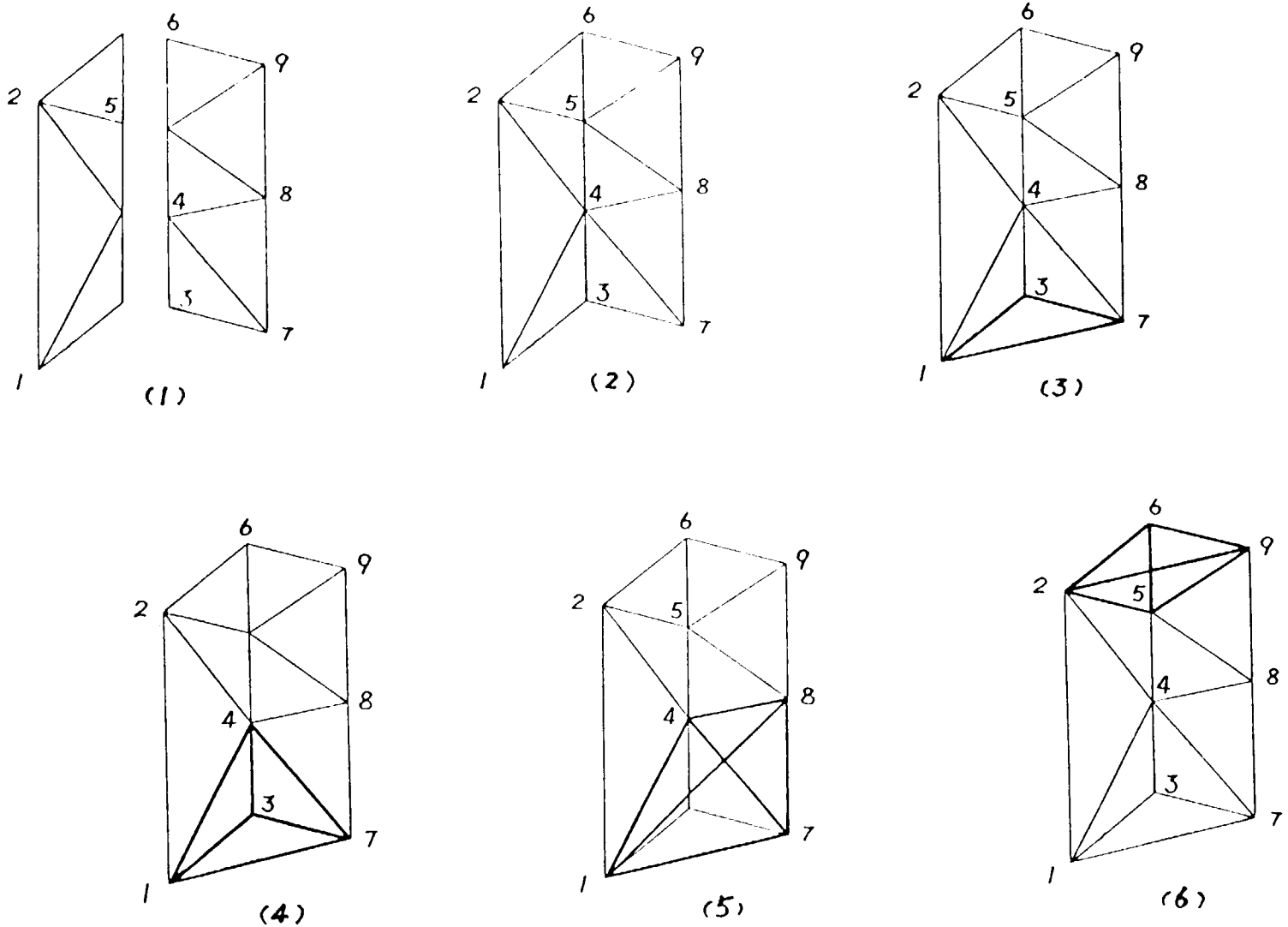

Figure (6.1.5) Triangular Bar Discretization into Tetrahedrons

the distance from node 7 to node 2. After linking node 8 to the three vertices on the triangular base, (1,7,4,1), an edge emanating form node 8 to node 1, as well as a triangle with nodes 1, 7, and 8, appear on the front wall of the strap, see graph (5) in Figure (6.1.5).

Now, the triangle (1,8,4,1) can be chosen as the new base for the third tetrahedron to continue the tetrahedral element filling process. In this process one repeats the above mentioned procedure as many times until the last tetrahedron {2,9,5,6} with nodes 2, 9, 5, and 6, at the top of the strap is completed, see graph (6) in Figure (6.1.5). It should be pointed out that the aforementioned search process to find candidates for the new vertex of each new tetrahedron has to be carefully formulated in such a manner that no edges of any tetrahedrons generated in the grid ever intersect. Figure (6.1.6) shows a view of the finished tetrahedral grid filling the strap.

This tetrahedral element filling technique, in corporated with the triangular prism super-elements, was successfully used to generate the 3D-FE grids for the MLA at hand. The whole grid structure was developed first by separately building several small grid modules using super-elements, then connecting the modules together using this filling technique. Also, the tetrahedral element filling technique has been found to be very useful in connecting the stator grid and the rotor grid to complete a global tetrahedral 3D-FE grid for the computation of magnetic fields in the MLA.

6.2 The 3D-FE Grid of the Stator

The stator 3D-FE grid of the MLA was developed for the example 4-pole, 14.3 kVA MLA in a modular fashion. The key FE stator grid module is a discretization into tetrahedral finite elements of a stator slot pitch which extends from the mid cross-sectional plane to one of the end-bells, see Figure (6.2.1). This module includes one armature end region and one field coil, in addition to the outer casing and borders the rotor in both the main and auxiliary airgaps, as shown in Figure (6.2.1).

Circumferential repetition of this stator slot module and mirror imaging yields the 3D-FE grid of the stator portion in the global solution volume. The resulting outer surface view of this stator 3D-FE grid is shown in Figure (6.2.2). Meanwhile the surface FE discretization of the inner boundary of the stator grid facing the rotor is shown in Figure (6.2.3). Notice, this is a 36 slot stator, thus only 18 slots pitch

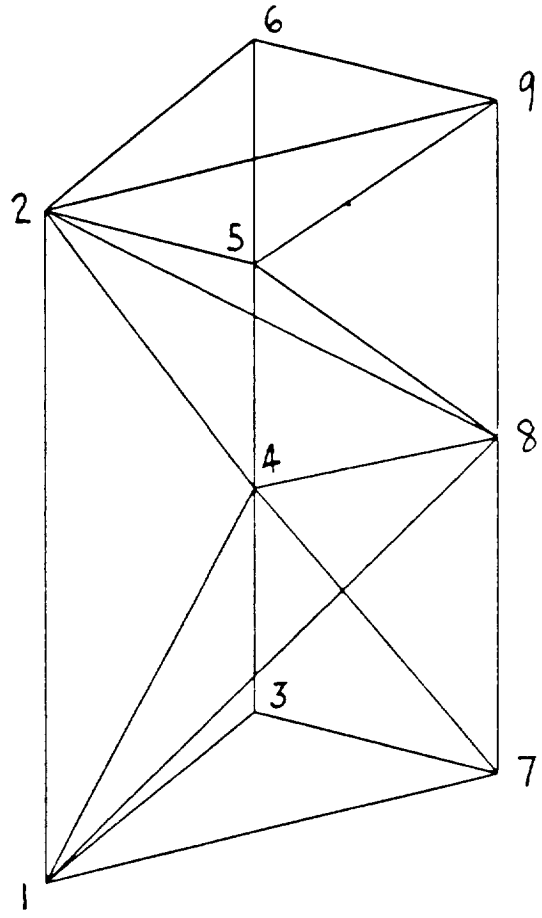

Figure (6.1.6) The FE grid Generated Using the Tetrahedral Element Filling Technique

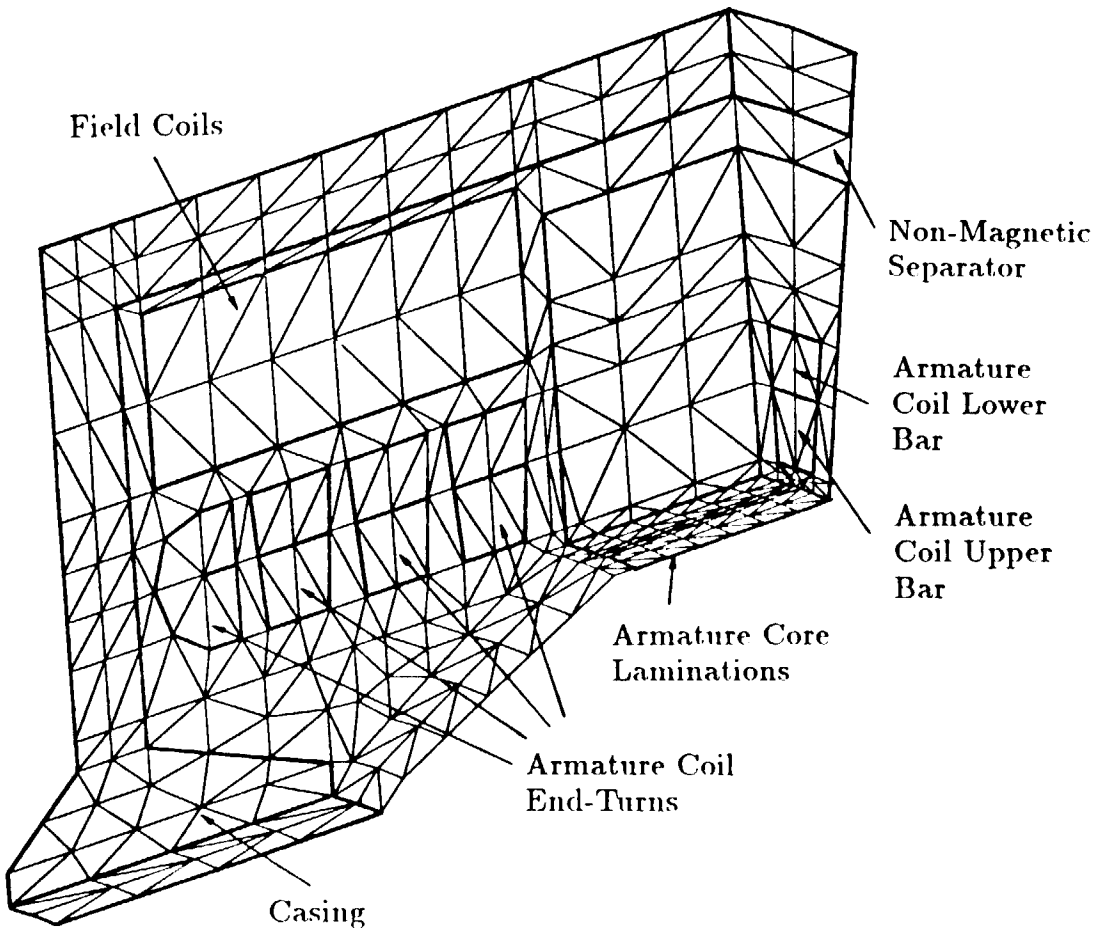

Figure (6.2.1) Tetrahedral 3D-FE Grid of a Stator Slot Module

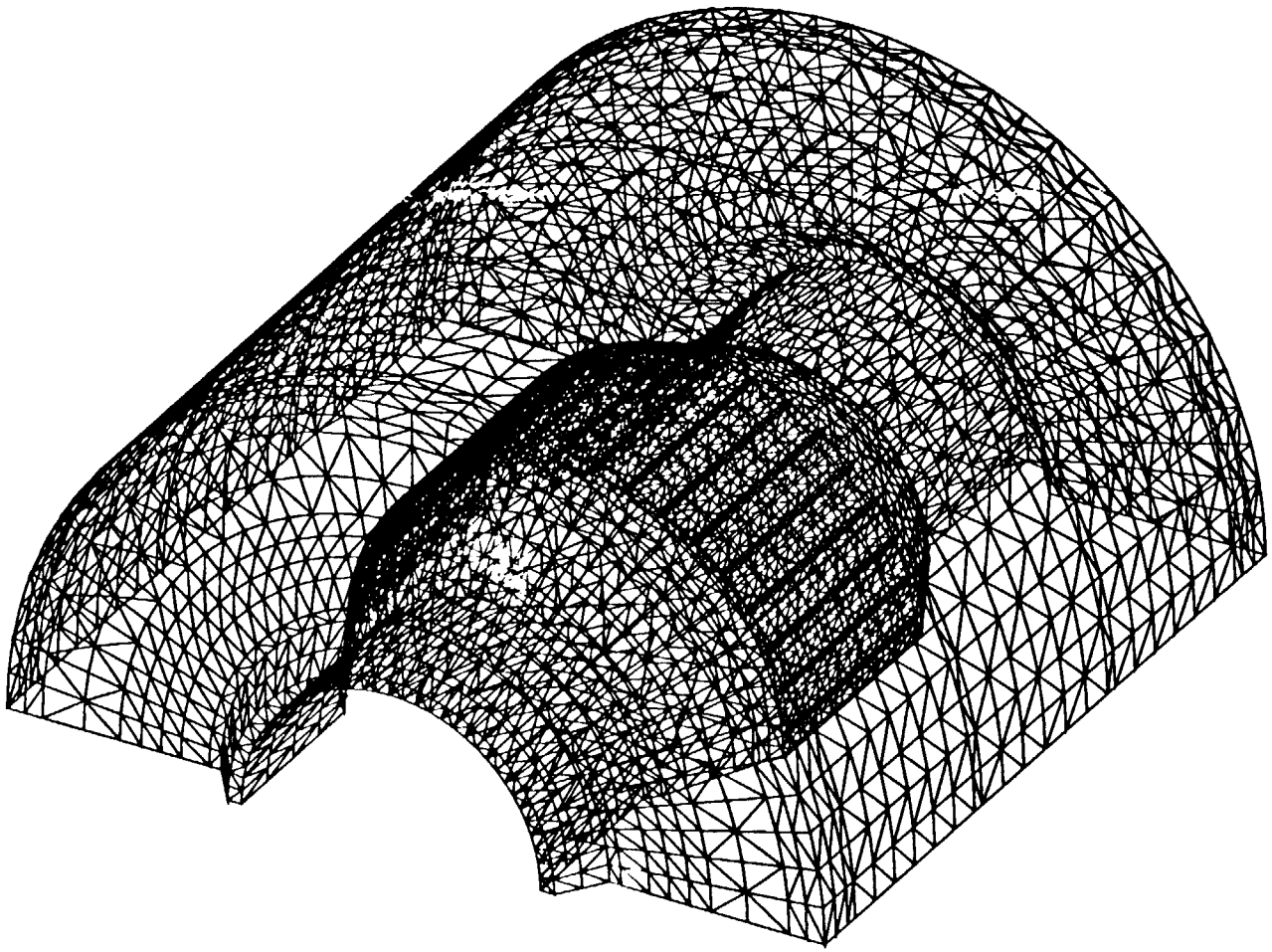

Figure (6.2.2) An Outer Surface View of the Stator 3D-FE Grid

imprints are shown in the FE surface pattern of Figure (6.2.3)

In order to further illustrate the complexity of the stator's 3D-FE grid, an outer view of the surfaces of the FE discretization of the stator core is shown in Figure (6.2.4). Furthermore, Figure (6.2.5) shows the complete 3D-FE discretization of an armature coil, while Figure (6.2.6) illustrates the nature of the end turn 3D-FE layout. Meanwhile, Figure (6.2.7) illustrates the embedding of the armature coils in the stator core. In addition, Figure (6.2.8) shows the outer surface of the 3D-FE discretization of the ring-shaped field coils.

Furthermore, Figure (6.2.9) and (6.2.10) show by vector arrows the directions of current flow (current density vector) in the 3D-FE discretization of an armature coil and the field coils, respectively. Finally, an outer view of the 3D-FE discretization of the casing of the MLA, from the bottom side of the stator gird shown in Figure (6.2.2), is shown in Figure (6.2.11)

6.3 The 3D-FE Grid of the Rotor

The 3D-FE grid module of the rotor was conceived in the form of one octant of the 4-pole rotor of the example 14.3 kVA MLA, whose outer FE grid surface facing the viewer is shown in Figure (6.3.1). This one octant module was mirror imaged and rotated to form the rotor grid covering a two-pole pitch span of the 4-pole rotor, as shown in the outer surface view of Figure (6.3.2). Figure (6.3.3) illustrates the 3D-FE grid structure in one of the rotor magnetic portions in the rotor grid span. Notice the narrowing nature of the pole arc on the surface from one end of the pole face to the other. Meanwhile, the 3D-FE discretization covering the two magnetic portions of the rotor in the rotor grid span is shown in Figure (6.3.4).

6.4 Element Filling in Between Stator and Rotor Grids - Global 3D-FE Grid

The 3D-FE stator and rotor grid were interfaced along the inner-most and outer-most boundary surfaces of the two grids, respectively. That is, the interfacing takes place in the main airgap, end-turn regions, and two auxiliary airgaps, respectively. This

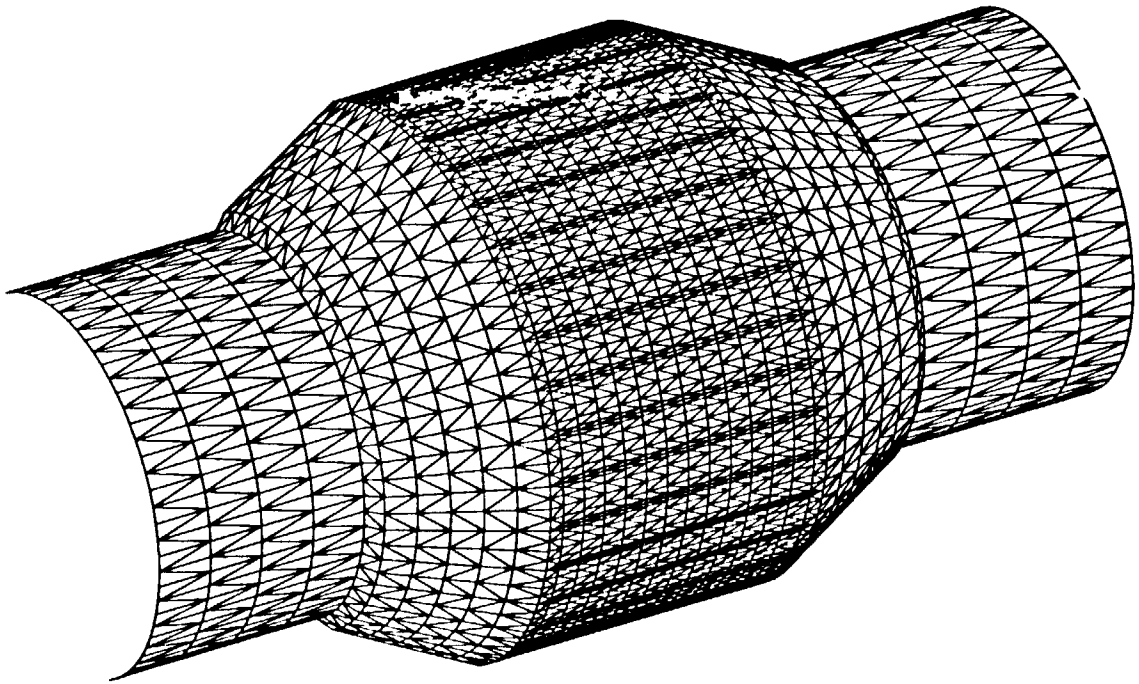

Figure (6.2.3) Surface FE Discretization of the Inner Boundary of the Stator

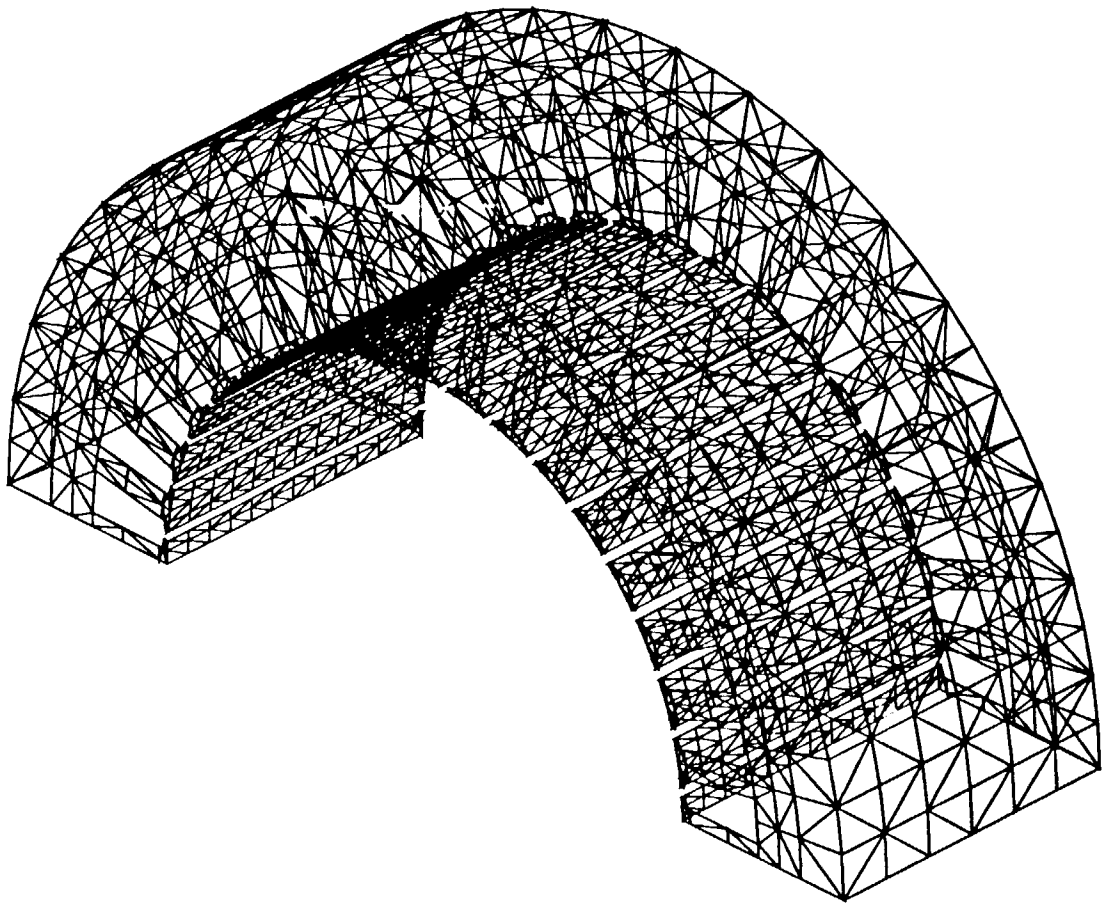

Figure (6.2.4) An Outer View of the 3D-FE Grid of Stator Core Laminations

Figure (6.2.5) 3D-FE Discretization of an Armature Coil

Figure (6.2.6) Armature Coil End Turn Layout

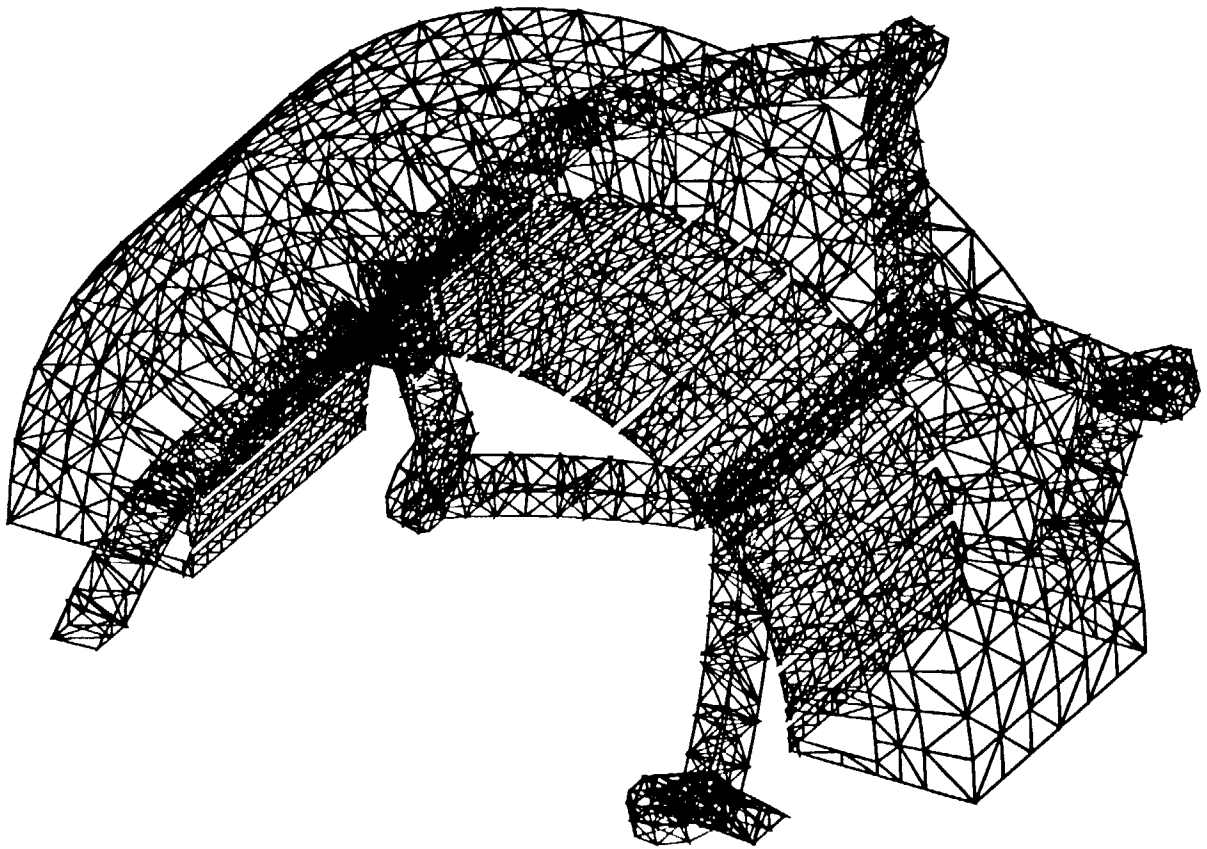

Figure (6.2.7) Embedding of the Armature Coils in the Stator Core

Figure (6.2.8) 3D-FE Grids of the Ring-Shaped Field Coils

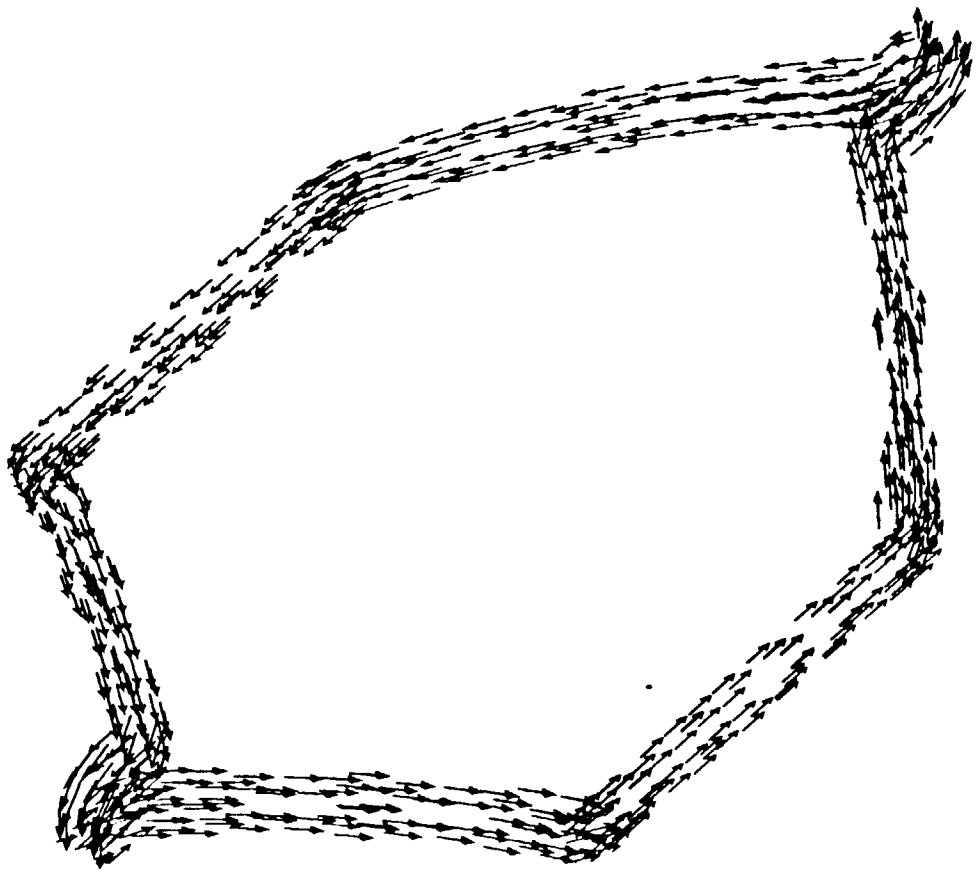

Figure (6.2.9) Electric Current Flow in 3D-FE Discretization of an Amarture Coil

Figure (6.2.10) Electric Current Flow in 3D-FE Discretization of Field Coils

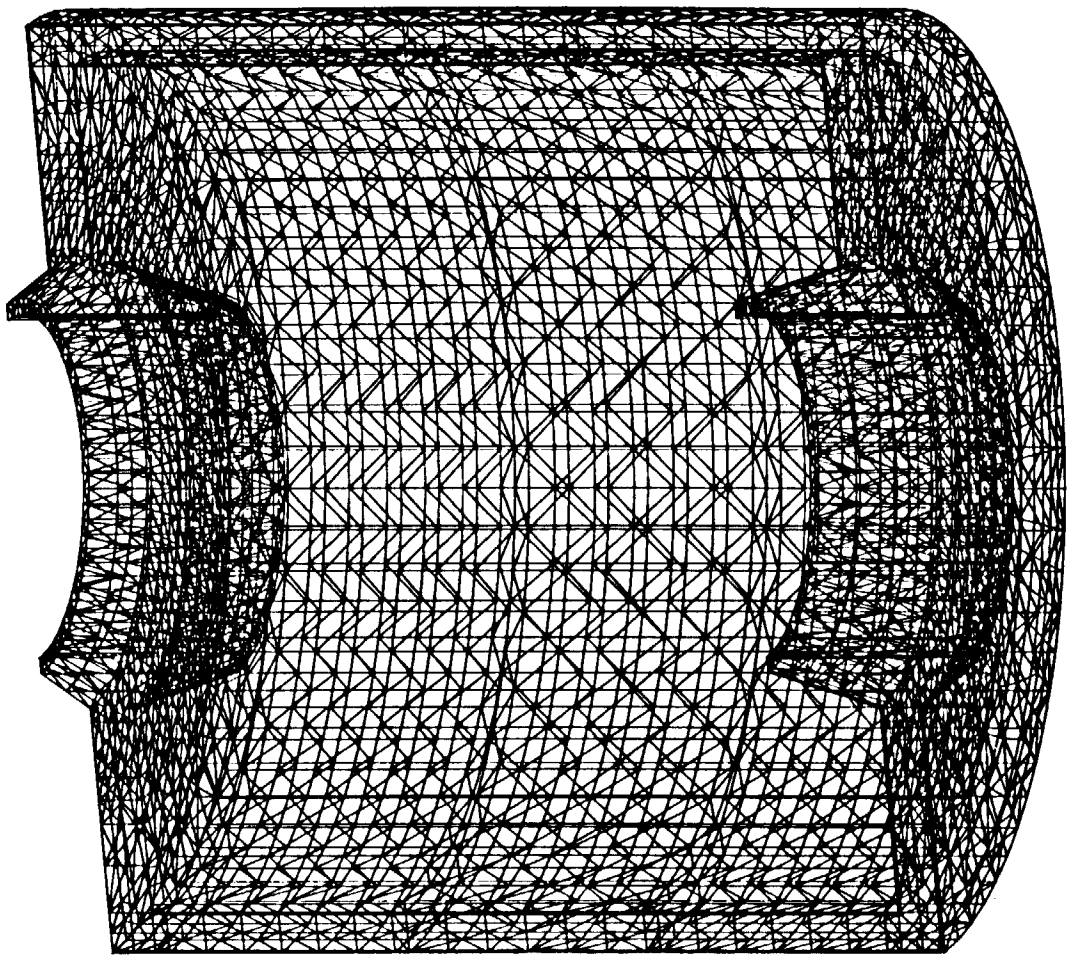

Figure (6.2.11) An Outer View of the 3D-FE Grid in the Casing of the MLA

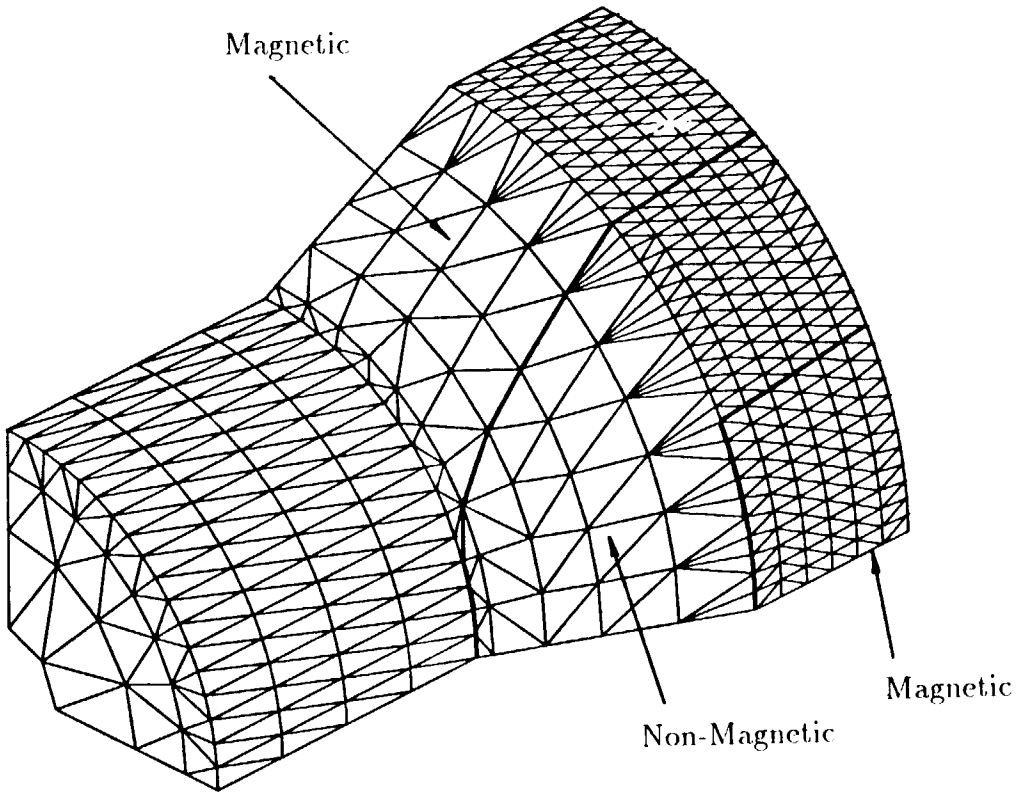

Figure (6.3.1) A Surface View of the Rotor 3D-FE Grid Module in One Octant

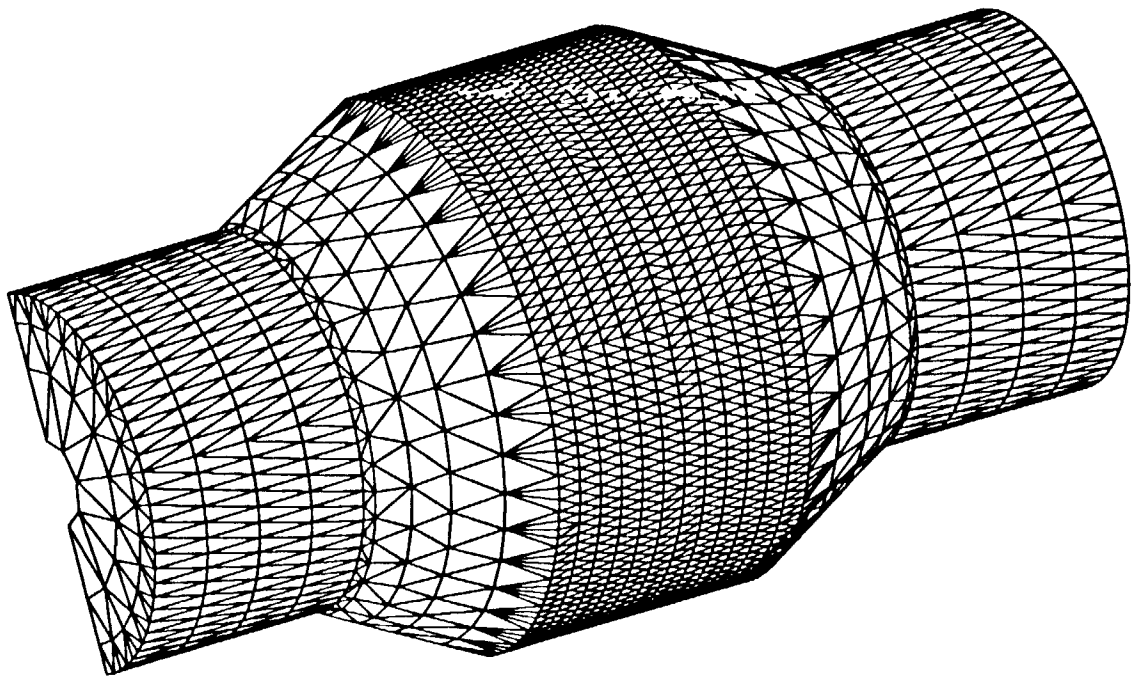

Figure (6.3.2) Outer Surface View of the Rotor 3D-FE Grid

Figure (6.3.3) 3D-FE Grid Structure in One of the Rotor Magnetic Portions

Figure (6.3.4) 3D-FE Grid Structure in Rotor Magnetic Portions

interfacing process leads to a layer of 3D finite elements which links the two grids. The 3D-FE gridding algorithm was developed in such a way that the interfacing can be carried out at all relative stator to rotor positions covering half an ac cycle, that is π electrical radians (180° electrical).

The inner-most boundary surface of the stator 3D-FE grid and the outer-most boundary surface of the rotor 3D-FE grid can be observed in Figures (6.2.3) and (6.3.2). Notice that the surface discretization patterns of the stator grid and the rotor grid are different. The tetrahedral element filling technique described in Section 6.1 was used to connect these two grids together by filling tetrahedral elements into the gap in between these two grids.

Examples of global 3D-FE grid, corresponding to two different rotor to stator relative positions are shown in Figures (6.4.1) and (6.4.2). Mid-plane cross-sectional views of the FE grid corresponding to the 3D-FE grids of Figure (6.4.1) and (6.4.2) are shown in Figures (6.4.3) and (6.4.4). In addition, a planar gridding view of the bottom of the 3D-FE gridding of the global solution volume is given in Figure (6.4.5).

The resultant global 3D-FE grid for the example 14.3 kVA MLA contains 113,660 element and approximately 20,600 grid nodes. The combined MVP-MSP solution method was carried out using this global 3D-FE gird to compute the magnetic fields at various rotor to stator positions and various current excitation conditions.

Figure (6.4.1) Global 3D-FE Grid at Rotor Position (1)

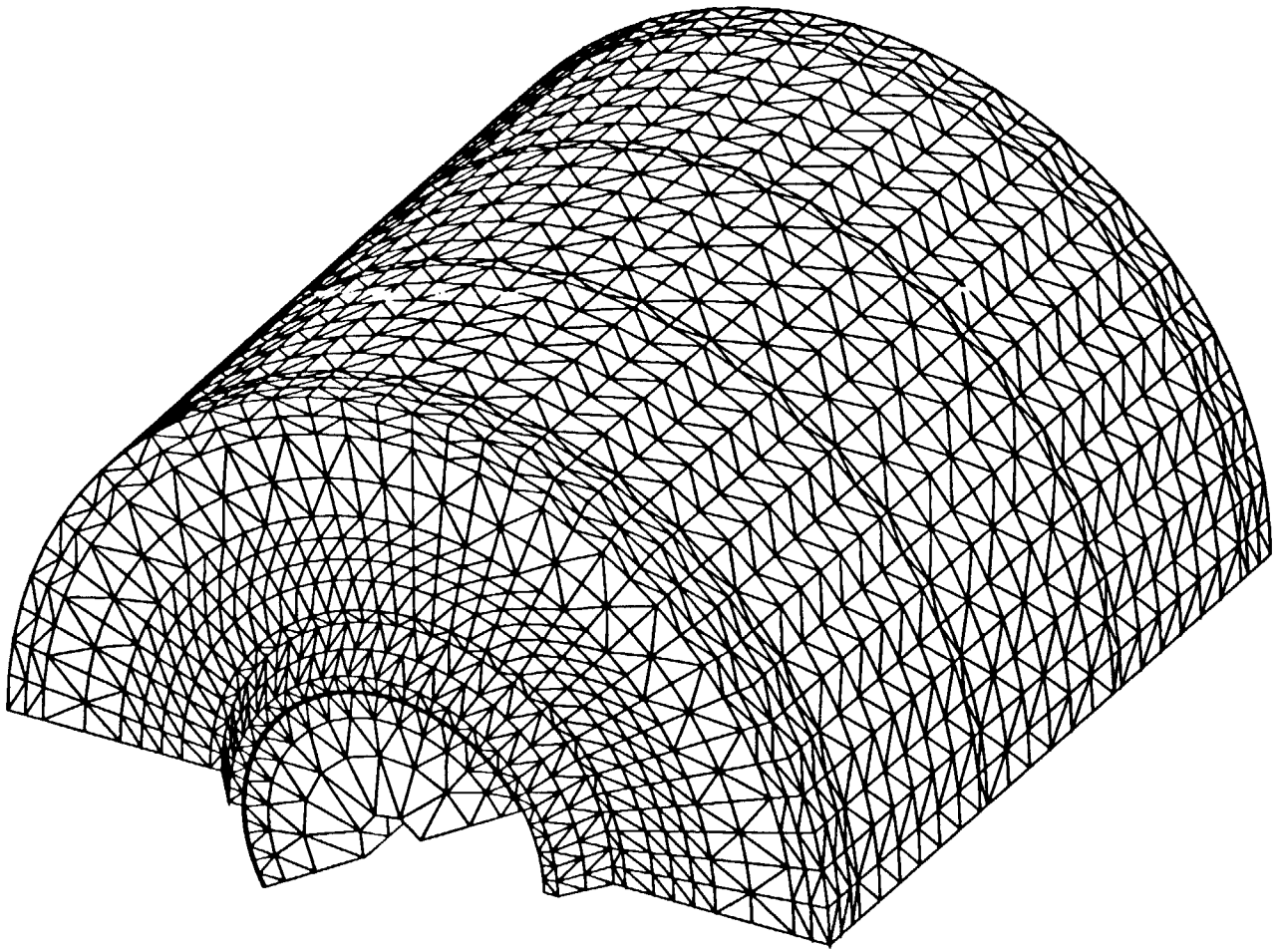

Figure (6.4.2) Global 3D-FE Grid at Rotor Position (2)

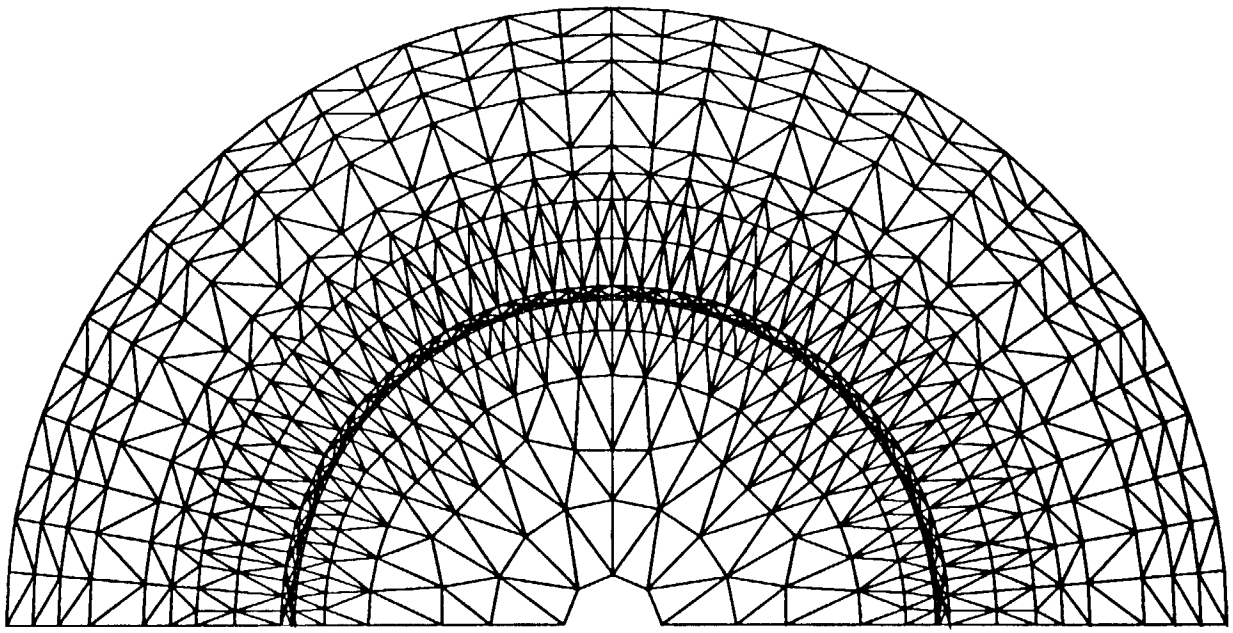

Figure (6.4.3) Mid-Plane Cross-Section View of the FE Grid Structure
at the Rotor Position (1)

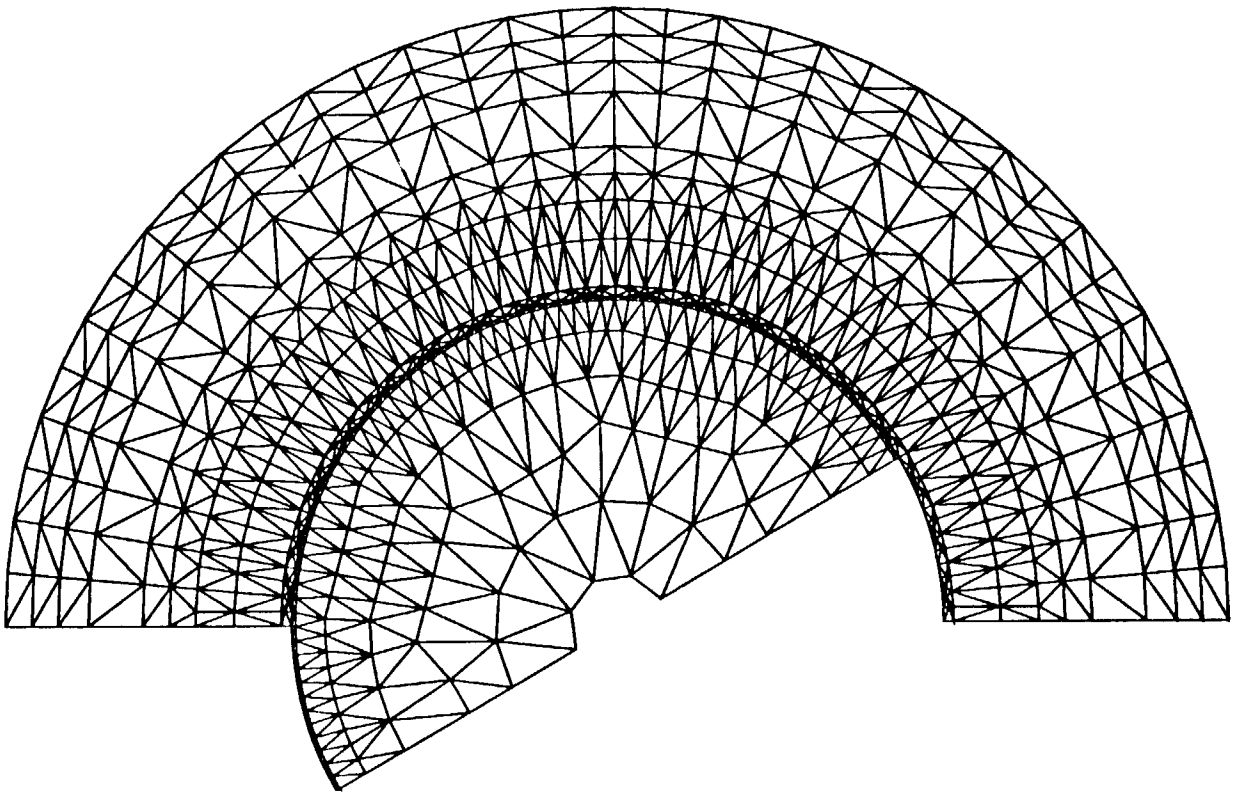

Figure (6.4.4) Mid-Plane Cross-Section View of the FE Grid Structure
at the Rotor Position (2)

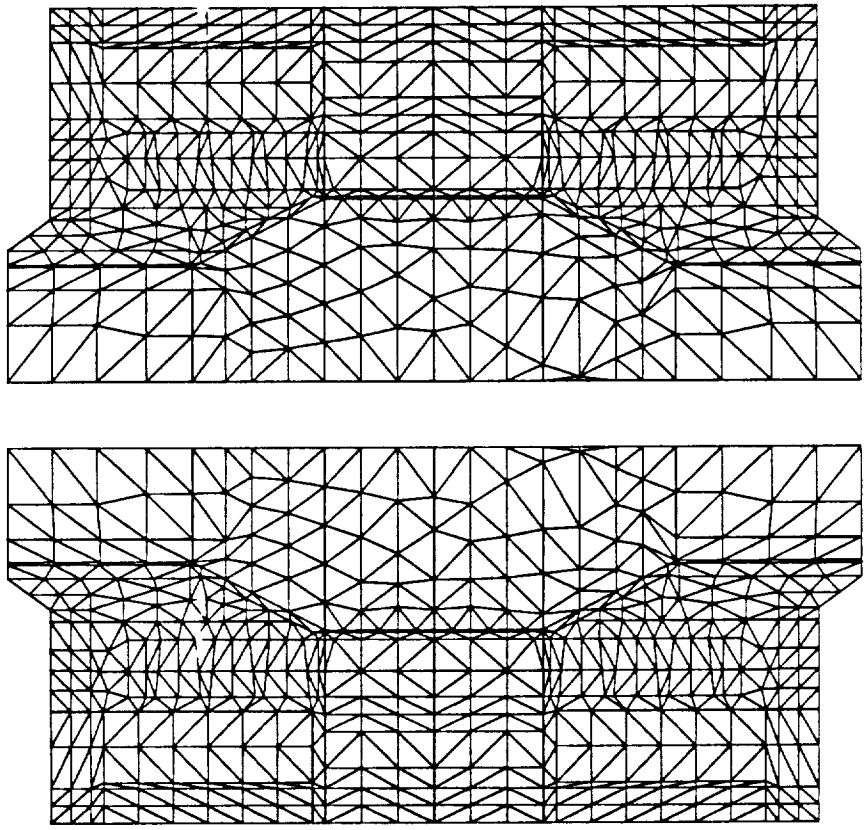

Figure (6.4.5) Bottom View of the Global 3D-FE Grid

Chapter 7

Three Dimensional Magnetic Field Computation in the 14.3 kVA MLA

In this chapter, the implementation of the MVP-MSP method to the computation of the 3D magnetostatic fields in the global solution volume of the 14.3 kVA MLA, is presented. This magnetic field computation includes full account of magnetic material nonlinearities, laminated core anisotropies, as well as complex geometries due to slotting and end-turn armature winding connections.

The detailed formulation of the combined MVP-MSP method of computation of 3D magnetic fields was developed in Chapter 3 through Chapter 5 of this dissertation. In this example 14.3 kVA MLA problem, the magnetic field is assumed to be confined within the outer boundaries of the casing of the MLA.

7.1 Geometry Partition of the MLA

Because of the nature of the magnetic circuit geometry of the 4-pole 14.3 kVA MLA, the global solution volume need only extend over two pole pitches of the rotor structure. Accordingly, a two-pole periodicity boundary condition was applied, and thus resulting in the global solution volume shown in the longitudinal cross-section of Figure (7.1.1-a) and the radial cross section shown in Figure (7.1.1-b).

The global solution volume shown in Figure (7.1.1) is divided into two sets of subregions, Subregion (1) and Subregion (2). Subregion (1) is a current-carrying MVP subregion, which contains all the windings including the iron portions in between. Furthermore, the MVP subregion consists of three separate portions. Two of the

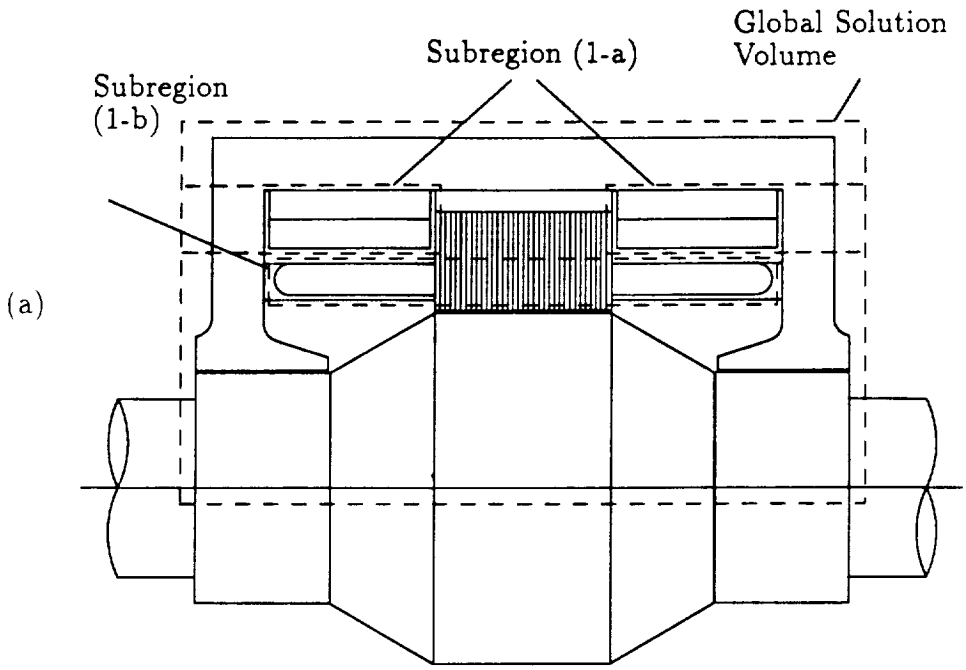

Subregion (2) = Global Solution Volume -
{ Subregion (1-a) ∪ Subregion (1-b) }

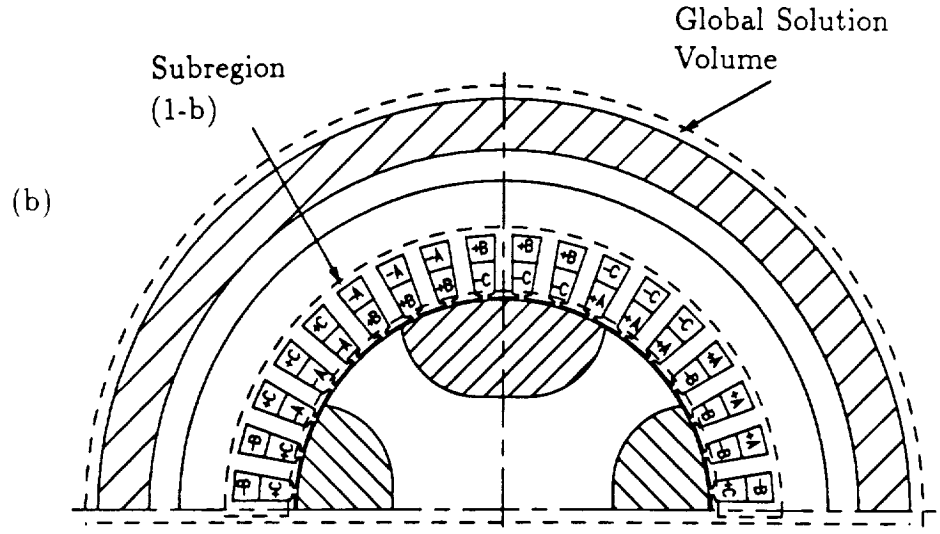

Figure (7.1.1) The MVP-MSP FE Solution Volume of the 14.3 kVA MLA

three portions, which are referred to as Subregion (1-a) in Figure (7.1.1-a), contain the stationary field windings on both ends of the MLA, respectively. These two MVP subregions extend axially through both ends of the global solution volume, see Figure (7.1.1-a). The 3D-FE grid of the MVP subregion for one half of the field coil is shown in Figure (7.1.2). The third portion of the MVP subregion contains the armature winding coils for phases, a, b, and c, as well as the portions of the stator teeth sandwiched in between, see Figure (7.1.1-b). This MVP subregion is a cylindrically shaped volume with a hollow cylindrical center. Figure (7.1.3) shows the 3D-FE grid which occupies one half of this MVP subregion within the global solution volume. Meanwhile, the current-free subregion, Subregion (2) in Figure (7.1.1), encompasses the global solution volume excluding the current-carrying MVP subregions (1-a) and (1-b), Figure (7.1.1).

It should be pointed out that any possible closed path within the confines of the current-free subregion cannot enclose net electric currents in the two field coils as well as in the armature winding coils. This is a necessary condition with which a single valued MSP can be used in the current-free subregion.

The inclusion of the iron portions sandwiched in between the armature coil bars in the MVP subregion has greatly simplified the geometry contours of this subregion. This ability of including iron in the current-carrying region is made possible by the use of the reduced magnetic vector potential (RMVP) in calculating the curl-component of the field intensity within the current carrying region, which is the unique feature of this combined MVP-MSP 3D-FE solution method.

As was discussed in Chapter 3, MSP jump distributions are to be enforced on the interfaces between the current carrying MVP subregions and the current-free subregions to guarantee the continuity of the tangential component of the field intensity computed on those interfaces. Such interfaces, in the case of the 14.3 kVA MLA, are the outer surface of the 3D-FE grid in Figure (7.1.2) for the MVP subregion of the field coil, and the outer surface of the 3D-FE grid in Figure (7.1.3) for the MVP subregion of the three phase armature windings. Meanwhile, discontinuities of the MSP derivatives are to be enforced on the interfaces between iron and air (conductor) within these MVP subregions to guarantee the continuity of the normal component of the flux density computed on those interfaces. In the MVP subregion for the field coil of Figure (7.1.2), there is a surface between the portion of the casing and the field coil, on which the discontinuity of the MSP derivative is to be enforced. In the

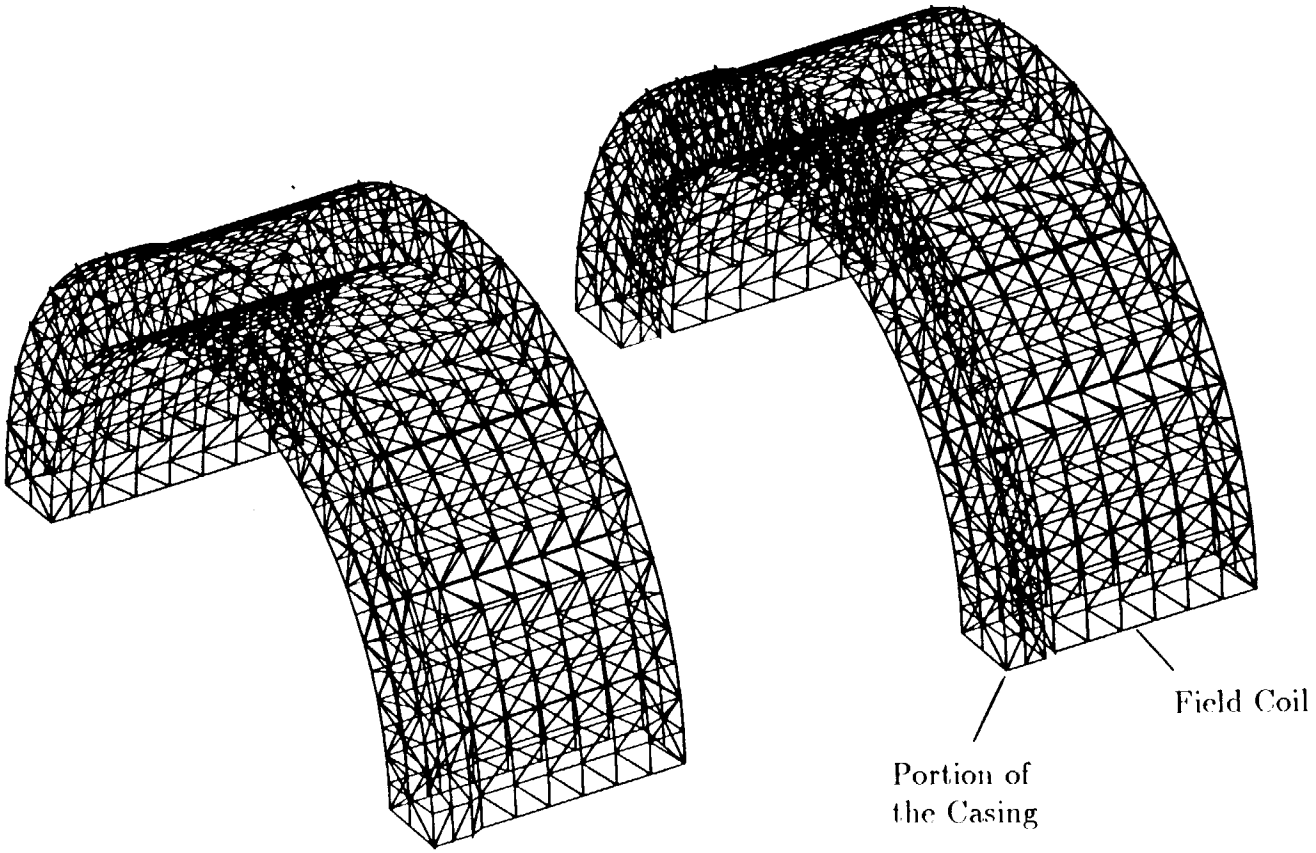

Figure (7.1.2) The MVP Subregion for One Field Coil of the 14.3 kVA MLA

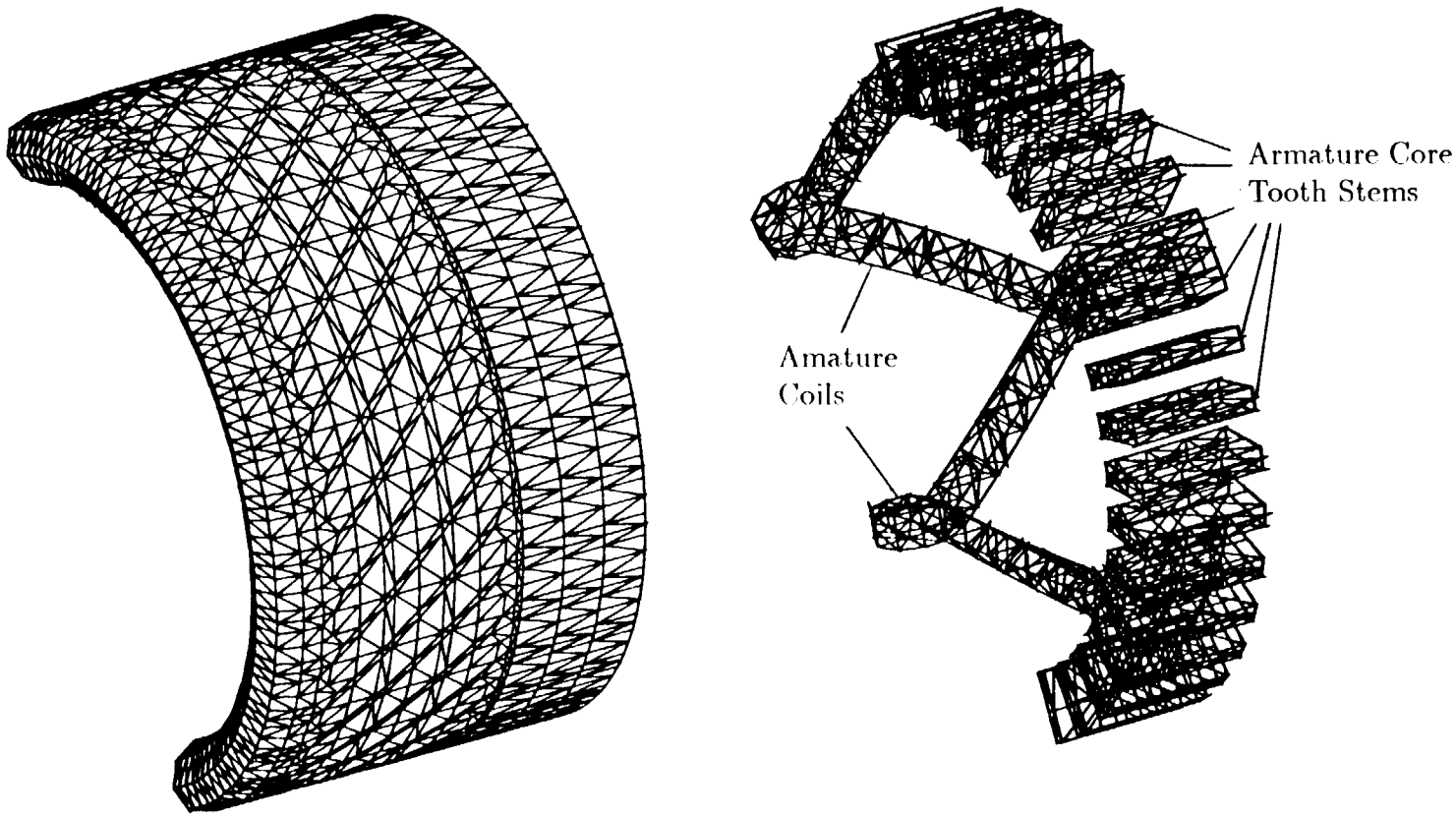

Figure (7.1.3) The MVP Subregion for the Armature Region of the 14.3 kVA MLA

MVP subregion for the armature windings of Figure (7.1.3), the discontinuities of the MSP derivatives are to be enforced on the interfaces between the armature core tooth stems and the armature coil bars.

7.2 The Computer Algorithm of the Combined MVP-MSP Method Applied to the MLA

The sequence of steps and flow of data in the resulting combined MVP-MSP computer algorithm is shown in Figure (7.2.1). This computer algorithm can be explained in detail as follows:

Step (1); Subroutine (Fortran File (FF)) slot.f

(1.1) Given an input data file containing the main MLA geometric parameters of the stator, for details see Table (1.3.1) and Figures (1.3.1) and (1.3.2) of Section 1.3, form a 3D-FE grid module for one stator slot pitch, Figure (6.2.1).

(1.2) Repeat the 3D-FE one stator slot module for the number of slots in a two-pole pitch span to obtain the 3D-FE grid portion of the stator, Figure (6.2.2).

(1.3) Pick the 3D-FE grid portions which cover the MVP solution Subregions (1-a) and (1-b), Figure (7.1.1), from the completed 3D-FE grid of the MLA's stator. These encompass the field winding and armature winding. Output data files are **gridvp.fw** and **gridvp.abc**, respectively.

Step (2); Subroutine (FF) rotor.f:

(2.1) Given an input data file containing the main MLA geometric parameters of the rotor, for details see Section 1.3 of this dissertation, form a 3D-FE grid module for one octant of the rotor geometry, see Figure (6.3.1).

(2.2) Repeat the 3D-FE grid module of the rotor obtained in (2.1) above, in conjunction with mirror imaging, to produce the 3D-FE rotor grid, Figures (6.3.2) through (6.3.4).

Step (3); Subroutine (FF) mvp3d.f:

(3.1) Perform the RMVP 3D-FE solution, Equation (3.1.2), in Subregion (1-a) of Figure (7.1.1), using a unit current assignment for the field current, i_f, and store the resulting normalized magnetic field solution data in a temporary

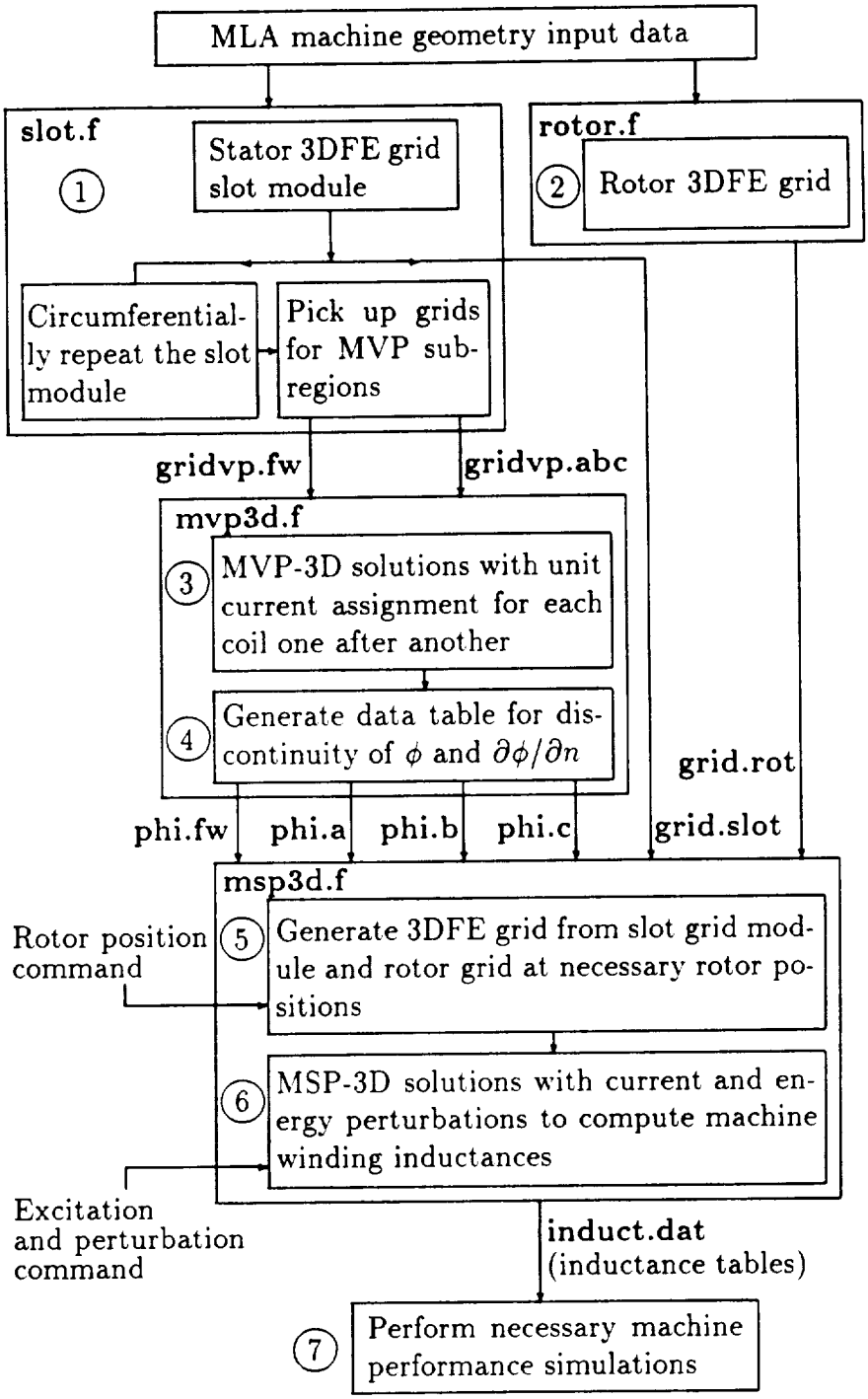

Figure (7.2.1) Sequence and Data Flow of the MVP-MSP 3D-FE Computation for the 14.3 kVA MLA

data file for use in forthcoming steps.

(3.2) Perform the RMVP 3D-FE solution, Equation (3.1.2), in Subregion (1-b) of Figure (7.1.1), using a unit phase (a) current assignment for i_a (while $i_b = i_c = 0$), and store the resulting normalized magnetic field solution data in the temporary data file of (3.1) above for use in forthcoming steps.

(3.3) Repeat the process in (3.2) above, using a unit phase (b) current assignment for i_b (while $i_a = i_c = 0$).

(3.4) Repeat the process in (3.2) above, using a unit phase (c) current assignment for i_c (while $i_b = i_c = 0$).

Step (4); Subroutine (FF) mvp3d.f:

From the normalized RMVP solution results obtained in step (3) above, compute the normalized discontinuity (jump) distribution in the MSP, Equations (3.1.16), on the outer surface of Subregions (1-a) and (1-b) and the distribution of the normal component of the derivative of the MSP, equation (3.1.17), at the air-iron boundary interfaces in Subregion (1-b), due to unit current values of i_f, i_a, i_b, and i_c. Store the results of the normalized $\Delta\phi$ and $\partial\phi/\partial n$ distributions in the data files, **phi.fw**, **phi.a**, **phi.b**, and **phi.c**, respectively, for use in the global MSP 3D-FE solutions.

Step (5); Subroutine (FF) msp3d.f:

Given a rotor position angle, θ, rotate the 3D-FE rotor grid obtained in Step (2) accordingly, and link the 3D-FE rotor grid to the 3D-FE stator grid obtained in Step (1), to obtain the 3D-FE grid covering the global solution volume of the MLA at the given rotor position. See Figures (6.4.1) and (6.4.2).

Step (6); Subroutine (FF) msp3d.f:

(6.1) Given a set of field excitation and armature winding currents i_f, i_a, i_b, and i_c, corresponding to a certain MLA operating condition (load or no-load, etc.), generate the corresponding forcing functions (actual $\Delta\phi$ and $\partial\phi/\partial n$) for the global 3D-FE MSP solution, using the normalized values of $\Delta\phi$ and $\partial\phi/\partial n$ stored in the data files, **phi.fw**, **phi.a**, **phi.b**, **phi.c**, obtained in Step (4) above. Also, perform the 3D-FE global MSP solution, ϕ, thus computing the magnetic field intensity, $\overline{H} = -\nabla\phi$, throughout the current-free region. Also generate the actual $\overline{A}_{rmvp}$ throughout the current-carrying regions, using the given currents i_f, i_a, i_b, and i_c, as well as the normalized values of $\overline{A}_{rmvp}$ stored in the data files, **phi.fw**, **phi.a**, **phi.b**, **phi.c** of Step (4), consequently compute

the magnetic field intensity, $\overline{H} = \nu_0(\nabla \times \overline{A}_{rmvp}) - \nabla\phi$, throughout the current-carrying region. Thus one completes the computation of the 3D magnetic field distribution throughout the magnetic circuit of the MLA, at the given rotor position angle, θ, for the given operating current conditions for i_f, i_a, i_b, and i_c.

(6.2) Compute all the self and mutual winding inductances, using the energy perturbation method, which will be explained later in Chapter 8 of this dissertation, at the given rotor position, θ, and its corresponding winding currents, i_f, i_a, i_b, and i_c.

(6.3) Repeat the computations in (6.1) and (6.2) above for incrementally increasing values of the rotor position, θ, while updating the corresponding values of the currents, i_f, i_a, i_b, and i_c, over half an ac cycle, that is π electrical radians (180° electrical), storing all inductances and necessary magnetic field data in the output file, **induct.dat**.

Step (7); Post Processing:

Based on the results of the 3D-FE magnetic field solutions and MLA winding parameters (inductances) computed in Step (6) above, compute the desired performance results.

7.3 Results of Computation of the 3D Magnetic Field in the 14.3 kVA MLA

The results of magnetic field computation for the example 14.3 kVA MLA are only included in this section to the extent that clearly demonstrates the 3D nature of the magnetostatic field distribution throughout its magnetic circuit. Other 3D-FE based computations and corresponding experimental verifications of the open-circuit (no-load), short-circuit, and load characteristics are reported in later chapters.

Consider the case of computation of the field distributions under open-circuit (no-load) conditions in this 14.3 kVA MLA; only the field excitation winding would carry current under such conditions. The 3D-FE computed flux flow patterns in the outer casing, rotor shaft and poles along the direct axis of the rotor are shown by vector $\overline{B}$ arrows in Figure (7.3.1). The flux flow pattern in the end-turn region along the direct axis of the rotor is shown in Figure (7.3.2). Meanwhile, Figure (7.3.3) shows the flux flow pattern by vector $\overline{B}$ arrows in a cross-section midway in the stator core.

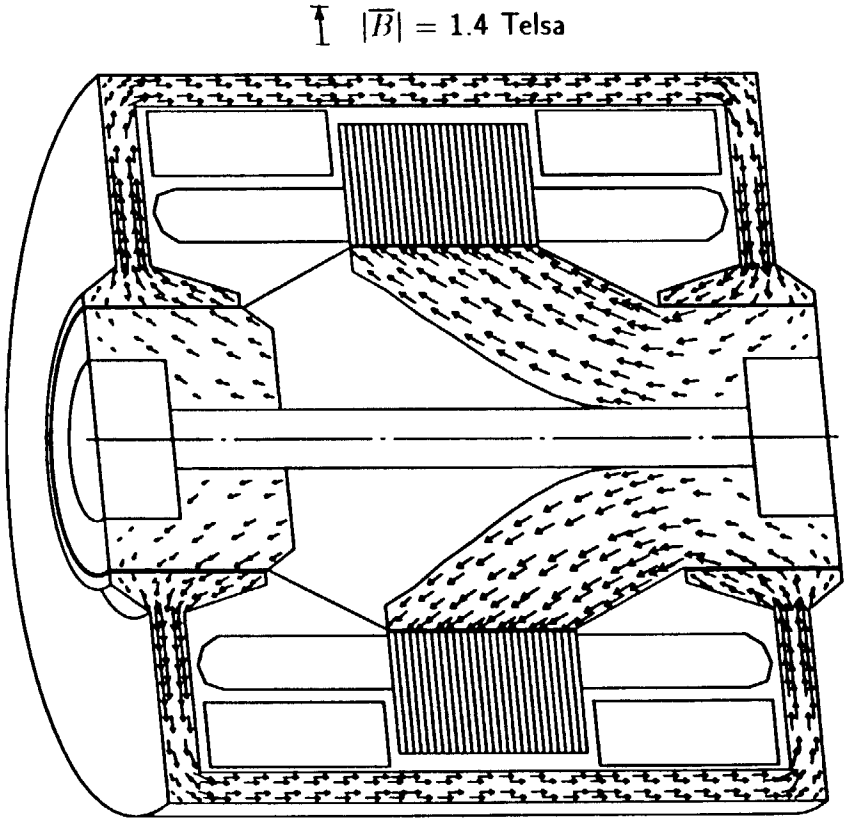

Figure (7.3.1) $\overline{B}$ Vector Plot in the Casing and Rotor Along a Longitudinal Cross-Section of the MLA

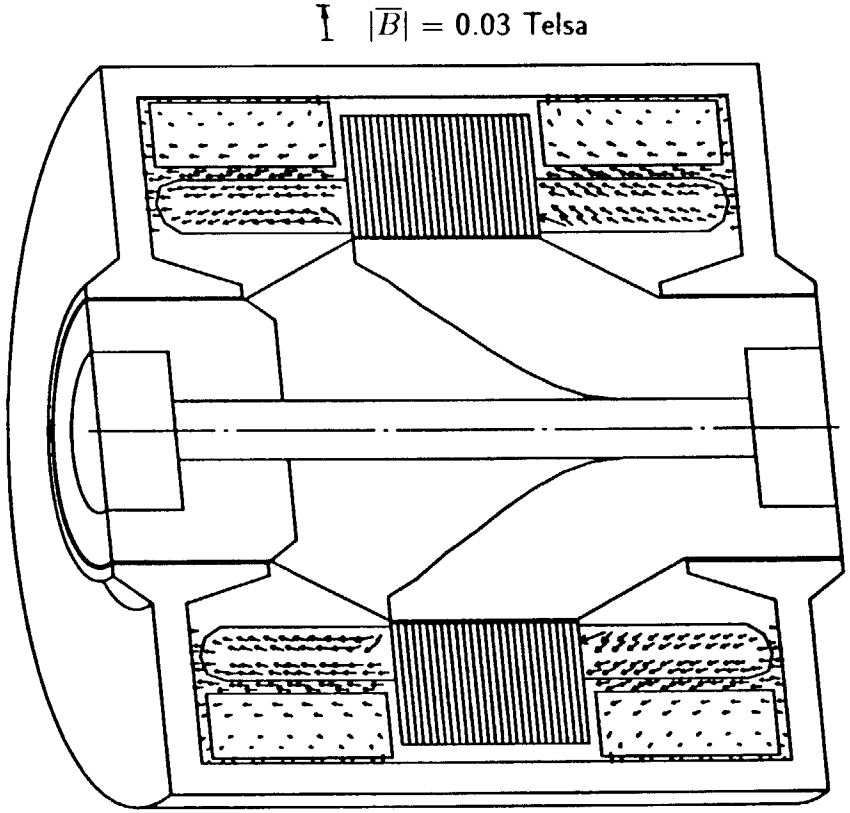

Figure (7.3.2) $\overline{B}$ Vector Plot in the Armature End-Turn Region Along a Longitudinal Cross-Section of the MLA

Figures (7.3.1) through (7.3.3) confirm the intuitive directions of the main flux flow pattern shown earlier in Figure (1.1.2) of Chapter 1. The 3D nature of the magnetic field is self evident in these figures.

In order to present the open-circuit rated voltage radial flux density distributions (waveforms) at the mid-airgap, consider the locations of nine cross-sections perpendicular to the axis of rotation shown in Figure (7.3.4). That is, at axial z-locations, $z = z_0$, $z = \pm z_1$, and $z = \pm z_2$, in the main airgap, as well as $z = \pm z_3$, and $z = \pm z_4$, in the auxiliary airgaps, as shown in the rotor schematic of Figure (7.3.4). The total field excitation ampere-turns at the rated voltage open-circuit condition were found to be 980 AT. At this level of field excitation the magnetic field was computed throughout the magnetic circuit of the MLA, and the radial flux density waveforms are shown in Figures (7.3.5) and (7.3.6) at locations $z = 0$, and $z = \pm 1.22$ cm. Also, Figure (7.3.7) shows the radial flux density wave forms at $z = \pm 1.92$ cm. This is in addition to an isometric presentation of B_r distribution in the main airgap, under one pole pitch, see Figure (7.3.8).

Notice the narrowing of the flux spread in the flux density waveforms as one proceeds from $z = 1.92$ cm to $z = 0$, and onto $z = -1.92$ cm. This narrowing is a direct result of the shape of the magnetic material constituting the pole face as depicted in the rotor schematic in Figure (7.3.4) as well as in Figure (6.3.3). This narrowing of flux spread in the flux density waveforms, and the dependence of the profiles of the waveforms on the axial z-location is most evident in the waveforms of Figure (7.3.7) obtained at, $z = \pm 1.92$ cm, in comparison to the waveform obtained at, $z = 0$. The lack of axial symmetry of the flux density waveforms in the main airgap is a clear demonstration of the fact that 2D-FE magnetic field computation methods could not have taken the above effects into account, and hence the resulting 3D nature of the field distribution.

The flux distributions were also computed at no-load in the two auxiliary airgaps at both ends of the machine at locations, $z = 5.13$ cm and $z = 7.72$ cm. These distributions are plotted in Figure (7.3.9) over two-pole pitches. Notice that the location, $z = 5.13$ cm, which is closer to the rotor pole face than $z = 7.72$ cm, exhibits a more modulated (nonuniform) flux density profile, despite the fact that the auxiliary airgap is uniform in nature. Both flux distributions are positive, which indicates a radially outward flux density orientation across the auxiliary airgap and into the end-bell. Once more, even in the auxiliary airgap, there is a lack of axial

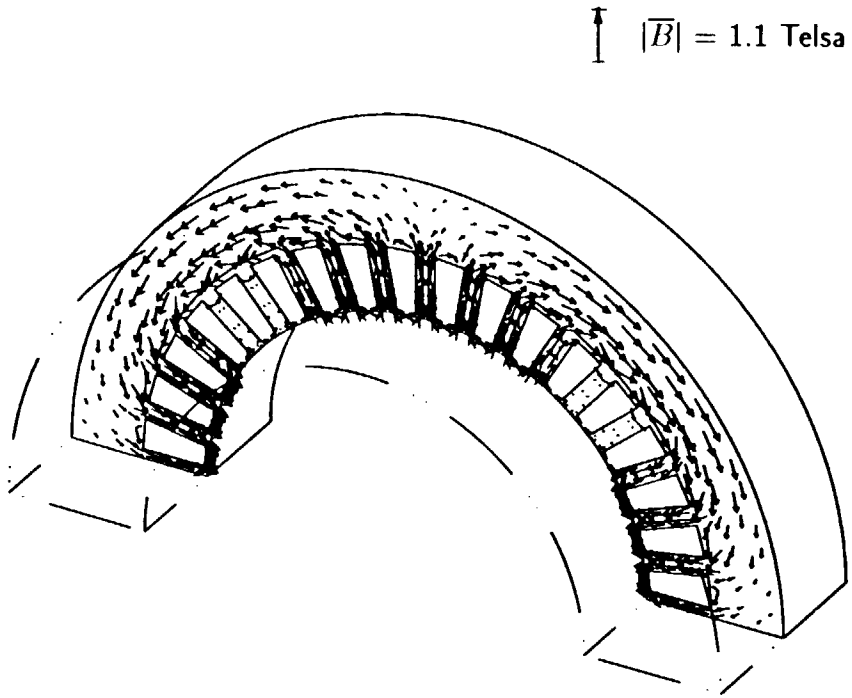

Figure (7.3.3) $\overline{B}$ Vector Plot in the Mid-Plane Cross-Section of the Stator Core of the MLA

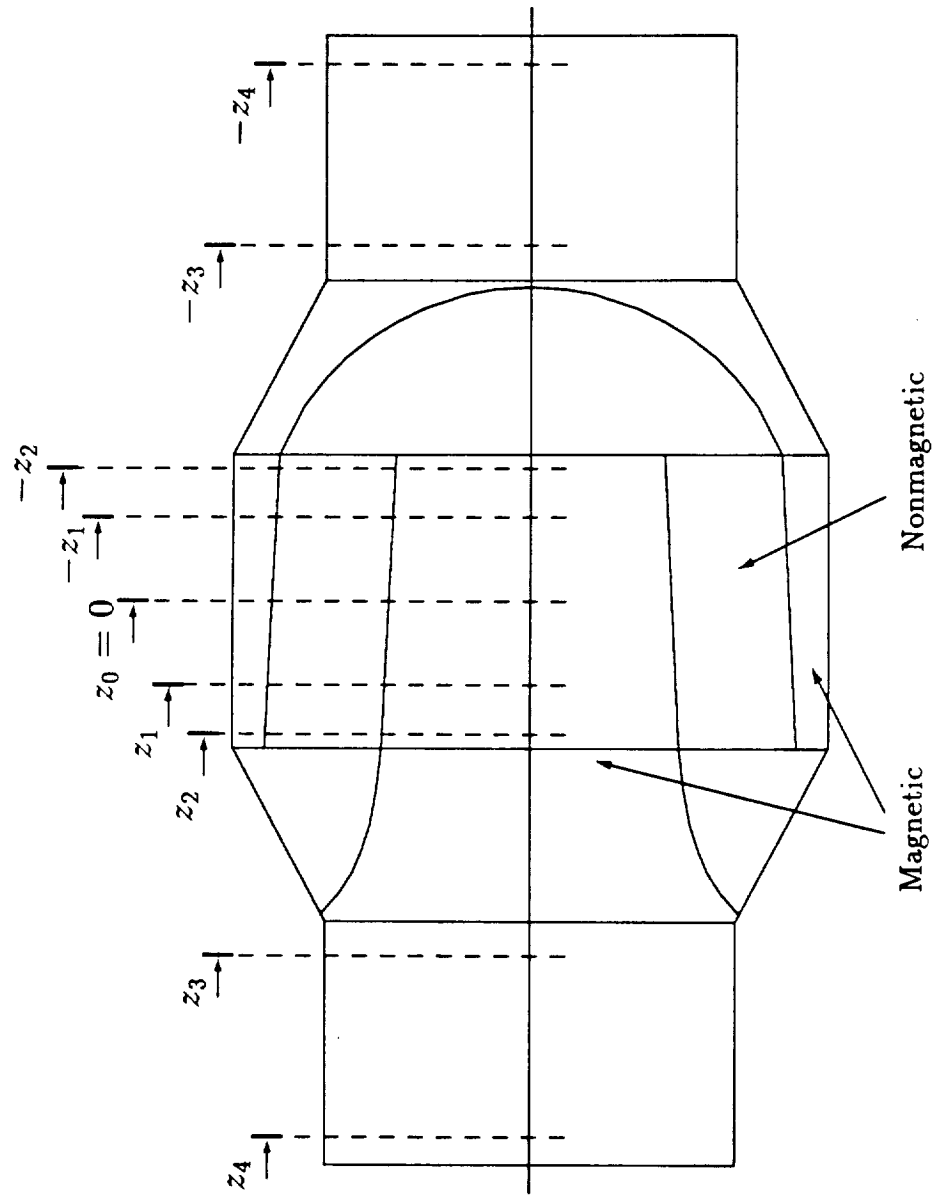

Figure (7.3.4) Locations of Cross-Sections for Mid-Airgap Plotting

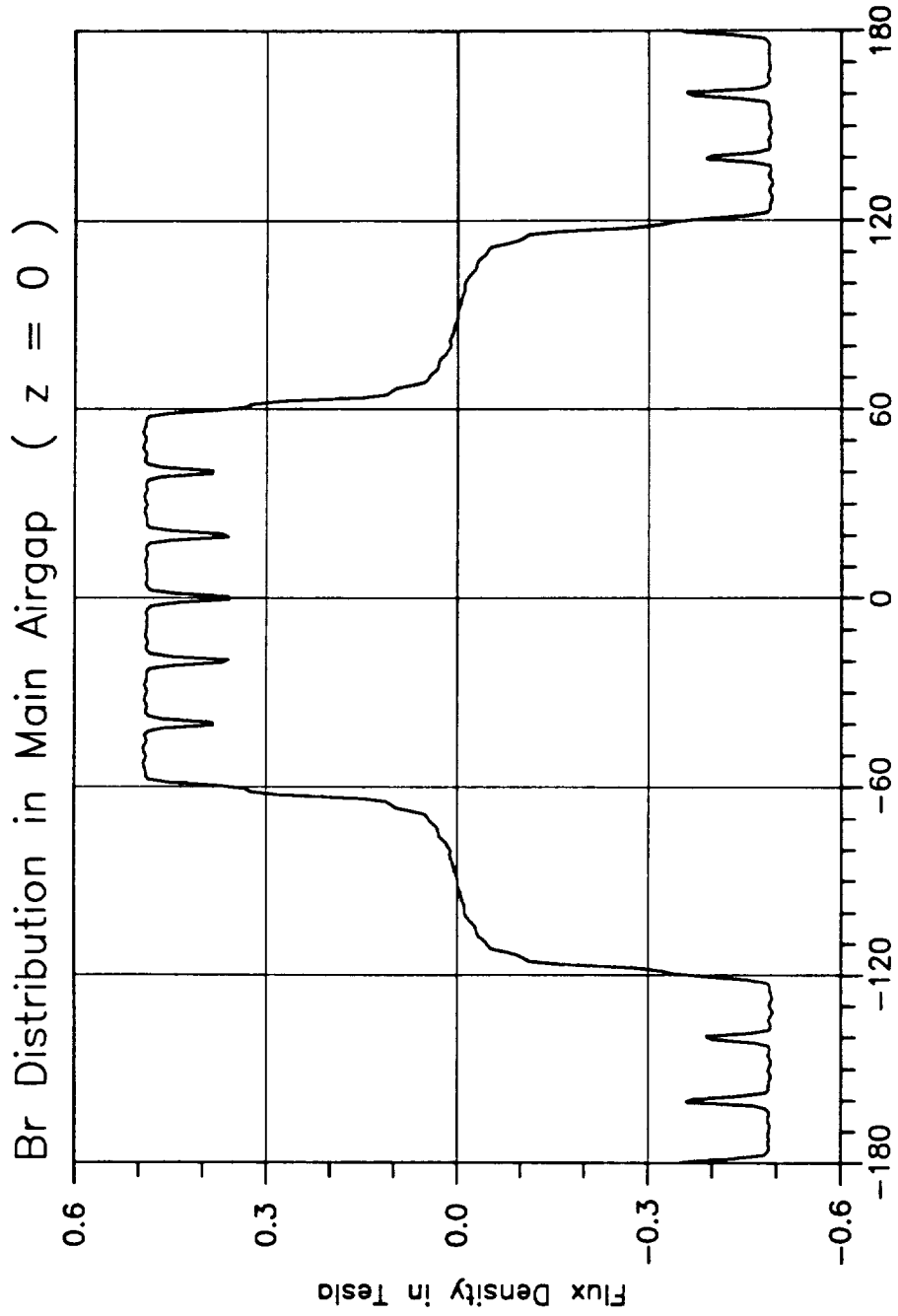

Figure (7.3.5) Plot of B_r Distribution in Main Airgap at $z = 0$

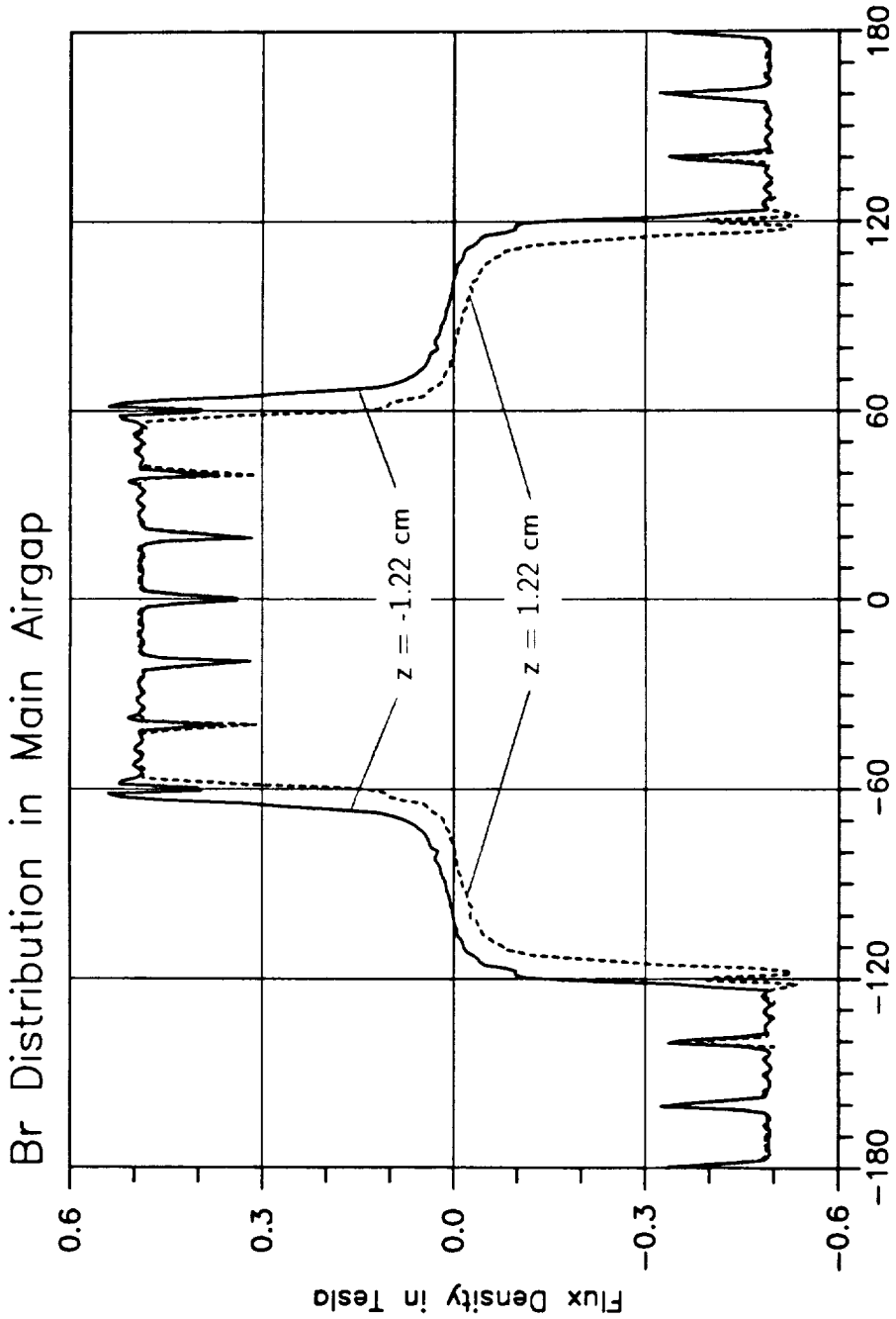

Figure (7.3.6) Plot of B_r Distribution in Main Airgap at $z = \pm z_1$

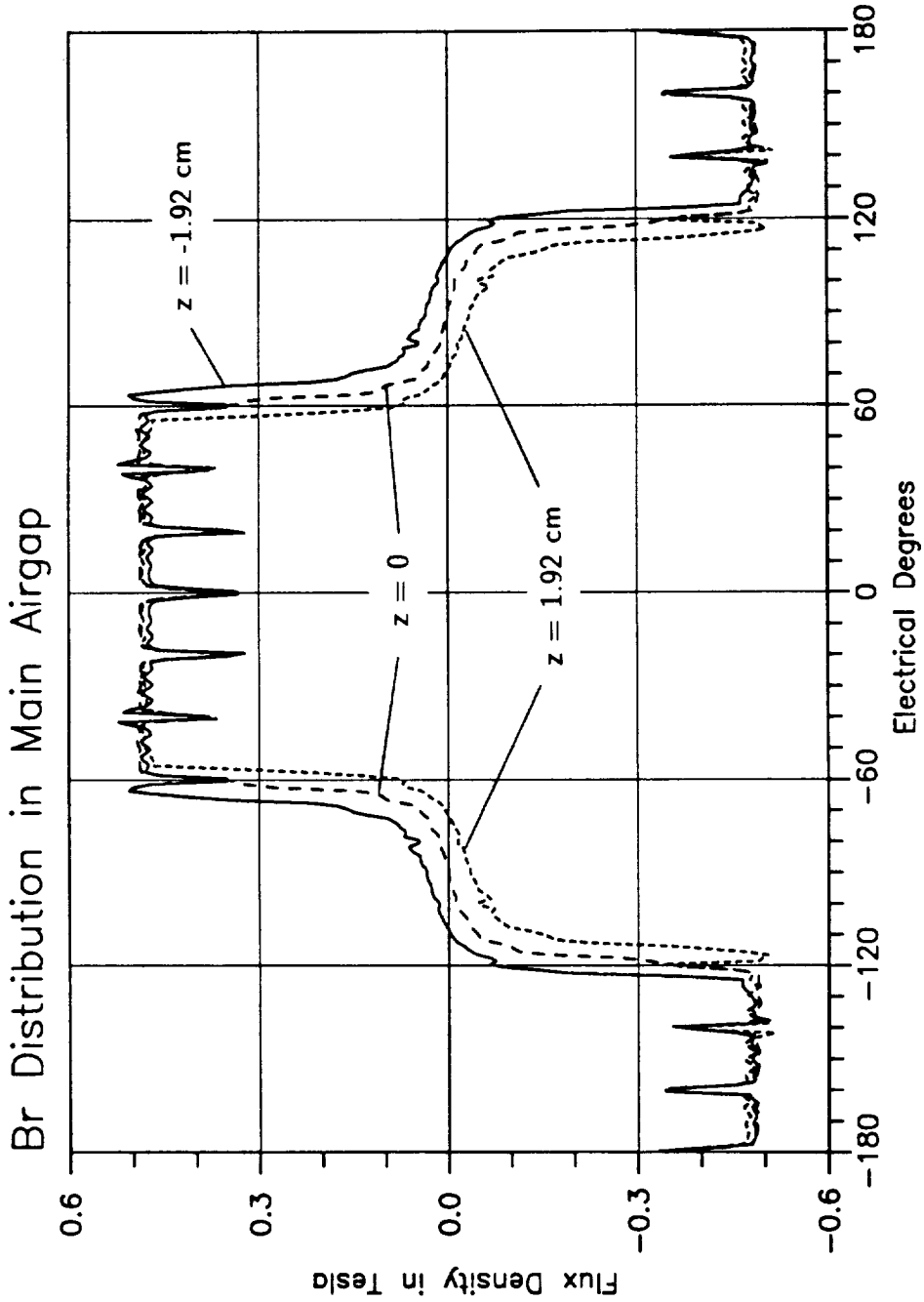

Figure (7.3.7) Plot of B_r Distribution in Main Airgap at $z = 0$ and $z = \pm z_2$

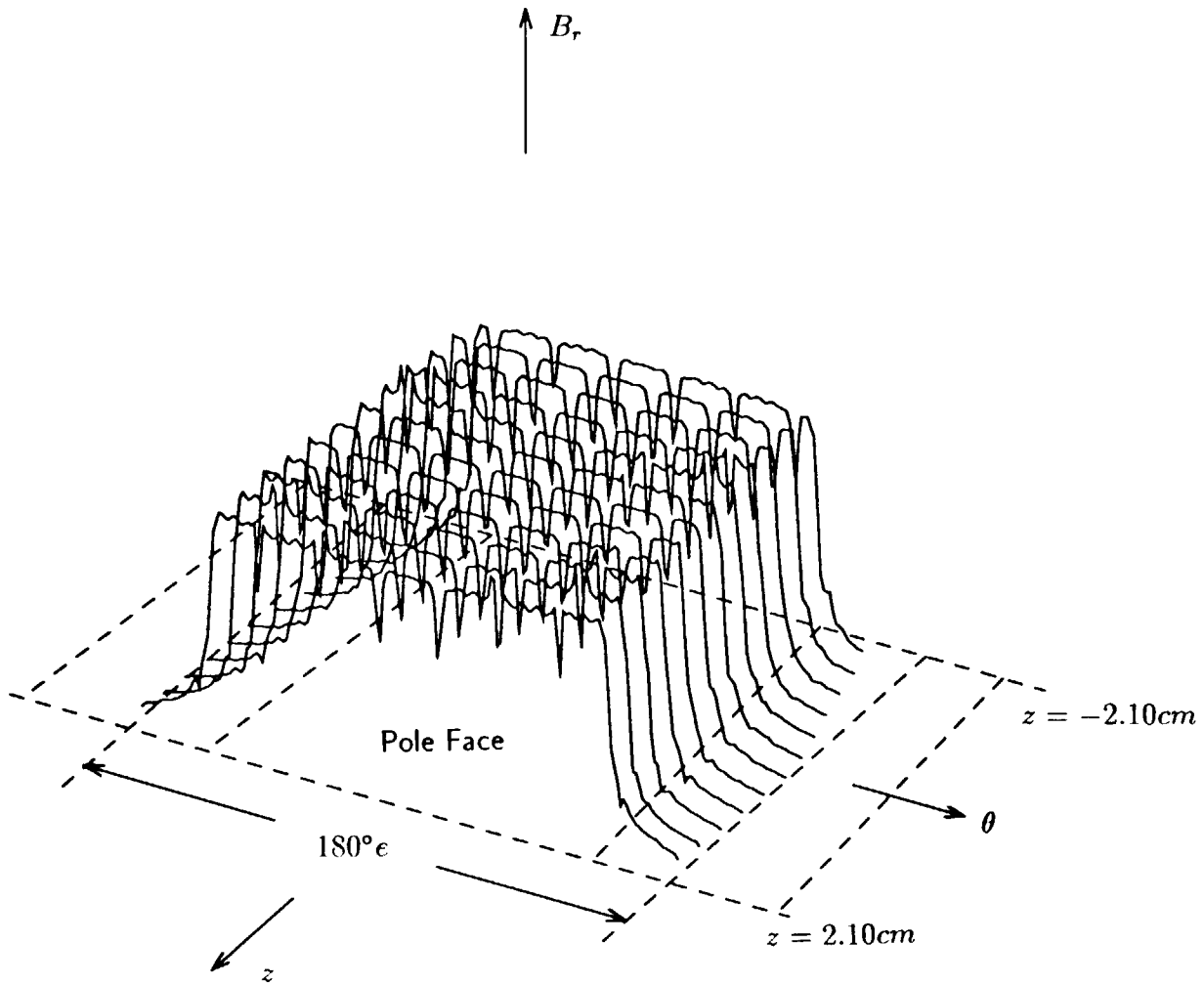

Figure (7.3.8) Isometric Presentation of B_r Distribution in Main Airgap of the 14.3 kVA MLA at No-Load

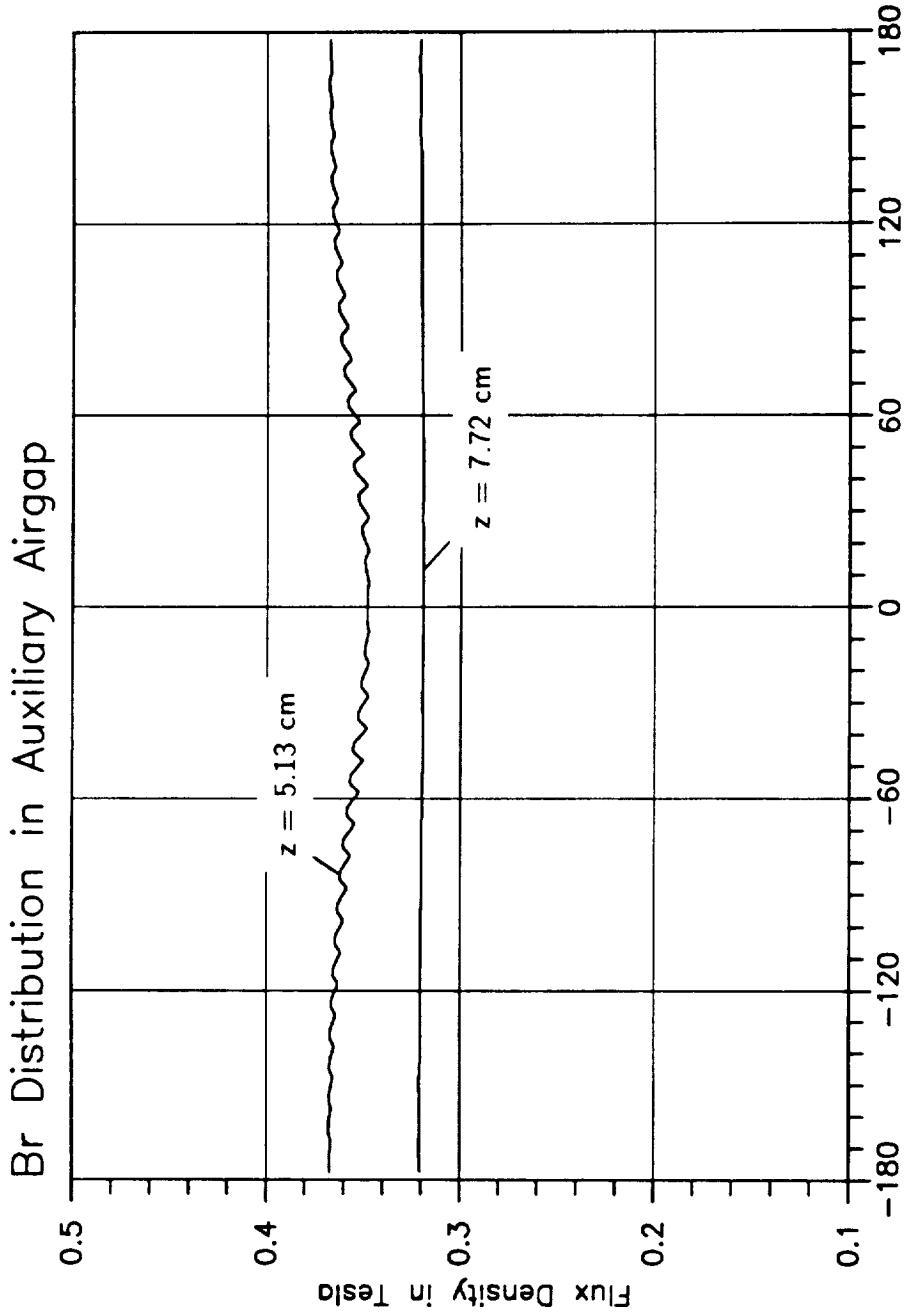

Figure (7.3.9) Plot of B_r Distribution in Auxiliary Airgap at $z = z_2$, and $z = z_3$

symmetry in the magnetic field, which is a further indication of the 3D nature of that field. Figure (7.3.10) contains the flux density profiles at $z = -5.13$ cm and $z = -7.72$ cm, which are identical in shape to those in Figure (7.3.9), except for a reversal in sign, which indicates a radially inward radial flux density orientation across the auxiliary airgap at the opposite end of the machine.

A typical quantification of the profile of the flux flow in the rotor shaft is shown in the longitudinal cross-section of Figure (7.3.11). One can easily observe that the radial outward flow from the rotor surface is not exclusively in the main airgap. The rotor shaft is seen to act like a manifold from and into which magnetic flux leaves and enters. Again, this is a further manifestation of the 3D nature of the magnetic field.

7.4 Advantages in the Computation Cost - A Comparison with the Global MVP formulation

The results of the MVP-MSP solution method were found to be accurate, reliable, and insensitive to the choice of grid geometries. In the 14.3 kVA MLA problem, the total number of second-order elements in Subregion (1-a), for one of the field coils, is 3,888, leading to a number of unknown RMVP components of 11,664. The total number of second-order elements in Subregion (1-b), for the armature region, is 11,880, leading to a number of unknown RMVP components of 34,776. Notice, the RMVP solution is a linear computation without involvement of any iterative process related to magnetic material saturation. Also, the RMVP solution is only carried out once for a given machine design geometry. In this example 14.3 kVA MLA problem, the total cpu time required by the Cray YMP super-computer in solving the RMVP problems is less than 120 seconds.

The major part of the magnetic field computation in the MVP-MSP method lies in the global MSP computation using the global first-order tetrahedral finite element grid. The total number of unknowns in this global MSP computation is 20,112. The ICCG method, reference [45], was used throughout in solving the systems of simultaneous algebraic equations resulting from the 3D-FE analysis. The cpu time

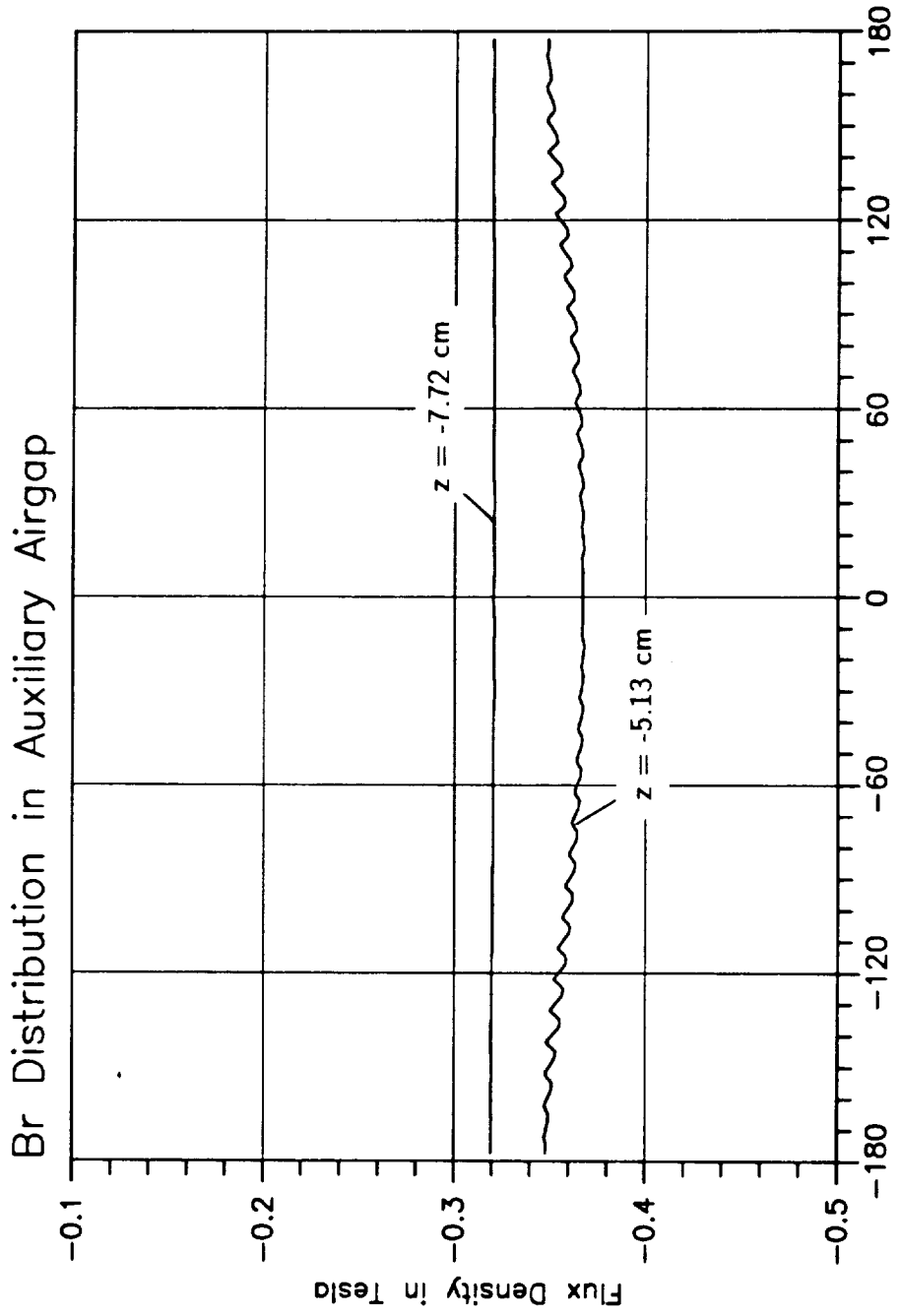

Figure (7.3.10) Plot of B_r Distribution in Auxiliary Airgap at $z = -z_2$, and $z = -z_3$

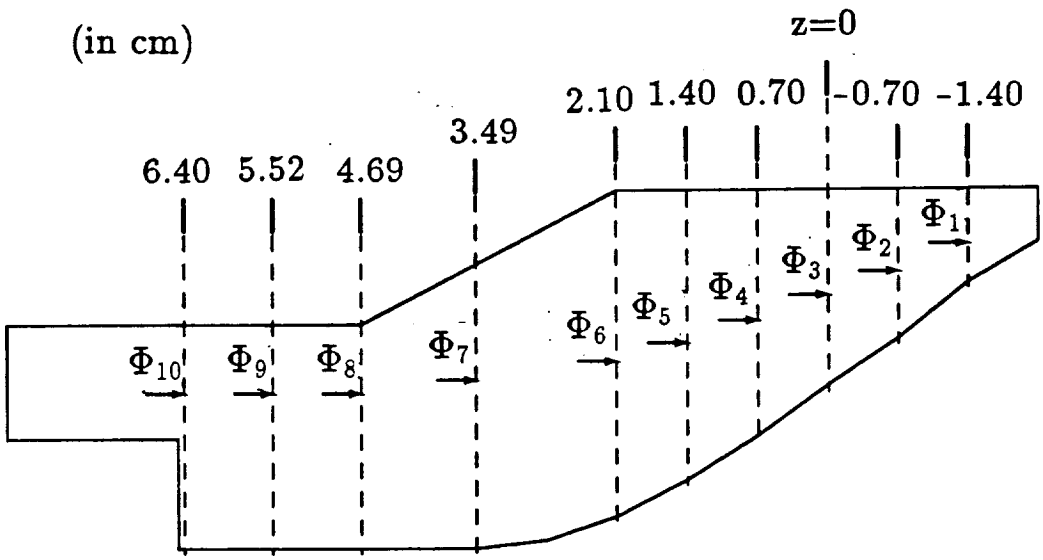

$\Phi_1 = 1.83 \times 10^4$ Wb
$\Phi_2 = 3.53 \times 10^4$ Wb
$\Phi_3 = 5.19 \times 10^4$ Wb
$\Phi_4 = 6.88 \times 10^4$ Wb
$\Phi_5 = 8.66 \times 10^4$ Wb
$\Phi_6 = 10.5 \times 10^4$ Wb
$\Phi_7 = 10.9 \times 10^4$ Wb
$\Phi_8 = 9.17 \times 10^4$ Wb
$\Phi_9 = 7.78 \times 10^4$ Wb
$\Phi_{10} = 5.45 \times 10^4$ Wb

Figure (7.3.11) Flux Flow in the Rotor Shaft

required by the Cray YMP super-computer for one linear MSP solution (without magnetic saturation) is about 18 seconds. The average cpu time required by the Cray YMP super-computer for the nonlinear MSP computation using the Newton-Raphson iterative procedure is less than 240 seconds for a given rotor position and a given set of field excitations. The computation size and cpu times mentioned above for the 14.3 kVA MLA problem are listed in Table (7.4.1).

In contrast to the MVP-MSP solution method, the global first-order MVP FE formulation and solution did not succeed in this MLA problem. The investigation using the first-order MVP formulation was carried out on the same 3D-FE grid as that used in the combined MVP-MSP solutions. As shown in Table (7.4.1), using this 3D-FE grid leads to a global system of equations with approximately 57,900 unknowns. This author found the computed magnetic field results to be dependent upon the particular grid geometries used in obtaining the solutions. This dependence was found to be due to the grid ill-conditioning of the first-order FE grid as explained earlier in Chapter 2 of this dissertation. This implies that in order to obtain an accurate result from the global MVP solution method with first-order elements, one has to use a much denser grid than that presented in Chapter 6.

Meanwhile, as shown in Table (7.4.1), solving the global system resulting from the global MVP method for one linear solution (without magnetic material saturation), using the ICCG method [45], required approximately 150 seconds of cpu time from a Cray YMP super-computer. This leads to an estimate of a total cpu time of 2,100 seconds (35 minutes) of the Cray YMP super-computer to compute the problem including magnetic material saturation at one rotor position. If one uses a denser grid to improve the accuracy of the results as discussed above, the required cpu time can be much higher than those listed in Table (7.4.1). Notice that for the whole task of the performance prediction of the MLA, one will be required to repeat such nonlinear 3D-FE field computations for many times (more than one hundred repetitions for different rotor positions and current excitations). Therefore, under the present status of super-computer state of the art, this approach requires unacceptably large amounts of cpu time.

The above discussed computation sizes and required cpu times for the global MVP method and the combined MVP-MSP method are listed side by side in Table (7.4.1). It is obvious that one of the main accomplishment of this work is the substantial savings in computer cpu time, which can be achieved by use of the MVP-MSP

Table (7.4.1): Required Cray-YMP Super-Computer cpu Time for the Global Magnetic Field Computation of the 14.3 kVA MLA

	Total Elements	Total Nodes	Total Unknowns	Cray YMP cpu Time (at One Rotor Position)	
				Linear Solution	Nonlinear Solution
Global MVP Method*	113,660	20,600	57,900	150 Sec.	35 Min.
MVP-MSP Method	113,660	20,600	20,112	18 Sec.	4 Min.

MVP Method* — Curl-Curl MVP FE Formulation Using First-Order Elements

method instead of the global fist-order MVP approach.

Chapter 8

MLA Open-Circuit and Short-Circuit Test Simulations

The combined MVP-MSP method of computation of 3D magnetic fields was used for global 3D field analysis and machine performance computations, under open-circuit and short-circuit conditions for the example 14.3 kVA MLA. In this chapter, the formulations and results of simulation of MLA open-circuit and short-circuit tests are given in detail.

The computed voltages and currents under these machine test conditions were verified and found to be in very good agreement with corresponding test data. These computer simulated results have automatically included all the effects of the 3D field distribution, axial, radial and tangential, throughout the whole magnetic circuits of such MLAs. Through the use of the global 3D-FE magnetic field computations, these results included the effects of the magnetic saturation in the iron core as well as armature end-turn effects. This agreement between simulation and test results confirms the validity and soundness of the combined MVP-MSP solution method for 3D magnetic field computations in such types of MLAs.

In addition, results of the use of this modeling and computation methods in the study of a design alteration example, in which the stator stack length of the example alternator is stretched in order to increase voltage and volt-ampere rating, are given in this chapter. These results demonstrate the inadequacy of conventional 2D-based design concepts and the imperative of use of this type of 3D magnetic field modeling in the design and investigation of such machines. This is a further confirmation of the need for such 3D magnetic field computation tools in analysis and design of the MLA class of machines, as well as any other machines involving substantial components of

axial flux flow side by side with conventional radial and tangential flux flow.

8.1 Computation of MLA Winding Inductances from 3D Magnetic Field Solutions

Consider the 14.3 kVA MLA subject of this investigation. There are four distinct windings in this machine. Namely, these are the a, b, and c armature phase windings, as well as the field winding, f, see the MLA winding schematic in Figure (8.1.1), and the MLA cross-sections in Figure (7.1.1).

It was shown in earlier work by Nehl and Demerdash [18, 79] that the apparent inductance terms ($L = \lambda/i$) can be expressed as second order partial derivatives of the stored magnetic energy, W, in such a device as the MLA at hand. That is, for the inductance term, L_{jk}, one can write:

$$L_{jk} = \frac{\partial^2 W}{\partial i_j \partial i_k} \tag{8.1.1}$$

where, in general j=1, 2, ..., n, in this case j=a, b, c, and f,

in general k=1, 2, ..., n, in this case k=a, b, c, and f.

The stored magnetic energy, W, can be calculated at any given machine operating condition of the MLA. That is, at a given set of winding currents, i_a, i_b, i_c and i_f, and a given rotor position angle, θ, from a 3D-FE magnetic field solution. Specifically, the winding inductance computations take place in Step (6) of the flow chart of Figure (7.2.1) of Chapter 7, following the complete 3D field solution, which yields the quiescent field solution point for a given rotor position. The energy perturbation process takes place along the apparent permeability line in each finite element throughout the magnetic circuit, see Figure (8.1.2). For details on the process of winding current - stored magnetic energy perturbation to compute winding inductances from magnetic field solutions, references [18, 79] should be consulted.

For computation of the self inductance of the jth winding, the current in this winding is increased to $(i_j+\Delta i_j)$, and decreased to $(i_j-\Delta i_j)$, respectively. The energy stored in the magnetic fields corresponding to these two current perturbations, $(i_j + \Delta i_j)$ and $(i_j-\Delta i_j)$, are computed. This yields the stored energy result $W(i_1, i_2, ..., i_j+\Delta i_j, ...)$ which will be referred to as $W(i_j + \Delta i_j)$, as well as the result $W(i_1, i_2, ..., i_j-$

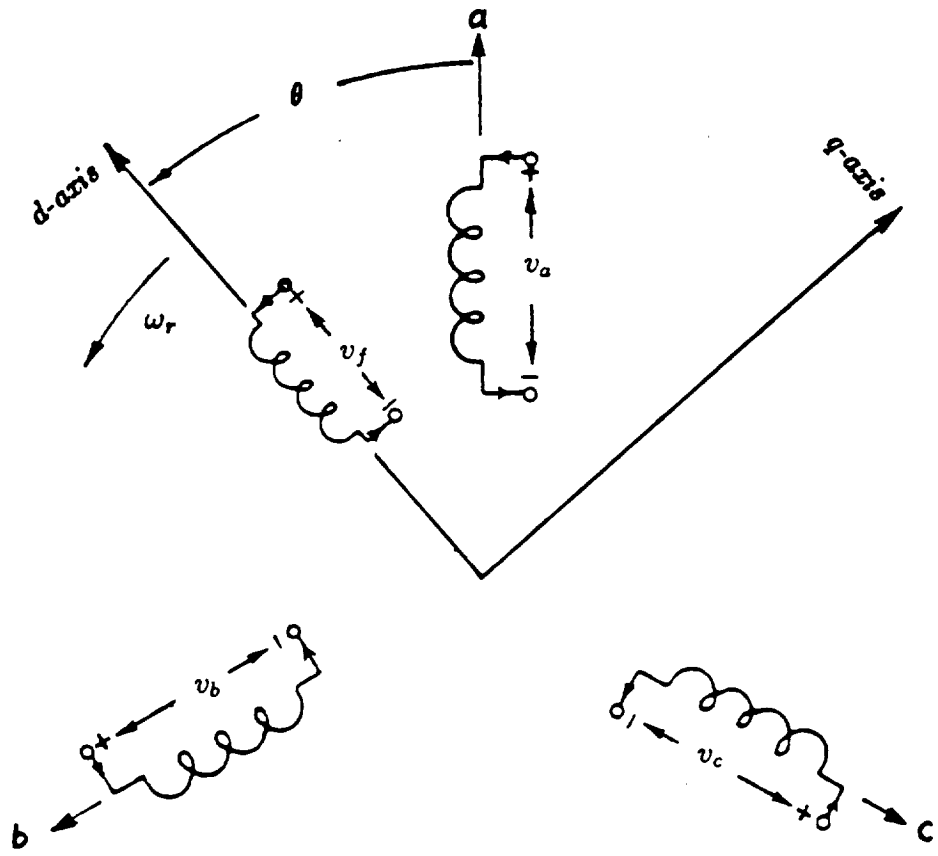

Figure (8.1.1) Schematic of the 14.3 kVA MLA Armature and Field Windings

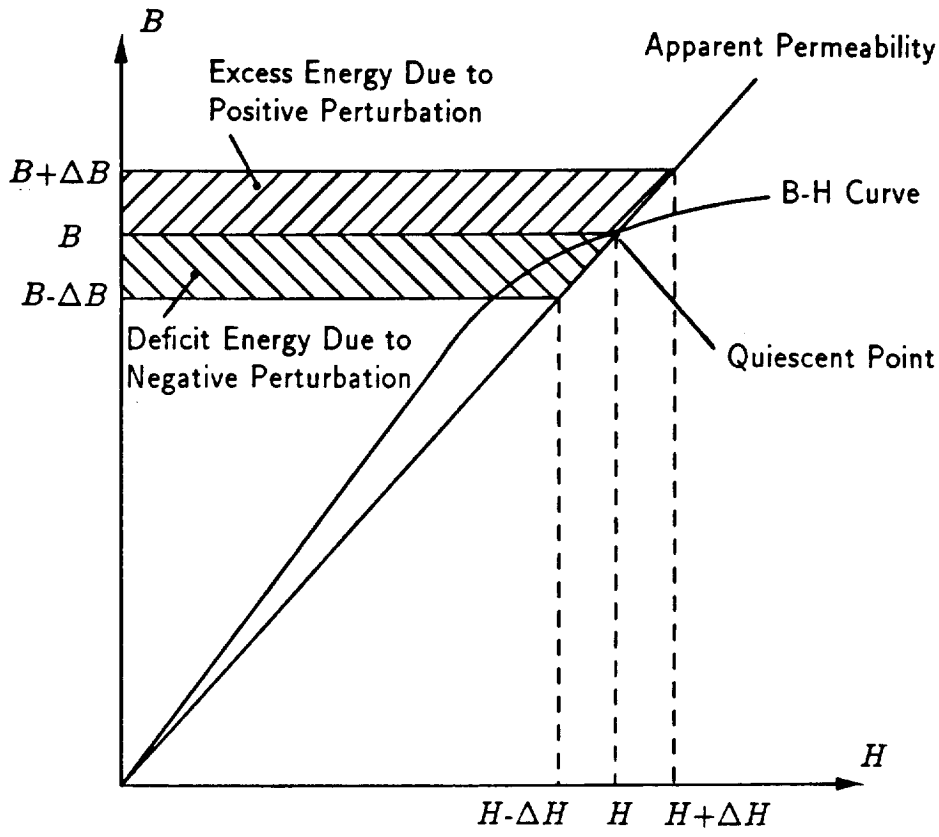

Figure (8.1.2) Energy Perturbation Along Elemental Apparent Permeability Line

$\Delta i_j, ...)$ which will be referred to as $W(i_j - \Delta i_j)$. Once these energy perturbations are obtained, the apparent self inductance, L_{jj}, can be computed as follows [18, 79]:

$$L_{jj} = \frac{W(i_j + \Delta i_j) + W(i_j - \Delta i_j) - 2W}{(\Delta i_j)^2} \tag{8.1.2}$$

In a similar fashion, for computation of the mutual inductances between windings, j and k, one computes the 3D magnetic fields and corresponding energies of the following current perturbations: $(i_j + \Delta i_j, i_k + \Delta i_k)$, $(i_j + \Delta i_j, i_k - \Delta i_k)$, $(i_j - \Delta i_j, i_k + \Delta i_k)$, $(i_j - \Delta i_j, i_k - \Delta i_k)$. These corresponding energies are namely the following: $W(i_j + \Delta i_j, i_k + \Delta i_k)$, $W(i_j + \Delta i_j, i_k - \Delta i_k)$, $W(i_j - \Delta i_j, i_k + \Delta i_k)$, $W(i_j - \Delta i_j, i_k - \Delta i_k)$. Once these four energy perturbations are obtained, the apparent mutual inductance, L_{jk}, can be computed as follows [18, 79]:

$$L_{jk} = [W(i_j + \Delta i_j, i_k + \Delta i_k) - W(i_j + \Delta i_j, i_k - \Delta i_k) -$$

$$W(i_j - \Delta i_j, i_k + \Delta i_k) + W(i_j - \Delta i_j, i_k - \Delta i_k)]/(4\Delta i_j \Delta i_k) \tag{8.1.3}$$

The energy perturbation approach summarized above was used repeatedly to obtain a complete tabulation of all these 14.3 kVA MLA winding (self and mutual) inductances over the entire (2π electrical radians) 360° electrical cycle of rotor positions. Thus all machine winding inductances were determined as a function of the rotor position angle, θ, see the rotor position command of Step (5) in Figure (7.2.1) of Chapter 7, including all the significant harmonic contents of these inductances arising from armature slotting, rotor saliency-like effects, effects of magnetic circuit saturations, etc. This process was used to obtain the various inductances at rated voltage, as well as lower and higher than rated voltage conditions. These apparent self and mutual inductances of the a, b, c, and f windings are as follows:

1) Armature phase self inductances; $L_{aa}(\theta)$, $L_{bb}(\theta)$, $L_{cc}(\theta)$,
2) Armature phase to phase mutual inductances; $L_{ab}(\theta) = L_{ba}(\theta)$, $L_{bc}(\theta) = L_{cb}(\theta)$, $L_{ca}(\theta) = L_{ac}(\theta)$,
3) Field winding self inductances; $L_{ff}(\theta)$,

and 4) Field winding to armature phase mutual inductances; $L_{af}(\theta) = L_{fa}(\theta)$, $L_{fb}(\theta) = L_{bf}(\theta)$, $L_{fc}(\theta) = L_{cf}(\theta)$.

Three sets of computed inductances under open-circuit test condition are pre-

sented here in this section. The first level of field excitation 980 AT was chosen in order to obtain a case (1) under which the open-circuit voltage is near the rated value, and hence there are only moderate magnetic saturation effects throughout the magnetic circuit of the example MLA. The second level of field excitation 500 AT was chosen to obtain a case (2) under which there is almost no magnetic saturation throughout the magnetic circuit of the example MLA. The third level of field excitation was chosen to obtain a case (3) under which there are substantial levels of magnetic saturation throughout the magnetic circuit of the example MLA. A total field excitation mmf of 3000 AT was chosen for this purpose, which is about 3 times the necessary excitation mmf needed to produced rated open-circuit voltage (at no-load).

For the 980 AT field excitation of case (1), the self inductance of the armature phase (a) winding, $L_{aa}(\theta)$, is shown in Figure (8.1.3) as a function of the rotor position angle, θ, in electrical degrees. Also, shown in the same figure is a tabulation of the harmonic decomposition of the self inductance, $L_{aa}(\theta)$, so that one can use the table to express this inductance in a Fourier series as follows:

$$L_{aa}(\theta) = A_0 + \sum_{n=2,4,}^{20} A_n Cos(n\theta - \psi_n) \tag{8.1.4}$$

where, n is the harmonic order 2, 4, ..., 20, and A_0 is the dc (average) component given in the table in Figure (8.1.3),

A_n is the amplitude of the nth harmonic component of the inductance in mH,

and ψ_n is a phase angle of the nth harmonic component in electrical radians.

Similar expressions can be written for L_{bb} and L_{cc}, by replacing the rotor position angle, θ, by $(\theta - 2\pi/3)$, $(\theta - 4\pi/3)$, for phases (b) and (c), respectively.

Meanwhile, for the 980 AT field excitation of case (1), the mutual inductance between the armature windings of phases (a) and (b), $L_{ab}(\theta)$, is shown in Figure (8.1.4) as a function of the rotor position angle, θ. Also, shown in the same figure is a tabulation of the harmonic decomposition for that inductance, so that one can use the table to express it in a Fourier series as follows:

$$L_{ab}(\theta) = A_0 + \sum_{n=2,4,}^{20} A_n Cos(n\theta - \psi_n) \tag{8.1.5}$$

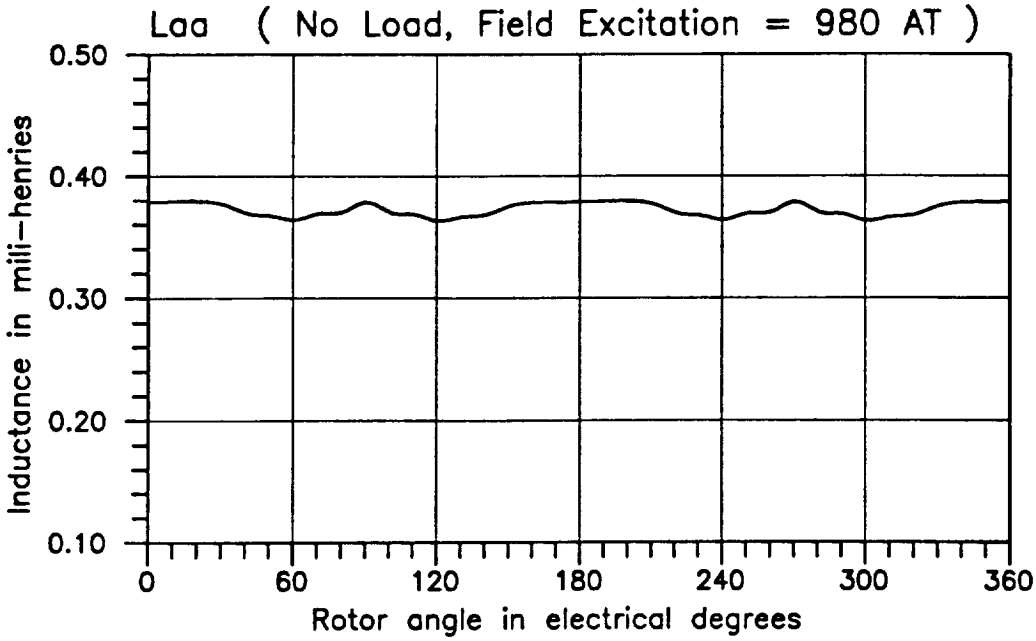

Harmonic Contents of Self Inductance L_{aa}		
DC Value: $A_0 = 0.3722\ (mH)$		
Order n	Amplitude $A_n\ (mH)$	Phase Angle $\psi_n\ (Rad)$
1	0.0000	——
2	0.0050	0.1673
3	0.0000	——
4	0.0048	0.1110
5	0.0000	——
6	0.0032	-3.0576
7	0.0000	——
8	0.0001	-2.6757
9	0.0000	——
10	0.0007	-2.9397
11	0.0000	——
12	0.0005	0.2114
13	0.0000	——
14	0.0001	-2.9155
15	0.0000	——
16	0.0008	0.3216
17	0.0000	——
18	0.0011	-2.8245
19	0.0000	——
20	0.0005	0.3125

Figure (8.1.3) Self Inductance L_{aa} Computed at $I_f = 980\ AT$

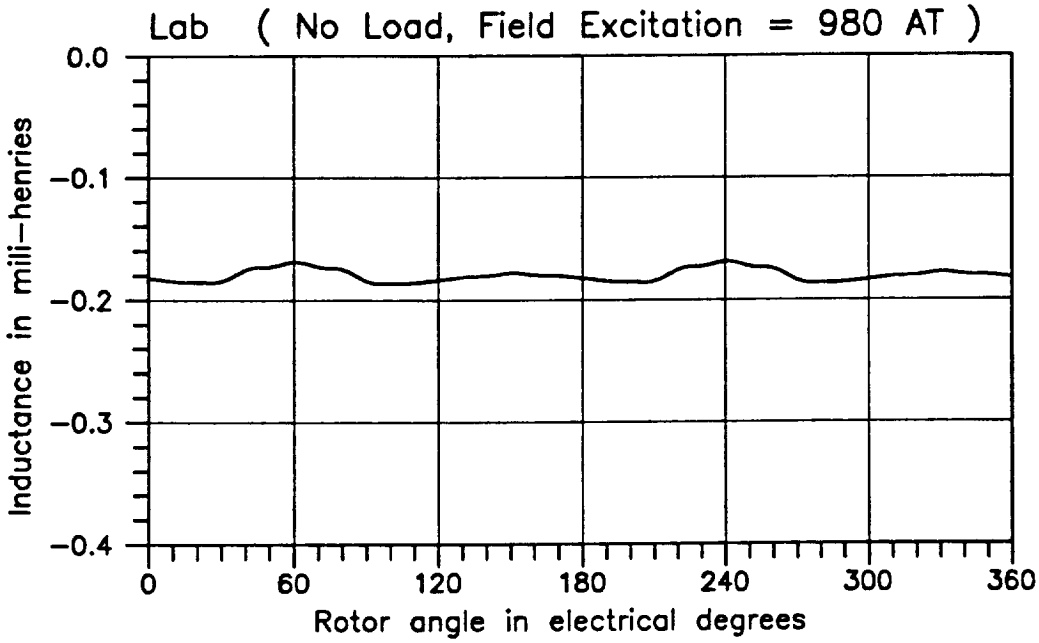

Harmonic Contents of Mutual Inductance L_{ab}		
DC Value: A_0 = -0.1801 (mH)		
Order n	Amplitude A_n (mH)	Phase Angle ψ_n (Rad)
1	0.0000	——
2	0.0033	1.9799
3	0.0000	——
4	0.0060	-2.0063
5	0.0000	——
6	0.0016	0.0825
7	0.0000	——
8	0.0001	-0.9393
9	0.0000	——
10	0.0007	1.2401
11	0.0000	——
12	0.0002	-2.8831
13	0.0000	——
14	0.0001	-0.7608
15	0.0000	——
16	0.0008	-1.7870
17	0.0000	——
18	0.0005	0.3171
19	0.0000	——
20	0.0005	2.4211

Figure (8.1.4) Mutual Inductance L_{ab} Computed at $I_f = 980\ AT$

where, A_0, A_n and ψ_n are as defined above. Again, similar expressions to Equation (8.1.5) can be written for L_{bc}=L_{cb}, and L_{ca}=L_{ac}, by replacing the rotor position angle θ, by $(\theta - 2\pi/3)$, and $(\theta - 4\pi/3)$, for the mutuals between b and c, and between c and a, respectively.

The self inductance of the excitation field winding, $L_{ff}(\theta)$, is given as a function of the rotor position angle, θ, in Figure (8.1.5), for case (1) with 980 AT field excitation. Again this inductance, $L_{ff}(\theta)$, can be expressed by a Fourier series type expression identical in nature to that given in Equations (8.1.4) and (8.1.5). The Fourier expression coefficients are given in the table of Figure (8.1.5). Notice that only the 18th harmonic component exists in this self inductance. This is directly a result of the fact that the number of slots per pair of poles is 18.

The mutual inductance between the field winding, f, and the phase (a) armature winding, $L_{af}(\theta)$, is given in Figure (8.1.6) as a function of the rotor position, θ. This is again for case (1) with 980 AT of field excitation. Also, shown in the same Figure (8.1.6) is a tabulation of the harmonic decomposition of that mutual inductance, so that one can use the table to express it in a Fourier series form as follows:

$$L_{fa}(\theta) = L_{af}(\theta) = \sum_{n=1,3,}^{19} A_n Cos(n\theta - \psi_n) \tag{8.1.6}$$

where, A_n is the amplitude of the nth harmonic component in H, for n=1, 3, ..., 19 and ψ_n is a phase angle of the nth harmonic component in electrical radians. Again, similar expressions to that in Equation (8.1.6) can be written for L_{fb}=L_{bf} and L_{fc}=L_{cf}, by replacing the rotor position angle, θ, by $(\theta - 2\pi/3)$, and $(\theta - 4\pi/3)$, for L_{fb} and L_{fc}, respectively.

The profiles and harmonic decompositions for this set of inductances, $L_{aa}(\theta)$, $L_{ab}(\theta)$, $L_{ff}(\theta)$, and $L_{fa}(\theta)$, were also computed for case (2) of 500 AT, and for case (3) of 3000 AT of field excitations, to assess the impact of magnetic saturation of the magnetic circuit of the example MLA on the magnitudes and profiles of these inductances. The results are given in profile in Figures (8.1.7) through (8.1.10) for L_{aa}, L_{ab}, L_{ff}, and L_{fa}, respectively. Upon examination of these profiles, one can see as expected the considerable reduction in the values of these inductances as the magnetic circuit of this example 14.3 kVA-MLA is driven into higher levels of magnetic saturation.

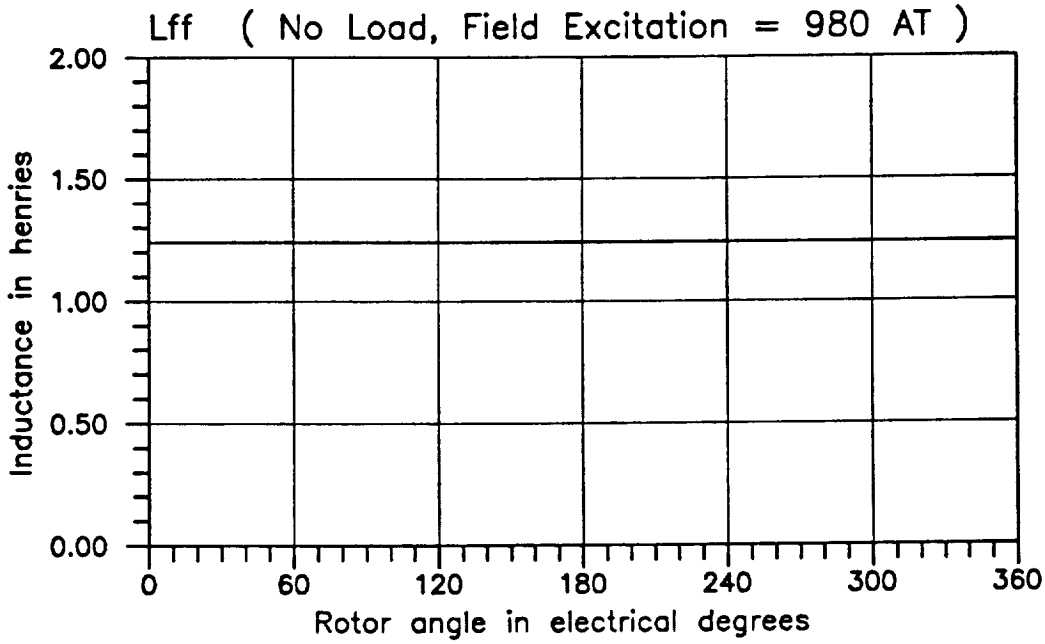

Harmonic Contents of Self Inductance L_{ff}		
DC Value: $A_0 = 1.2405\ (H)$		
Order n	Amplitude $A_n\ (H)$	Phase Angle $\psi_n\ (Rad)$
1	0.0000	——
2	0.0000	——
3	0.0000	——
4	0.0000	——
5	0.0000	——
6	0.0000	——
7	0.0000	——
8	0.0000	——
9	0.0000	——
10	0.0000	——
11	0.0000	——
12	0.0000	——
13	0.0000	——
14	0.0000	——
15	0.0000	——
16	0.0000	——
17	0.0000	——
18	0.0004	-2.8245
19	0.0000	——
20	0.0000	——

Figure (8.1.5) Self Inductance L_{ff} Computed at $I_f = 980\ AT$

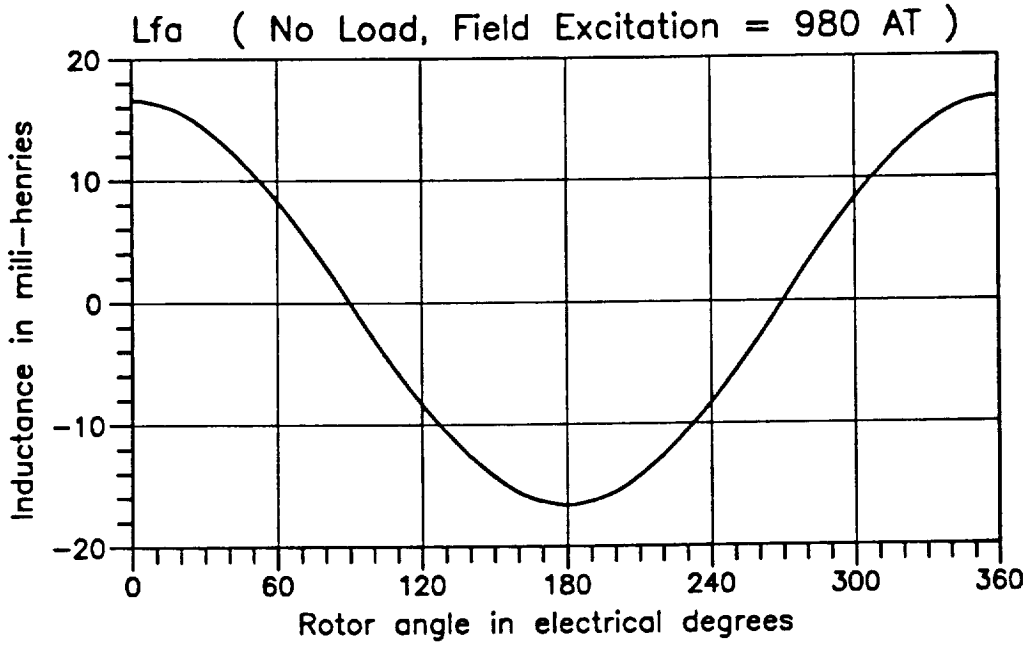

Harmonic Contents of Mutual Inductance L_{fa}		
Order n	Amplitude A_n (mH)	Phase Angle ψ_n (Rad)
1	16.5450	0.0000
2	0.0000	——
3	0.0021	-2.8830
4	0.0000	——
5	0.0908	0.0942
6	0.0000	——
7	0.0469	-3.0318
8	0.0000	——
9	0.0005	-2.0558
10	0.0000	——
11	0.0076	-2.9035
12	0.0000	——
13	0.0100	0.2656
14	0.0000	——
15	0.0005	0.6653
16	0.0000	——
17	0.0127	0.3197
18	0.0000	——
19	0.0102	0.3144
20	0.0000	——

Figure (8.1.6) Mutual Inductance L_{af} Computed at $I_f = 980\ AT$

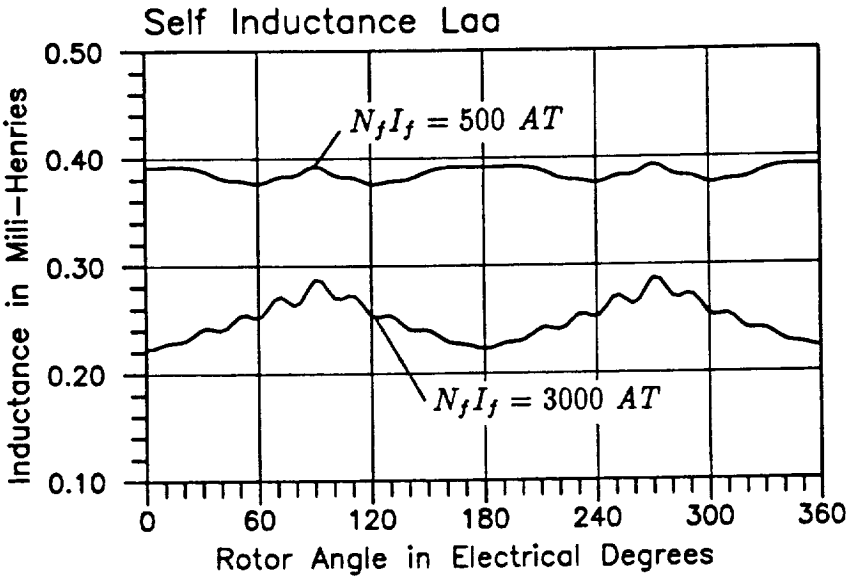

Harmonic Contents of Self Inductance L_{aa}		
Order n	Amplitude A_n ($N_f I_f$=500 AT)	Amplitude A_n ($N_f I_f$=3000 AT)
0	0.3850 mH	0.2487 mH
2	0.0043 mH	0.0247 mH
4	0.0056 mH	0.0024 mH
6	0.0032 mH	0.0028 mH
8	0.0001 mH	0.0007 mH
10	0.0007 mH	0.0008 mH
12	0.0005 mH	0.0009 mH
14	0.0001 mH	0.0007 mH
16	0.0007 mH	0.0020 mH
18	0.0010 mH	0.0040 mH
20	0.0005 mH	0.0013 mH

Figure (8.1.7) 3D-FE Computed Self Inductance L_{aa}

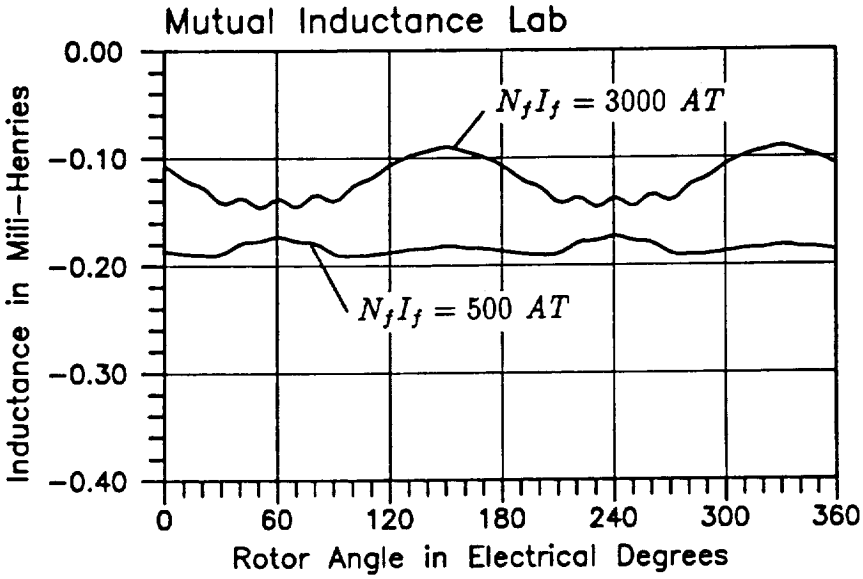

Harmonic Contents of Mutual Inductance L_{ab}		
Order n	Amplitude A_n ($N_f I_f$=500 AT)	Amplitude A_n ($N_f I_f$=3000 AT)
0	-0.1841 mH	-0.1202 mH
2	0.0030 mH	0.0264 mH
4	0.0062 mH	0.0039 mH
6	0.0016 mH	0.0014 mH
8	0.0001 mH	0.0001 mH
10	0.0007 mH	0.0007 mH
12	0.0003 mH	0.0005 mH
14	0.0000 mH	0.0003 mH
16	0.0007 mH	0.0018 mH
18	0.0005 mH	0.0020 mH
20	0.0005 mH	0.0011 mH

Figure (8.1.8) 3D-FE Computed Mutual Inductance L_{ab}

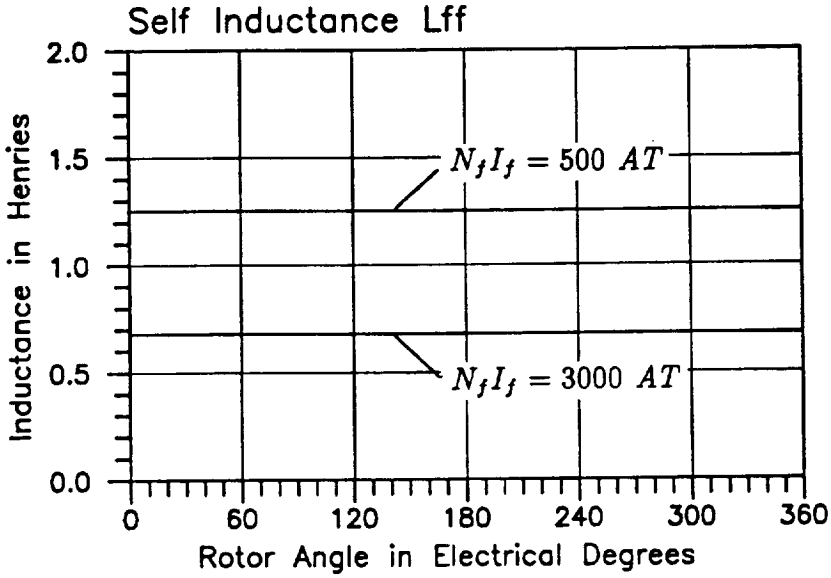

Harmonic Contents of Self Inductance L_{ff}		
Order n	Amplitude A_n ($N_f I_f$=500 AT)	Amplitude A_n ($N_f I_f$=3000 AT)
0	1.2525 H	0.6789 H
18	0.0004 H	0.0004 H

Figure (8.1.9) 3D-FE Computed Self Inductance L_{ff}

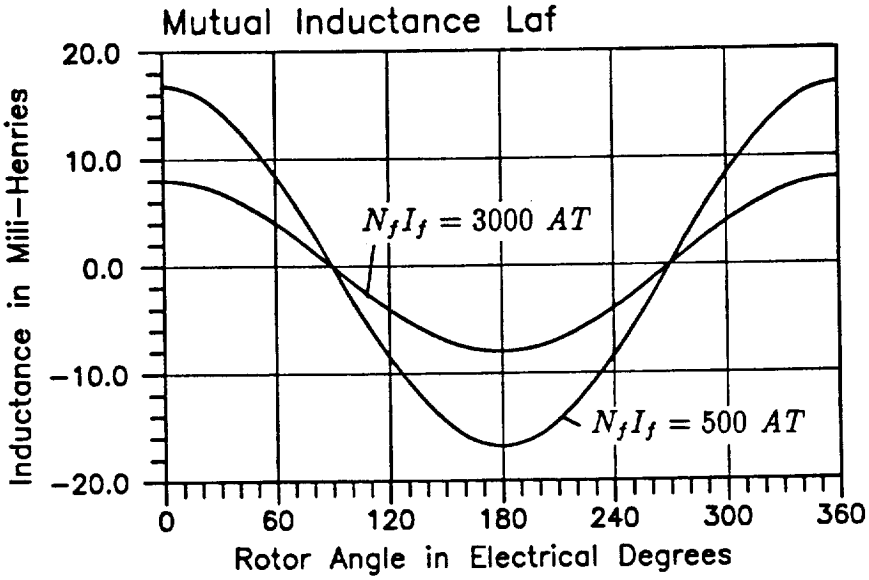

Harmonic Contents of Mutual Inductance L_{af}		
Order n	Amplitude A_n ($N_f I_f$=500 AT)	Amplitude A_n ($N_f I_f$=3000 AT)
1	16.740 mH	7.9848 mH
3	0.0060 mH	0.0065 mH
5	0.0910 mH	0.0228 mH
7	0.0471 mH	0.0143 mH
9	0.0003 mH	0.0070 mH
11	0.0081 mH	0.0060 mH
13	0.0103 mH	0.0036 mH
15	0.0004 mH	0.0050 mH
17	0.0121 mH	0.0049 mH
19	0.0097 mH	0.0039 mH

Figure (8.1.10) 3D-FE Computed Mutual Inductance L_{af}

The main incentive for computation of the apparent winding inductance terms from energy perturbation considerations is to avoid having to compute various winding flux linkages from the resulting extremely complex 3D magnetic field distributions throughout the various turns and coils of a winding. This is an extremely difficult (if not impossible) task, particularly in the presence of the very complex topologies of the 3D-FE grids which have to accompany such 3D solutions. Furthermore, it is far easier to process scalar quantities such as stored magnetic energy, rather than processing 3D vector quantities such as the flux density field, and integrating it over surfaces of 3D nature to obtain flux and flux linkages, including partial flux linkage effects.

Once these apparent self and mutual inductance terms of the windings are obtained for this type of MLA, the a, b, c, and f winding flux linkages, λ_a, λ_b, λ_c, and λ_f, can be expressed in terms of the winding currents and apparent inductances as follows:

$$\begin{bmatrix} \lambda_a \\ \lambda_b \\ \lambda_c \\ \lambda_f \end{bmatrix} = \begin{bmatrix} L_{aa} & L_{ab} & L_{ac} & L_{af} \\ L_{ba} & L_{bb} & L_{bc} & L_{bf} \\ L_{ca} & L_{cb} & L_{cc} & L_{cf} \\ L_{fa} & L_{fb} & L_{fc} & L_{ff} \end{bmatrix} \begin{bmatrix} i_a \\ i_b \\ i_c \\ i_f \end{bmatrix} \tag{8.1.7}$$

In compact matrix notation one can rewrite Equation (8.1.7) as follows:

$$\underline{\Lambda} = \underline{L} \cdot \underline{I} \tag{8.1.8}$$

where, $\underline{\Lambda}$ is the vector of winding flux linkages,

$\underline{L}$ is the matrix of apparent winding inductances,

and $\underline{I}$ is the vector of winding currents.

These apparent inductance parameters of the a, b, c, and f windings of an MLA can therefore be computed, at any desired set of currents, and any corresponding rotor position, using the present 3D-FE method based on the combined MVP-MSP formulations, see the flow chart of Figure (7.2.1). The results of such parameter computations were used to calculate the open-circuit and short-circuit characteristics of the example 14.3 kVA MLA as described next.

8.2 Computation of the Open-Circuit Voltage Characteristics and Waveforms

As stated earlier, because of the intrinsically 3D nature of the magnetic field in such MLAs, the voltages induced in the armature phase windings were directly calculated from the derivatives of the flux linkages, λ_a, λ_b, and λ_c, of the armature phase windings. These flux linkages were in turn calculated in terms of the apparent winding inductances which were computed from 3D field solutions, and the a, b, c and f winding currents as stated above in Equation (8.1.7).

It must be pointed out that the full impact of the 3D magnetic field, including its effects within the end-turn zone, as well as the impact of the peculiar rotor geometry, stator slotting and the axial nature of the flux flow on both ends of such MLAs, are incorporated in the armature flux linkage calculations through the apparent inductance terms in Equation (8.1.7), which are computed from 3D-FE field solutions. This includes the full impact of magnetic saturation throughout the various iron portions of the magnetic circuit, and the full 3D impact of the magnetic circuit's configuration.

Accordingly, under open-circuit (no-load) conditions, the phase (a) open-circuit (oc) line to neutral voltage, $v_a(oc)$, which equals the no-load induced emf in phase (a), e_a, can be expressed as follows:

$$v_a(oc) = e_a = \frac{d\lambda_a}{dt} = \frac{d(L_{af} i_f)}{dt} = (\frac{dL_{af}}{dt}) i_f + L_{af}(\frac{di_f}{dt}) \tag{8.2.1}$$

which can be rewritten as follows:

$$v_a(oc) = e_a = (\frac{dL_{af}}{d\theta})(\frac{d\theta}{dt}) i_f + L_{af}(\frac{di_f}{dt}) \tag{8.2.2}$$

where, $(d\theta/dt) = \omega$, is the instantaneous speed of the rotor in electrical radians per second.

Hence, the open-circuit line to neutral voltage for phase (a) can be expressed as follows:

$$v_a(oc) = e_a = \omega i_f(\frac{dL_{af}}{d\theta}) + L_{af}(\frac{di_f}{dt}) \tag{8.2.3}$$

Meanwhile, the field excitation current, i_f, under open-circuit no-load conditions is related to the field winding's input terminal voltage, v_f, by the following:

$$v_f = r_f i_f + \frac{d\lambda_f}{dt} = r_f i_f + \frac{d(L_{ff} i_f)}{dt} \tag{8.2.4}$$

That is,

$$v_f = r_f i_f + (\frac{dL_{ff}}{d\theta})(\frac{d\theta}{dt}) i_f + L_{ff}(\frac{di_f}{dt})$$

Hence,

$$\frac{di_f}{dt} = -[\frac{r_f}{L_{ff}} + (\frac{\omega}{L_{ff}})(\frac{dL_{ff}}{d\theta})] i_f + (\frac{1}{L_{ff}}) v_f \tag{8.2.5}$$

Solution of the differential Equation (8.2.5) subject to the proper initial conditions yields the instantaneous value of the field current and its derivative at the corresponding rotor position. In this work the field winding was energized from an ideal voltage source, v_f.

For a value of v_f = 6.83 V, the corresponding field current profile is given in Figure (8.2.1), which yields a total field excitation mmf of 980 AT. This is the excitation which was used in the 3D-FE magnetic field analysis to obtain the field winding inductance given in Figure (8.1.5). These conditions yield an open-circuit line to neutral voltage waveform, $v_a(oc)$ as given in Figure (8.2.2). Also, given in the same Figure (8.2.2) is the corresponding oscillogram of $v_a(oc)$ under the same open-circuit test conditions. Notice, the almost identical nature of the profile of the computed voltage waveform and the test voltage oscillogram. The peak value of the computed voltage waveform is 180 V, in comparison to a peak value of almost 175 V for the voltage oscillogram. Hence, the computed open-circuit voltage is not only in agreement with the test voltage profile, but also the magnitudes are in good agreement.

The validity of the computed open-circuit voltage profile is a direct indicator of the validity of the computed winding inductance profiles, which resulted from the computed 3D magnetic fields using the combined MVP-MSP solution method. A harmonic breakdown of the computed open-circuit voltage waveform for $v_a(oc)$ and its corresponding open-circuit test oscillogram is given in Table (8.2.1). Incidentally, a photograph of the example 14.3 kVA MLA during laboratory testing is displayed

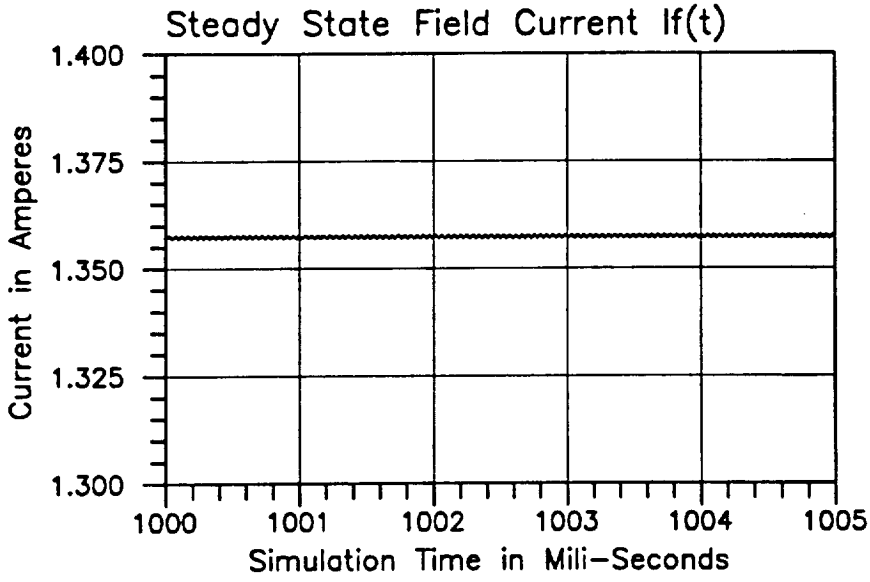

Figure (8.2.1) Steady State Field Current Under No-Load

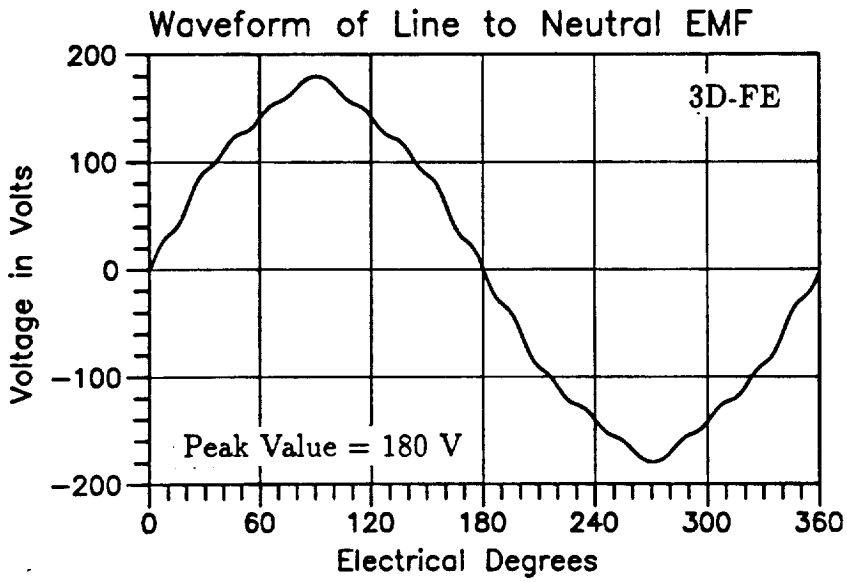

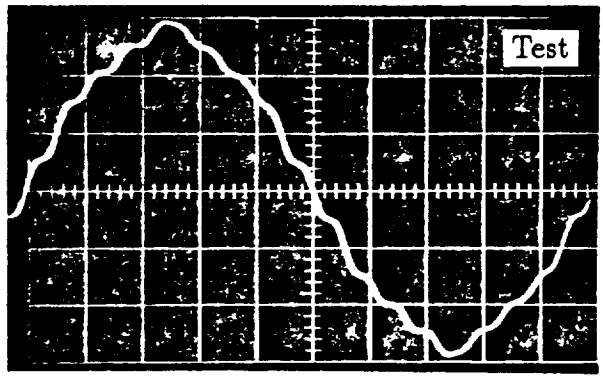

Peak Value = 175 V

Figure (8.2.2) Comparison of Computed and Test No-Load EMF Profiles

Table (8.2.1): Comparison of Computed and Test No-Load emf Harmonics

Harmonic Contents of Open-Circuit Voltage		
Order n	Amplitude A_n From 3D-FE (%)	Amplitude A_n From Test (%)
1	100.0	100.0
3	0.038	0.021
5	2.734	3.087
7	1.971	2.070
11	0.501	0.755
13	0.767	1.087
17	1.529	1.859
19	1.415	2.119

in Figure (8.2.3).

The same procedure was repeated in the computation of the line to neutral open-circuit voltage waveform, from 3D magnetic field solutions, at various field winding excitations. The corresponding rms values of the open-circuit voltages were obtained from these computed waveforms. These values are plotted in Figure (8.2.4) and shown by the square markers. The same Figure (8.2.4) contains a plot of the rms open-circuit test voltage versus field excitation mmf, excluding the effects of residual magnetism (permanent magnetism). Again, very good agreement between computed and experimental values of the open-circuit voltage is evident. This is a further strong evidence of the validity of the combined MVP-MSP method of computation of 3D magnetic fields by FE techniques, in the simultaneous presence of the strong 3D nature of the magnetic field and substantial magnetic core saturation.

8.3 Computation of Steady-State Short-Circuit Characteristics and Current Waveforms

In order to compute the steady-state short-circuit (sc) characteristics of MLAs, consider the following equation which governs the relationship between the armature and field windings' terminal voltages, v_a, v_b, v_c, and v_f, as well as the flux linkages, λ_a, λ_b, λ_c, and λ_f:

$$\begin{bmatrix} v_a \\ v_b \\ v_c \\ v_f \end{bmatrix} = \begin{bmatrix} r_a & 0 & 0 & 0 \\ 0 & r_b & 0 & 0 \\ 0 & 0 & r_c & 0 \\ 0 & 0 & 0 & r_f \end{bmatrix} \begin{bmatrix} i_a \\ i_b \\ i_c \\ i_f \end{bmatrix} + \frac{d}{dt} \begin{bmatrix} \lambda_a \\ \lambda_b \\ \lambda_c \\ \lambda_f \end{bmatrix} \tag{8.3.1}$$

where r_a, r_b, and r_c are the armature phase resistances, and r_f is the field winding resistance. Recall that the flux linkages are related to the armature and field winding currents by Equations (8.1.7) and (8.1.8). Accordingly, Equation (8.3.1) can be

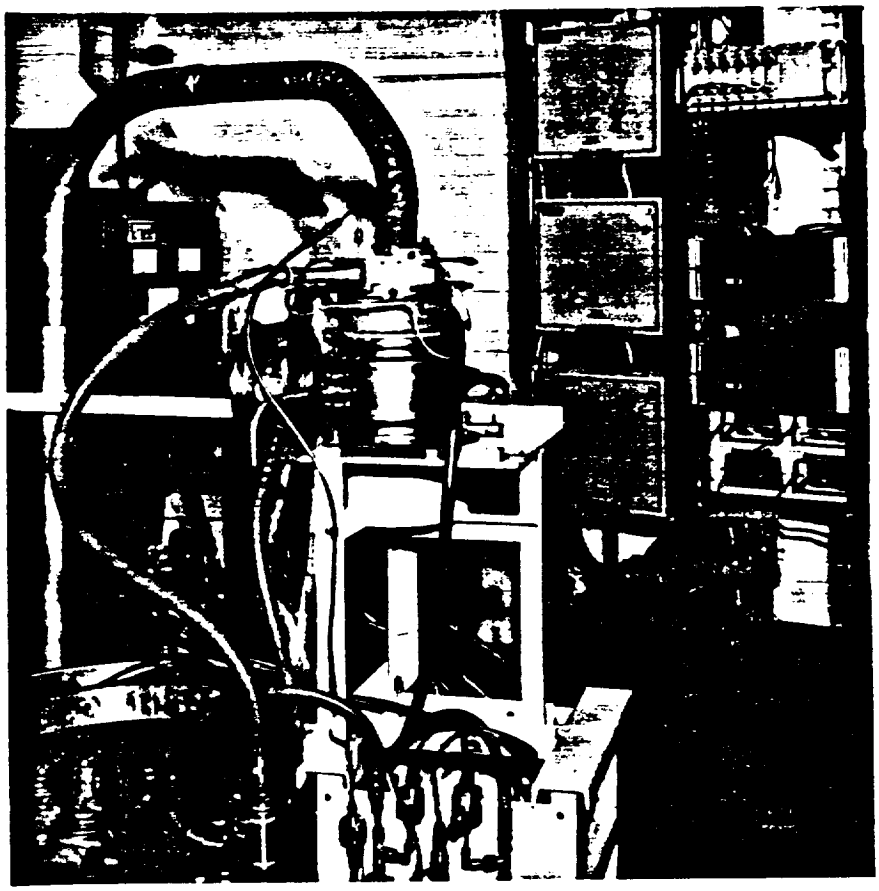

Figure (8.2.3) The 14.3 kVA MLA Under Test

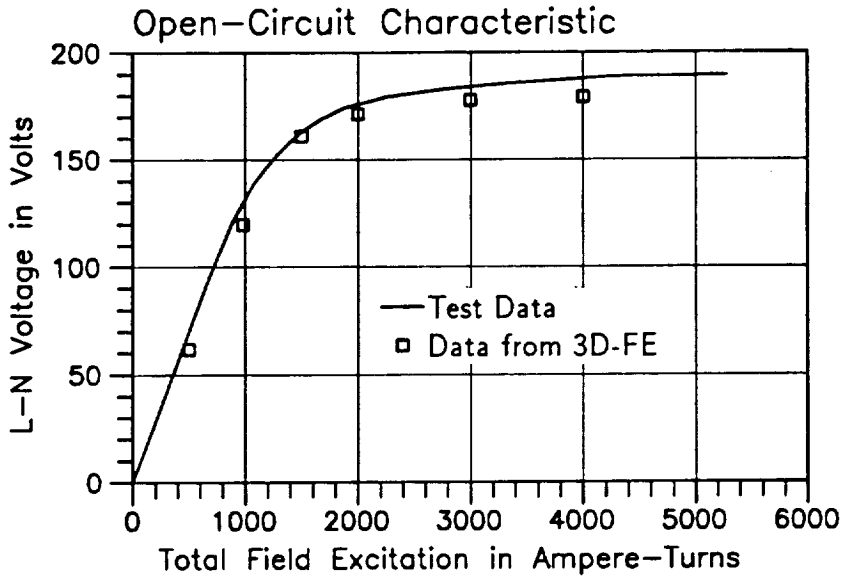

Figure (8.2.4) Open-Circuit Characteristic of the 14.3 kVA MLA

rewritten in compact matrix form as follows:

$$\underline{V} = \underline{R} \cdot \underline{I} + \frac{d}{dt}\underline{\Lambda} \tag{8.3.2}$$

where, $\underline{V}$ is the voltage vector, $\underline{I}$ is the current vector, $\underline{\Lambda}$ is the flux linkage vector, and $\underline{R}$ is the winding resistance matrix. Meanwhile, from Equation (8.1.8), one can express the current vector, $\underline{I}$ in terms of the flux linkage vector, $\underline{\Lambda}$, as follows:

$$\underline{I} = \underline{L}^{-1} \cdot \underline{\Lambda} \tag{8.3.3}$$

Substituting for $\underline{I}$ from Equation (8.3.3) into Equation (8.3.2) and rearranging yields the following:

$$\frac{d}{dt}(\underline{\Lambda}) = -\underline{R}(\underline{L}^{-1}) \cdot \underline{\Lambda} + \underline{V}$$

or

$$\dot{\underline{\Lambda}} = -\underline{R}(\underline{L}^{-1}) \cdot \underline{\Lambda} + \underline{V} \tag{8.3.4}$$

Solution of the state model Equation (8.3.4) in terms of the MLA winding flux linkages, and subsequent use of Equation (8.3.3), yield the flux linkage vector, $\underline{\Lambda}$, and the current vector, $\underline{I}$. Under three phase to neutral short circuit conditions $v_a = v_b = v_c = 0$, the state model in Equation (8.3.4) can be rewritten in expanded form as follows:

$$\begin{bmatrix} \dot{\lambda}_a \\ \dot{\lambda}_b \\ \dot{\lambda}_c \\ \dot{\lambda}_f \end{bmatrix} = - \begin{bmatrix} r_a & 0 & 0 & 0 \\ 0 & r_b & 0 & 0 \\ 0 & 0 & r_c & 0 \\ 0 & 0 & 0 & r_f \end{bmatrix} \begin{bmatrix} L_{aa} & L_{ab} & L_{ac} & L_{af} \\ L_{ba} & L_{bb} & L_{bc} & L_{bf} \\ L_{ca} & L_{cb} & L_{cc} & L_{cf} \\ L_{fa} & L_{fb} & L_{fc} & L_{ff} \end{bmatrix}^{-1} \begin{bmatrix} \lambda_a \\ \lambda_b \\ \lambda_c \\ \lambda_f \end{bmatrix} + \begin{bmatrix} 0 \\ 0 \\ 0 \\ v_f \end{bmatrix} \tag{8.3.5}$$

Numerical solution of the state Equation (8.3.5) yields the MLA's windings' flux linkage vector, $\underline{\Lambda}_{sc}$, under short-circuit conditions, from which the corresponding current

vector, $\underline{I}_{sc}$, is obtained, using the $\underline{\Lambda}$ - $\underline{I}$ relationship in Equation (8.3.3). Notice that the MLA windings' apparent inductance matrix, $\underline{L}$, is a function of the armature and field currents, as well as the corresponding rotor position.

Implementation of the numerical solution of Equation (8.3.5) governing the MLA's characteristics under steady-state short-circuit conditions can best be understood by means of the algorithms' steps outlined in Figure (8.3.1). Notice that solution of Equation (8.3.5) is coupled to the 3D magnetic field and winding inductance computation and 3D field effects on the steady state short-circuit characteristics. The algorithm can be explained as follows:

Step (1): Obtain the profiles of winding currents, i_a, i_b, i_c, and i_f, by the state space model, Equation (8.3.5), using unsaturated inductance values obtained under no-load conditions.

Step (2): Compute the 3D magnetic field throughout the MLA magnetic circuit to obtain a set of updated inductances at a series of rotor position angles covering 360° electrical. In this step, the excitation currents of the magnetic field model, namely, i_a, i_b, i_c, and i_f corresponding to a given rotor position must be taken from the current profiles of Step (1), or from the updated current profiles of Step (4). Also, in this step full account of magnetic nonlinearity must be taken into the 3D-FE computations to include any possible effects of magnetic circuit saturation on the MLA inductances.

Step (3): Using updated inductance values from Step (2), re-compute profiles of i_a, i_b, i_c, and i_f through numerical integration of the state space model in Equation (8.3.5).

Step (4): Check whether the change in the rms values of i_a, i_b, i_c, and i_f from the previous iteration is ≤ 0.5 per cent. If "No", use the updated current profiles to begin a new iteration, that is go to Step (2). If "Yes", output desired results, stop.

The steady-state part of the solution of Equation (8.3.5), using the algorithm described above yields the steady-state short-circuit armature currents and characteristics of a given MLA at a given field excitation voltage, v_f. The steady-state short-circuit waveforms for i_a, i_b, and i_c were obtained at a field excitation mmf of 980 AT for the 14.3 kVA MLA example, and are shown in Figure (8.3.2-a,b,c), respectively. The corresponding field excitation current profile is given in Figure (8.3.3). Notice the presence of a sustained ripple effect in the field winding's current profile,

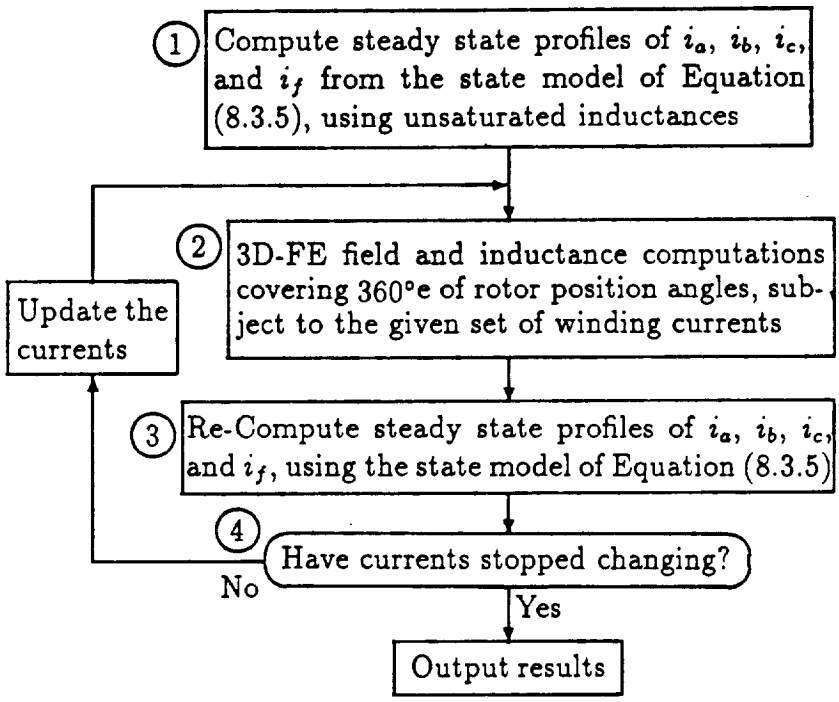

Figure (8.3.1) Flow Chart of Short-Circuit Simulation Procedure

(a)

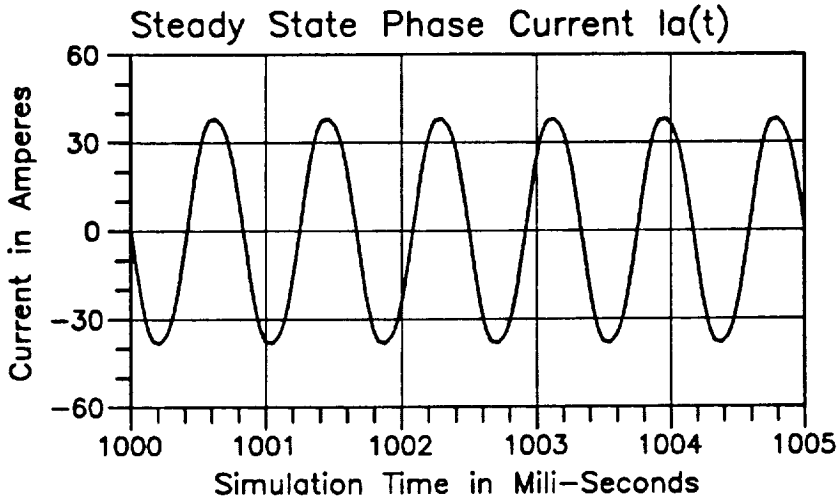

(b)

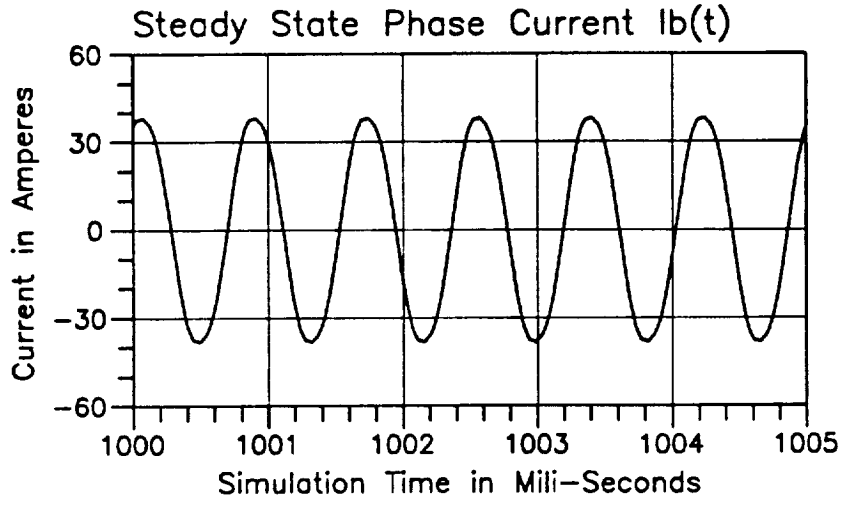

(c)

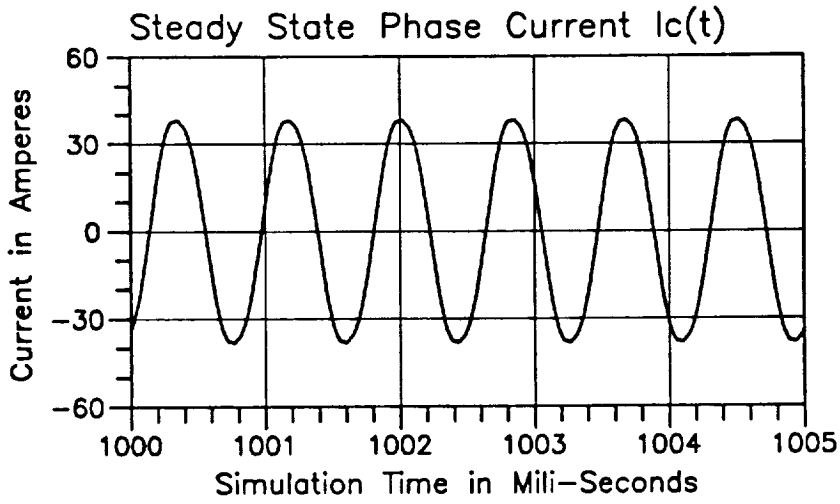

Figure (8.3.2) Profiles of Steady State Short-Circuit Phase Currents

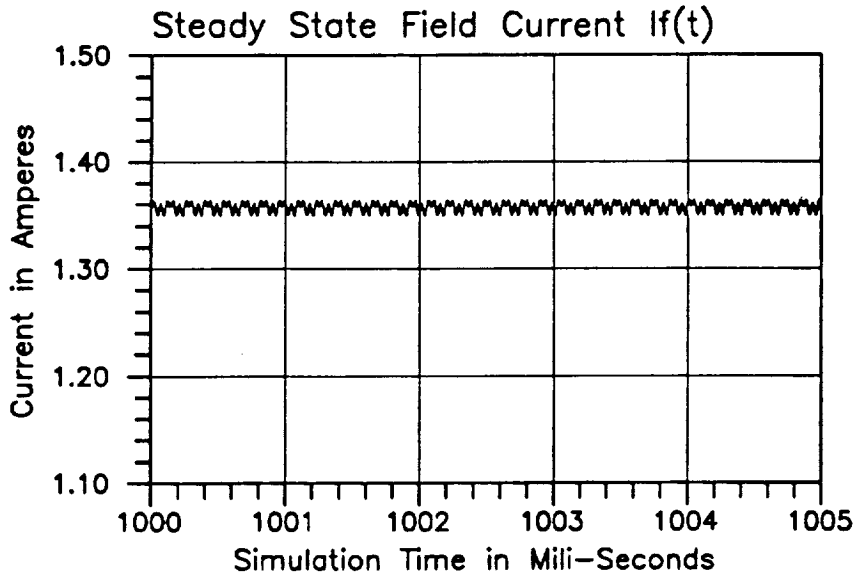

Figure (8.3.3) Profile of Steady State Field Current Under Short-Circuit

caused by the rotor's peculiar magnetic circuit configuration as well as stator core slotting.

These simulations of the steady-state short-circuit conditions were repeated for various values of field excitation voltage (various values of field mmf), and the resulting steady-state rms values of the armature short-circuit current were plotted versus the total field mmf. These results are shown by the square markers in Figure (8.3.4). Also plotted in Figure (8.3.4) are the results of an actual steady-state short-circuit test which was performed earlier [3] on the example 14.3 kVA MLA excluding the effect of residual magnetism (permanent magnetism). These test results compare very favorably with the 3D-FE based computation of the steady-state short circuit characteristic. This is a further evidence of the validity and soundness of the short-circuit model of Equation (8.3.5), and more importantly it validates the combined MVP-MSP based 3D-FE method of computing the magnetic field and winding inductances for performance calculations in this type of MLAs.

Graphical representations of the flux density, $\overline{B}$, by means of vector arrows of the flux density distributions along a longitudinal cross-section in the 14.3 kVA MLA, and perpendicular to the axis of rotation, are shown in Figures (8.3.5-a,b) as well as (8.3.6-a,b) for the no-load and short-circuit conditions, under the same field mmf of 980 AT. As can be seen and expected from examination of the $\overline{B}$ arrow orientations, the main flux crosses the main airgap into the armature region under no-load, while this main flux is largely deflected from the armature region under short-circuit conditions. This is a direct result of the strong demagnetizing armature reaction (mmf) which is expected under short-circuit conditions. These graphical displays of the $\overline{B}$ field are further confirmation of the soundness of the 3D field solutions at hand.

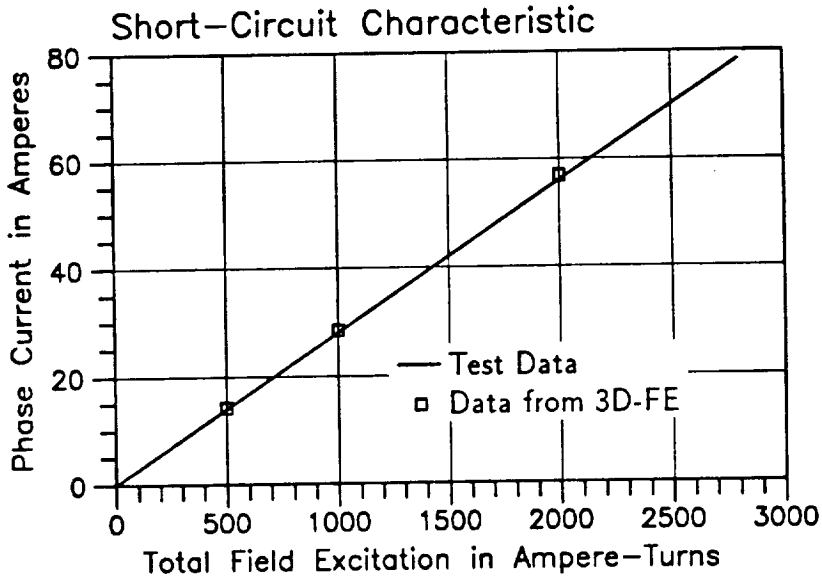

Figure (8.3.4) Short-Circuit Characteristic of the 14.3 kVA MLA

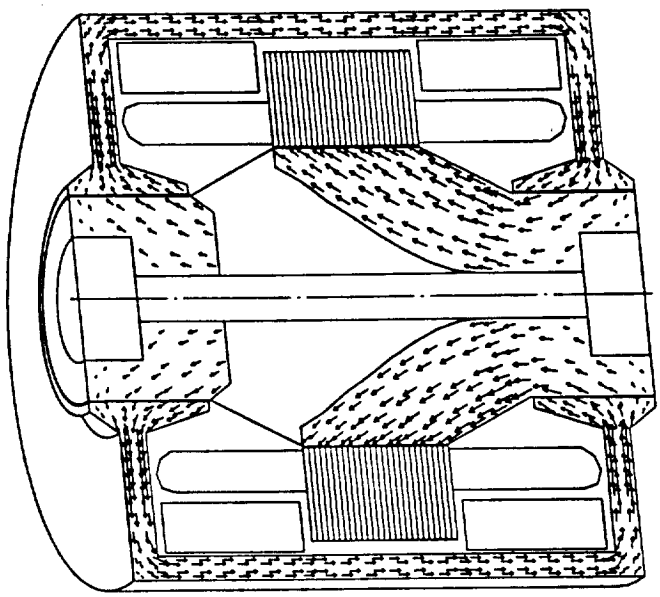

(a) No-Load Condition $|\overline{B}| = 1.4$ Telsa

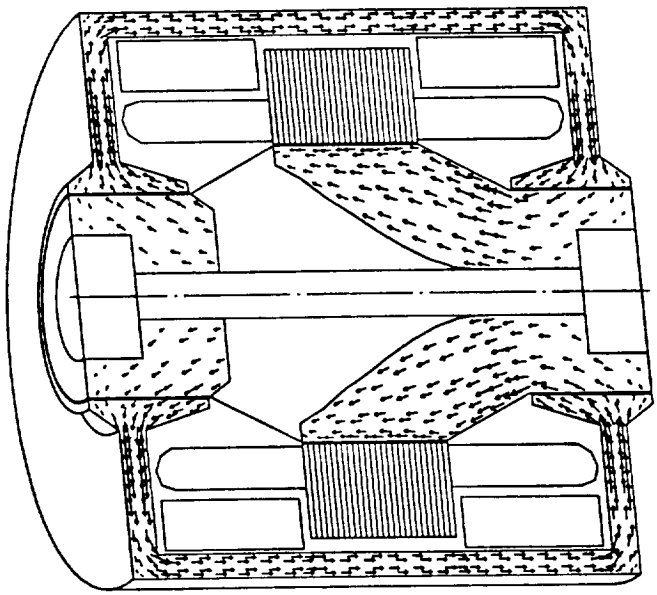

(b) Short-Circuit Condition $|\overline{B}| = 0.073$ Telsa

Figure (8.3.5) Flux Flow Pattern Along a Longitudinal Cross-Section

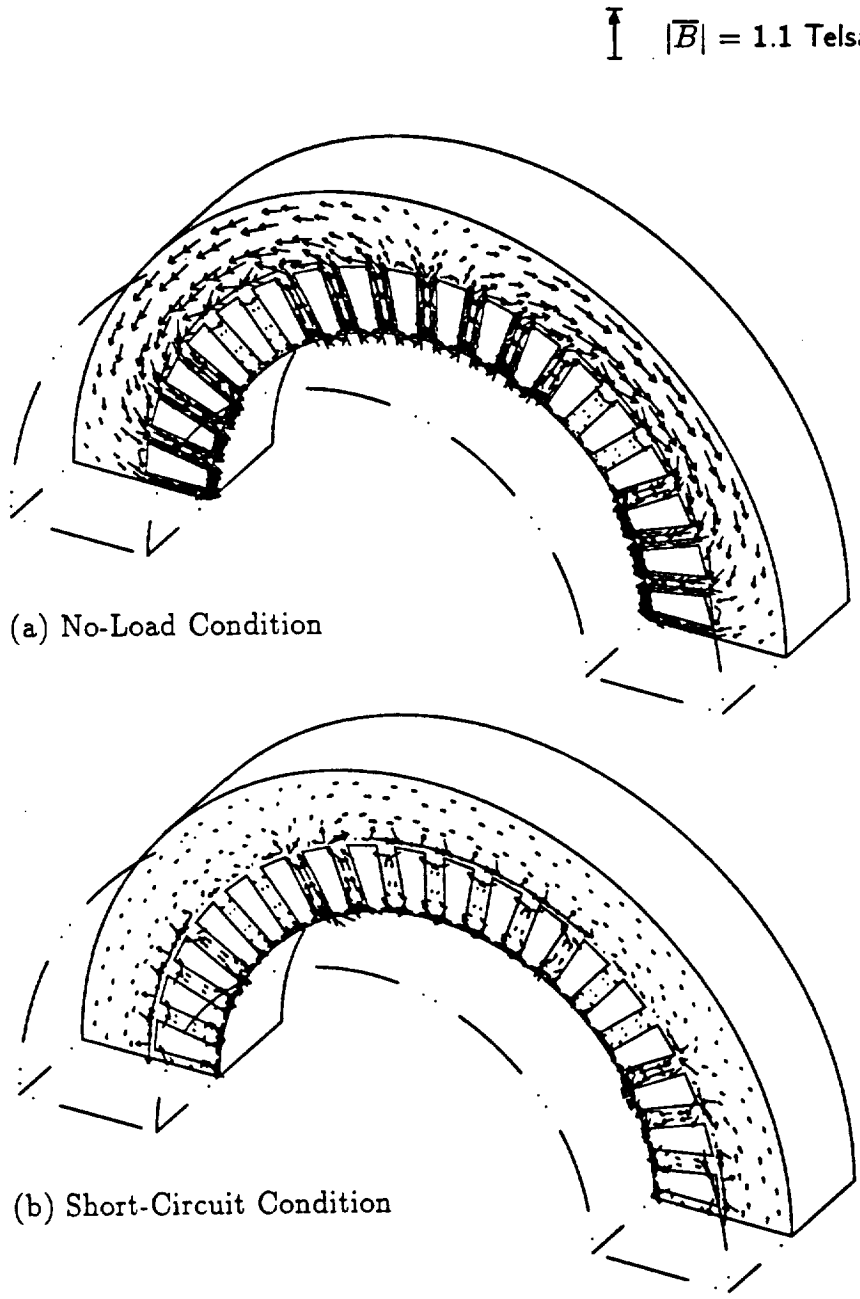

Figure (8.3.6) Flux Flow Pattern in the Mid-Plane Cross-Section of the Stator Core

8.4 Computation of Synchronous Reactances of the Example 14.3 kVA MLA from Test and 3D-FE Based Results

Conventional synchronous machine theory [88], and standard methods of calculation of direct-axis synchronous reactance, x_d, enable one to state the following:

$$x_d(sc) = \frac{E(oc)}{I(sc)} \tag{8.4.1}$$

where $E(oc)$ is the open-circuit voltage for a given field excitation current, I_f, and $I(sc)$ is the steady-state short-circuit armature current obtained at the same field excitation, I_f, associated with $E(oc)$.

The open-circuit and short-circuit test data of Figures (8.2.2) and (8.3.4) yield values of $E(oc)$ and $I(sc)$ of 67.0 volts and 14.0 amperes, respectively, at a field excitation mmf of 500 AT, which is a value of field mmf that is well within the unsaturated range of the magnetic circuit of the example 14.3 kVA MLA. Hence, using Equation (8.4.1) results in a direct axis synchronous reactance, $x_d = 4.78\ \Omega$ (test). Meanwhile, the 3D-FE magnetic field solutions and the resulting computed open-circuit and short-circuit characteristics yield values of $E(oc)$ and $I(sc)$ of 61.8 volts and 14.21 amperes, respectively, at the same field excitation of mmf of 500 AT. Hence this results in an $x_d = 4.35\ \Omega$ (3D-FE). The two values of x_d of 4.78 Ω and 4.35 Ω are well within 9% in the normal range of combined instrumentation error, and variations in the $B - H$ characteristics of the rotor and stator iron cores which result from heat treatments associated with the bimetallic rotor manufacturing process.

Another method of computation of the direct axis and quadrature axis synchronous reactances, x_d and x_q, from the results of the 3D-FE field solution and winding inductance computations is now presented and used for further comparison. This method is based on the well-known conventional Park's d-q theory and transformation [88]. This theory is based on the inherent d-q transformation assumption that the armature mmfs, field mmf, and resulting flux density waveforms produced by each winding a, b, c, and f, in a synchronous machine are sinusoidally distributed around the circumference of the airgap with no harmonics. Park's theory assumes that saturation is neglected. This is of course not the case for the 14.3 kVA MLA.

Nevertheless, idealized d-q theory will be used here for the sake of gaining some physical insight into the numbers. In this d-q theory the self and mutual inductances, $L_{aa}(\theta)$ and $L_{ab}(\theta)$, can be expressed as follows [88]:

$$L_{aa}(\theta) = L_{sa} + L_{sv}Cos(2\theta) \tag{8.4.2}$$

and

$$L_{ab}(\theta) = -L_{ma} + L_{mv}Cos(2\theta - 2\pi/3) \tag{8.4.3}$$

Comparing Equation (8.4.2) with Equation (8.1.4) one can see that the following can be stated (see the tabulation of harmonic breakdown of $L_{aa}(\theta)$ in Figure (8.1.7) for the case of 500 AT field excitation):

$$L_{sa} = A_0 = 0.3850\,mH \quad \text{and} \quad L_{sv} = A_2 = 0.0043\,mH$$

Meanwhile, comparing Equation (8.4.3) with Equation (8.1.5) one can see that (see the tabulation of harmonic breakdown of $L_{ab}(\theta)$ in Figure (8.1.8) for the case of 500 AT field excitation):

$$L_{ma} = -A_0 = 0.1841\,mH \quad \text{and} \quad L_{mv} = A_2 = 0.0030\,mH$$

From the algebraic development of Park's d-q transformation, and the theory surrounding it [88], it is well known that the direct and quadrature axes synchronous inductances can be expressed in terms of L_{sa}, L_{sv}, L_{ma} and L_{mv} as follows:

$$L_d = (L_{sa} + L_{ma}) + (1/2L_{sv} + L_{mv}) = 0.5743\,mH \tag{8.4.4}$$

and

$$L_q = (L_{sa} + L_{ma}) - (1/2L_{sv} + L_{mv}) = 0.5640\,mH \tag{8.4.5}$$

Meanwhile,

$$x_d = \omega L_d = 2\pi f L_d = 4.33\,\Omega \tag{8.4.6}$$

and

$$x_q = \omega L_q = 2\pi f L_q = 4.25\,\Omega \tag{8.4.7}$$

Certainly, the value of x_d, computed from 3D-FE data and Parks formulation, compares well with that obtained from 3D-FE data and the resulting open-circuit and short-circuit simulations, which yield an $x_d = 4.35\ \Omega$.

Meanwhile, the L_d and L_q expressions in Equations (8.4.4) and (8.4.5) were also applied to the open-circuit cases with 980 AT field excitation, and 3000 AT field excitation, respectively. That is, the values of the self and mutual inductances of L_{sa}, L_{ma}, L_{sv}, and L_{mv} in Equations (8.4.4) and (8.4.5) are taken from the inductance tabulations in Figures (8.1.3) and (8.1.4) for the case of 980 AT, and from the inductance tabulations in Figures (8.1.7) and (8.1.8) for the case of 3000 AT, respectively. The calculated values of x_d and x_q versus different field excitations are listed in Table (8.4.1). As expected, the computed $d-q$ type reactance values decreased as the higher field excitations drive the magnetic circuit of the MLA into higher levels of saturation. The above results certainly present further evidence on the soundness and validity of the 3D-FE magnetic field computation programs, and the associated post-processors which generate the necessary MLA parameters, and other performance characteristics such as open-circuit and short-circuit simulations, etc.

8.5 Effect of Geometric Design Alterations on Performance Characteristics from 3D-FE Magnetic Field Computations

In this section, a demonstration of use of the 3D-FE magnetic field computation program in the determination of the effects of magnetic circuit design changes (or alterations) on the performance of MLAs such as the example 14.3 kVA unit is presented. This is done here through the calculation of the impact of an increase in the axial stator core length from 4.19 cm to 5.33 cm, which is about 27% longer. The rotor is also stretched correspondingly. Meanwhile, the radial dimensions such as various diameters in the magnetic circuit and windings are kept constant at their original values.

Table (8.4.1): Effects of Magnetic Saturation on $d-q$ Type Inductances

Field Excitation	X_d	X_q
500 AT	4.33 Ω	4.25 Ω
980 AT	4.21 Ω	4.12 Ω
3000 AT	2.89 Ω	2.75 Ω
Computed by 3D-FE at No-Load Conditions		

The resulting open-circuit characteristic obtained from 3D-FE magnetic field solutions, for the altered MLA design with a stator stack of 5.33 cm, is compared in Figure (8.5.1) with the corresponding 3D-FE computed open-circuit characteristic of the original 4.19 cm long stator core case of the 14.3 kVA-MLA. As can be expected, the resulting increase in magnetic circuit reluctance of the altered MLA design is in the portions of the magnetic circuit in which the predominant orientation of flux flow is axial, consequent to the stretch of the stack by 27%. Only a modest increase in the open-circuit voltage of about 8% to 9% is predicted. This is despite the fact that the magnetic reluctance was reduced in portions of the magnetic circuit in which the predominant flux orientation is radial and circumferential, such as in the stator armature core and rotor pole area near the main airgap. The lack of proportionate increase in the open circuit voltage is a further strong evidence of the 3D nature of the magnetic field in the example MLA, in which flux flow orientations are a mix of radial, axial, and circumferential directions in their nature.

If the magnetic flux flow was predominantly radial and circumferential, as the case would be in generators with conventional rotor mounted radial field excitation design, an increase of 27% in the stack length would have caused an increase of about the same percentage in the voltage induced in the armature conductors for the same main airgap radial height and same excitation field mmf. Thus, one can see the effect of predominance of the axial flow portion of the flux path in precluding such an increase (27%) in the armature induced voltage (only 8% to 9%) in this case.

Furthermore, radial flux density waveforms in the main airgap were computed for a field mmf = 980 AT, at a location midway along the length of the stator stack, that is at z =0. These flux density waveforms are shown in Figure (8.5.2) in the cases of 4.19 cm and 5.33 cm armature stack lengths, respectively. Notice the reduction in the flux densities for the longer stack length of 5.33 cm in comparison with those flux densities for a stack length of 4.19 cm. This is a confirmation of the predominance of an axial flux flow nature in the magnetic field in this type of MLAs. These present computer codes of the combined MVP-MSP method for solving the 3D magnetic field in MLAs can be used further to vary other dimensions, slotting and winding arrangements, as well as material characteristics, and assess their impact on the performance of various MLA designs and performance characteristics. Thus, these computer programs can serve as an excellent design tool in obtaining or searching for the best possible designs of such MLAs. Use of this method and resulting computer

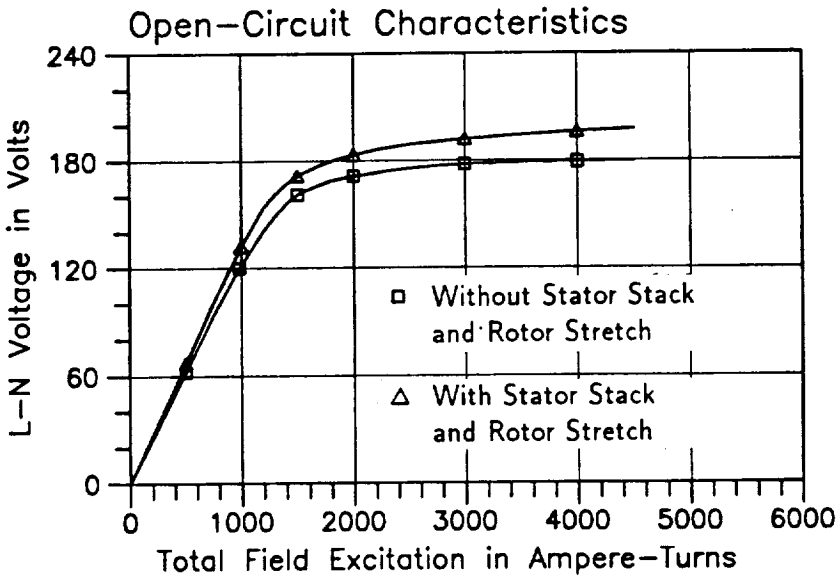

Figure (8.5.1) Effects of Stator and Rotor Stretch on Open-Circuit EMF

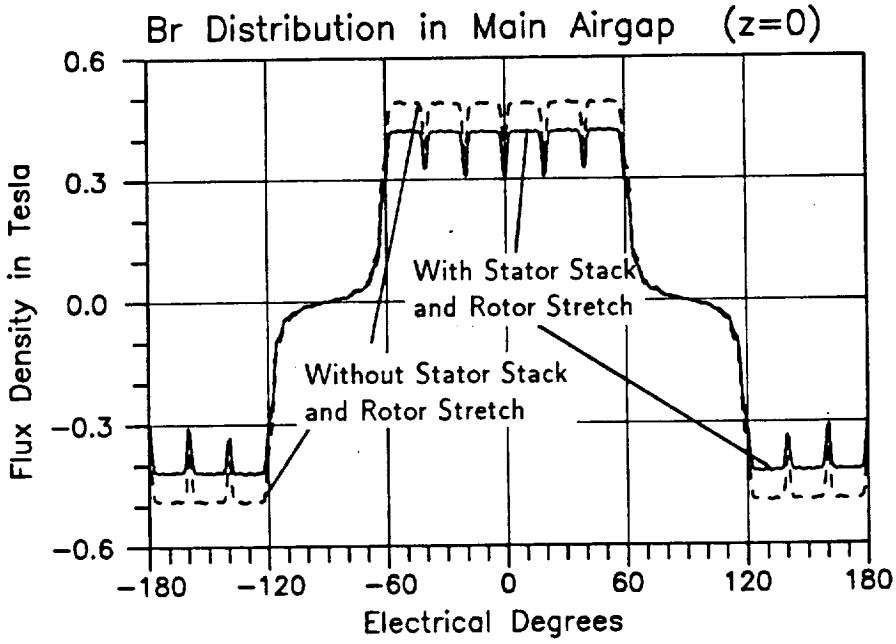

Figure (8.5.2) Effects of Stator and Rotor Stretch on Mid-Airgap B_r Distribution

programs, in computation of the performance of such MLAs under load conditions, is demonstrated next.

Chapter 9

MLA Load Performance Simulations

Because of the periodic, yet nonsinusoidal nature of the flux distributions and winding inductances with substantially high harmonic content, the anticipated armature currents and terminal voltages of the MLA under load conditions are periodic, yet nonsinusoidal in their nature, when such an MLA is supplying an isolated 3-phase static load. Hence, the resulting electromagnetic torque contains substantial ripples, which cannot be ignored in vibration considerations associated with the design of the space station's structure. Consequently, steady-state frequency-domain ac phasor concepts are not used in the determination of load performance characteristics of such MLAs, which result in a uniform torque with no ripples, and are only based on pure sinusoidal voltages and currents. Thus, as stated earlier in Section 1.3, the d-q theory and accompanying phasor diagrams, stemming from Park's transformation, which are based on pure sinusoidal spatial flux and mmf distributions cannot be the basic tool for use in this work. The natural abc phase windings' frame of reference was chosen to form the basis of the present method.

The method of determination of the periodic nonsinusoidal armature currents and voltages (load characteristics) is based on obtaining the steady-state (forced solution) portion of the current-voltage governing differential equations (state model). It is well known that the damper effects, due to induced eddy currents in machines with solid metallic rotors or damper windings, play a significant role only in shaping the solution of the differential equations during the subtransient and transient periods. Therefore, the steady state periodic nonsinusoidal solution of the MLA's state model was obtained excluding rotor damping. Only R-L type loads are included in the results presented in this chapter. The MLA-load system schematic is shown in Figure (9.0.1). The well known consumer notation (or load) is used throughout this investigation.

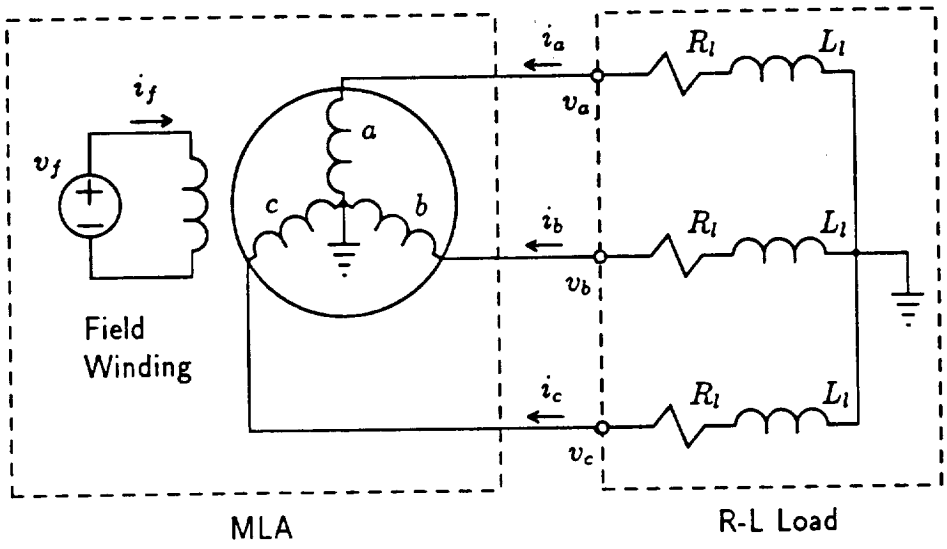

Figure (9.0.1) The 14.3 kVA MLA Load Test Schematic

9.1 Determination of Periodic Nonsinusoidal Steady-State Voltage and Current Waveforms

The main interest lies in the sustained steady-state periodic nonsinusoidal (or forced) solution of the state model equations, which govern the instantaneous relationships between the voltages and currents of the MLA armature and field windings under load conditions. This set of governing differential equations can be written in compact matrix form, using the consumer notation in terms of the voltages, currents and flux linkages of the armature phase windings, a, b, and c, as well as the field winding, f, as follows:

$$\underline{V} = \underline{R}_m \cdot \underline{I} + \frac{d}{dt}(\underline{\Lambda}_m) \tag{9.1.1}$$

and

$$\underline{\Lambda}_m = \underline{L}_m \cdot \underline{I} \tag{9.1.2}$$

or

$$\underline{I} = \underline{\mathrm{L}}_m^{-1} \cdot \underline{\Lambda}_m \tag{9.1.3}$$

where, $\underline{V}$ is the vector of machine windings' terminal voltages,
$\underline{I}$ is the vector of machine windings' currents,
$\underline{R}_m$ is the machine windings' resistance matrix,
$\underline{L}_m$ is the machine windings' apparent inductance matrix, computed from global 3D-FE magnetic field results using the combined MVP-MSP solution method,
and $\underline{\Lambda}_m$ is the vector of machine windings' flux linkages.

All these physical quantities, $\underline{V}$, $\underline{I}$, $\underline{\Lambda}_m$, and $\underline{L}_m$, are instantaneous values. It should be emphasized that the effects of space harmonics and magnetic saturation under load are fully included in the coefficients of the machine inductance matrix, $\underline{L}_m$. These apparent inductance coefficients were obtained from a set of successive 3D-FE field solutions at rotor position angles which covered a complete 360°e. Each one of these 3D-FE field solutions and corresponding inductance computations were

obtained at these rotor positions with their corresponding sets of armature and field currents. Notice that currents are taken positive when flowing into the terminals of the windings of the MLA, Figure (9.0.1).

In expanded matrix form Equations (9.1.1) through (9.1.3) can be rewritten as follows:

$$\begin{bmatrix} v_a \\ v_b \\ v_c \\ v_f \end{bmatrix} = \begin{bmatrix} r_s & 0 & 0 & 0 \\ 0 & r_s & 0 & 0 \\ 0 & 0 & r_s & 0 \\ 0 & 0 & 0 & r_f \end{bmatrix} \cdot \begin{bmatrix} i_a \\ i_b \\ i_c \\ i_f \end{bmatrix} + \frac{d}{dt} \begin{bmatrix} \lambda_{am} \\ \lambda_{bm} \\ \lambda_{cm} \\ \lambda_{fm} \end{bmatrix} \tag{9.1.4}$$

and

$$\begin{bmatrix} \lambda_{am} \\ \lambda_{bm} \\ \lambda_{cm} \\ \lambda_{fm} \end{bmatrix} = \begin{bmatrix} L_{aa} & L_{ab} & L_{ac} & L_{af} \\ L_{ba} & L_{bb} & L_{bc} & L_{bf} \\ L_{ca} & L_{cb} & L_{cc} & L_{cf} \\ L_{fa} & L_{fb} & L_{fc} & L_{ff} \end{bmatrix} \cdot \begin{bmatrix} i_a \\ i_b \\ i_c \\ i_f \end{bmatrix} \tag{9.1.5}$$

or

$$\begin{bmatrix} i_a \\ i_b \\ i_c \\ i_f \end{bmatrix} = \begin{bmatrix} L_{aa} & L_{ab} & L_{ac} & L_{af} \\ L_{ba} & L_{bb} & L_{bc} & L_{bf} \\ L_{ca} & L_{cb} & L_{cc} & L_{cf} \\ L_{fa} & L_{fb} & L_{fc} & L_{ff} \end{bmatrix}^{-1} \cdot \begin{bmatrix} \lambda_{am} \\ \lambda_{bm} \\ \lambda_{cm} \\ \lambda_{fm} \end{bmatrix} \tag{9.1.6}$$

For a given set of terminal voltages, $\underline{V} = [v_a\ v_b\ v_c\ v_f]^t$, the state Equation (9.1.1) can be rewritten using Equation (9.1.3) as follows:

$$\underline{V} = \underline{R}_m \cdot (\underline{L}_m^{-1} \cdot \underline{\Lambda}_m) + \dot{\underline{\Lambda}}_m \tag{9.1.7}$$

or

$$\dot{\underline{\Lambda}}_m = -(\underline{R}_m \cdot \underline{L}_m^{-1})\underline{\Lambda}_m + \underline{V} \tag{9.1.8}$$

Equation (9.1.8) constitutes the state model of the MLA in terms of flux linkages. Again, $\underline{L}_m$ is rotor position dependent (all significant space harmonics included), including full impact of magnetic saturation. Meanwhile, Equation (9.1.3) relates the flux linkages to the currents. In expanded form Equation (9.1.8) can be rewritten as follows:

$$\begin{bmatrix} \dot{\lambda}_{am} \\ \dot{\lambda}_{bm} \\ \dot{\lambda}_{cm} \\ \dot{\lambda}_{fm} \end{bmatrix} = - \begin{bmatrix} r_s & 0 & 0 & 0 \\ 0 & r_s & 0 & 0 \\ 0 & 0 & r_s & 0 \\ 0 & 0 & 0 & r_f \end{bmatrix} \begin{bmatrix} L_{aa} & L_{ab} & L_{ac} & L_{af} \\ L_{ba} & L_{bb} & L_{bc} & L_{bf} \\ L_{ca} & L_{cb} & L_{cc} & L_{cf} \\ L_{fa} & L_{fb} & L_{fc} & L_{ff} \end{bmatrix}^{-1} \cdot \begin{bmatrix} \lambda_a \\ \lambda_b \\ \lambda_c \\ \lambda_f \end{bmatrix} + \begin{bmatrix} v_a \\ v_b \\ v_c \\ v_f \end{bmatrix} \tag{9.1.9}$$

If a given MLA is connected to an isolated three phase Y-connected balanced load of resistance, r_l, and inductance, L_l, per phase, see the network schematic in Figure (9.0.1), the a, b, and c armature terminal voltages, v_a, v_b, and v_c, can be expressed in terms of the MLA's phase currents, i_a, i_b, and i_c, as follows:

$$\begin{bmatrix} v_a \\ v_b \\ v_c \end{bmatrix} = - \begin{bmatrix} r_l & 0 & 0 \\ 0 & r_l & 0 \\ 0 & 0 & r_l \end{bmatrix} \cdot \begin{bmatrix} i_a \\ i_b \\ i_c \end{bmatrix} - \frac{d}{dt} \begin{bmatrix} \lambda_{al} \\ \lambda_{bl} \\ \lambda_{cl} \end{bmatrix} \tag{9.1.10}$$

where

$$\begin{bmatrix} \lambda_{al} \\ \lambda_{bl} \\ \lambda_{cl} \end{bmatrix} = \begin{bmatrix} L_l & 0 & 0 \\ 0 & L_l & 0 \\ 0 & 0 & L_l \end{bmatrix} \cdot \begin{bmatrix} i_a \\ i_b \\ i_c \end{bmatrix} \tag{9.1.11}$$

Substituting for $[v_a\ v_b\ v_c]^t$ from Equation (9.1.10) into Equation (9.1.4), and rearranging gives the following:

$$\begin{bmatrix} 0 \\ 0 \\ 0 \\ v_f \end{bmatrix} = \begin{bmatrix} (r_s + r_l) & 0 & 0 & 0 \\ 0 & (r_s + r_l) & 0 & 0 \\ 0 & 0 & (r_s + r_l) & 0 \\ 0 & 0 & 0 & r_f \end{bmatrix} \cdot \begin{bmatrix} i_a \\ i_b \\ i_c \\ i_f \end{bmatrix} + \frac{d}{dt} \begin{bmatrix} \lambda_a \\ \lambda_b \\ \lambda_c \\ \lambda_f \end{bmatrix} \tag{9.1.12}$$

where,

$$\begin{bmatrix} \lambda_a \\ \lambda_b \\ \lambda_c \\ \lambda_f \end{bmatrix} = \begin{bmatrix} (\lambda_{am} + \lambda_{al}) \\ (\lambda_{bm} + \lambda_{bl}) \\ (\lambda_{cm} + \lambda_{cl}) \\ (\lambda_{fm}) \end{bmatrix}$$

$$= \begin{bmatrix} (L_{aa} + L_l) & L_{ab} & L_{ac} & L_{af} \\ L_{ba} & (L_{bb} + L_l) & L_{bc} & L_{bf} \\ L_{ca} & L_{cb} & (L_{cc} + L_l) & L_{cf} \\ L_{fa} & L_{fb} & L_{fc} & L_{ff} \end{bmatrix} \cdot \begin{bmatrix} i_a \\ i_b \\ i_c \\ i_f \end{bmatrix} \tag{9.1.13}$$

or

$$\begin{bmatrix} i_a \\ i_b \\ i_c \\ i_f \end{bmatrix} = \begin{bmatrix} (L_{aa}+L_l) & L_{ab} & L_{ac} & L_{af} \\ L_{ba} & (L_{bb}+L_l) & L_{bc} & L_{bf} \\ L_{ca} & L_{cb} & (L_{cc}+L_l) & L_{cf} \\ L_{fa} & L_{fb} & L_{fc} & L_{ff} \end{bmatrix}^{-1} \begin{bmatrix} \lambda_a \\ \lambda_b \\ \lambda_c \\ \lambda_f \end{bmatrix} \tag{9.1.14}$$

Accordingly, the overall MLA state model equation in terms of the total flux linkages, λ_a, λ_b, λ_c, and λ_f, including load effect, can be written as follows:

$$\begin{bmatrix} \dot{\lambda}_a \\ \dot{\lambda}_b \\ \dot{\lambda}_c \\ \dot{\lambda}_f \end{bmatrix} = - \begin{bmatrix} (r_s+r_l) & 0 & 0 & 0 \\ 0 & (r_s+r_l) & 0 & 0 \\ 0 & 0 & (r_s+r_l) & 0 \\ 0 & 0 & 0 & r_f \end{bmatrix} \cdot$$

$$\begin{bmatrix} (L_{aa}+L_l) & L_{ab} & L_{ac} & L_{af} \\ L_{ba} & (L_{bb}+L_l) & L_{bc} & L_{bf} \\ L_{ca} & L_{cb} & (L_{cc}+L_l) & L_{cf} \\ L_{fa} & L_{fb} & L_{fc} & L_{ff} \end{bmatrix}^{-1} \cdot \begin{bmatrix} \lambda_a \\ \lambda_b \\ \lambda_c \\ \lambda_f \end{bmatrix} + \begin{bmatrix} 0 \\ 0 \\ 0 \\ v_f \end{bmatrix} \tag{9.1.15}$$

Equations (9.1.13) through (9.1.15) constitute the main model of an MLA supplying an isolated three phase balanced load. In compact matrix form these equations can be rewritten as follows:

$$\underline{\Lambda} = \underline{L} \cdot \underline{I} \tag{9.1.16}$$

$$\underline{I} = \underline{L}^{-1} \cdot \underline{\Lambda} \tag{9.1.17}$$

and

$$\dot{\underline{\Lambda}} = -\underline{R} \cdot \underline{L}^{-1} \cdot \underline{\Lambda} + \underline{V} \tag{9.1.18}$$

Differentiating Equation (9.1.16) with respect to time yields the following:

$$\dot{\underline{\Lambda}} = \omega \hat{\underline{L}} \cdot \underline{I} + \underline{L} \cdot \dot{\underline{I}} \tag{9.1.19}$$

where, $\hat{\underline{L}} = (d\underline{L}/d\theta)$ and $\omega = d\theta/dt$, from which it follows that:

$$\dot{\underline{I}} = \underline{L}^{-1} \cdot \dot{\underline{\Lambda}} - \omega(\underline{L}^{-1} \cdot \hat{\underline{L}}) \cdot \underline{I} \tag{9.1.20}$$

Equation (9.1.20) yields the derivatives of the currents, that is, (di_a/dt), (di_b/dt), (di_c/dt), and (di_f/dt) from which the armature terminal voltages, v_a, v_b, and v_c can directly be derived from Equation (9.1.10) and (9.1.11). Therefore, these voltages can be computed from the armature currents, and their derivatives, as follows:

$$\begin{bmatrix} v_a \\ v_b \\ v_c \end{bmatrix} = - \begin{bmatrix} r_l & 0 & 0 \\ 0 & r_l & 0 \\ 0 & 0 & r_l \end{bmatrix} \begin{bmatrix} i_a \\ i_b \\ i_c \end{bmatrix} - \begin{bmatrix} L_l & 0 & 0 \\ 0 & L_l & 0 \\ 0 & 0 & L_l \end{bmatrix} \begin{bmatrix} \frac{di_a}{dt} \\ \frac{di_b}{dt} \\ \frac{i_c}{dt} \end{bmatrix} \tag{9.1.21}$$

In order to minimize the required computer CPU time to carry out the complete numerical solution (integration) of the state model of the MLA, Equation (9.1.15), well into the sustained periodic nonsinusoidal steady-state region, it was found that an initial estimate of the rotor position angle, σ_0, is best obtained from a conventional d-q phasor diagram under load, Figure (9.1.1). The angle, σ_0, is defined as the angle at time, $t = 0$, subtended between the rotor's direct axis, d, and the axis of phase (a), which is usually taken as the reference in conventional d-q phasor analysis as depicted in Figure (9.1.1). Notice that consumer (load) system notation is used throughout this investigation, including the phasor diagram of Figure (9.1.1). Under this system of notations the main phasor diagram relationship can be expressed as follows:

$$\overline{V}_a = \overline{E}_f + r_s \overline{I}_a + jx_q \overline{I}_q + jx_d \overline{I}_d \tag{9.1.22}$$

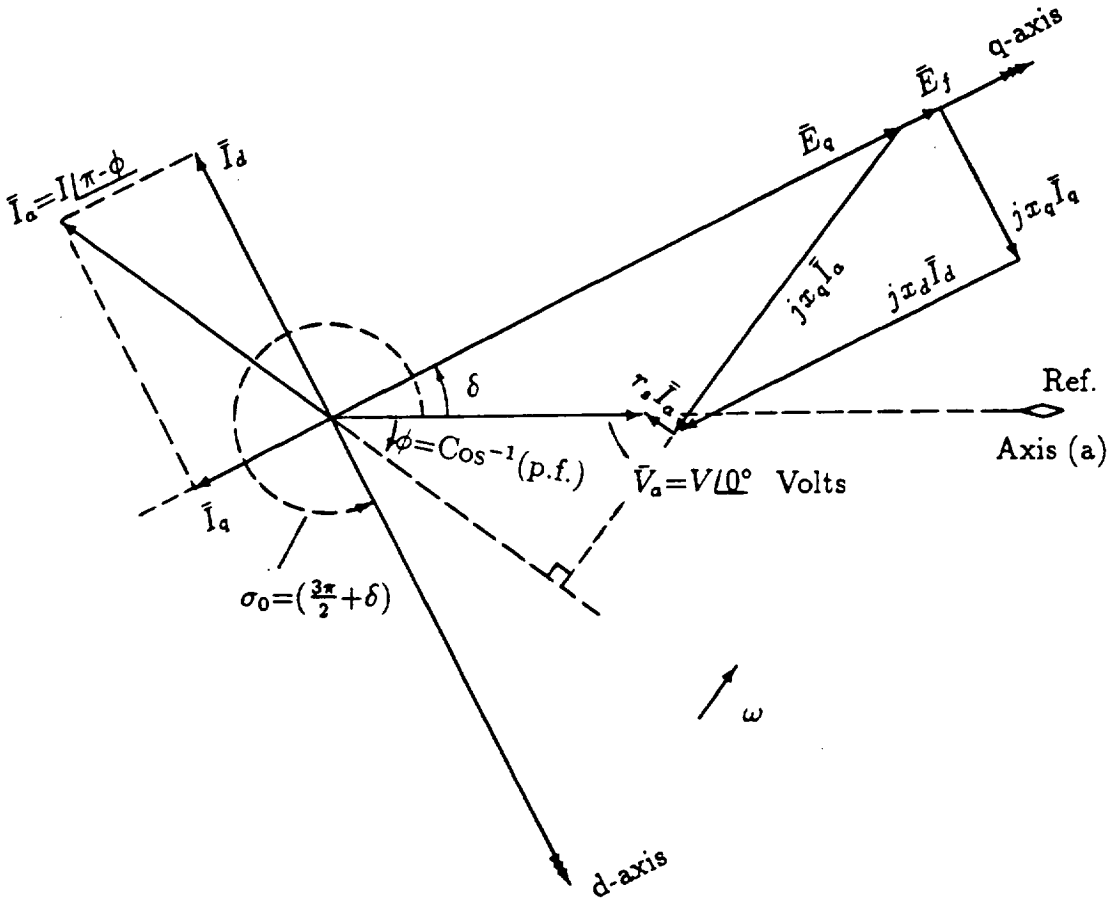

Figure (9.1.1) Conventional Synchronous Machine d-q Phasor Diagram (Consumer Notation)

the variables, $\overline{V}_a$, $\overline{I}_a$, $\overline{E}_f$, $\overline{I}_d$ and $\overline{I}_q$ are defined in the phasor diagram of Figure (9.1.1). The initial rotor position angle, σ_0, is therefore obtained in terms of the power (or torque) angle, δ, as follows:

$$\sigma_0 = \frac{3\pi}{2} + \delta \tag{9.1.23}$$

Accordingly, under steady-state operation, the rotor position angle, σ, at any instant in time, t, is given as follows:

$$\sigma(t) = \sigma_0 + \omega t \tag{9.1.24}$$

where ω is the rotor's steady-state (synchronous) speed in electrical rad/sec.

The amplitude of the excitation emf, E_f, leads to an initial estimate of the necessary field excitation voltage, V_f, as follows:

$$V_f = r_f I_f = r_f \frac{\sqrt{2} E_f}{\omega L_{afm}} \tag{9.1.25}$$

where L_{afm} is the amplitude of the fundamental component of the armature to field mutual winding inductance.

The above use of the d-q phasor diagram to obtain an estimate of the initial conditions for the process of starting the computation of the 3D magnetic fields and consequent MLA performance under load should not be interpreted as an endorsement of the set of assumptions and simplifications underlying the d-q theory, but only as an initial guess in a much more complicated numerical solution process. This process and its accompanying algorithm developed here for the computation of the global 3D magnetic fields in the MLAs as well as their winding inductances and other characteristics, under load conditions, is described in the next section.

9.2 Algorithm for Computation of the Global 3D Field Distribution and Inductances as Well as Load Performance

At the heart of this computer algorithm is the computation of the global 3D magnetic fields in MLAs. The combined MVP-MSP method of global 3D field computation using FE techniques constitutes the core of this analysis. In the application of this combined MVP-MSP method to the MLAs, the 3D-FE solution volume is divided into current-carrying MVP subregions, and a current-free subregion, as shown in Figure (7.1.1) of Chapter 7. Details of the computer algorithm of the combined MVP-MSP method applied to such MLAs were discussed in Chapter 7. The computational steps used to obtain the machine parameters (inductances), and other performance characteristics under load, from global 3D-FE field solutions, can best be described by means of a detailed explanation of the flow chart, Steps (1) through (11), in Figure (9.2.1). The steps of computation proceed as follows:

Step (1): Estimate the initial condition for the starting of the 3D magnetic field and performance computation process.

(1.1) Given a three phase balanced load with a complex power, $\overline{S}_l = P_l + jQ_l$ at a line to neutral load terminal voltage, $\overline{V}_l = V_l/\underline{0°}$, and load power factor angle, $\phi_l = Cos^{-1}(P.F.)$, using consumer (load) notation throughout, compute the load current $\overline{I}_l = I_l/\underline{-\phi_l}$ from:

$$\overline{S}_l = P_l + jQ_l = 3\overline{V}_l\overline{I}_l^* = 3V_lI_lCos\phi_l + j3V_lI_lSin\phi_l$$

(1.2) Compute a load equivalent resistance r_l and a load equivalent inductance per phase as follows:

$$r_l = (P_l/3I_l^2) \quad \Omega/\text{phase} \tag{9.2.1}$$

and

$$L_l = x_l/\omega = Q_l/(3I_l^2\omega) \quad \text{H/phase} \tag{9.2.2}$$

These are the load resistance and inductance per phase used in the MLA's state model, Figure (9.0.1) and Equations (9.1.15) through (9.1.21), throughout the iterative process of this algorithm.

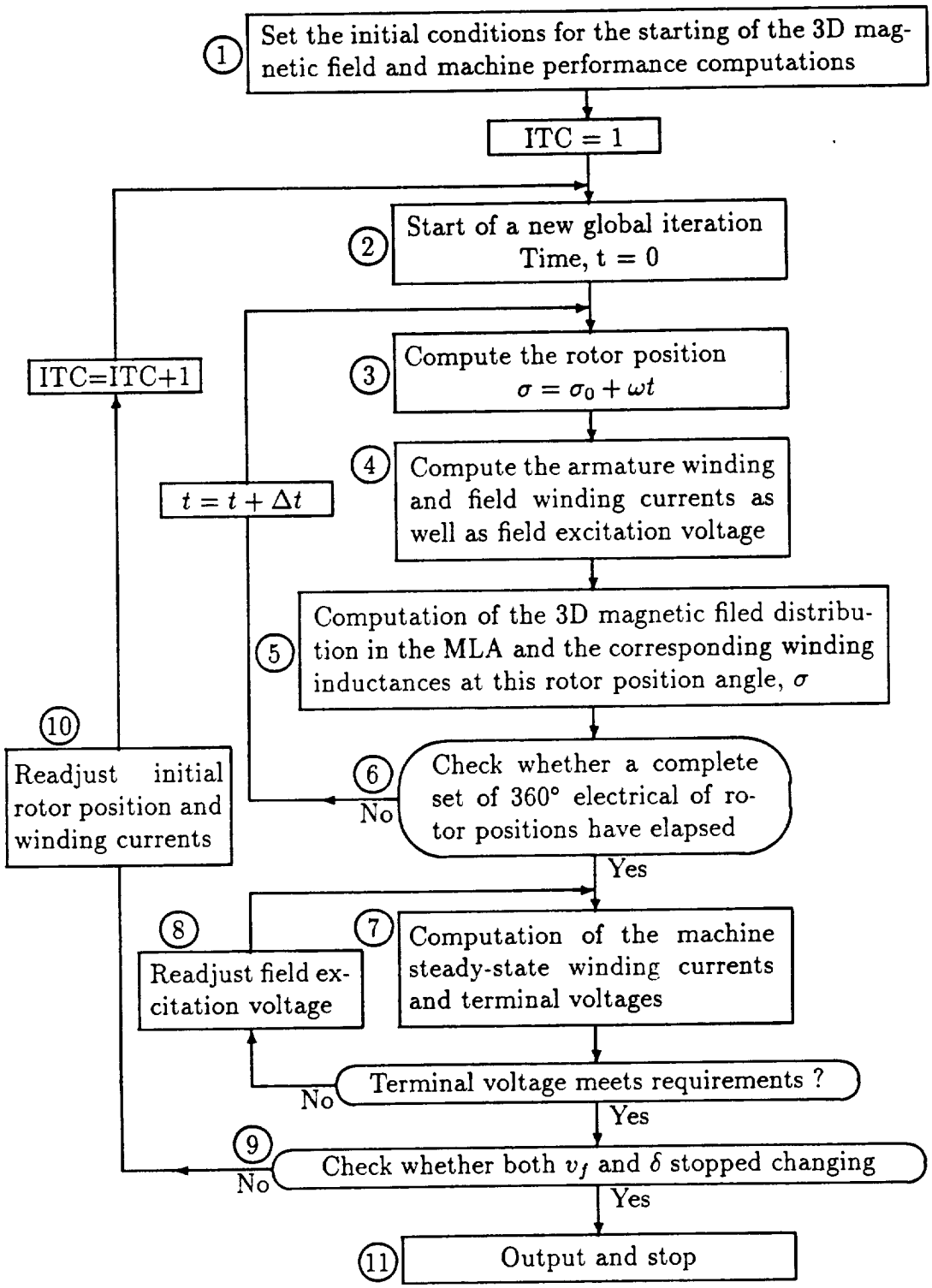

Figure (9.2.1) Flow Chart of MLA Load Simulation Procedure

(1.3) The MLA's power factor angle, ϕ, and rms current per phase, I, are accordingly given by

$$I = I_l, \qquad \phi = \phi_l \tag{9.2.3}$$

Accordingly the phasor values of the a, b, and c phase currents of the MLA, i_a, i_b and i_c, are given by the following:

$$\left.\begin{aligned} \overline{I}_a &= I/\underline{(\pi - \phi)} \\ \overline{I}_b &= I/\underline{(\pi - \phi) - 2\pi/3} \\ \overline{I}_c &= I/\underline{(\pi - \phi) - 4\pi/3} \end{aligned}\right\} \tag{9.2.4}$$

(1.4) Use the direct axis and quadrature axis synchronous reactances, x_d and x_q, computed at rated voltage no-load in Section 8.4, in the conventional d-q phasor diagram, Figure (9.1.1), to calculate the initial estimates of the d-axis rotor position angle, σ_0, Equation (9.1.23), and the steady-state field excitation voltage, V_f, Equation (9.1.25). Set the global iteration count, ITC, that is ITC=1.

Step (2): Start a new global computation iteration. Set the time, $t = 0$.

Step (3): Compute the rotor position, that is , obtain the direct axis position angle, $\sigma = \sigma_0 + \omega t$.

Step (4): Compute the instantaneous values of i_a, i_b, i_c, i_f and v_f, at this rotor position angle, σ.

If ITC=1, use the following

$$\left.\begin{aligned} i_a &= \sqrt{2}ICos[\omega t + (\pi - \phi)] \\ i_b &= \sqrt{2}ICos[\omega t + (\pi - \phi) - 2\pi/3] \\ i_c &= \sqrt{2}ICos[\omega t + (\pi - \phi) - 4\pi/3] \\ i_f &= \sqrt{2}E_f/\omega L_{afm} \\ v_f &= V_f \text{ (from Equation(9.1.25))} \end{aligned}\right\} \tag{9.2.5}$$

If ITC$\neq$1, use the most recently adjusted value of v_f from Step (7) of the (ITC-1) global iteration, and obtain the instantaneous values of i_a, i_b, i_c and

i_f, from the most recent output of the (ITC-1) global iteration current profiles, corresponding to the present rotor position angle, σ. Inject these instantaneous currents into the proper locations in the 3D-FE global solution volume, Figure (7.1.1).

Step (5): Compute the global 3D magnetic field distribution in the MLA, and the corresponding winding inductances at the given rotor position angle, σ, using the combined MVP-MSP method, the computer algorithm of which and its flow chart are given in Figure (7.2.1) of Chapter 7.

Step (6): Check whether the elapsed rotor position angle $(\sigma - \sigma_0) \geq 2\pi$ electrical radians ?

IF No: Increment time; $t = t + \Delta t$, and Go To Step (3).

IF Yes: The profiles of MLA winding inductances covering a complete ac cycle (2π electrical radians) have been obtained. Thus the alternator's parameters have been computed. Proceed to Step (7).

Step (7): Solve for the MLA's winding currents and terminal voltages using the state model formulated earlier in Equations (9.1.15) through (9.1.21), in the following order until steady-state winding current and terminal voltage profiles are attained:

(7.1) Use Equation (9.1.15) to solve for the instantaneous values of the flux linkages of the combined load - machine windings, λ_a, λ_b, λ_c, and λ_f.

(7.2) Use Equation (9.1.14) to compute the instantaneous values of the machine winding currents, i_a, i_b, i_c, and i_f, from the instantaneous flux linkages, λ_a, λ_b, λ_c, and λ_f.

(7.3) Use Equation (9.1.20) to compute the instantaneous rates of change of machine winding currents with respect to time. That is, compute di_a/dt, di_b/dt, di_c/dt, and di_f/dt.

(7.4) Use Equation (9.1.21) to compute the instantaneous values of the armature phase windings' voltages, v_a, v_b, and v_c.

If the rms voltages obtained from the steady-state voltage profiles of v_a, v_b, and v_c, are not within range of required values, Go To Step (8) for field excitation adjustment.

If the rms voltages obtained from the steady-state voltage profiles of v_a, v_b, and v_c, are within range of required values, Go To Step (9).

Step (8): Readjust the field excitation voltage, v_f, in proportion to the deviation of the rms values of armature voltages from required value. That is, multiply the field excitation voltage, v_f, by the ratio of the rated MLA terminal voltage and the rms value of the terminal voltage obtained from Step (7). Go To Step (7).

Step (9): Compute the power angle, δ, of the phasor diagram of Figure (9.1.1) from the latest simulation results, that is, the angle shift between the rotor q-axis and the fundamental of the terminal voltage v_a in the computed results.

Check whether the field excitation voltage v_f and the torque angle δ obtained from Step (7) stopped changing from their respective values in the previous iteration, (ITC-1), i.e. normalized change ≤ 0.5 per cent.

If Yes, Go To Step (11).

If No, Go To Step (10).

Step (10): Re-calculate the initial rotor position angle, $\sigma_0 = (3\pi)/2 + \delta$, for machine winding inductance and 3D magnetic field recomputations. Also, store the computed steady-state profiles of i_a, i_b, and i_c, for the inductance and magnetic field recomputations.

Increment the global iteration count, ITC=ITC+1,

Go To Step (2).

Step (11): Steady-state solution for the prescribed load has been achieved. Output and plot all desired MLA parameters and performance characteristics under the given load condition. End of load case computations, Stop.

The above algorithm which combines the computation of the steady-state load performance characteristics, in which the steady-state periodic nonsinusoidal armature voltage and current waveforms are obtained, together with their corresponding global 3D magnetic field distributions, was used in actual MLA performance calculations. The 3D magnetic field and load performance of the example 14.3 kVA MLA was computed at rated load of 14.3 kVA, 0.75 lagging P.F. and over-rated load of 21.5 kVA, 0.75 lagging P.F., respectively. The results of these computations are given in Section 9.4.

9.3 The Method of Electromagnetic Torque Calculation

The electromagnetic torque of the example 14.3 kVA MLA is computed based on the machine terminal voltages and currents as well as the stored magnetic energy of the MLA obtained from 3D-FE magnetic field computations. The terminal voltages and currents are the results of the computer simulation procedure using the state space model discussed in previous sections. Meanwhile, the stored magnetic energy can be obtained from the results of 3D-FE computations at the stage of machine winding inductance calculation as described in Step (5) of the flow chart in Figure (9.2.1). The method is explained next.

Consider the energy conservation principle with regard to the MLA-load system shown in Figure (9.0.1). The energy balance for the MLA under load can be stated as follows:

$$\begin{pmatrix} \text{Input} \\ \text{Electrical} \\ \text{Energy} \end{pmatrix} + \begin{pmatrix} \text{Input} \\ \text{Mechanical} \\ \text{Energy} \end{pmatrix} = \begin{pmatrix} \text{Increase} \\ \text{in Stored} \\ \text{Energy} \end{pmatrix} + \begin{pmatrix} \text{Energy} \\ \text{Dissipated} \\ \text{as Heat} \end{pmatrix} \quad (9.3.1)$$

Under the steady state load condition, the term "Increase in Stored Energy" in the above expression only includes the increase in the stored magnetic field energy ($\int \overline{H} \cdot d\overline{B}$), for the reason that the electric field energy ($\int \overline{E} \cdot d\overline{D}$) in a rotating electric machine is insignificant. The change in the stored magnetic energy during a very short period of time, dt, is denoted here as dW_{mag}.

Meanwhile, the term "Energy Dissipated as Heat" in the expression of Equation (9.3.1) includes the energy dissipations due to the machine windings' ohmic loss, and iron core loss, as well as the mechanical friction and windage losses. At the present stage of this investigation, the effect of iron loss on the electromagnetic torque of the MLA is not included. Thus during the time, dt, the dissipated energy in the form of heat, denoted here as dW_{diss}, can be written as follows:

$$dW_{diss} = (i_a^2 r_a + i_b^2 r_b + i_c^2 r_c + i_f^2 r_f)dt + dW_{f\&w} \quad (9.3.2)$$

where, i_a, i_b, i_c, and i_f are the instantaneous values of the three phase armature winding currents and the field current, respectively. Meanwhile, r_a, r_b, r_c, and r_f are

the winding resistances of the three phase armature windings and the field winding, respectively. Here, $W_{f\&w}$ in Equation (9.3.2) is the energy dissipation related to mechanical losses such as the bearing friction loss, and windage associated with the rotational motion of the rotor, etc.

The term "Input Mechanical Energy" in (9.3.1), denoted here as dW_m, for the time, dt, can be expressed by the mechanical torque exerted on the MLA's shaft, T_m, and the shaft angular speed, ω_m, as follows:

$$dW_m = T_m \omega_m dt \tag{9.3.3}$$

Further, during the very short time, dt, the term "Input Electrical Energy" can be expressed through the armature voltages and currents, as well as the field voltage and current, as follows:

$$dW_e = (v_a i_a + v_b i_b + v_c i_c + v_f i_f) dt \tag{9.3.4}$$

where dW_e is the notation for the input electrical energy during the time dt.

Accordingly, Equation (9.3.1) can be rewritten for the MLA steady state load case as follows:

$$dW_e + dW_m = dW_{mag} + dW_{diss} \tag{9.3.5}$$

Substituting dW_{diss} from Equation (9.3.2), dW_m from Equation (9.3.3) and dW_e from Equation (9.3.4) into Equation (9.3.5) yields the following:

$$\begin{aligned} &(v_a i_a + v_b i_b + v_c i_c + v_f i_f) dt + T_m \omega_m dt \\ &= dW_{mag} + (i_a^2 r_a + i_b^2 r_b + i_c^2 r_c + i_f^2 r_f) dt + dW_{f\&w} \end{aligned} \tag{9.3.6}$$

Equation (9.3.6) can be re-arranged into the following form:

$$\begin{aligned} T_m(\omega_m dt) - dW_{f\&w} = dW_{mag} &+ (i_a^2 r_a + i_b^2 r_b + i_c^2 r_c + i_f^2 r_f) dt \\ &- (v_a i_a + v_b i_b + v_c i_c + v_f i_f) dt \end{aligned} \tag{9.3.7}$$

Dividing Equation (9.3.7) by $(\omega_m dt)$, one obtains the following:

$$T_m - (\frac{1}{\omega_m})(\frac{dW_{f\&w}}{dt}) = (\frac{1}{\omega_m})(\frac{dW_{mag}}{dt}) + \frac{1}{\omega_m}(i_a^2 r_a + i_b^2 r_b + i_c^2 r_c + i_f^2 r_f)$$

$$- (\frac{1}{\omega_m})(v_a i_a + v_b i_b + v_c i_c + v_f i_f) \tag{9.3.8}$$

Notice, the two terms at the left hand side of Equation (9.3.8) are mechanical torques. Under the steady state condition, the resultant of these two terms must be equal to the negative of the electromagnetic torque generated in the MLA, such that the total resultant torque on the MLA's shaft equals zero which yields a necessary condition for the MLA to keep its constant rotor speed. Thus one can write the equation for the electromagnetic torque, T_e, as follows:

$$T_e = -(\frac{1}{\omega_m})(\frac{dW_{mag}}{dt}) - \frac{1}{\omega_m}(i_a^2 r_a + i_b^2 r_b + i_c^2 r_c + i_f^2 r_f)$$

$$+ \frac{1}{\omega_m}(v_a i_a + v_b i_b + v_c i_c + v_f i_f) \tag{9.3.9}$$

The term W_{mag} in Equation (9.3.9) can be obtained from 3D-FE computations at the quiescent points at the stage of machine inductance calculation as described in Step (5) of the flow chart in Figure (7.2.1). These values are obtained as functions of the rotor position angle, θ_e, and can be expressed in a Fourier series as follows:

$$W_{mag} = A_0 + \sum_{n=2,4,}^{20} A_n Cos(n\theta_e - \psi_n) \tag{9.3.10}$$

where A_n is the n-th harmonic component of the computed magnetic energy profile versas rotor angle position, θ_e, and ψ_n is the phase angle of the n-th harmonic component of the torque. Consequently, the derivative of W_{mag} can be computed as:

$$\frac{dW_{mag}}{dt} = \omega_e \frac{dW_{mag}}{d\theta_e} = -\omega_e \sum_{2,4,}^{20} n A_n Sin(n\theta_e - \psi_n) \tag{9.3.11}$$

The component of electromagnetic torque stemming from the change in the stored magnetic energy, described as $-(1/\omega_m)(dW_{mag}/dt)$ in Equation (9.3.9), can also be

expressed in a Fourier series form as follows:

$$T = \frac{\omega_e}{\omega_m} \sum_{2,4,}^{20} nA_n Sin(n\theta_e - \psi_n) = \frac{p}{2} \sum_{2,4,}^{20} nA_n Sin(n\theta_e - \psi_n) \tag{9.3.12}$$

where p is the number of poles of the machine. Thus, the electromagnetic torque profile can be computed by the following:

$$T_e = -\frac{1}{\omega_m}(i_a^2 r_a + i_b^2 r_b + i_c^2 r_c + i_f^2 r_f) + \frac{1}{\omega_m}(v_a i_a + v_b i_b + v_c i_c + v_f i_f)$$

$$+ \frac{p}{2} \sum_{2,4,}^{20} nA_n Sin(n\theta_e - \psi_n) \tag{9.3.13}$$

In order to study the improvement on the accuracy of the torque calculation by including the term related to the change in the stored magnetic energy, two methods, Method #1 based entirely on Equation (9.3.13), and Method #2 using Equation (9.3.13) without the term related to the stored magnetic energy, were applied to an example torque calculation of the MLA rated load case. The results are shown in Figure (9.3.1) and its accompanying table. One can see that both methods yield the identical average torque value. However, as shown in Figure (9.3.1), the torque profiles computed by Method #1 and Method #2 are not congruent. Also, as shown in the accompanying table, there is noticeable difference in magnitudes and phase angles of harmonic components between these two torque results. Therefore, in case that there is a need of thorough investigation on the harmonic contents of the machine electromagnetic torque profile, the method described in Equation (9.3.13) should be used.

Because of the consumer notation system used in this research, the total electromagnetic torque is expected to be negative under a generator operating condition. The physical meaning of the negative sign of the electromagnetic torque is that such a torque opposes the rotor's direction of rotation. Results of torque calculation for the MLA as well as other performance characteristics, under various load conditions, are further presented in the following sections. The torque calculation is carried from this point forward using Method #1 of Equation (9.3.13) above.

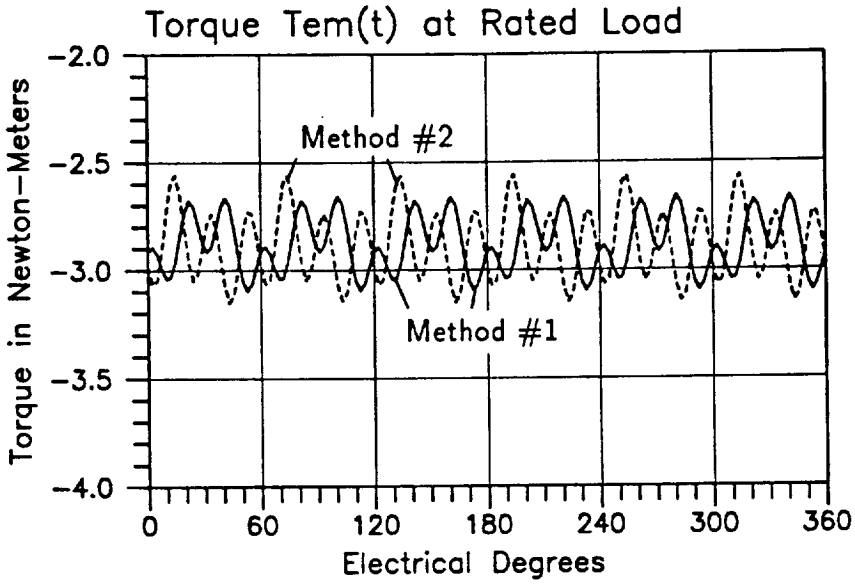

Harmonic Contents of Electromagnetic Torque				
Oder n	Amplitude, T_n $(N \cdot M)$		Phase Angle, ψ_n (Rad)	
	Method #1	Method #2	Method #1	Method #2
0	-2.881	-2.881	—	—
6	0.1217	0.0872	3.25148	1.4597
12	0.0289	0.0296	2.8678	3.3144
18	0.1280	0.1987	0.5435	4.3215

Figure (9.3.1) Example Torque Calculations

9.4 The MLA's 3D Magnetic Field Distributions and Performance Characteristics Under Load

9.4.1 The 14.3 kVA, 0.75 Lagging Power Factor Rated Load Case

The formulations and computer algorithm described in the above sections, were used to compute the 3D global magnetostatic field distributions throughout the magnetic circuit of the example 14.3 kVA machine, at a rated load of 14.3 kVA, 0.75 lagging power factor (over-excited generator mode generating both Watts and Vars) at rated voltage conditions. These 3D magnetic field computations were performed at 36 rotor positions covering the 360°e ac cycle, at a sampling rate every 10°e. The inherently 3D nature of the magnetic field distributions in this MLA example will next be demonstrated by studying typical samples of the magnetic field distributions under load.

The distributions of the radial flux density at various axially located (z - axis locations) cross-sections, see Figure (7.3.4) of Section 7.3, for $z = z_0$, and $z = \pm z_2$ in the main airgap, and for $z = \pm z_3$, as well as $\pm z = z_4$ in the auxiliary airgaps, are given next.

In the main airgap, the radial flux density waveforms, for one of the 36 rotor position samples, covering two complete pole pitches (360°e) at $z = z_0 = 0$ and $z = \pm z_2 = \pm 1.92$ cm are given in Figures (9.4.1) and (9.4.2), respectively. It can easily be seen that the three radial flux density waveforms are not congruent. That is, the waveform profiles and magnitudes are dependent on the z-axis locations of the cross-sections. This can be further demonstrated through an isometric presentation of the radial flux density component, B_r, distribution in the main airgap, under one pole pitch, see Figure (9.4.3). Meanwhile, as expected for a generator in an over-excited mode (generating Vars) the highest flux density peaks occur on the trailing side of a pole pitch. Further, these peaks vary with the axial location, thus further highlighting the 3D nature of the magnetic field in such machines.

In spite of the uniform nature of the geometry of the auxiliary airgaps at both ends of the machine, the radial flux density distributions are dependent on the axial-z locations of the cross-sections, as well as the circumferential-θ locations within these

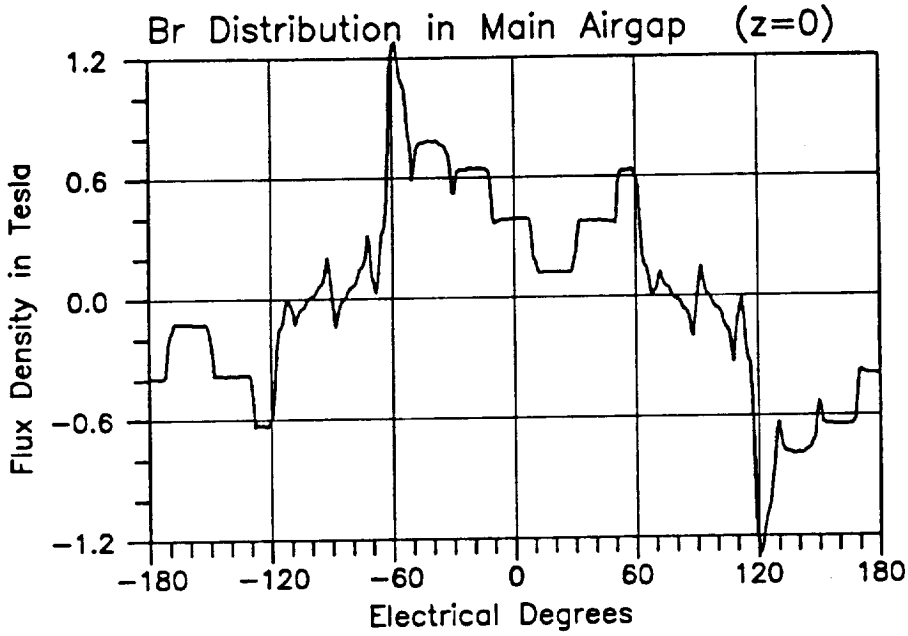

Figure (9.4.1) B_r Distributions in Main Airgap at $z = 0$ at Rated Load

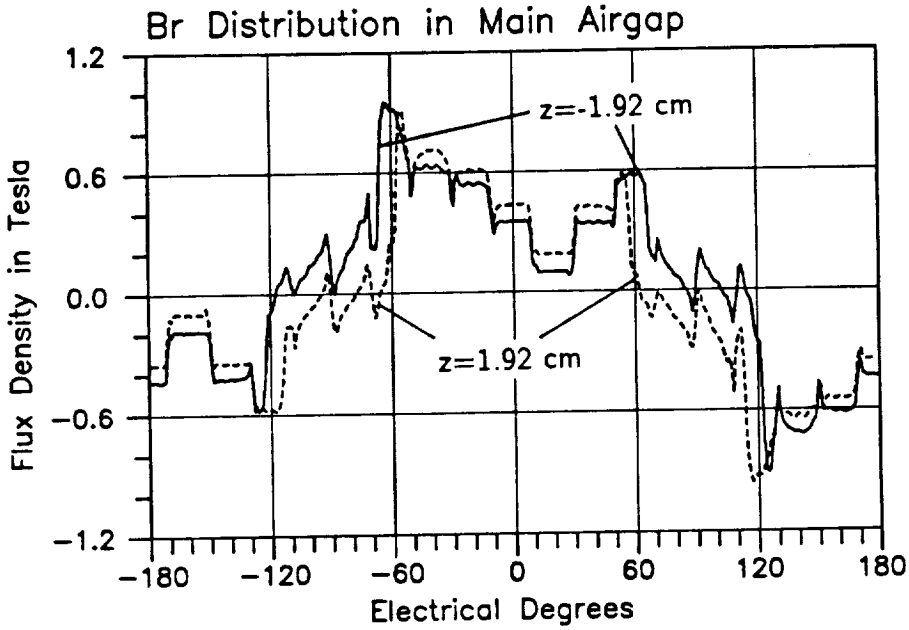

Figure (9.4.2) B_r Distributions in Main Airgap at z=±1.92 cm at Rated Load

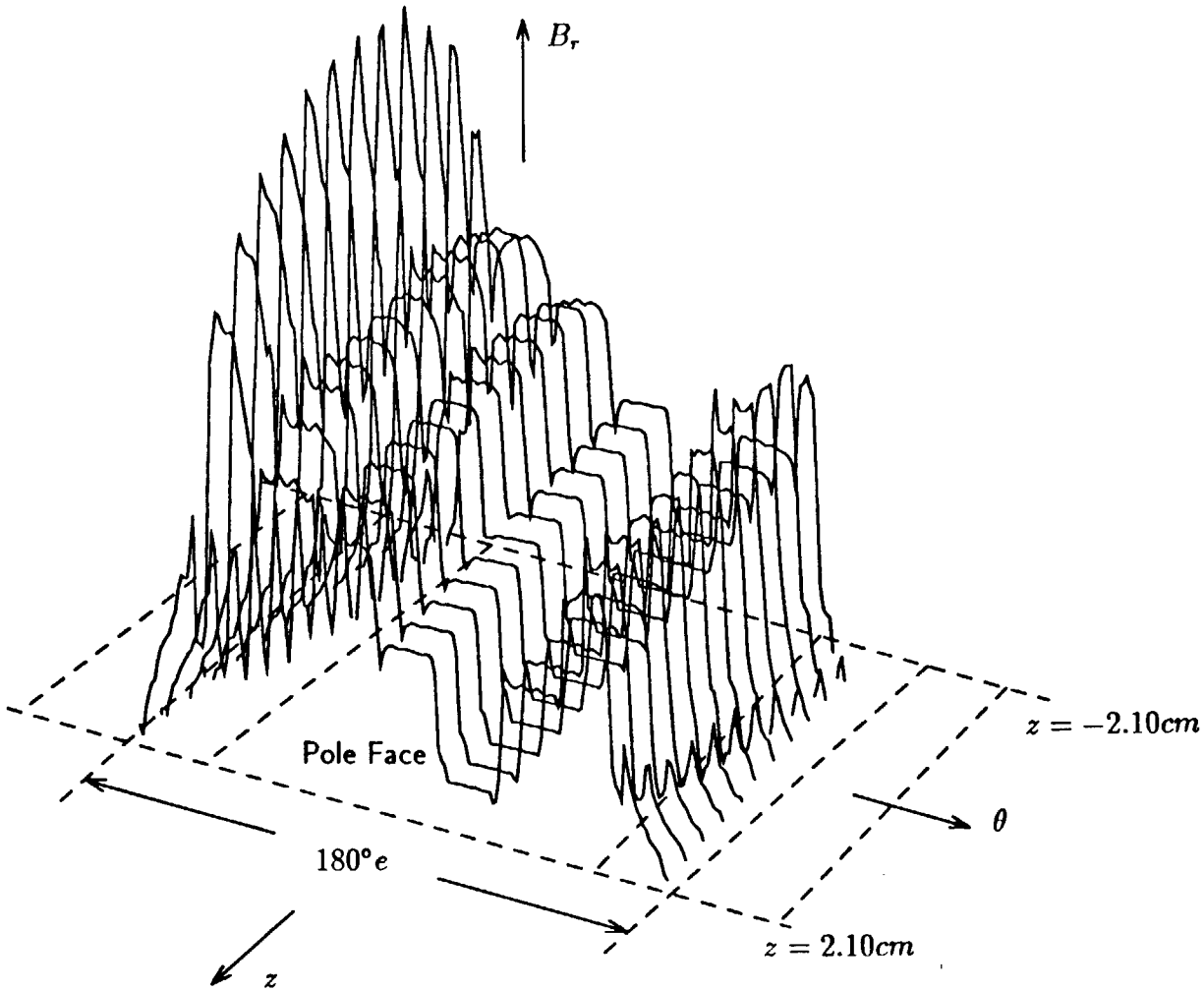

Figure (9.4.3) Isometric Presentation of B_r Distribution in Main Airgap of the 14.3 kVA MLA at Rated Load

cross-sections. For example, the radial flux distributions at $z = z_3$ =5.13 cm and at $z = z_4$ =7.72 cm within the auxiliary airgaps are given in Figure (9.4.4), for the same rotor position of the flux density distributions in Figures (9.4.1) through (9.4.3). The radial flux density at $z = 5.13$ cm is not uniform here despite the uniformity of the geometry of the auxiliary airgap (constant airgap length). It can be said that the flux density distribution here has also been modulated by the peculiar nature of the rotor magnetic circuit geometry. This is a further confirmation of the 3D nature of the magnetic field within such MLAs. The positive values of the radial flux densities in one of the auxiliary airgaps, Figure (9.4.4), indicate a radially outward flux flow across the auxiliary airgap from the shaft into the end bells and outer casing. A similar situation with opposite sign can be observed for $z = -z_3 = -5.13$ cm and $z = -z_4 = -7.72$ cm in the other auxiliary airgap, see Figure (9.4.5), which indicates radially inward oriented flux flow.

The various MLA winding inductances, specifically all the terms in the state model, Equations (9.1.4) through (9.1.21), have been computed using the 3D-FE algorithms as described above. Samples of these inductance profiles versus the rotor position angle over a complete cycle of 360°e, calculated every 10°e change in rotor position, are given in Figures (9.4.6) through (9.4.9), for L_{aa}, L_{ab}, L_{af}, and L_{ff}, respectively. These inductance profiles were computed under rated load conditions. Also given in the same figures are the no-load rated voltage profiles of these inductances. The harmonic contents of the inductances under no-load and rated load are compared in the accompanying tables in each of these figures. As anticipated, the inductances are lower in value under load in comparison with their corresponding no-load values, due to the higher degrees of saturation throughout the magnetic circuit of the MLA.

The MLA is shown in Figure (9.4.10) during testing. Figure (9.4.11) shows some typical computer simulation results. These results are the line to neutral terminal voltage of phase (a), v_a, the phase current, i_a, the field winding current, i_f, and the electromagnetic torque, T_{em} using the Method #1 of Equation (9.3.13). As can be seen in Figure (9.4.11), the required field excitation current for this rated load operation is 3.019 A (2180 Ampere-Turns total).

The line to neutral terminal voltage waveform of phase (a), v_a, as well as its harmonic breakdown is given in Figure (9.4.12). Figure (9.4.13-a,b) shows the comparison of the computed terminal voltage waveform and the corresponding test oscillogram

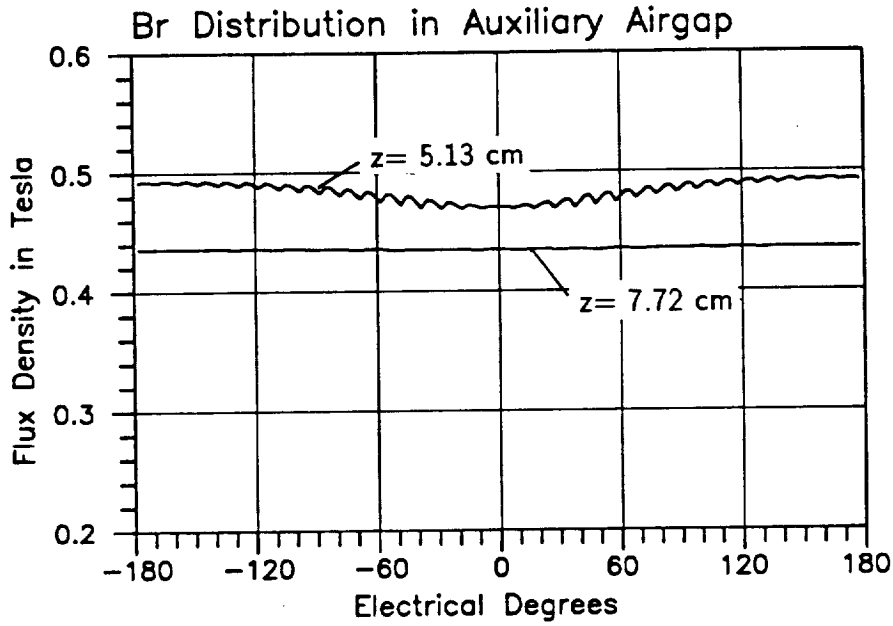

Figure (9.4.4) B_r Distributions in Auxiliary Airgap at Rated Load
(z=5.13 cm and z=7.72 cm)

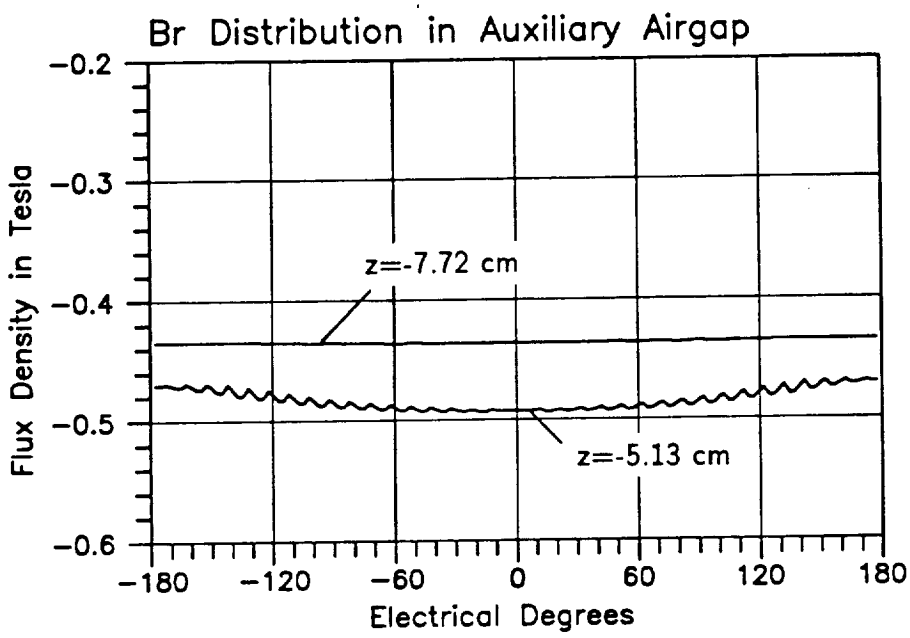

Figure (9.4.5) B_r Distributions in Auxiliary Airgap at Rated Load (z=-5.13 cm and z=-7.72 cm)

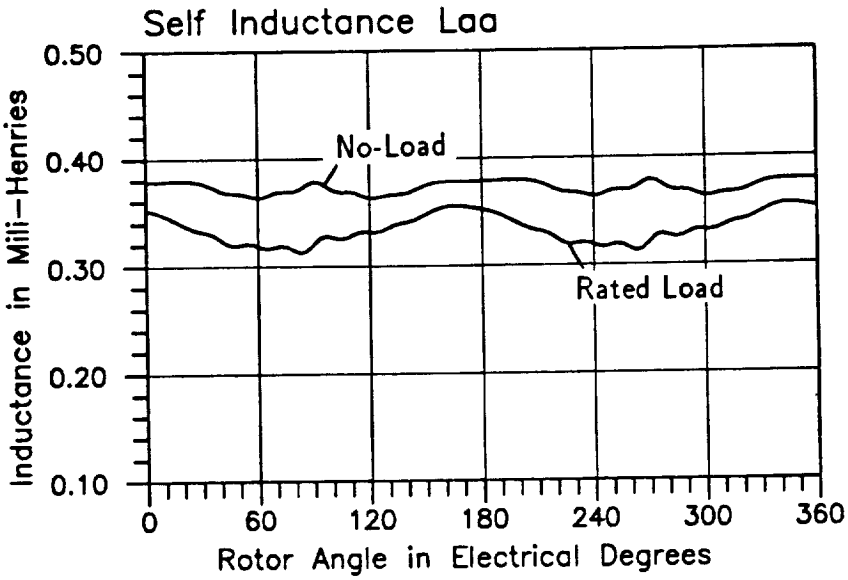

Harmonic Contents of Self Inductance L_{aa}		
Order n	Amplitude A_n (No-Load)	Amplitude A_n (Rated Load)
0	0.3722 mH	0.3338 mH
2	0.0050 mH	0.0180 mH
4	0.0048 mH	0.0032 mH
6	0.0032 mH	0.0015 mH
8	0.0001 mH	0.0008 mH
10	0.0007 mH	0.0009 mH
12	0.0005 mH	0.0010 mH
14	0.0001 mH	0.0002 mH
16	0.0008 mH	0.0011 mH
18	0.0011 mH	0.0015 mH
20	0.0005 mH	0.0007 mH

Figure (9.4.6) 3D-FE Computed Machine Self Inductance L_{aa}

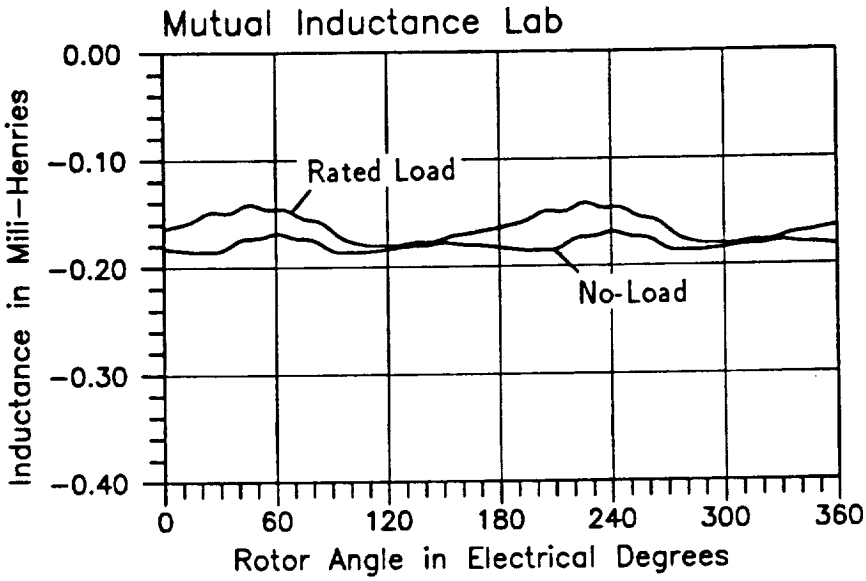

Harmonic Contents of Mutual Inductance L_{ab}		
Order n	Amplitude A_n (No-Load)	Amplitude A_n (Rated Load)
0	-0.1801 mH	-0.1632 mH
2	0.0033 mH	0.0176 mH
4	0.0060 mH	0.0039 mH
6	0.0016 mH	0.0007 mH
8	0.0001 mH	0.0007 mH
10	0.0007 mH	0.0007 mH
12	0.0002 mH	0.0005 mH
14	0.0001 mH	0.0002 mH
16	0.0008 mH	0.0011 mH
18	0.0005 mH	0.0007 mH
20	0.0005 mH	0.0007 mH

Figure (9.4.7) 3D-FE Computed Machine Mutual Inductance L_{ab}

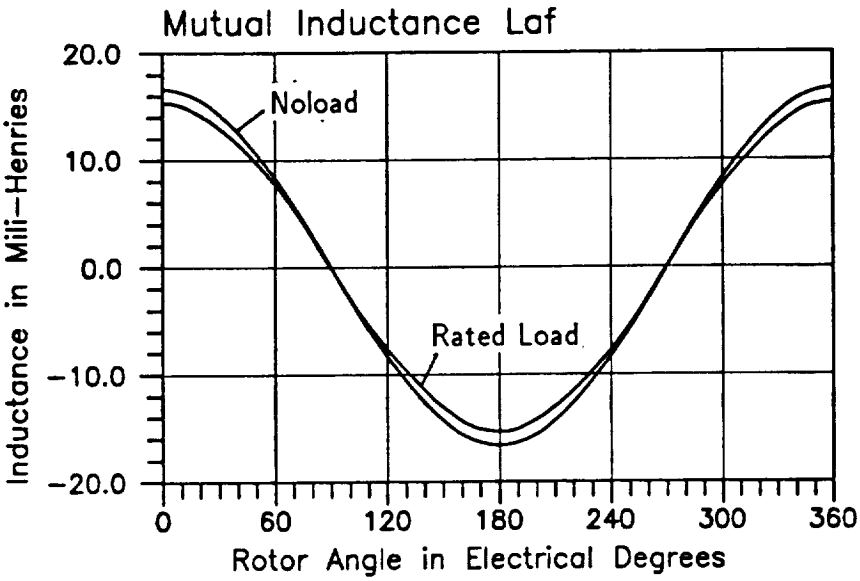

Harmonic Contents of Mutual Inductance L_{af}		
Order n	Amplitude A_n (No-Load)	Amplitude A_n (Rated Load)
1	16.545 mH	15.374 mH
3	0.0021 mH	0.0045 mH
5	0.0908 mH	0.1679 mH
7	0.0469 mH	0.0371 mH
9	0.0005 mH	0.0015 mH
11	0.0076 mH	0.0063 mH
13	0.0100 mH	0.0134 mH
15	0.0005 mH	0.0003 mH
17	0.0127 mH	0.0195 mH
19	0.0102 mH	0.0159 mH

Figure (9.4.8) 3D-FE Computed Machine Mutual Inductance L_{af}

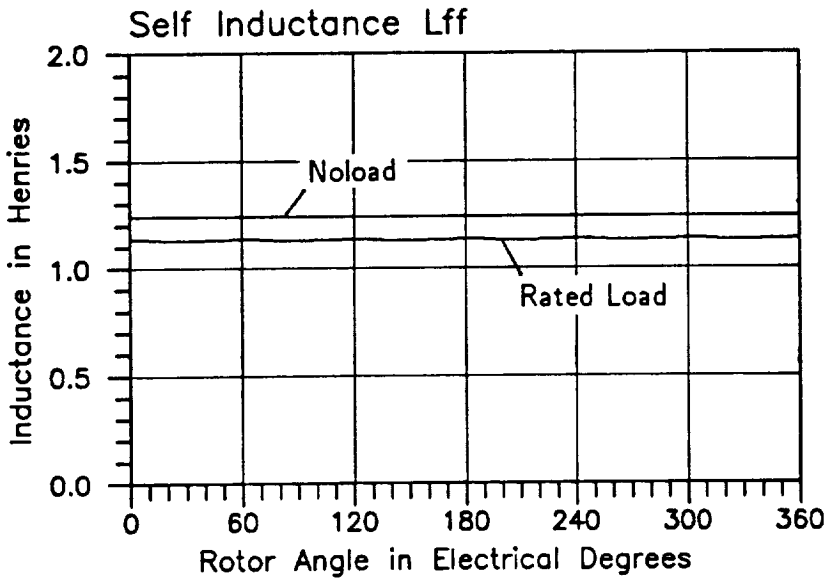

Harmonic Contents of Self Inductance L_{ff}		
Order n	Amplitude A_n (No-Load)	Amplitude A_n (Rated Load)
0	1.2405 H	1.1453 H
6	0.0000 H	0.0023 H
12	0.0000 H	0.0006 H
18	0.0004 H	0.0003 H

Figure (9.4.9) 3D-FE Computed Machine Self Inductance L_{ff}

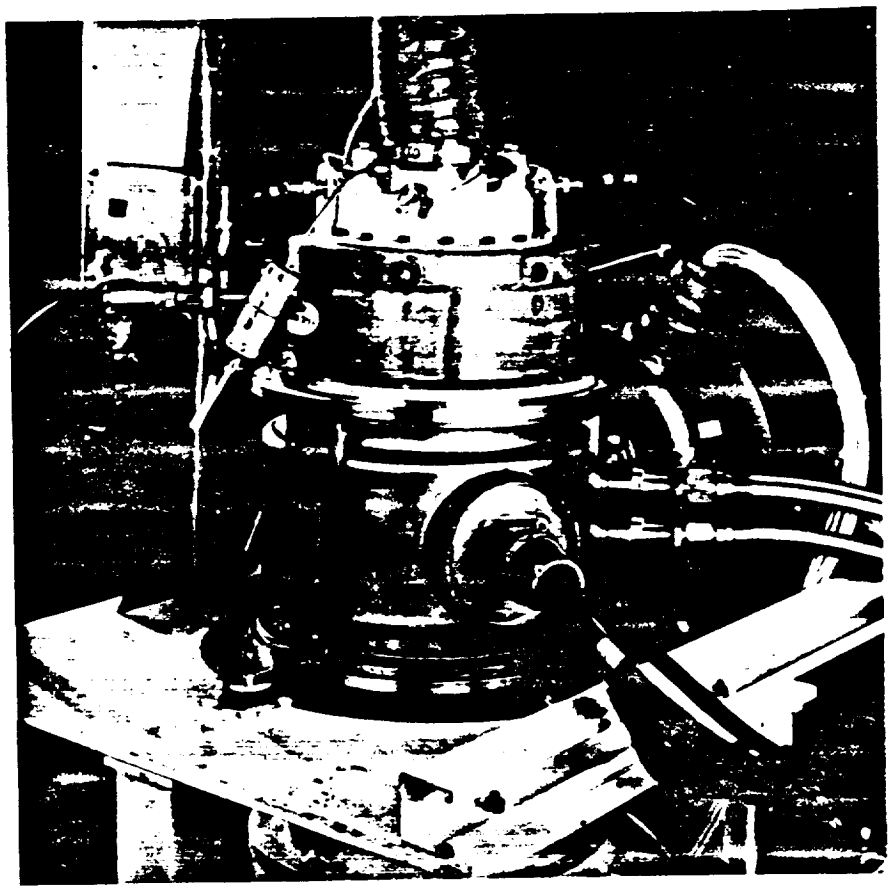

Figure (9.4.10) The 14.3 kVA MLA Under Load Test

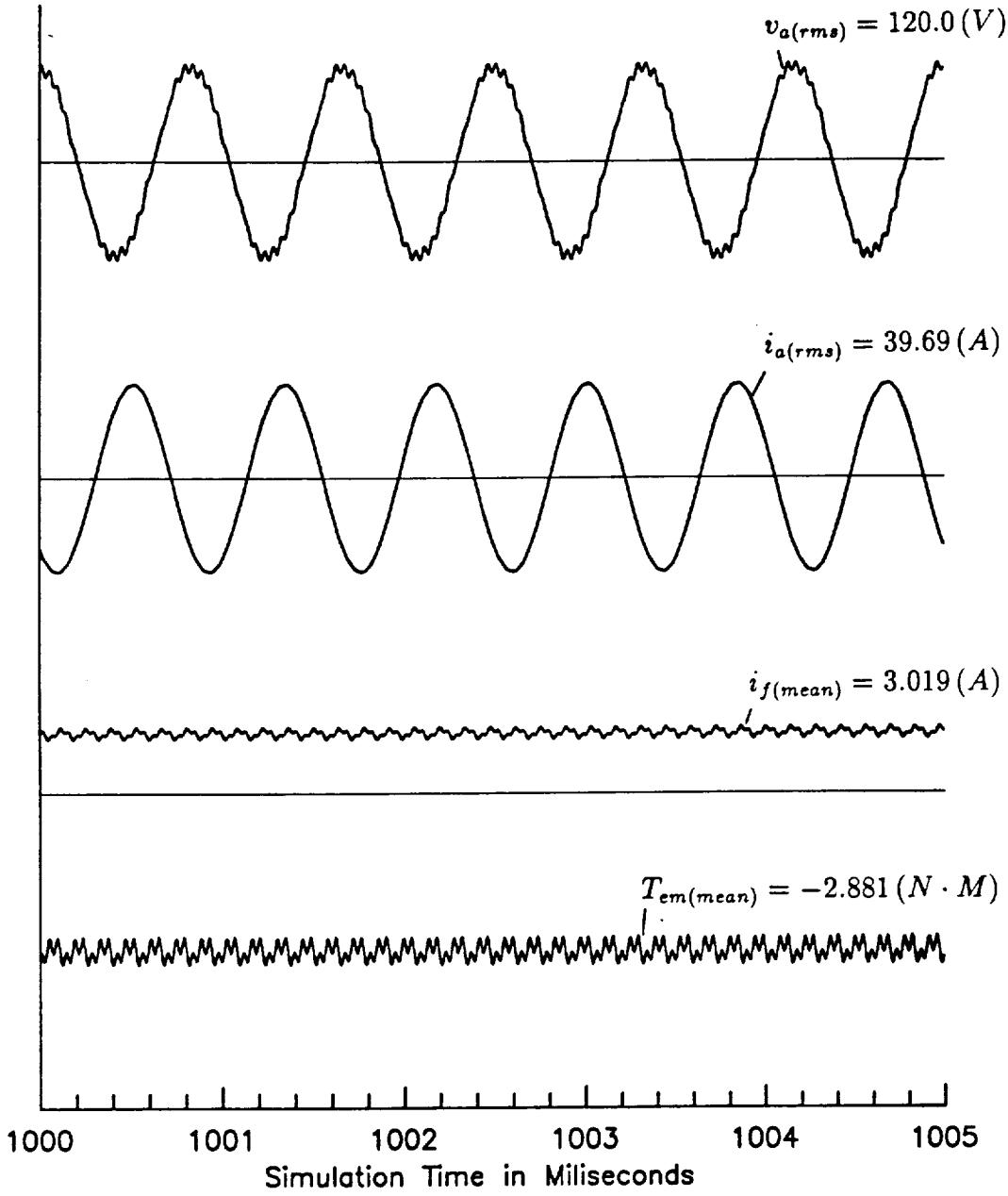

Figure (9.4.11) Plot of Typical Computer Simulation Results of the 14.3 kVA MLA at Rated Load

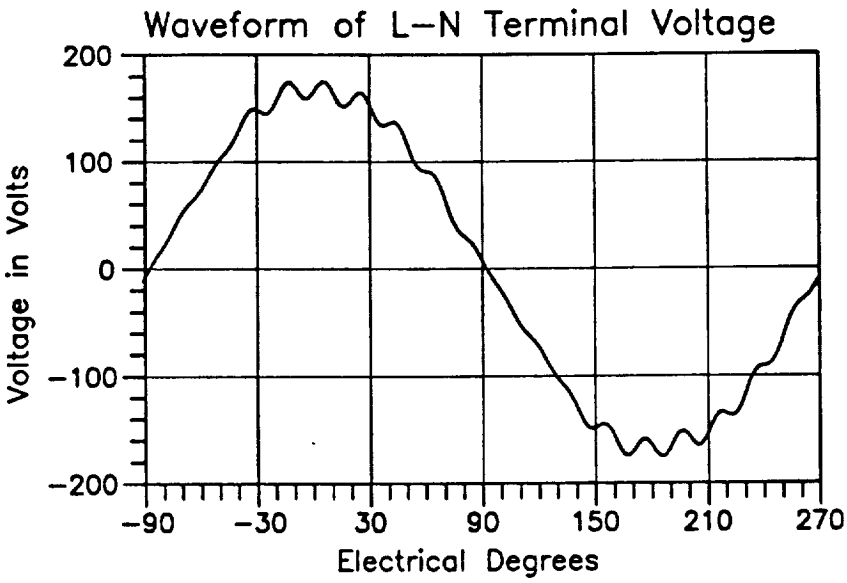

Harmonic Contents of Terminal Voltage, v_a		
Order n	Amplitude V_n (V)	Phase Angle ψ_n (Rad)
1	169.54	0.0000
3	0.5750	-1.9006
5	3.1194	-2.5405
7	0.0637	-2.0352
9	0.3698	-0.1816
11	1.7609	-1.3281
13	1.3084	2.5155
15	0.1211	2.4597
17	4.6244	0.8330
19	5.0888	1.3897

Figure (9.4.12) Computed Waveform of Line to Neutral Voltage at Rated Load

[3] under the same load conditions. The very strong similarity that exists between the two voltage profiles, coupled with the computed and test peak voltages of 175 Volts and 171 Volts in Figures (9.4.13-a) and (9.4.13-b), respectively, confirm the validity of the 3D magnetostatic field and resulting MLA performance computations obtained under rated load conditions.

The corresponding computed profiles and harmonics breakdowns of the steady-state current of phase (a), i_a, and steady-state field current profile, i_f, are given in Figures (9.4.14) and (9.4.15), at rated load conditions (over-excited 0.75 lagging power factor) for the 14.3 kVA MLA, respectively. Test oscillograms are not available at this time. Meanwhile, the electromagnetic torque profile, is given in Figure (9.4.16), together with a breakdown of the harmonic components of the torque in the accompanying table. These harmonics could not have been calculated without use of the abc frame of reference coupled to the global 3D magnetic field computation method at hand. As expected the torque is of negative magnitude for this generation mode, which is due to the adoption of the consumer (load) notation throughout this investigation. Notice the substantial magnitude of the 18th harmonic (more than 4% of the average torque) in the torque profile, which can directly be attributed to the number of slots per pair of poles in the example 4-pole 14.3 kVA machine, whose number of stator slots is 36.

9.4.2 The 21.5 kVA, 0.75 Lagging Power Factor Load Case

The same algorithm and procedure were used to compute the 3D magnetostatic field distribution throughout the magnetic circuit of the example MLA, and its corresponding machine winding inductances, at an over-rated load of 21.5 kVA, 0.75 lagging power factor (over excited generator mode generating both Watts and Vars) and rated voltage conditions.

The radial flux density distributions (waveforms) in the main airgap of this MLA, at the same rotor position associated with Figures (9.4.1) through (9.4.3), were obtained at various axial z locations, namely at $z = 0$, and $z = \pm z_2$, see Figure (7.3.4). The flux density waveforms are given in Figures (9.4.17) and (9.4.18) for $z = 0$, and $z = \pm 1.92$ cm, respectively. An isometric presentation of the radial component of the flux density, B_r, distribution under one pole pitch (showing only the positive portion of B_r) is given in Figure (9.4.19). Again, examination of these

(a)

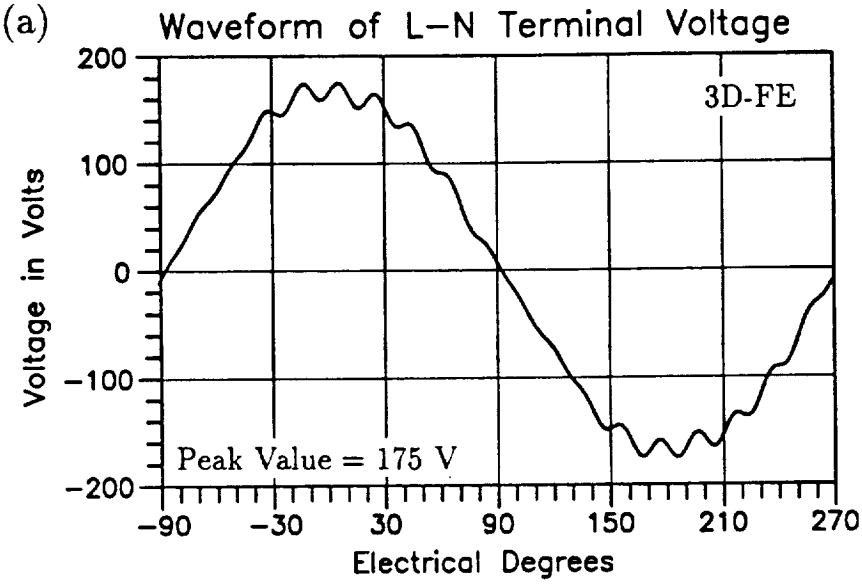

(b)

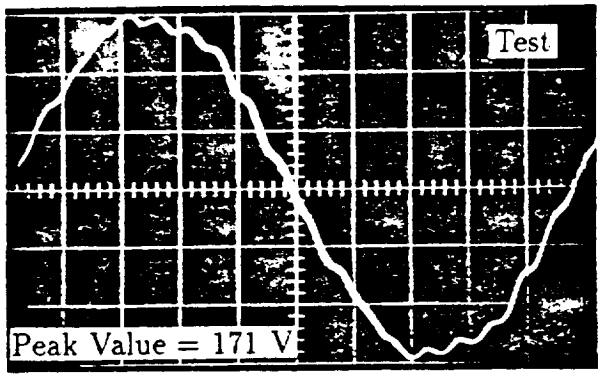

Figure (9.4.13) Comparison of Computed Waveform and Test Oscillogram of Line to Neutral Voltage at Rated Load

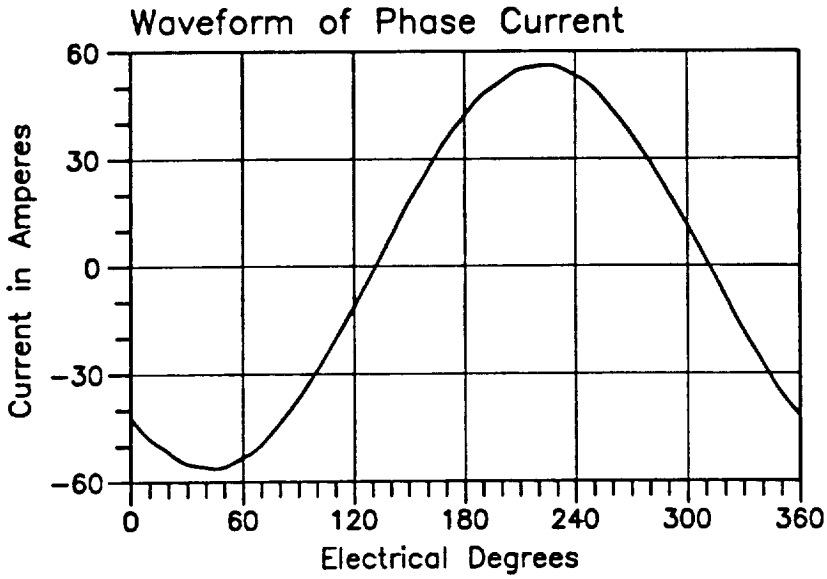

Harmonic Contents of Armature Phase Current, i_a		
Order n	Amplitude I_n (A)	Phase Angle ψ_n (Rad)
1	56.1230	-2.4190
3	0.0897	2.4506
5	0.3045	1.9489
7	0.0045	2.5185
9	0.0204	-1.8778
11	0.0797	-3.0016
13	0.0502	0.8577
15	0.0040	0.8132
17	0.1358	-0.8045
19	0.1338	-0.2408

Figure (9.4.14) Computed Waveform of Phase Current at Rated Load

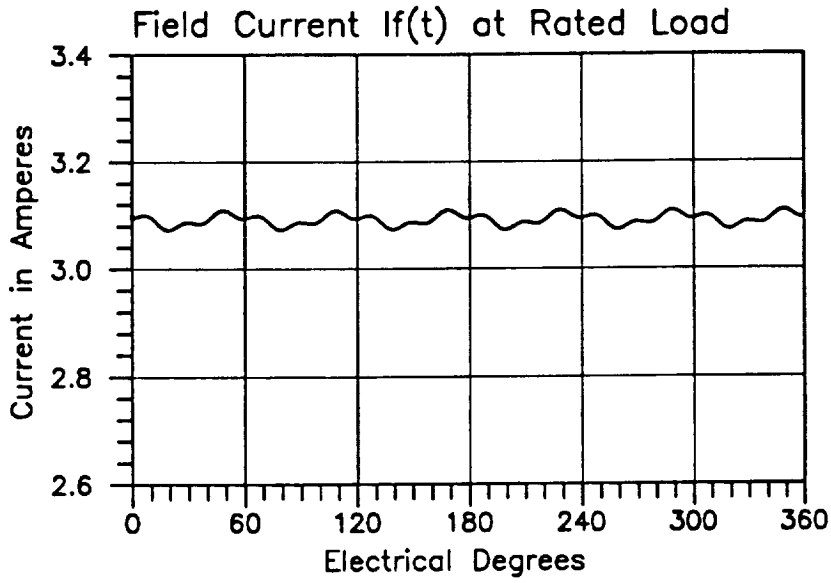

Harmonic Contents of Field Current, i_f		
Mean Value: 3.0912 (A)		
Order n	Amplitude I_n (A)	Phase Angle ψ_n (Rad)
6	0.0124	-0.7526
12	0.0011	2.1439
18	0.0068	2.5779

Figure (9.4.15) Computed Waveform of Field Current at Rated Load

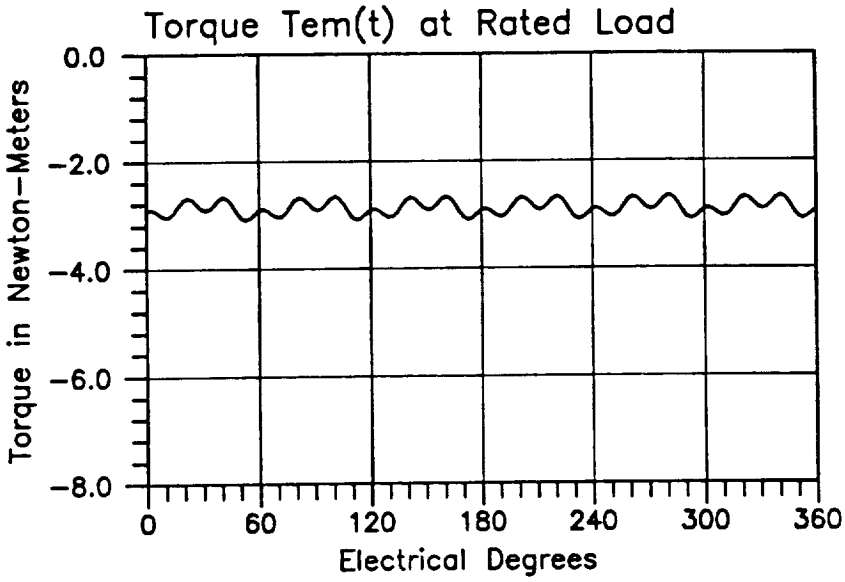

Harmonic Contents of Electromagnetic Torque		
Mean Value: T_0 = -2.881 $(N \cdot M)$		
Order n	Amplitude T_n $(N \cdot M)$	Phase Angle ψ_n (Rad)
6	0.1217	-3.0317
12	0.0289	2.8678
18	0.1280	0.5435

Figure (9.4.16) Computed Waveform of Electromagnetic Torque at Rated Load

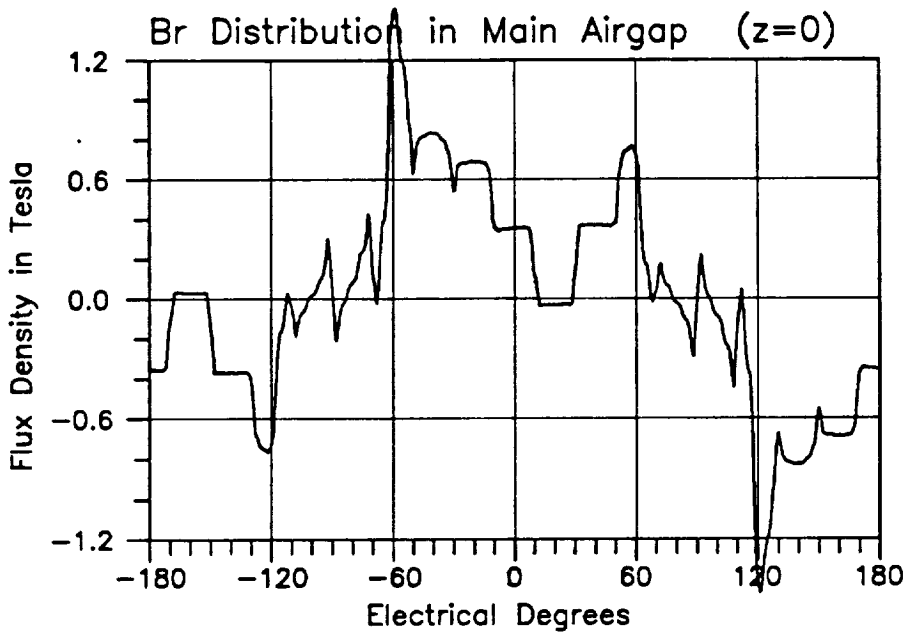

Figure (9.4.17) B_r Distributions in Main Airgap at $z = 0$ at Over-Rated Load

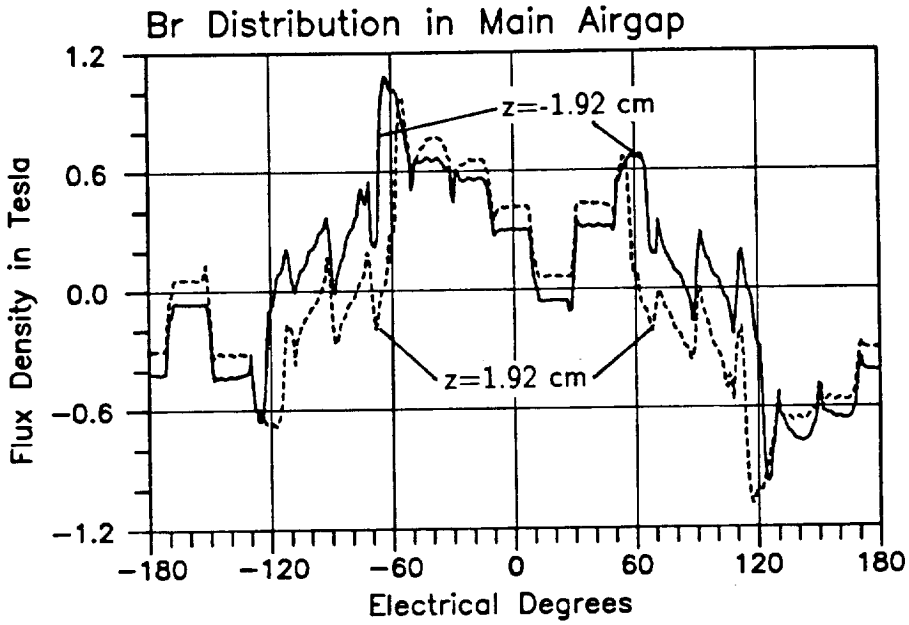

Figure (9.4.18) B_r Distributions in Main Airgap at z=±1.92 cm at Over-Rated Load

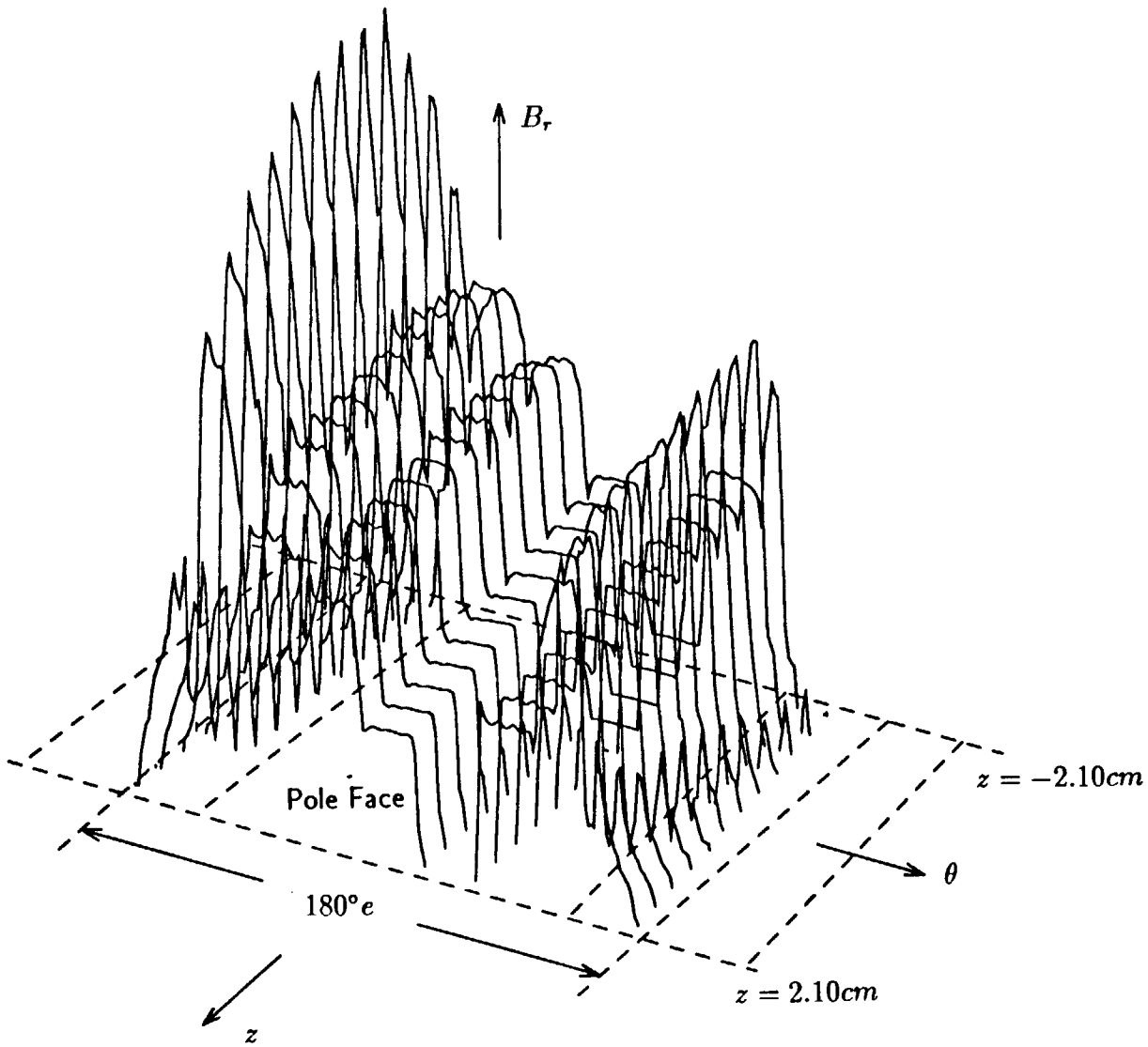

Figure (9.4.19) Isometric Presentation of the B_r Distribution in Main Airgap of the 14.3 kVA MLA at Over-Rated Load

flux density waveforms reveals their dependency on the axial-z location. Hence there is a lack of axial symmetry confirming the three dimensional nature of the magnetic field distribution in this MLA.

The computed machine inductances at this over-rated load, together with the inductances under no-load and rated load, are given in Figures (9.4.20) through (9.4.23). As expected, there is a further decrease in inductance values when the MLA is working under over-loaded condition.

Figure (9.4.24) shows some typical computer simulation results, from which one can see that a field excitation current of 4.426 A (3195 Ampere-Turns total), is required for this over-rated operation. The steady-state line to neutral voltage waveform, v_a, and current waveform, i_a, for phase (a) are given for this overload condition in Figures (9.4.25) and (9.4.26), respectively. Notice the ripple-prone nature of the line to neutral voltage waveforms, and the near absence of such ripples in the current. The corresponding field current, i_f, profile is given in Figure (9.4.27), which again is not ripple free. No test data are available for this load condition at this time.

For this over-rated load condition the steady-state torque profile was also computed from the results of the 3D magnetic field and accompanying state model algorithms and is given in Figure (9.4.28), which shows a substantial ripple content. This is in addition to a table containing the harmonic breakdown of the torque given in the same figure, which again reveals substantial 6th and 18th harmonic components. Again, the 18th harmonic component is related directly to the number of stator slotting (18 slots per pair of poles).

9.5 Effects of Load on Flux Distributions and Other MLA Parameters

The computed main flux flow pattern is shown in Figures (9.5.1) and (9.5.2) by means of $\overline{B}$ vector arrows along a direct axis plane of the 14.3 kVA MLA, for the 14.3 kVA, 0.75 lagging P.F., rated voltage case, in the cores and in the end-turn region, respectively. For the same rated load case, the $\overline{B}$ field plot in the mid armature cross-sectional plane is given in Figure (9.5.3). These figures again show the truly 3D

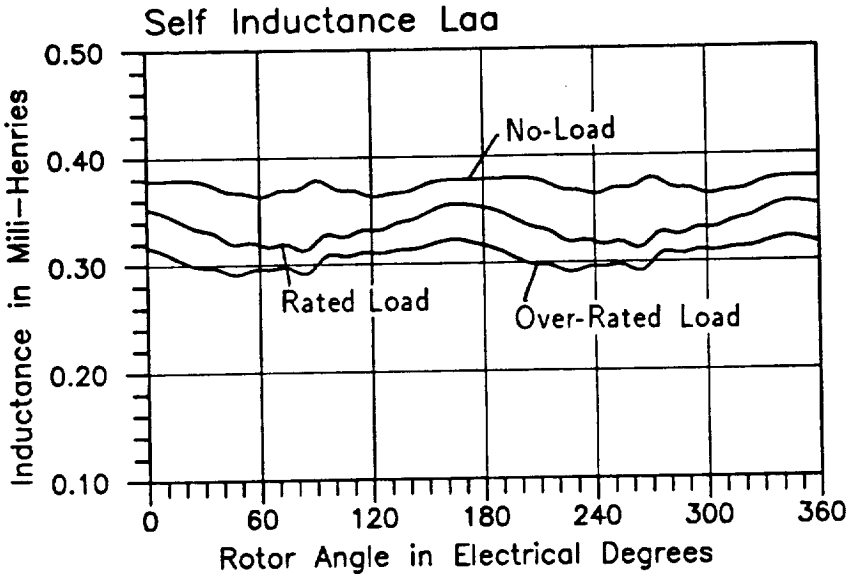

Figure (9.4.20) 3D-FE Computed Machine Self Inductance L_{aa} at Over-Rated Load

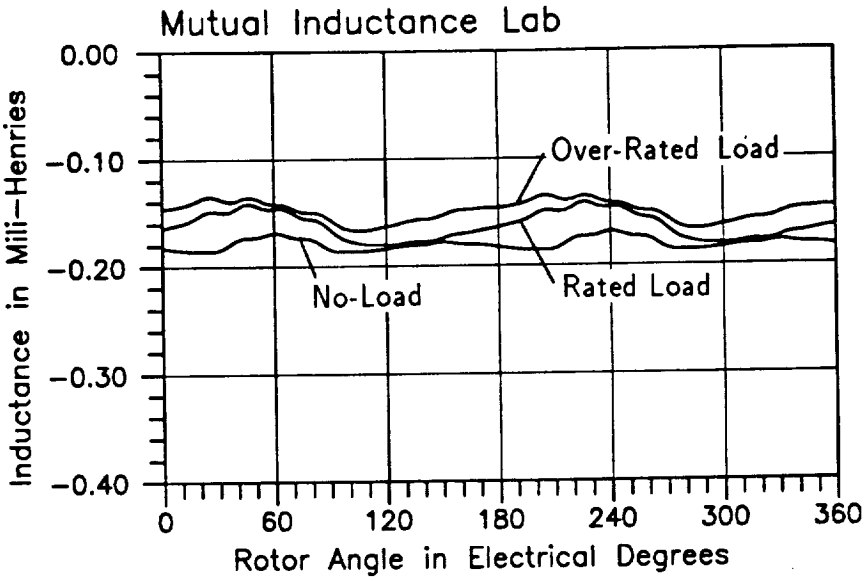

Figure (9.4.21) 3D-FE Computed Machine Mutual Inductance L_{ab} at Over-Rated Load

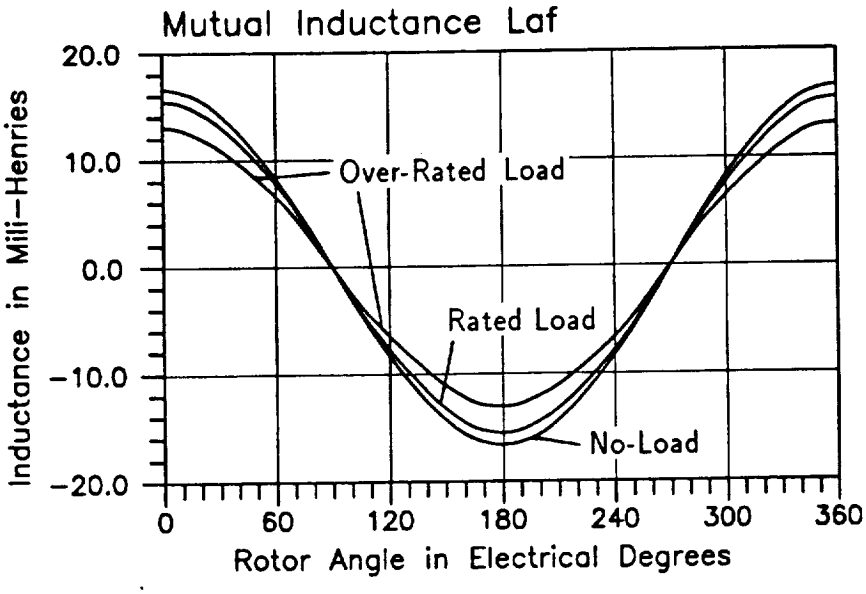

Figure (9.4.22) 3D-FE Computed Machine Mutual Inductance L_{af} at Over-Rated Load

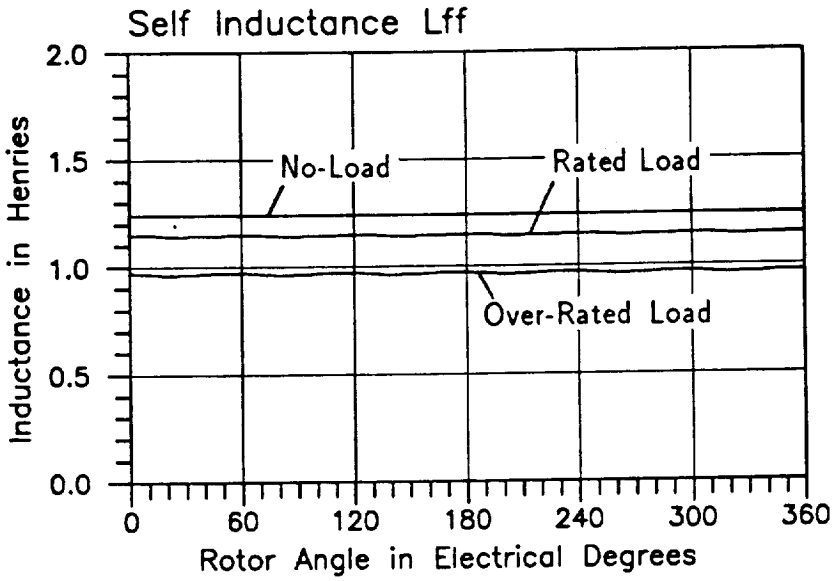

Figure (9.4.23) 3D-FE Computed Machine Self Inductance L_{ff} at Over-Rated Load

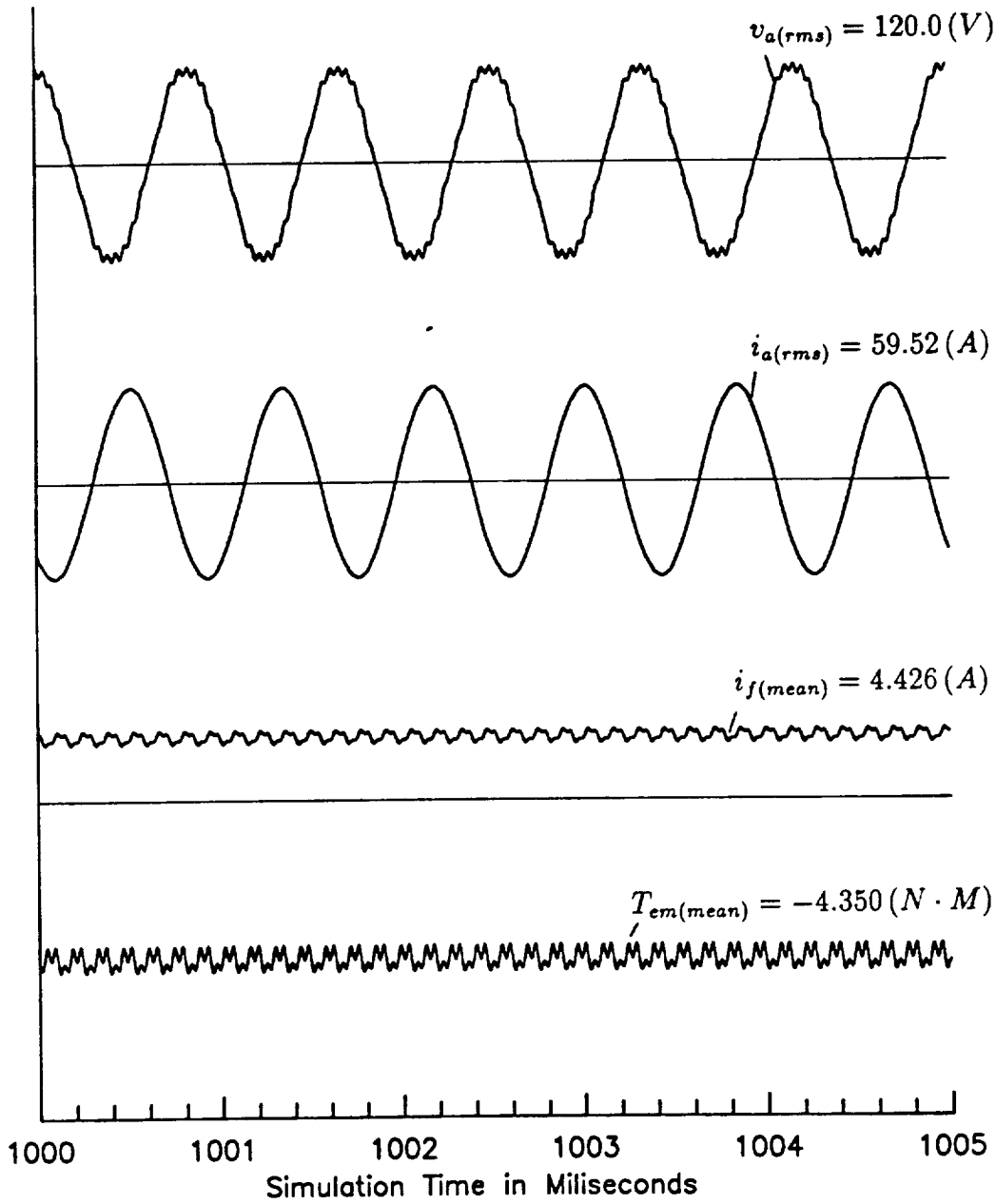

Figure (9.4.24) Plot of Typical Computer Simulation Results of the 14.3 kVA MLA at Over Rated Load

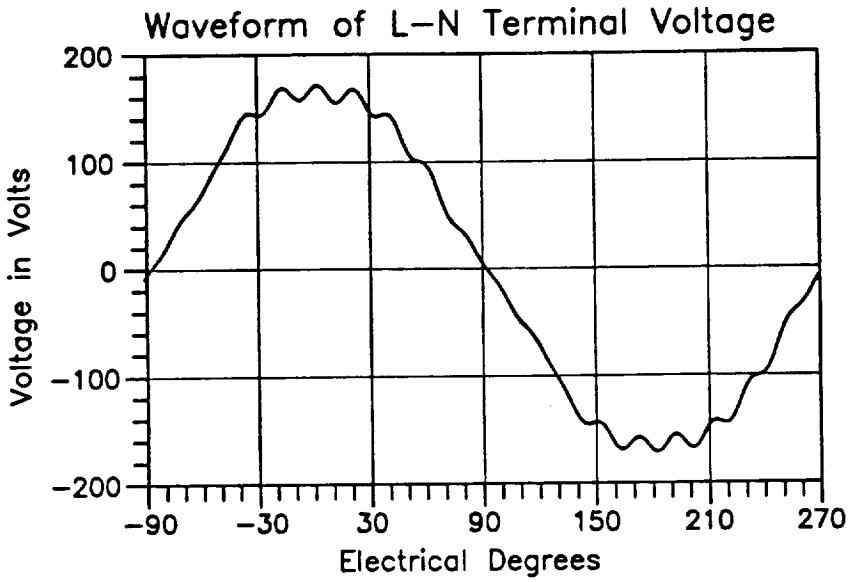

Harmonic Contents of Terminal Voltage, v_a		
Order n	Amplitude V_n (V)	Phase Angle ψ_n (Rad)
1	169.51	0.0000
3	0.7772	-2.0605
5	5.1410	-2.9827
7	0.8527	1.3353
9	0.3961	-0.6318
11	1.9057	-2.0050
13	1.4155	1.8762
15	0.1896	1.7478
17	3.6773	-0.3814
19	4.3673	0.2651

Figure (9.4.25) Computed Waveform of Line to Neutral Voltage at Over-Rated Load

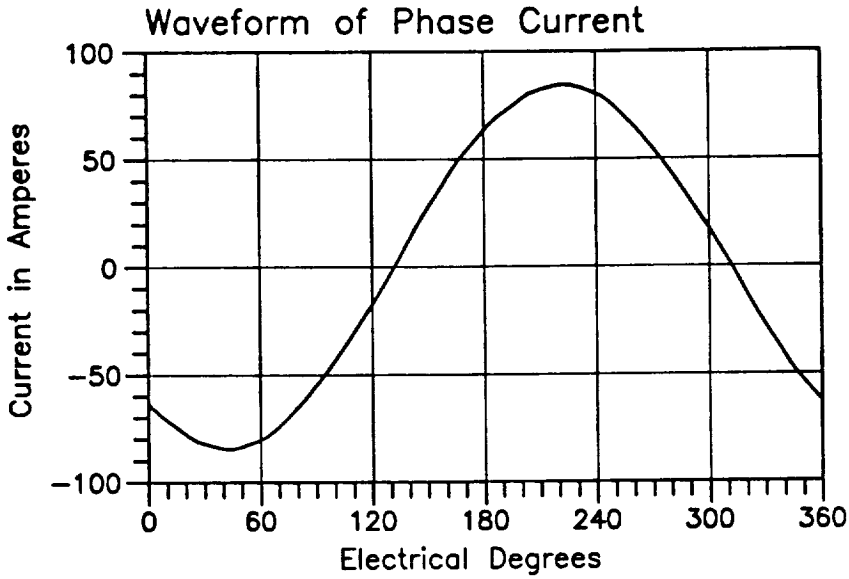

Harmonic Contents of Armature Phase Current, i_a		
Order n	Amplitude I_n (A)	Phase Angle ψ_n (Rad)
1	84.168	-2.4188
3	0.1819	2.2906
5	0.7527	1.5067
7	0.0903	-0.3962
9	0.0327	-2.3279
11	0.1294	2.6046
13	0.0814	0.2184
15	0.0095	0.1013
17	0.1620	-2.0188
19	0.1722	-1.3653

Figure (9.4.26) Computed Waveform of Phase Current at Over-Rated Load

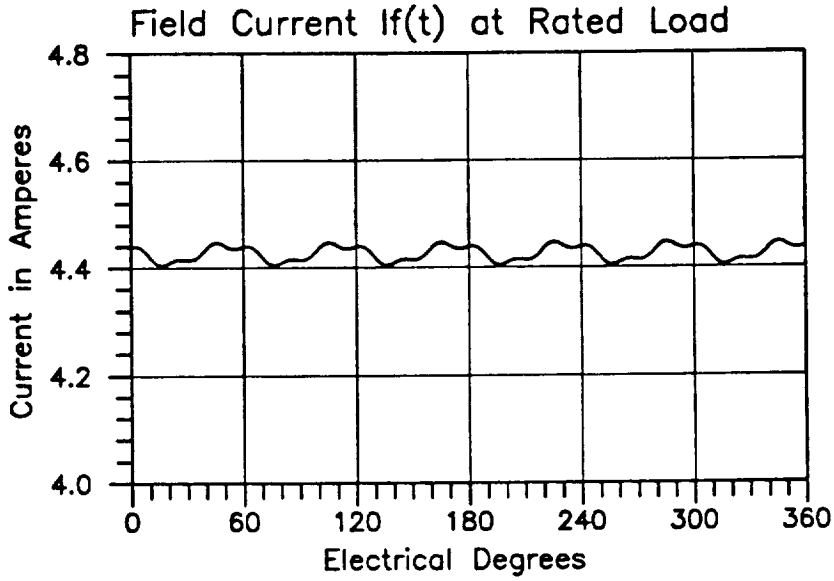

Harmonic Contents of Field Current, i_f		
Mean Value: 4.4262(A)		
Order n	Amplitude I_n (A)	Phase Angle ψ_n (Rad)
6	0.0178	-0.8935
12	0.0015	1.3687
18	0.0067	1.4170

Figure (9.4.27) Computed Waveform of Field Current at Over-Rated Load

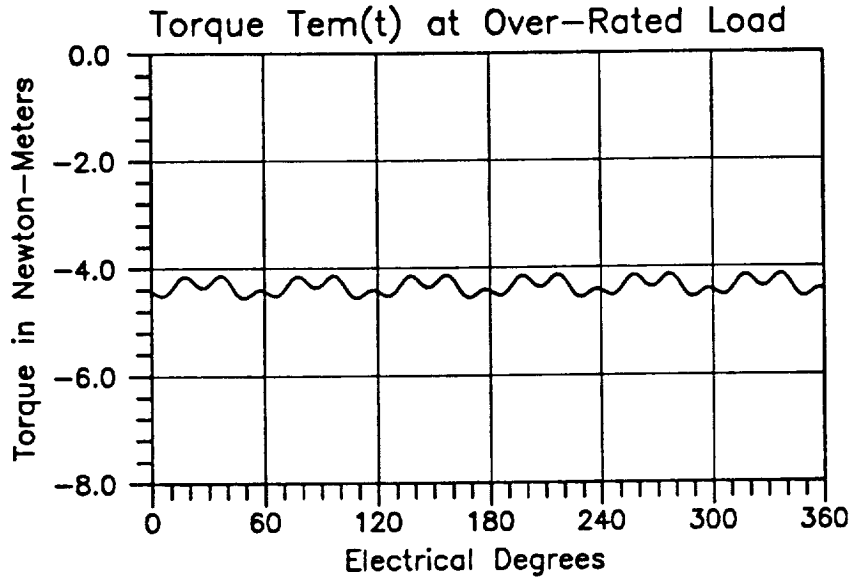

Harmonic Contents of Electromagnetic Torque		
Mean Value: $T_0 = -4.3502(N \cdot M)$		
Order n	Amplitude $T_n\ (N \cdot M)$	Phase Angle $\psi_n\ (Rad)$
6	0.1395	2.8195
12	0.0368	2.2098
18	0.1163	-0.8069

Figure (9.4.28) Computed Waveform of Electromagnetic Torque at Over-Rated Load

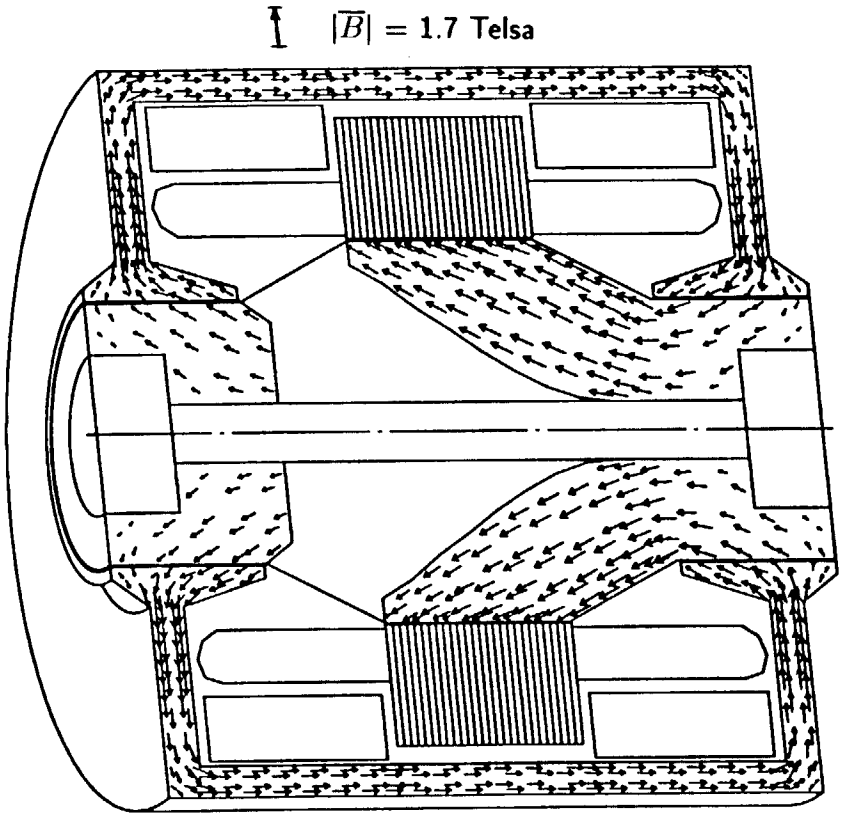

Figure (9.5.1) Flux Flow Pattern Along a Longitudinal Cross-Section of the 14.3 kVA MLA, at Rated Load

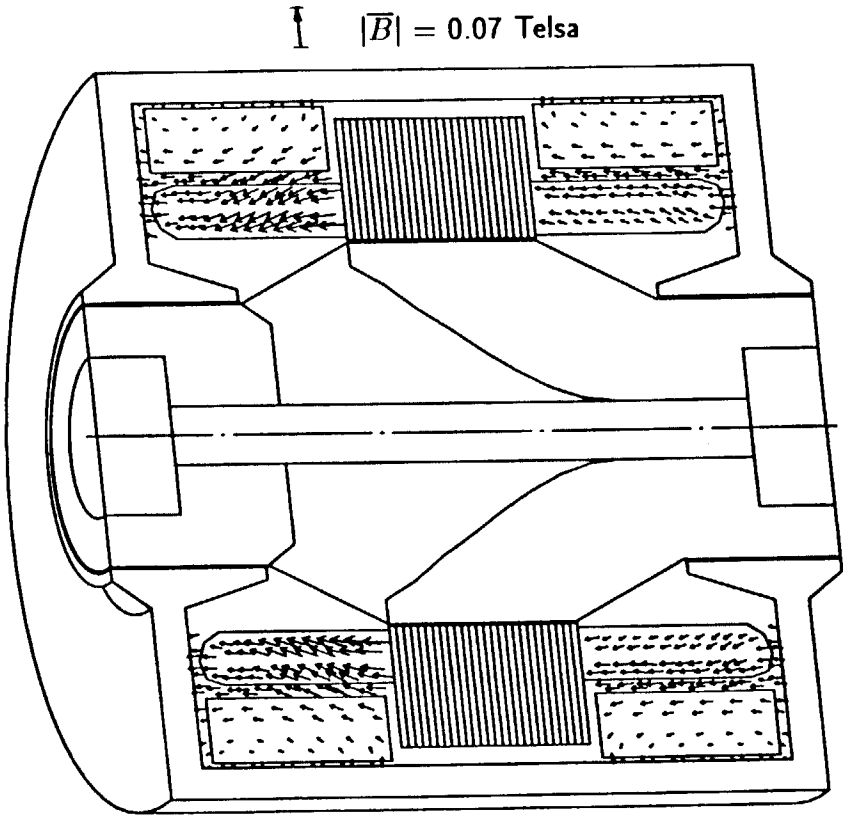

Figure (9.5.2) Flux Pattern in Armature End-Turn Region, Along a Longitudinal Cross-Section of the 14.3 kVA MLA, at Rated Load

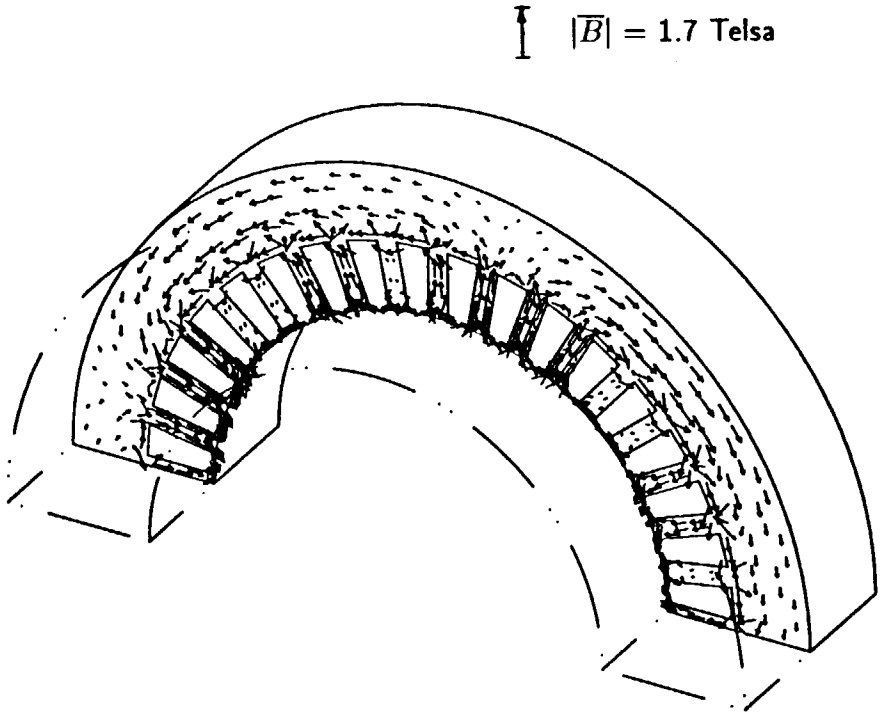

Figure (9.5.3) Flux Pattern in the Mid-Plane Cross-Section of the Stator Core of the 14.3 kVA MLA, at Rated Load

nature of the magnetic field distribution in the MLA class of machines.

The resultant flux densities at typical magnetic circuit locations in the rotor, (1) through (6), see Figure (9.5.4) for these locations, are given in the table included within this figure for the rated voltage no-load, 14.3 kVA and 21.5 kVA load conditions, respectively. Notice the significant increase in the magnitudes of flux densities at all six locations, and in particular at locations(2), (4) and (5) designated in the longitudinal rotor cross-section in Figure (9.5.4), where flux densities higher than 1.4 Tesla were computed.

Furthermore, the resultant flux densities at typical stator core locations, (1) through (4), shown in the stator laminations' FE cross-sectional grid of Figure (9.5.5). are given in the table attached to the same figure for the three above mentioned operating conditions, respectively. As expected, the higher level of magnetic saturation occurs at the stator tooth tips, location (1), at which the flux density reaches magnitudes near 2 Teslas under both load conditions studied here.

Effects of load on the synchronous reactances, x_d and x_q, is given in Table (9.5.1), with comparison to the no-load reactance values. This is given only for insight into the global effects of load magnetic saturation levels, and should not be construed as an endorsement of d-q modeling for such MLAs.

Again, the combined MVP-MSP 3D-FE magnetic field computation in conjunction with the abc-frame state-model of the load conditions in the MLA, allows one to determine the magnetic field distributions and profiles as well as the steady state waveforms of the armature and field currents and voltages, at any desired load conditions. These field distributions and voltage as well as current profiles cannot be computed using conventional design methods and formulas because of the very complex 3D nature of the magnetic field and magnetic circuit configurations in this class of alternators (MLAs). This method allows the incorporation of the full impact of magnetic nonlinerities and space harmonics caused by the magnetic and geometric complexities into the computation of the terminal voltage waveforms, current waveforms, and most importantly electromagnetic torque profiles associated with these machines under load. Knowledge of the harmonics in the torque profiles is of importance for vibration studies associated with aerospace applications.

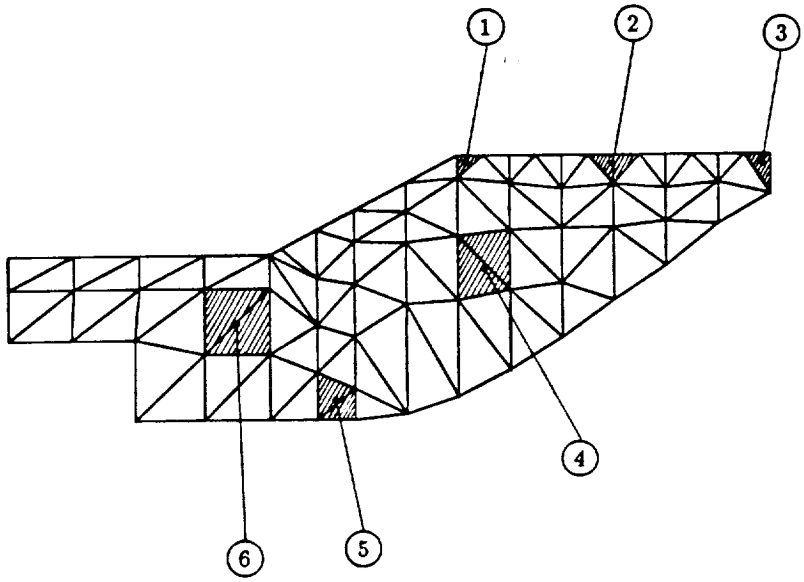

Typical MLA rotor flux density values (Teslas)			
Location	No-Load	14.3 kVA	21.5 kVA
(1)	1.02	1.28	1.33
(2)	0.96	1.29	1.40
(3)	0.58	0.85	0.99
(4)	1.04	1.37	1.43
(5)	0.82	1.26	1.42
(6)	0.87	1.20	1.27

Figure (9.5.4) Effects of Load on Typical Flux Densities in the Rotor Magnetic Portion of the 14.3 kVA MLA

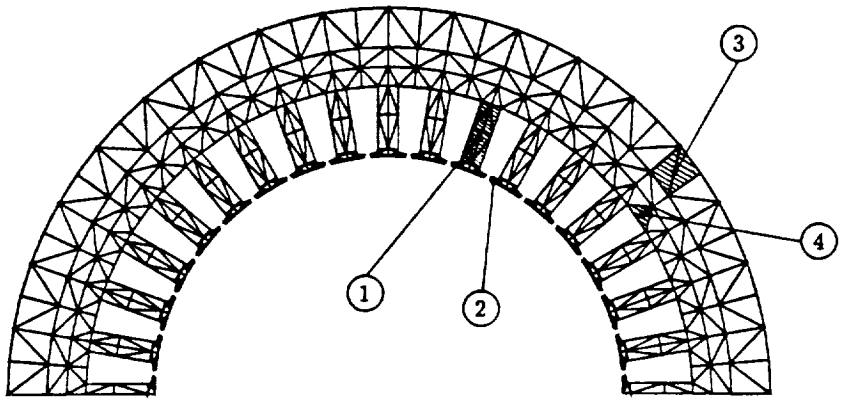

Typical MLA stator flux density values (Teslas)			
Location	No-Load	14.3 kVA	21.5 kVA
(1)	1.21	1.89	1.96
(2)	1.06	1.58	1.58
(3)	0.86	0.98	0.91
(4)	1.08	1.24	1.23

Figure (9.5.5) Effects of Load on Typical Flux Densities in Stator Core of the 14.3 kVA MLA

Table (9.5.1) Effects of Load on $d-q$ Inductances

Reactance	No-Load	14.3 kVA	21.5 kVA
x_d (Ohms)	4.33	3.88	3.72
x_q (Ohms)	4.25	3.47	3.31

Chapter 10

Conclusions and Recommendations for Future Work

A novel method of combined use of MVP based FE formulations and MSP based FE formulations for computation of 3D magnetostatic fields was developed in this dissertation. This method provides a powerful tool for 3D magnetostatic field computation, which makes it practical, using state of the art super-computer resources, to globally compute and analyze the magnetic fields in rotating electric machines. The advantages of this method over the other existing methods [32, 33, 34, 38, 37] which are exclusively based on MVP formulations or MSP formulations, can be listed as follows:

(1) The combined MVP-MSP solution method leads to considerable reduction by nearly a factor of 3 in the number of unknowns in comparison to the number of unknowns which must be computed in global MVP solutions. Accordingly, this method achieves substantial cpu time savings in the solution of large scale problems in comparison to MVP based methods.

(2) The method employs second-order finite element curl-curl MVP formulation to compute the curl component of the magnetic field intensity in the current carrying region. Hence, it eliminates the difficulty of FE grid ill-conditioning associated with the MVP based first-order FE formulations as explored and detailed in Chapter 2.

(3) The method allows one to incorporate portions of iron cores sandwiched in between coils (conductors), which is a unique feature of this method among the MSP based class of methods. Thus, it greatly simplifies the

geometries of current carrying regions in electric machinery applications.

(4) The method leads to global MSP solutions which are single valued in nature, that is, no branch cut is needed. This is again a unique feature in this approach among the MSP based class of magnetic field computation methods.

(5) The method eliminates the need for having to perform the difficult tasks associated with integral type (Biot-Savart) and other formulations which must be used in exclusively MSP based solution algorithms. Accordingly, this method leads to a substantial advantage in handling very complex conductor geometries associated with rotating electric machinery.

(6) A simple surface finite element technique used in the calculation of the magnetic scalar potential jumps, which is necessary for linking the MVP and MSP based portions of the solution algorithm, was achieved and implemented.

In addition, a Newton-Raphson procedure with a novel concept of an adaptive relaxation factor was developed and successfully used in solving the 3D-FE MSP problem with magnetic material anisotropy and nonlinearity. Accordingly, the method is most suited for solution of large scale global type magnetostatic field computations in rotating electric machinery with very complex geometries and magnetic circuit topologies, as well as nonlinear and anisotropic material properties.

The combined MVP-MSP 3D-FE method, in conjunction with the state space equations using the natural abc-frame of reference, forms a complete computer aided model to analyze and predict machine parameters and performances. This modeling tool was applied to 3D magnetic field analysis and machine performance computations of an example 14.3 kVA MLA. The energy perturbation approach [18, 79] was successfully used in this investigation to compute machine winding inductances from 3D-FE computed magnetic field results. The effects of magnetic material nonlinearity and the space harmonics due to complex magnetic circuit geometries were fully included in the results of machine winding inductances. Results of computed open-circuit, short-circuit, as well as rated load and over-rated load conditions were found to be in excellent agreement with corresponding test values. The computed waveforms of armature phase line to neutral voltages compared favorably to the test oscillograms. Meanwhile, the electromagnetic torque profiles including their ripples (harmonics) were computed in terms of terminal voltage and current profiles as well as stored

magnetic energies. Knowledge of the harmonics in the torque profile is important for vibration studies associated with aerospace applications. Also, results of study of load effects on the flux densities in typical locations in rotor and stator lamination cores were carried out. This modeling technique and algorithm can serve as an excellent design tool and means of gaining insight into the workings of such MLAs with very complex 3D magnetic field patterns and complex magnetic circuit geometries. The generic nature of this modeling allows one to use it in design optimization and design synthesis studies.

In addition, results of use of this modeling and computation method in a design alteration, in which the stator stack length of the example alternator is stretched in order to increase voltage and volt-ampere rating, were studied in this investigation. These results demonstrate the inadequacy of conventional 2D-based design concepts and the imperative of this type of 3D magnetic field modeling in analysis of such MLA class of machines. This includes almost all machines of the axial flux flow variety.

As a recommendation for the future work, this author suggests that further effort should be made to expand the capability of this computer aided model to computation of electromagnetic forces on windings and computation of ferromagnetic core losses. This expansion should also include the capability of computing machine transient and damping parameters, which would enable one to analyze rectifier-type load effects on such MLAs.

Meanwhile, this author believes that studies and developments of methods of 3D magnetic field computations should be carried on further. Because of the volume current distributions, complex geometries, and magnetic material nonlinearities in electric machine problems, the global MVP formulation seems to be the most convenient method to use in such applications. In seeking global MVP methods suitable for such complex and large scale problems, the 3D-FE MVP edge element formulation [47] should be further investigated. Also, with the fast advances of the modern computer capabilities, the second-order 3D-FE MVP formulation, if it can effectively handle magnetic material nonlinearity, can be a convenient and powerful tool in solving large scale electromagnetic fields in rotating electric machines.

Bibliography

[1] R.R. Secunde, T.L. Labus and R.G. Lovely, "Solar Dynamic Power Module Design," *24th Intersociety Energy Conversion Engineering Conference*, Washington D.C., NASA TM 102055, 1989.

[2] B.D. Ingle and C.S. Corcoran, "Development of a 1200-Hertz Alternator and Controls for Space Power System," *NASA Report*, NASA TM X-52453, 1968.

[3] D.S. Repas and R.A. Edkin, "Performance Characteristics of a 14.3-Kilovolt-Ampere Modified Lundell Alternator for 1200 Hertz Brayton-Cycle Space-Power System," *NASA Report*, NASA TN D-5404, 1969.

[4] F.C. Trutt and E.A. Erdelyi, "The Non-Linear Potential Equations and Its Numerical Solution for Highly Saturated Electrical Machines," *IEEE Transactions on Aero-Space*, Vol. 1, pp. 417-429, 1963.

[5] S.V. Ahamed and E.A. Erdelyi, "Non-Linear Vector Potential Equations for Highly Saturated Heteropolar electrical Machines," *IEEE Transactions on Aero-Space*, Vol. 2, pp. 896-903, 1964.

[6] E.A. Erdelyi, S.V. Ahamed and R.E. Hopkins, "Non-Linear Theory of Synchronous Machines On-Load," *IEEE Transactions on Power Apparatus and Systems*, Vol. PAS-85, pp. 792-801, 1966.

[7] E.A. Erdelyi and E.F. Fuchs, "Non-Linear Vector Potential Magnetic Field Analysis of DC Machines - Part I : Theoretical Fundamentals," *IEEE Transactions on Power Apparatus and Systems*, Vol. PAS-89, pp. 1546-1554, 1970.

[8] E.F. Fuches and Erdelyi, "Non-Linear Vector Potential Magnetic Field Analysis of DC Machines - Part II : Application of the Improved Treatment," *IEEE*

Transactions on Power Apparatus and Systems, Vol. PAS-89, pp. 1555-1564, 1970.

[9] N.A. Demerdash, H.B. Hamilton and G.W. Brown, "Simulation for Design Purposes of Magnetic Fields in Turbogenerators with Symmetrical and Assymmetrical Rotors - Part I - Model Development and Solution Technique," *IEEE Transactions on Power Apparatus and Systems*, Vol. PAS-91, pp. 1985-1992, 1972.

[10] N.A. Demerdash and H.B. Hamilton, "Simulation for Design Purposes of Magnetic Fields in Turbogenerators with Symmetrical and Assymmetrical Rotors - Part II - Model Calibration and Applications," *IEEE Transactions on Power Apparatus and Systems*, Vol. PAS-91, pp. 1992-1999, 1972.

[11] P.P. Silvester and M.V.K. Chari, "Finite Element Solution of Saturable Magnetic Field Problems," *IEEE Transactions on Power Apparatus and Systems*, Vol. PAS-89, pp. 1642-1652, 1970.

[12] M.V.K. Chari and P.P. Silvester, "Analysis of Turbo Alternator Magnetic Field by Finite Elements," *IEEE Transactions on Power Apparatus and Systems*, Vol. PAS-90, pp. 454-464, 1971.

[13] M.V.K. Chari, "Finite Element Solution of Eddy Current Problems in Magnetic Structures," *IEEE Transactions on Power Apparatus and Systems*, Vol. PAS-93, pp. 62-72, 1974.

[14] N.A. Demerdash and T.W. Nehl, "Flexibility and Economics of Implementation of the Finite Element and Difference Techniques in Nonlinear Magnetic Fields of Power Devices," *IEEE Transactions on Magnetics*, Vol. MAG-12, pp. 1036-1038, 1976.

[15] N.A. Demerdash and T.W. Nehl, "An Evaluation of the Method of Finite Element and Finite Difference in the Solution of Nonlinear Electromagnetic Fields in Electrical Machines," *IEEE Transactions on Power Apparatus and Systems*, Vol. PAS-98, pp. 74-87, 1979.

[16] P.P. Silvester and A. Konrad, "Analysis of Transformer Leakage Phenomena by High-Order Finite Elements," *IEEE Transactions on Power Apparatus and Systems*, Vol. PAS-92, pp. 1843-1855, 1973.

[17] F.A. Fouad, T.W. Nehl and N.A. Demerdash, "Permanent Magnetic Modeling for Use in Vector Potential Finite Element Analysis in Electrical Machinery," *IEEE Transactions on Magnetics*, Vol. MAG-17, pp. 3002-3004, 1981.

[18] T.W. Nehl, F.A. Fouad and N.A. Demerdash, "Determination of Saturated Values of Rotating Machinery Incremental and Apparent Inductances by an Energy Perturbation Method," *IEEE Transactions on Power Apparatus and Systems*, Vol. PAS-101, pp. 4441-4451, 1982.

[19] E.A. Heighway and C.S. Biddlecombe, "Two Dimensional Automatic Triangular Mesh Generation for the Finite Element Electromagnetic Package PE2D," *IEEE Transactions on Magnetics* Vol. MAG-18, pp. 594-598, 1982.

[20] P. Masse, J.L. Coulomb and B. Ancelle, "System Design Methodology in CAD Programs Based on Finite Element Method," *IEEE Transactions on Magnetics* Vol. MAG-18, pp. 609-616, 1982.

[21] C.S. Holzinger, "Computation of Magnetic Fields Within Three Dimensional Highly Nonlinear Media," *IEEE Transactions on Magnetics* Vol. MAG-6, p. 60. 1970.

[22] D.J. Kozakoff and F.O. Simons, "Three Dimensional Nonlinear Magnetic Field Boundary Value Problem and Its Numerical Solution," *IEEE Transactions on Magnetics* Vol. MAG-6, p. 8, 1970.

[23] W. Muller and Wolff, "Numeishe Berechung Dreidimensionaler Magnet Felder Fur Grosse Turbogeneratoren Bei Feodabhangiger Permeabilitat Und Beliebiger Strondichte," *ETZ-A*, 94, pp. 276-282, 1973.

[24] M. Djurovic and C.J. Carpenter, "3-Dimensional Computation of Transformer Leakage Fields and Associated Losses," *IEEE Transactions on Magnetics*, Vol. MAG-11, p. 1535, 1975.

[25] E. Guancial, and S. DasGupta, "Three Dimensional Finite Element Program for Magnetic Field Problems", *IEEE Transactions on Magnetics*, Vol. MAG-13, pp. 1012-1015, 1977.

[26] O.C. Zienkiewicz, J. Lyness and D.J.R. Owen, "Three Dimensional Magnetic Field Determination using a scalar Potential," *IEEE Transactions on Magnetics*, Vol. MAG-13, pp. 1649-1656, 1977.

[27] J. Simkin, and C.W. Trowbridge, "Three-Dimensional Nonlinear Electromagnetic Field Computations, Using Scalar Potentials," *IEE Proceedings*, Vol. 1.27, Part B, No. 6, pp. 368-347, 1980.

[28] S. Zheng, and R. Wang, "A New Method for the Solution of Three-Dimensional Magnetostatic Fields, Using a Scalar Potential," *IEEE Transactions on Magnetics*, Vol. MAG-21, pp. 2177-2176, 1985.

[29] I.D. Mayergoyz, M.V.K. Chari and J. D'Angelo, "A New Scalar Potential Formulation for Three-Dimensional Magnetostatic Problems," *IEEE Transactions on Magnetics*, Vol. MAG-23, pp. 1649-1656, 1987.

[30] P. Campbell, M.V.K. Chari and J. D'Angelo, "Three Dimensional Finite Element Solution of Permanent Magnet Machines," *IEEE Transactions on Magnetics*, Vol. MAG-17, pp. 2997-2999, 1981.

[31] M. Liese, K. Lenz, K. Senske, and J. Spiegl, "Comparison of Vector Potential and Extended Scalar Potential Methods and True Three-Dimensional Magnetic Field Calculation" *IEEE Transactions on Power Apparatus and Systems*, Vol. PAS-103, pp. 1339-1347, 1984.

[32] N.A. Demerdash, T.W. Nehl and F.A. Fouad, "Finite Element Formulation and Analysis of Three Dimensional Magnetic Field Problems," *IEEE Transactions on Magnetics*, Vol. MAG-16, pp. 1092-1094, 1980.

[33] N.A. Demerdash, T.W. Nehl, F.A. Fouad and O.A. Mohammed, "Three Dimensional Finite Element Vector Potential Formulation of Magnetic Fields in Electrical Apparatus," *IEEE Transactions on Power Apparatus and Systems*, Vol. PAS-100, pp. 4104-4111, 1981.

[34] N.A. Demerdash, T.W. Nehl, O.A. Mohammed and F.A. Fouad, "Experimental Verification and Application of the Three Dimensional Finite Element Magnetic Vector Potential Method in Electrical Apparatus," *IEEE Transactions on Power Apparatus and Systems*, Vol. PAS-100, pp. 4112-4122, 1981.

[35] N.A. Demerdash, T.W. Nehl, "Nonlinear Three Dimensional Magnetic Vector Potential Finite Element Solution of Field Problems Including Experimental Verification," *IEEE Transactions on Magnetics*, Vol. MAG-17, pp. 3408-3410, 1981.

[36] O.A. Mohammed, N.A. Demerdash and T.W. Nehl, "Nonlinear Vector Potential Formulation and Experimental Verification of Newton-Raphson Solution of Three Dimensional Magnetostatic Fields in Electrical Devices," *IEEE Transactions on Energy Conversion*, Vol. EC-1, pp. 177-185, 1986.

[37] M.V.K. Chari, P.P. Silvester, A. Konrad and M.A. Palmo, "Three-Dimensional Magnetostatic Field Analysis of Electrical Machinery by the Finite Element Method," *IEEE Transactions on Power Apparatus and Systems*, Vol. PAS-100, pp. 4007-4019, 1981.

[38] J.L. Coulomb, "Finite Element Three Dimensional Magnetic Field Computation," *IEEE Transactions on Magnetics*, Vol. MAG-17, pp. 3241-3246, 1981.

[39] P.R. Kotiuga and P.P. Silvester, "Vector Potential Formulation for Three-Dimensional Magnetostatics," *Journal of Applied Physics*, Vol. 53, pp. 8399-8401. 1982.

[40] C.J. Csendes, J. Weiss and S.R. Hoole, "Alternative Vector Potential Formulations of 3-D Magnetostatic Field Problems," *IEEE Transactions on Magnetics*, Vol. MAG-18, pp. 367-372, 1982.

[41] O.A. Mohammed, W.A. Davis, B.D. Popovic, T.W. Nehl and N.A. Demerdash, "On the Uniqueness of Solution of Magnetostatic Vector Potential Problems by Three-Dimensional Finite Element," *Journal of Applied Physics*, Vol. 53, 11, pp. 8402-8404, 1982.

[42] O.A. Mohammed, N.A. Demerdash and T.W. Nehl, "Validity of Finite Element Formulation and Solution of Three Dimensional Magnetostatic Problem in Electrical Devices with Applications to Transformers and Reactors," *IEEE Transactions on Power Apparatus and Systems*, Vol. PAS-103, pp. 1848-1853, 1984.

[43] S.R.H. Hoole, R. Rios and S. Yoganathan, "Vector Potential Formulations and Finite Element Trial Functions," *International Journal of Numerical Methods in Engineering*, Vol. MAG-26, pp. 95-108, 1988.

[44] J.A. Meijerink and H.A. Von Der Vorst, "An Iterative Solution for Linear Systems of which the Coefficient Matrix Is a Symmetric M-matrix", *Mathematics of Computation*, Vol. 31, No. 137, 1977.

[45] M.A. Ajiz and A. Jennings, "A Robust Incomplete Choleski- Conjugate Gradient Algorithm," *International Journal of Numerical Methods in Engineering*, Vol. 20, pp. 946-966, 1984.

[46] A. Bossavit, "On Finite Elements for Electricity Equation," in *The Mathematics of Finite Elements and Application* (Edited by J.R. Whiteman), Acad. Press, London, pp. 85-92, 1982.

[47] M.L. Barton and C.J. Cendes, "New Vector Finite Elements for Three Dimensional Magnetic Field computation," *Journal of Applied Physics* vol. 61, pp. 3919-3921, 1987.

[48] T.W. Nehl and D.A. Field, "Adaptive Refinement of First Order Tetrahedral Meshes for Magnetostatic Using Local Delaunay Subdivisions," Paper No. EB-05, *The Fourth Biennial IEEE Conference on Electromagnetic Field Computation*, Toronto, Canada, Oct. 1990.

[49] E.F. Fuchs and E.A. Erdelyi, "Nonlinear Theory of Turboalternators Part II: Load Dependent Synchronous Reactances," *IEEE Transactions on Power Apparatus and Systems*, Vol. PAS-92, pp. 592-599, 1973.

[50] M.V.K. Chari, Z.J. Csendes, S.H. Minnich, S.C. Tandon and J. Berkery, "Load Characteristics of Synchronous Generators by the Finite Element Method," *IEEE Transactions on Power Apparatus and Systems*, Vol. PAS-100, pp. 1-13, 1981.

[51] F.A. Fouad, T.W. Nehl and N.A. Demerdash, "Magnetic Field Modeling of Permanent Magnet Type Electronically Operated Synchronous Machines Using Finite Elements," *IEEE Transactions on Power Apparatus and Systems*, Vol. PAS-100, pp. 4125-4135, 1981.

[52] N.A. Demerdash, T.W. Nehl, "Determination of Winding Inductances in Ferrite Type Permanent Magnet Electric Machinery by Finite Elements," *IEEE Transactions on Magnetics*, Vol. MAG-18, 99. 1052-1054, 1982.

[53] T.W. Nehl, N.A. Demerdash, T.M. Hijazi and T.L. McHale, "Automatic Formulation of Models for Simulation of the Dynamic Performance of Electrically Commutated DC Machines," *IEEE Transactions on Power Apparatus and Systems*, Vol. PAS-104, pp. 2214-2222, 1985.

[54] T.A. Nyamusa and N.A. Demerdash, "Integrated Nonlinear Magnetic Field - Network Simulation of an Electronically Commutated Permanent Magnet Motor System Under Normal Operation," *IEEE Transactions on Energy Conversion*, Vol. EC-2, pp. 77-85, 1987.

[55] T.A. Nyamusa and N.A. Demerdash, "Transient Analysis of Partial Armature Short Circuit in an Electronically Commutated Permanent Magnet Motor," *IEEE Transactions on Energy Conversion*, Vol. EC-2, pp. 86-92, 1987.

[56] A.A. Arkadan, T.M. Hijazi, N.A. Demerdash, J.G. Vaidya and V.K. Maddali, "Theoretical Development and Experimental Verification of a DC-AC Electronically Rectified Load-Generaor System Model Compatible with Common network Analysis Software Packages," *IEEE Transactions on Energy Conversion*, Vol. EC-3, pp. 123-131, 1988.

[57] T.M. Hijazi and N.A. Demerdash, "Computer-Aided Modeling and Experimental Verification of the Performance of Power Conditioner Operated Permanent Magnet Brushless DC Motors Including Rotor Damping Effects," *IEEE Transactions on Energy Conversion*, Vol. EC-3, pp. 714-721, 1988.

[58] T.S.Kulig, G.W. Buckley, D. Lambrecht and M. Liese, "A New Approach to Determine Transient Generator Winding and Damper Currents in Case of Internal and External Faults and Abnormal Operation - Part 1: Fundamentals," Paper No. 87 WM 203-3, IEEE-PES 1987 Winter Meeting, New Orleans, Louisiana, Feb. 1-6, 1987.

[59] T.S.Kulig, G.W. Buckley, D. Lambrecht and M. Liese, "A New Approach to Determine Transient Generator Winding and Damper Currents in Case of Internal and External Faults and Abnormal Operation - Part 2: Analysis," Paper No. 87 WM 204-1, IEEE-PES 1987 Winter Meeting, New Orleans, Louisiana, Feb. 1-6, 1987.

[60] T.S.Kulig, G.W. Buckley, D. Lambrecht and M. Liese, "A New Approach to Determine Transient Generator Winding and Damper Currents in Case of Internal and External Faults and Abnormal Operation - Part 3: Results," Paper No. 89 SM 752-7, IEEE-PES 1989 Summer Meeting, Long Beach, California, July 9-14, 1989.

[61] J.Mizia, K. Admiak, A.R. Eqstham and G.E. Dawson, "Finite element Force Calculation: Comparison of Methods for Electric Machines," *IEEE Transactions on Magnetics*, Vol. MAG-24, pp. 447-450, 1988.

[62] A.N. Wignall, A.J. Gilbert and S.J. Yang, "Calculation of Force on Magnetised Ferrous Cores Using the Maxwell Stress Method," *IEEE Transactions on Magnetics*, Vol. MAG-24, pp. 459-462, 1988.

[63] M.K. Jamil and N.A. Demerdash, "Effects of Chopper Controled Circuit on Core Lossed of Permanent Magnet dc Motors," *IEEE Transactions on Magnetics*, Vol. MAG-25, pp. 3572-3574, 1989.

[64] J.A. Tegopoulos, "Currents Equivalent to End-Winding Currents of Turbine-Generator Stator and Rotor," *IEEE Transactions on Power System and Apparatus*, Vol. PAS-81, pp. 695-700, Feb. 1963.

[65] J.A. Tegopoulos, "Flux Impinging on the endplate of turbine generators," *IEEE Transactions on Power System and Apparatus*, Vol. PAS-81, pp. 700-707, Feb. 1963.

[66] J.A. Tegopoulos and R.H. Boyer, "Magnetic Vector Potential as a Result of Elementary Currents Between Two Parallel Planes," *IEEE Transactions on Power System and Apparatus*, Vol. PAS-81, pp. 559-562, Aug. 1963.

[67] J.A. Tegopoulos, "Determination of the Magnetic Field in the End Zone of Turbine-Generators," *IEEE Transactions on Power System and Apparatus*, Vol. PAS-81, pp. 562-572, Aug. 1963.

[68] J.A. Tegopoulos, "Forces on the end Winding of Turbine-Generators, I- Determination of Flux Densities," *IEEE Transactions on Power System and Apparatus*, Vol PAS-85, pp. 105-113, Feb. 1966.

[69] J.A. Tegopoulos, "Forces on the end Winding of Turbine Generators, II- Determination of forces" *IEEE Transactions on Power System and Apparatus*, Vol PAS-85, pp. 114-122, Feb. 1966.

[70] J. Weiss and C.M. Stephens, "Finite Elements For Three-Dimensional Magnetic Fields and Its Applicationto Turbine Generator End Regions," *IEEE Transactions on Power System and Apparatus*, Vol PAS-100, pp. 1591-1596, 1981.

[71] K.R. Davey and E.J. King, "A Three Dimensional Scalar Potential Field Solution and Its Application to Turbine-Generator End Regions," *IEEE Transactions on Power System and Apparatus*, Vol PAS-100, pp. 2302-2310, 1981.

[72] F.L. Zeisler and J.R. Brauer, "Automotive Alternator Electromagnetic Calculations Using Three Dimensional Finite Elements," *IEEE Transactions on Magnetics*, Vol. 21, pp. 2453-2456, 1985.

[73] J.R. Brauer, G.A. Zimmerlee, T.A. Bush, R.J. Sandel and R.D. Schultz, "3D Finite Element Analysis of Automotive Alternators Under Any Load," *IEEE Transactions on Magnetics*, Vol. MAG-24, pp. 500-503, 1988.

[74] J.R. Brauer, E.A. Aronson, K.G. McCaughey and W.N. Sullivan, "Three Dimensional Finite Element Calculation of Saturable Magnetic Flux and Torques of an Actuator," *IEEE Transactions on Magnetics*, Vol. MAG-24, pp. 455-458, 1988.

[75] T.W. Nehl and D.A. Field, "Accuracy of Force Calculations Using First Order Tetrahedral for Electromagnetic Devices with Small Air Gaps," Paper No. FA-09, *The Fourth Biennial IEEE Conference on Electromagnetic Field Computation*, Toronto, Canada, Oct. 1990.

[76] G. Bollenbacher, "Description and Evaluation of Digital-Computer Program for Analysis of Stationary Outside-Coil Lundell Alternators," *NASA Report*, NASA TN D-5814, 1970.

[77] N.A. Demerdash and R. Wang, "Theoretical and Numerical Difficulties in 3-D Vector Potential Methods in Finite Element Magnetic Computations," *IEEE Transactions on Magnetics*, Vol. MAG-26, pp. 1656-1658, 1990.

[78] R. Wang and N.A. Demerdash, "On the Effects of Grid Ill-Conditioning in Three Dimensional Finite Element Vector Potential Magnetostatic Field Computations," *IEEE Transactions on Magnetics*, Vol. MAG-26, pp. 2190-2192, 1990.

[79] N.A. Demerdash, T.M. Hijazi and A.A. Arkadan, "Computation of Winding Inductances of Permanent Magnet Brushless DC Motor with Damper Windings by Energy Perturbation," *IEEE Transactions on Energy Conversion*, Vol. EC-3, pp. 705-713, 1988.

[80] O.A. Mohammed, "Magnetic Vector Potential Based Formulation and Computation of Nonlinear Three Dimensional Magnetic Fields and Forces in Electrical Devices," *Ph.D Thesis*, Virginia Polytechnic Institute and State University, 1983.

[81] M.V.K. Chari, and A. Konrad, Discussion to "Experimental Verification and Application of the Three Dimensional Finite Element Magnetic Vector Potential Method in Electrical Apparatus," *IEEE Transactions on Power Apparatus and Systems*, Vol. 100, pp. 4120, 1981.

[82] J. Simkin and C.W. Trowbridge, "On the Use of Total Scalar Potential in the Numerical Solution of Field Problems in Electromagnetics," *International Journal of Numerical Methods in Engineering*, Vol. 14, pp. 423-440, 1979.

[83] P. Tong, and J.N. Rossettos, *Finite Element Method Basic Technique and Implementation*, The MIT Press, Cambridge, Massachusetts, 1977.

[84] R.H. Gallagher, *Finite Element Analysis - Fundamentals*, Prentice-Hall, Inc., Englewood Cliffs, New Jersey, 1975.

[85] O.C. Zienkiewicz, *The Finite Element Method*, Third Edition, McGraw-Hill Book Company (UK) Limited, 1977.

[86] J.A. Stratton, *Electromagnetic Theory*, McGraw-Hill Book Company, 1941.

[87] R.L. Burden and J. Faires, *Numerical Analysis*, Third Edition, Pridle, Weber & schmiett, Boston.

[88] A.E. Fitzgerald, Charles Kingsler Jr and Stephen D. Umans, *Electric Machinery*, 4th Edition, McGraw-Hill Book Company, 1983.

Appendix A

A.1 Element Equation of the Unconstrained Curl-Curl MVP 3D-FE Formulation

The element equation of the unconstrained curl-curl MVP 3D-FE formulation using first-order tetrahedral elements was given in details by Demerdash et al in references [32, 33, 34]. This element equation can be rewritten here in a compact form as follows:

$$\begin{bmatrix} \underline{S}_{1,1} & \underline{S}_{1,2} & \underline{S}_{1,3} & \underline{S}_{1,4} \\ \underline{S}_{2,1} & \underline{S}_{2,2} & \underline{S}_{2,3} & \underline{S}_{2,4} \\ \underline{S}_{3,1} & \underline{S}_{3,2} & \underline{S}_{3,3} & \underline{S}_{3,4} \\ \underline{S}_{4,1} & \underline{S}_{4,2} & \underline{S}_{4,3} & \underline{S}_{4,4} \end{bmatrix} \begin{Bmatrix} \underline{A}_1 \\ \underline{A}_2 \\ \underline{A}_3 \\ \underline{A}_4 \end{Bmatrix} = \begin{Bmatrix} \underline{I}_1 \\ \underline{I}_2 \\ \underline{I}_3 \\ \underline{I}_4 \end{Bmatrix} \tag{A.1.1}$$

The coefficient matrix of (A.1.1) is a 12×12 square matrix. Each of the terms, $\underline{S}_{i,k}$, $i, j = 1, 2, 3, 4$, in the coefficient matrix is a (3×3) sub-matrix which can be written as

$$\underline{S}_{i,k} = Vol \left[\begin{array}{c|c|c} \nu_z \alpha_{i3}\alpha_{k3} + \nu_y \alpha_{i4}\alpha_{k4} & -\nu_z \alpha_{i3}\alpha_{k2} & -\nu_y \alpha_{i4}\alpha_{k2} \\ \hline -\nu_z \alpha_{i2}\alpha_{k3} & \nu_x \alpha_{i4}\alpha_{k4} + \nu_z \alpha_{i2}\alpha_{k2} & -\nu_x \alpha_{i4}\alpha_{k3} \\ \hline -\nu_y \alpha_{i2}\alpha_{k4} & -\nu_x \alpha_{i3}\alpha_{k4} & \nu_y \alpha_{i2}\alpha_{k2} + \nu_x \alpha_{i3}\alpha_{k3} \end{array}\right] \tag{A.1.2}$$

where, ν_x, ν_y, and ν_z are the elemental reluctivities, Vol is the volume of the tetrahedral element. In Equation (A.1.2), α_{ik}, $i,k = 1,2,3,4$, are the coefficients related to the geometry of the element, which are detailed in Appendix B of this dissertation.

The term, $\underline{A}_i$, for $i = 1,2,3,4$ in Equation (A.1.1), is a (3×1) sub-column-vector given by

$$\underline{A}_i = \begin{Bmatrix} A_{ix} \\ A_{iy} \\ A_{iz} \end{Bmatrix} \tag{A.1.3}$$

where, A_{ix}, A_{iy}, and A_{iz}, are the directional components of the nodal MVP, $\overline{A}_i$, at the i-th node of the tetrahedral element.

The term, $\underline{I}_i$, for $i = 1,2,3,4$, in the element forcing function of Equation (A.1.1), is a (3×1) sub-column-vector which can be written as follows:

$$\underline{I}_i = \begin{Bmatrix} J_x \dfrac{Vol}{4} \\ J_y \dfrac{Vol}{4} \\ J_z \dfrac{Vol}{4} \end{Bmatrix} \tag{A.1.4}$$

where, J_x, J_y, and J_z are the directional components of the known elemental current density vector.

A.2 Element Equation of the Constrained Curl-Curl MVP 3D-FE Formulation

According to reference [38], the element equation of the constrained curl-curl MVP 3D-FE formulation can be written as follows:

$$\begin{bmatrix} \underline{S}_{1,1} & \underline{S}_{1,2} & \underline{S}_{1,3} & \underline{S}_{1,4} \\ \underline{S}_{2,1} & \underline{S}_{2,2} & \underline{S}_{2,3} & \underline{S}_{2,4} \\ \underline{S}_{3,1} & \underline{S}_{3,2} & \underline{S}_{3,3} & \underline{S}_{3,4} \\ \underline{S}_{4,1} & \underline{S}_{4,2} & \underline{S}_{4,3} & \underline{S}_{4,4} \end{bmatrix} \begin{Bmatrix} \underline{A}_1 \\ \underline{A}_2 \\ \underline{A}_3 \\ \underline{A}_4 \end{Bmatrix} = \begin{Bmatrix} \underline{I}_1 \\ \underline{I}_2 \\ \underline{I}_3 \\ \underline{I}_4 \end{Bmatrix} \tag{A.2.1}$$

The coefficient matrix of (A.2.1) is a 12 × 12 square matrix. Each of the terms, $\underline{S}_{i,k}$, $i,j = 1,2,3,4$, in the coefficient matrix is a (3×3) sub-matrix which can be written as

$$\underline{S}_{i,k} = Vol \left[\begin{array}{c|c|c} \begin{array}{r}\nu_z a_{i3}a_{k3} \\ +\nu_y a_{i4}a_{k4} \\ +\lambda a_{i2}a_{k2}\end{array} & \begin{array}{l}-\nu_z a_{i3}a_{k2} \\ +\lambda a_{i2}a_{k3}\end{array} & \begin{array}{l}-\nu_y a_{i4}a_{k2} \\ +\lambda a_{i2}a_{k4}\end{array} \\ \hline \begin{array}{l}-\nu_z a_{i2}a_{k3} \\ +\lambda a_{i3}a_{k2}\end{array} & \begin{array}{r}\nu_x a_{i4}a_{k4} \\ +\nu_z a_{i2}a_{k2} \\ +\lambda a_{i3}a_{k3}\end{array} & \begin{array}{l}-\nu_x a_{i4}a_{k3} \\ +\lambda a_{i3}a_{k4}\end{array} \\ \hline \begin{array}{l}-\nu_y a_{i2}a_{k4} \\ +\lambda a_{i4}a_{k2}\end{array} & \begin{array}{l}-\nu_x a_{i3}a_{k4} \\ +\lambda a_{i4}a_{k3}\end{array} & \begin{array}{r}\nu_y a_{i2}a_{k2} \\ +\nu_x a_{i3}a_{k3} \\ +\lambda a_{i4}a_{k4}\end{array} \end{array}\right] \tag{A.2.2}$$

where, ν_x, ν_y, and ν_z are the elemental reluctivities, *Vol* is the volume of the tetrahedral element. In Equation (A.2.2), a_{ik}, $i,k = 1,2,3,4$, are the coefficients related to the geometry of the element, which are detailed in Appendix B of this dissertation. In Equation (A.2.2), λ is a parameter which sights to set the Coulomb Gauge condition, $\nabla \cdot \overline{A} = 0$, in the MVP solution. As recommanded in reference [38], this parameter can be chosen to be equal to the reluctivity, ν.

The term, $\underline{A}_i$, for $i = 1,2,3,4$, in Equation (A.2.1), is a (3×1) sub-column-vector given by

$$\underline{A}_i = \begin{Bmatrix} A_{ix} \\ A_{iy} \\ A_{iz} \end{Bmatrix} \tag{A.2.3}$$

where, A_{ix}, A_{iy}, and A_{iz}, are the directional components of the nodal MVP, $\overline{A}_i$, at the i-th node of the tetrahedral element.

The term, $\underline{I}_i$, for $i = 1,2,3,4$, in the element forcing function of Equation (A.2.1), is a (3×1) sub-column-vector which can be written as follows:

$$\underline{I}_i = \begin{Bmatrix} J_x \dfrac{Vol}{4} \\ J_y \dfrac{Vol}{4} \\ J_z \dfrac{Vol}{4} \end{Bmatrix} \tag{A.2.4}$$

where, J_x, J_y, and J_z are the directional components of the known elemental current density vector.

A.3 Element Equation of the Poisson Equation Based MVP 3D-FE Formulation

The element equation of the Poisson equation based MVP 3D-FE formulation was given in reference [37]. This element equation can be rewritten here as follows:

$$\begin{bmatrix} \underline{S}_{1,1} & \underline{S}_{1,2} & \underline{S}_{1,3} & \underline{S}_{1,4} \\ \underline{S}_{2,1} & \underline{S}_{2,2} & \underline{S}_{2,3} & \underline{S}_{2,4} \\ \underline{S}_{3,1} & \underline{S}_{3,2} & \underline{S}_{3,3} & \underline{S}_{3,4} \\ \underline{S}_{4,1} & \underline{S}_{4,2} & \underline{S}_{4,3} & \underline{S}_{4,4} \end{bmatrix} \begin{Bmatrix} \underline{A}_1 \\ \underline{A}_2 \\ \underline{A}_3 \\ \underline{A}_4 \end{Bmatrix} = \begin{Bmatrix} \underline{I}_1 \\ \underline{I}_2 \\ \underline{I}_3 \\ \underline{I}_4 \end{Bmatrix} \tag{A.3.1}$$

The coefficient matrix of (A.3.1) is a 12 × 12 square matrix. Each of the terms, $\underline{S}_{i,k}$, $i,k = 1,2,3,4$, in the coefficient matrix is a (3×3) diagonal type sub-matrix which can be written as

$$\underline{S}_{i,k} = \nu\, Vol \begin{bmatrix} \alpha_{i2}\alpha_{k2} + \alpha_{i3}\alpha_{k3} + \alpha_{i4}\alpha_{k4} & 0 & 0 \\ 0 & \alpha_{i2}\alpha_{k2} + \alpha_{i3}\alpha_{k3} + \alpha_{i4}\alpha_{k4} & 0 \\ 0 & 0 & \alpha_{i2}\alpha_{k2} + \alpha_{i3}\alpha_{k3} + \alpha_{i4}\alpha_{k4} \end{bmatrix} \tag{A.3.2}$$

where, ν is the elemental reluctivity, *Vol* is the volume of the tetrahedral element. In Equation (A.3.2), α_{ik}, $i,k = 1,2,3,4$, are the coefficients related to the geometry of the element, which are detailed in Appendix B of this dissertation.

The term, $\underline{A}_i$, for $i = 1, 2, 3, 4$, in Equation (A.3.1), is a (3×1) sub-column-vector given by

$$\underline{A}_i = \begin{Bmatrix} A_{ix} \\ A_{iy} \\ A_{iz} \end{Bmatrix} \tag{A.3.3}$$

where, A_{ix}, A_{iy}, and A_{iz}, are the directional components of the nodal MVP, $\overline{A}_i$, at the i-th node of the tetrahedral element.

The term, $\underline{I}_i$, for $i = 1, 2, 3, 4$, in the element forcing function of Equation (A.3.1), is a (3×1) sub-column-vector which can be written as follows:

$$\underline{I}_i = \begin{Bmatrix} J_x \dfrac{Vol}{4} \\ J_y \dfrac{Vol}{4} \\ J_z \dfrac{Vol}{4} \end{Bmatrix} \tag{A.3.4}$$

where, J_x, J_y, and J_z are the directional components of the known elemental current density vector.

Appendix B

In the work of 3D-FE formulation, one frequently deals with the element shape functions and their derivative terms:

$$N_i, \quad \frac{\partial N_i}{\partial u}, \quad \text{for } u = x, y, z \tag{B.0.1}$$

as well as the following type of integrations:

$$\int_{V_e} \frac{\partial N_i}{\partial u} dv, \qquad \text{for } u = x, y, z \tag{B.0.2}$$

where N_i is the shape function or interpolate coefficient of the finite element; V_e is the elemental volume. In the case of first order tetrahedral element, these shape functions are piecewise linear polynomials. According to the derivation work in references [32, 33, 34], such shape functions can be expressed using α-coefficients as follows:

$$\left.\begin{aligned} N_1 &= \alpha_{11} + \alpha_{12}x + \alpha_{13}y + \alpha_{14}z \\ N_2 &= \alpha_{21} + \alpha_{22}x + \alpha_{23}y + \alpha_{24}z \\ N_3 &= \alpha_{31} + \alpha_{32}x + \alpha_{33}y + \alpha_{34}z \\ N_4 &= \alpha_{41} + \alpha_{42}x + \alpha_{43}y + \alpha_{44}z \end{aligned}\right\} \tag{B.0.3}$$

Also shown in references [32, 33, 34], these α-coefficients can be obtained in terms of elemental nodal coordinates using the following equation:

$$\begin{bmatrix} \alpha_{11} & \alpha_{21} & \alpha_{31} & \alpha_{41} \\ \alpha_{12} & \alpha_{22} & \alpha_{32} & \alpha_{42} \\ \alpha_{13} & \alpha_{23} & \alpha_{33} & \alpha_{43} \\ \alpha_{14} & \alpha_{24} & \alpha_{34} & \alpha_{44} \end{bmatrix} = \begin{bmatrix} 1 & x_1 & y_1 & z_1 \\ 1 & x_2 & y_2 & z_2 \\ 1 & x_3 & y_3 & z_3 \\ 1 & x_4 & y_4 & z_4 \end{bmatrix}^{-1} \tag{B.0.4}$$

where, x_i, y_i, and z_i, $i = 1,2,3,4$, are the elemental nodal coordinates for the i-th node, $i = 1,2,3,4$, respectively. The explicit form of each α-coefficient was also given in references [32, 33, 34, 80].

Accordingly, based on (B.0.3) the partial derivatives of the shape functions with respect to x, y, and z, can be written as follows:

$$\left.\begin{aligned} \frac{\partial N_i}{\partial x} &= \alpha_{i2} \\ \frac{\partial N_i}{\partial y} &= \alpha_{i3} \\ \frac{\partial N_i}{\partial z} &= \alpha_{i4} \end{aligned}\right\} \qquad \text{for } i = 1,2,3,4 \tag{B.0.5}$$

Notice that the α-coefficients are constants within a given tetrahedral element. Thus, the integration terms in Equation (B.0.2) can be expressed in terms of the α-coefficients as follows:

$$\left.\begin{aligned} \int_{V_e} \frac{\partial N_i}{\partial x} dv &= (\alpha_{i2})\, Vol \\ \int_{V_e} \frac{\partial N_i}{\partial y} dv &= (\alpha_{i3})\, Vol \\ \int_{V_e} \frac{\partial N_i}{\partial z} dv &= (\alpha_{i4})\, Vol \end{aligned}\right\} \qquad \text{for } i = 1,2,3,4 \tag{B.0.6}$$

where Vol is the volume of the element. The α-coefficients are used in the computer program routines for various 3D-FE computations in this research.